THE INTERACTION BETWEEN DEEPWATER CHANNEL SYSTEMS AND GROWING THRUSTS AND FOLDS, TOE-THRUST REGION OF THE DEEPWATER NIGER DELTA

Thesis submitted for the degree of

Doctor of Philosophy and Diploma of Imperial College

By

Byami Andrew Jolly

Department of Earth Science and Engineering

Imperial College London

July 2014

THESIS DECLARATION

I certify that this thesis is the product of my own work, and the research was carried out under the supervision of Dr Lidia Lonergan and Dr Alexander C. Whittaker. Full citation and adequate referencing have been made where any material could be construed as the work of others. No part of this work has been previously submitted to this or any other academic institution for a degree or diploma, or any other qualification.

Byami A. Jolly

Department of Earth Science and Engineering

Imperial College London

COPYRIGHT

The copyright of this thesis rests with the author and is made available under a Creative Commons Attribution Non-Commercial No Derivatives licence. Researchers are free to copy, distribute or transmit the thesis on the condition that they attribute it, that they do not use it for commercial purposes and that they do not alter, transform or build upon it. For any reuse or redistribution, researchers must make clear to others the licence terms of this work.

ABSTRACT

The Niger Delta fold and thrust belt occurs in an area of tectonic shortening – caused by the thin-skinned gravitational collapse of large deltaic sediment wedges above a ductile overpressured shale. Syn-sedimentary processes such as down-slope flowing gravity currents interact with the deforming seafloor topography to produce growth packages that record the deformation history of the folds. The thesis documents the spatial and temporal interaction between Pleistocene to Recent submarine channels, and folds/thrusts that have been growing since 12.8 million years ago (Ma). 3D seismic reflection data and key stratigraphic/horizon ages are used to constrain and analyse the spatial and temporal variation in shortening of major folds having seabed relief. Geomorphic techniques were applied to quantify the geomorphic responses of submarine channels developing coevally with structural deformation.

This thesis documents two types of structures (fault-propagation folds and a detachment fold) whose cumulative strain (shortening) varies spatially and through time. The maximum interval shortening rate occurred between 9.5 Ma and 3.7 Ma, and has reduced significantly from that time to present. Channels show a range of interactions with structures, from simple deflection to fold tips to complete diversion. However, channels are capable of crossing the actively growing fault-propagation folds in positions of recent strain minima and at interval strain rates that are generally less than 15 m/Myr. In contrast, channels have been completely diverted by the broad detachment fold albeit growing at comparably lower rates. This thesis emphasizes that careful fold displacement – distance measurements which bracket the time interval of channel system development are very important for predicting sediment pathways in deepwater settings.

Detailed geomorphic analysis showed that the bathymetry longitudinal profiles of the active channels are relatively linear with concavity values that range from -0.08 to -0.34, with an average profile gradient between 0.9^{o} and 1^{o}. In contrast, channel systems that have been abandoned and buried for long period of time, have longitudinal profiles that are more convex. The profiles of both the active and buried channels are characterized by knickzones that are apparent near mapped structures – and implicitly record variations in substrate uplift rate. The recently active channels (the modern thalweg) show no systematic width change down-system but they do show an increase in incision depth/erosion of up to 70 % at structural locations. However, the channel system (made of several cut-and-fill sequences), shows clear width narrowing together with time-integrated incision and erosion in response to time-integrated structural uplift. Estimates of the down-system variation in channel bed-shear stress and flow velocity, using the thalweg-geometry of the active channels,

suggests that near growing folds and thrusts, the enhanced bed-shear stress-driven incision is up to 200 Pa. and the flow velocity is up to 5 m s^{-1}. In essence, the linear nature of the active channel profiles, in comparison to the convex nature of the buried channel profiles, suggests that the active channels are able to keep pace with the time-integrated uplift of folds and thrusts, and therefore appear to be in topographic steady-state with respect to structural uplift since at least 1.7 Ma.

Facies analysis using the seismic data showed that the main seismic facies include: (i) channel axes sands and top-channel sands (ii) sheet-sands or crevasse splays (iii) slump deposits and (iv) pelagic drapes. The growth of structures with seabed relief has affected the location of channel avulsion, the locus and the deposition/distribution of sheet-sands (splays). These splays can spill over the growing fault-propagation folds in areas of lower fold growth rates, and absence of seabed scarps; but are completely blocked, and subsequently incorporated onto the limb of a broad detachment fold in the east of the study area as incoming channels are forced to divert through time.

This thesis has contributed to the understanding of:

(1) Deformation by thrust-related folds that have been growing since ca. 12 Ma, and attained maximum interval growth rates between 9.5 Ma and 3.7 Ma. These maximum growth rates have reduced significantly in the last 3.7 million years during which submarine channels that are generally less than 1.3 million years old also occurred.

(2) How modern seabed channels (i.e., recently active channels) have responded to the time-integrated growth of structures along their paths; and the related effect on the positioning of channels pathways, which in-turn, governs the depositional system – especially the distribution of sands in the toe-thrust area of the deepwater Niger Delta.

(3) The time-integrated channel system erosivity, the evolution of the channel system geometry and the channel system fill as these systems interact with active structures through time.

(4) How submarine channels in the deepwater Niger Delta achieve, and maintain bathymetric steady-state over periods of approximately 1 – 1.3 million years.

TABLE OF CONTENTS

THESIS DECLARATION 2
COPYRIGHT 3
ABSTRACT 4
TABLE OF CONTENTS 6
LIST OF FIGURES 10
ACKNOWLEDGEMENTS 17

Chapter 1 18

INTRODUCTION AND LITERATURE REVIEW

1.1 Rationale 18
1.2 Overview of submarine channel system geometry: shelf to basin floor 20
1.3 Turbidity current sources and flow evolution 24
1.4 Structural impact on submarine channel geometry and longitudinal profile 26
1.5 Structural growth, accommodation space and controls on slope deposition models 28
1.5.1 Deepwater slope sedimentation models 29
1.6 Questions arising from the literature 30
1.7 Thesis aim and structure 32

Chapter 2 34

GEOLOGICAL SETTING AND DATASET

2.1 Location of Niger Delta and study area 34
2.2 Regional structural setting 36
2.3 Regional stratigraphy 37
2.4 3D seismic volume and age data 39

Chapter 3 41

GROWTH HISTORY OF FAULT-PROPAGATION FOLDS AND INTERACTION WITH SEABED CHANNELS IN THE TOE-THRUST REGION OF THE DEEPWATER NIGER DELTA

3.1 Introduction 41
3.2 Methods 44
3.2.1 Seismic interpretation 44
3.3 Results and observations 53
3.3.1 Structures and fold geometries 53
3.3.2 Channels and interaction with structures 58
3.3.3 Temporal and spatial variation in fold shortening 60
3.3.4 Strain variation and submarine channel response 64
3.4 Discussion 67
3.4.1 Strain rate reduction in the last 3.7 Ma 67
3.4.2 Fold growth 68
3.4.3 Channel response to active deformation 71
3.4.4 Shortening versus vertical uplift 72
3.4.5 Limitations 75
3.5 Conclusions 76

Chapter 4 78

QUANTIFYING GEOMORPHIC RESPONSE OF MODERN SUBMARINE CHANNELS TO ACTIVELY GROWING FOLDS AND THRUSTS, DEEPWATER NIGER DELTA

4.1 Study aims 78
4.2 Previous work 79
4.3 Existing constraints based on analysis in chapter 3 83
4.4 Methods 86
4.4.1 Seismic interpretation and DEM derivation 86
4.4.2 Channel morphometric parameters and long-profiles 86
4.4.3 Distribution of structural uplift down-channel system 91
4.5 Results 94
4.5.1 Modern seabed channels 94

4.5.2 Modern seabed channels profiles....98
4.5.3 Relationship between profile shape, structural uplift and channel geometry....100
4.5.4 Down-system evolution of channel shear stress and flow velocity....106
4.6 Discussion....111
4.6.1 Channel response to seabed structures: morphology....111
4.6.2 Channel response to seabed structures: deflection/diversion and incision....112
4.6.3 Are these channels in topographic steady-state?....115
4.7 Conclusions....119

Chapter 5....120
EVOLUTION OF PLEISTOCENE SUBMARINE CHANNELS IN RESPONSE TO THE GROWTH OF ACTIVE STRUCTURES FROM 3D SEISMIC ANALYSIS, NIGER DELTA

5.1 Introduction and previous work....120
5.2 Methods....124
5.3 Results....129
5.3.1 Container interaction with growing structures....129
5.3.2 Seismic expression of channel containers....134
5.3.3 Comparison of container and modern channel profiles....142
5.3.4 Active containers: profile, gradient, width and depth....144
5.3.5 Buried containers: profile, gradient, width and depth....149
5.4 Discussion....152
5.4.1 Container evolution: a combination of tectonic perturbations and channel processes....152
5.4.2 Fold uplift and the evolution of container fill over fold crest....155
5.4.3 Equilibrium long-profile: modern channel versus container....161
5.5 Conclusions....164

Chapter 6....165
STRUCTURAL CONTROLS ON SEISMIC FACIES DISTRIBUTION IN THE TOE-THRUST OF DEEPWATER NIGER DELTA

6.1 Introduction....165
6.2 Previous studies on deepwater structures and seismic facies....166
6.3 Descriptive terminology used in this study....170

6.4 Methods 171
6.4.1 Fold growth and submarine channels 171
6.4.2 Seismic facies analysis 172
6.4.3 Seismic attributes analysis 176
6.5 Results 177
6.5.1 Channel-axis sands and levees 177
6.5.2 Sheet-sands (splays) and relationship to structures in the west 183
6.5.3 Syn-kinematic sedimentation in the east, north of Fold C 186
6.5.4 Channel/sheet-sand evolution in the piggyback basin 189
6.6 Discussion 194
6.6.1 Summary of the main points and interpretations 194
6.6.2 Controls on facies distribution and facies architecture 196
6.7 Conclusions 199

Chapter 7 200

DISCUSSION

7.1 Growth history of folds/thrusts and their effects on channel pathways 201
7.1.1 Comparison with fluvial settings 203
7.2 Controls on channel geometry and long-profiles 205
7.3 Controls on container architecture and seismic facies distribution 208
7.4 What are the circumstances in which channels can cut across growing folds and thrusts in deepwater fold and thrust belts? 210
7.5 General study application 214
7.6 Research limitations 215
7.7 Further work 216

Chapter 8 218

CONCLUSIONS

References cited 222

LIST OF FIGURES

Figure 1.1: (a) 3D sketch of a passive margin setting (after Nelson et al., 2009) showing a submarine channel system – from shelf to basin floor; and seismic sections (b), (c) and (d) and a sketch (e) from Babonneau et al. (2004) and Stow and Mayall (2000). 22

Figure 1.2: Types of submarine mass flows [a], [b] and [c], which are generally distinguished based on the degree of internal deformation and sediment-fluid mixture; and [d] shows turbiditic flow generation/transformation (Figure from Covault, 2011). 25

Figure 1.3: Shows a schematic diagram of the equilibrium profile model for slope and deepwater settings modified from Ferry et al. (2005). 27

Figure 2.1: Map showing the location of the Niger Delta region and associated sedimentary basins and tectonic features (After Corredor et al., 2005). 35

Figure 2.2: (a) Map of the Niger Delta region showing structural zonation (modified from Corredor et al., 2005); (b) regional seismic profile across the Niger Delta (modified from Corredor et al., 2005); (c) regional stratigraphy of the Niger Delta showing delta progradation from the NE to the NW (from Corredor et al, 2005). 38

Figure 2.3: (a) Map of the Niger Delta mega-survey (by PGS) showing the study area located in OPL block 256; (b) is a confidential tie-line X – Y (provided by Shell-Nigeria) showing stratigraphic ages that were used to calibrate seismic reflections in the 3D survey 40

Figure 3.1: (a) 3D bathymetry map; and (b) edge-attribute map of the seabed over the study area showing studied channel systems and actively growing structures. 45

Figure 3.2: A dip-orientated section showing the general structural style in the west of the study area.. 46

Figure 3.3: Diagram showing the methodology for measuring strain based on the concept of line-length balancing. 49

Figure 3.4: Representative sections across Folds A and Fold B in the study area, illustrating potential seismic interpretation problems and how they are treated.. 50

Figure 3.5: (a) Seismic section across Fold A showing the stratigraphic horizons used for strain measurement; (b) graph of cumulative strain measured from stratigraphic horizons shown in Figure 3.5a; (c) is the interval strain rates derived from Figure 3.5b. 51

Figure 3.6: Isochron map of the growth sequence interval over the study area showing a series of NW – SE orientated depocentres and growing folds. 53

Figure 3.7: (a) and (c) are un-interpreted, and (b) and (d) are interpreted sections across Fold A respectively. 55

Figure 3.8: (a) and (c) un-interpreted, and (b) and (d) interpreted sections across Fold B respectively; (e) and (f) un-interpreted and interpreted section across Fold D. 56

Figure 3.9: (a) and (b) represent un-interpreted section, and interpreted versions of a section across Fold C. 57

Figure 3.10: (a) uninterpreted; (b) interpreted seismic section across a buried channel system, and channel 4 illustrating the geometry of the studied channel systems, and how the downlap surface of channels levees is used as a proxy to estimate channel age; (c) a geomorphic map of the seabed showing details of channel – structure interactions..... 59

Figure 3.11: (a) Plots of cumulative strain against stratigraphic age determined from representative sections in the study area; (b) plots of interval strain rate against stratigraphic age. 61

Figure 3.12: Shows the plots of cumulative strain for horizons at 23.2, 7.4, 3.7 Ma and present day seabed along the strike of Folds A to D. 63

Figure 3.13: Shows examples of cumulative strain, seabed map and measured interval strain rates for Folds A to D at channel locations. 65

Figure 3.14: Sketched diagrams (a) to (d) illustrating end-member relationship between structural uplift rate and sediment accumulation rate 68

Figure 3.15: (a) Section across Fold A showing mainly overlapping seismic horizons over the structure since 3.7 Ma; (b) section across Fold D also showing the same geometric relationship as in (a); (c) section across Fold C showing seismic horizons which largely onlap the growing structure since 3.7 Ma. 70

Figure 4.1: (a) 3D depth-structure map of the seabed over the study area showing the modern, seabed channel systems and growing structures at, or near the seabed; (b) a graph of cumulative strain through time for four folds (Fold A – D) and (c) shows the interval strain rates over the last 3.7 Ma derived from Figure 4.1b 85

Figure 4.2: (a) Shows the plan-view sketch of a channel system and the method for extracting bathymetry long profile; (b) is a sketched section across the channel system in (a) showing the method for measuring channel morphometric parameters. 90

Figure 4.3: (a) A diagram describing how to measure, and use sediment thickness as a proxy for the relative structural elevation of horizons from long channel profiles; (b) seismic section taken along channel 1 showing relative structural elevation of the 3.7 Ma and the 1.7 Ma horizons; (c) shows the result of the relative uplift of the 3.7 Ma and the 1.7 Ma horizons measured using the seismic section shown in Figure 4.3b; (d) shows the result of cumulative strain along the strike of Fold B/E. 93

Figure 4.4: shows the 3D depth-structure map of the seabed in the study area showing modern channels and structures that occur at, or near the seabed; and representative graphs that show plots of water depth against transect distance for four channels depicted on the map. 96

Figure 4.5: Shows the frequency distribution of channel depths and widths for: channel 1 (a) and (b); channel 2 (c) and (d); channel 3 (e) and (f); and channel 4 (g) and (h)..... 97

Figure 4.6: (a) Shows modern seabed long-profiles of channels 1, 2, 3 and 4, and the variations in down-system gradient; (b) shows the normalised modern channel profiles..... 99

Figure 4.7: (a), (b), (c) and (d) Show the relationship between relative uplift along the paths of channels 1, 2, 3 and 4 respectively; and the geomorphic responses of the channel systems to fold uplift since 1.7 Ma..... 102

Figure 4.8: Shows the plot of aspect ratio of the modern channels in the study area, against channel slope. 105

Figure 4.9: (a), (b), (c) and (d) show the down-system variations in bed-shear stress and flow velocity in response to fold uplift along the paths of channels 1, 2, 3 and 4 respectively 109

Figure 4.10: A graph showing plots of fold uplift versus excess channel incision since 1.7 Ma; testing whether the modern channels are in a topographic (bathymetric) steady-state. 118

Figure 5.1: Schematic diagram of an erosionally to valley-confined channel belt complex (a), and a valley-fill complex set (b) all from Janocko et al. (2013); (c) shows a 3rd order channel complex system and sub-divisions from Jones et al. (2012); (d) is a 3D bathymetry map; and (e) is an edge-attribute map of the seabed over the study area. 123

Figure 5.2: (a) Transect across active channel 4 showing channel geometry in the study area, and how the several cut-and-fill sequences are bounded within an erosionally-confined surface called the container; (b) shows a 3D sketch representing the channel container across growing structures; (c) and (d) illustrate the methodology of measuring channel system morphometric parameters. 128

Figure 5.3: (a) Shows the 3D perspective view of all the mapped channel containers including those that are buried; (b) is an RMS amplitude map showing the spatial relationship between channel systems (including buried ones) and structures (including buried ones) in the study area. 132

Figure 5.4: (a) Map showing growing structures (folds/thrusts) with seabed relief and those truncated by submarine channels; and (b) shows a similar map which also contain buried channel container systems. 133

Figure 5.5: (a) Seismic section along-active container 4; (b), (c) and (d) are transects across the same container. 137

Figure 5.6: (i) Seismic section along -buried container 2; (ii), (iii) and (iv) are transects across the same container. 139

Figure 5.7: (a) and (b) Un-interpreted and interpreted version of an RMS amplitude map showing evidence of westward shifts in buried channel 2 container through time. 140

Figure 5.8: Un-interpreted (a), (c); and interpreted (b), (d) seismic sections across buried container 2 showing evidence of westward channel migration 141

Figure 5.9: Normalised modern channel profiles; and the active container, and buried container profiles.. 143

Figure 5.10: (a); (b) Graphs of modern channel profiles and their associated container profiles along channels 3 and 4 respectively; (c); (d) are graphs of container width and container depth for containers 3 and 4 respectively; (e); (f) are graphs of modern channel width and modern channel incision for channels 3 and 4 respectively.. 146

Figure 5.11: Graphs of container depth versus modern channel incision down-system of active containers 1 – 4; and the graphs of container depth versus preserved container fill thickness measured along the centre of the active containers. 148

Figure 5.12: (a), (c) and (e) Are buried containers 1, 2 and 5 profiles and their slopes repectively; (b), (d) and (f) are plots of container width and container depth in buried containers 1, 2 and 5 respectively. 151

Figure 5.13: (a) Schematic diagram of stacking patterns of cut-and-fill channels within a channel complex showing lateral migration and aggradation (Modified from Kolla et al. 2007); (b) is a schematic diagram of a channel-levee complex that developed purely by compensational stacking through time (from Janocko et al., 2013). 154

Figure 5.14: (a) Sketch of a channel profile across a growing fold, with knickpoint; and the predicted channel incision and abandonment fill (b); and (c) is a sketch illustrating the down-system variations in preserved, time-integrated container fill due to continued fold growth and channel incision through time. 159

Figure 5.15: (a) and (b) and (c) Are graphs of modern channel profile and container profile, preserved thickness of the container fill, modern channel incision and the apparent distribution of uplift derived by differencing the modern profile from the container profile for active containers 4 , 3; and buried container 1 respectively. 160

Figure 5.16: Schematic diagrams (a) to (f) describing the processes by which channel systems in the study area attain equilibrium profile 163

Figure 6.1: (a) and (b) show amplitude maps of submarine channels; (c) and (d) are seismic sections A – A' and B – B' in Figure 6.1a and 6.1b respectively; (e) is an amplitude map showing channels with associated frontal splays; (f) is a section along the frontal splays shown in Figure 6.1e. These figures are from Cross et al. (2009) and Janocko et al. (2013) 169

Figure 6.2: (a) Edge-attribute map of the seabed in the study area showing the outline of major folds having seabed relief, and modern seabed channel systems and a buried channel; (b), (c) and (d) are section lines across folds in Figure 6.2a 174

Figure 6.3: (a) Transect across the buried channel 5 and active channel 4 showing the different seismic facies in the study area; (b) shows the methodology for iso-proportional slicing of the Pleistocene channel interval within the piggyback basin in the study area. 175

Figure 6.4: (a) Shows the RMS amplitude maps of the channel containers (extracted from both active and buried channel systems) draped on the seabed edge-map of the study area; (b) is an enlarged area in Figure 6.4a; and (c) is a section across active channel 1 container showing high amplitude channel-axis reflections at the base of the container 180

Figure 6.5: (a) Transects across active channel 4 container showing the seismic characteristic of an active channel fill 181

Figure 6.6: (a) to (d) Transects across buried channel 1 and 5 containers showing the seismic characteristics of the various facies within the containers.. 182

Figure 6.7: (a) Shows RMS amplitude map calculated using a time window of 10 ms and 20 ms above and below the high amplitude splay horizon; (b) and (c) show seismic sections across splays 1 and 2 in Figure 6.7a..... 185

Figure 6.8: (a) Shows the two-way-time thickness map of the Plio-Pleistocene channel interval within the piggyback basin in the study area; (b) shows a seismic section across the piggyback basin; and (c) shows the interpreted version of the section..... 188

Figure 6.9: Show zone-RMS amplitude maps of the Pleistocene channels interval within the piggyback basin: (a) zone 4, (b) zone 3 and (c), is a seismic section showing northward shift of channel systems within zones 4 and 3..... 191

Figure 6.10: Shows zone-RMS amplitude maps of the Pleistocene channels interval within the piggyback basin: (a) zone 2, (b) zone 1; and (c) seismic section showing channel/sheet-sands development in zones 2 and 1. 192

Figure 6.11: (a) and (b) are the edge-map and dip-azimuth map of the top horizon in Sands 'X' draped on seabed edge-map; (c) is an E – W seismic section showing the seismic characteristics of the sands 'X' 193

Figure 6.12: Shows cartoon description of structural controls on sheet-sands (splays) distribution in the west of the study area (a); and within the piggyback basin in the east of the study area (b). 198

Figure 7.1: Shows sketches; (a) and (b) respectively show a map-view and section of a broad fold that is associated with more than 5 km counter-regional dip and c.140 m topographic height; (c) and (d) respectively show a map-view and section of a narrow fold that is associated with less than 2 km counter-regional dip and c.80 m topographic height; and (e), (f) show a fold characterized by a hiatus in growth and coeval channel development..... 213

LIST OF TABLES

Table 1.1: Shows the dimensions of some modern fan/channel systems associated with different sea-level states..... 23

Table 3.1: Shows the measurements of maximum shortening and shortening rate; strain and strain rate since 3.7 Ma across the fault-propagation folds (A, B and C) and the detachment fold (Fold C) in the study area.. 75

ACKNOWLEDGEMENTS

I would like to thank my supervisors (Dr Lidia Lonergan and Dr Alex Whittaker) for the privilege of working with them. It had been a rewarding experience working with you both, especially having to learn and integrate your expertise for a better insight into channel – structure interactions in deepwater Niger Delta.

Special thanks to Petroleum Technology Development Fund (PTDF), Nigeria for funding the PhD research.

I am grateful to Petroleum Geo-Services (PGS) for providing the 3D seismic reflection data used for this research, and for the permission conceded to publish this thesis. I also thank Shell – Nigeria (specifically Bruce Levell) for providing the age data; and Landmark is acknowledged for the provision of seismic interpretation software. I am highly indebted to you all.

I would like to also thank Professor Sanjeev Gupta and Professor Hugh Sinclair for agreeing to examine the thesis, and for their constructive comments towards making the results of this research more meaningful.

My gratitude goes to God for the reason I am alive, healthy and able to pursue a PhD research. I would not forget my dear Parents who believed in me, and have encouraged and prayed for me every day of my life. Special gratitude to Felmum, De-Best (Marvel) and Juniour for their unconditional support, I love you all.

Finally, I would like to thank all my friends wherever they may be, and PhD colleagues here at Imperial for their support and encouragement. Nuff-respect!

CHAPTER 1

INTRODUCTION

1.1 RATIONALE

Deepwater fold and thrust belts, such as the Niger Delta toe-thrust region, occur where shortening is driven by the thin-skinned gravitational collapse of large deltaic sediment wedges above a ductile substrate, such as overpressured shale (e.g., Niger Delta) or salt (e.g., the Gulf of Mexico and offshore Angola). Syn-sedimentary processes such as down-slope flowing gravity currents interact with the deforming seafloor topography to produce growth packages that record the history of deformation, and can also be important hydrocarbon targets in deepwater settings. While considerable work has addressed submarine channel geometry, evolution and associated depositional facies on passive margins (e.g., Normark, 1970, 1978; Damuth and Flood, 1985; Damuth et al., 1983, 1988; Mutti and Normark, 1987, 1991; Mayall and Stewart, 2000; Posamentier and Kolla, 2003; Deptuck et al., 2003, 2007; Mayall et al., 2006; Kolla et al., 2007 amongst many), and the geological structures of the associated deltaic deposits (e.g., Morley and Guerin, 1996; Cohen and McClay, 1996; Wu and Bally, 2000; Rowan et al., 2004; Billoti and Shaw, 2005; Corredor et al., 2005; Higgins et al., 2009; Maloney et al., 2010 amongst many), only a handful of studies have exploited the growing availability of 3D seismic reflection data to explore the *interactions* between deepwater channels and seafloor structures (e.g., Pirmez et al., 2000; Huyghe et al., 2004; Ferry et al., 2005; Gee and Gawthorpe, 2006; Gee et al., 2007; Henio and Davies, 2007; Clark and Cartwright, 2009, 2011; Mayall et al., 2010; Geogiopoulou and Cartwright, 2013 amongst others). This is in direct contrast to channels in terrestrial settings, where a large body of work now documents the detailed interactions between fluvial incision and active faulting from both field and modelling perspectives (e.g., Howard, 1994; Whipple and Tucker, 2002; Tucker and Bras, 1998; Tucker and Whipple, 2002; Whittaker et al., 2007a; Whittaker et al., 2008; Yanites et al., 2011). However, a better understanding of this interaction in deepwater setting is a particularly important problem to address, owing to the fact that active geological structures at, or near, the seabed in deepwater settings constantly affect submarine channel pathways, their geometry (width, depth), and hence, how they evolve and distribute sediment over a range of geological time scales.

In this thesis, I have used 3D seismic data covering an area of approximately 2500 km^2 in the toe-thrust region of the deepwater Niger Delta, to carry out a linked structural and sedimentological analysis of the Plio-Pleistocene channel systems and actively growing folds and thrusts in the study area. A detailed analysis of the development and interactions between features such as thrust-related folds, submarine channel levee systems and growth sequences was carried out with the view to constraining the history of fold growth both along and across strike. The thesis also documents how submarine channels respond to detailed changes in timing and rate of fold growth over time. The spatio-temporal variations in submarine channel geometry and erosivity are also documented with the view to understanding the circumstances in which submarine channels are capable of cutting across growing faults and folds. Consequently, this PhD research project aims to increase our knowledge of how sedimentary systems interact with growing structures in deep water settings, and more specifically, to develop better insights into the general principles that govern the evolution of these submarine channel systems in response to active shortening, and the implications this has for understanding the pathways, characteristics and locus of channels in such settings. This information is particularly important given the growing focus on deepwater reservoirs in the petroleum industry.

1.2 OVERVIEW OF SUBMARINE CHANNEL SYSTEM GEOMETRY: SHELF TO BASIN FLOOR

Submarine channel systems are commonly associated with major fan systems (e.g., Amazon Fan, Mississippi Fan and the Congo/Zaire Fan), sourced from large rivers and deltas, that develop in passive margin settings such as the Equatorial Atlantic and the Gulf of Mexico (Fig. 1.1a; Nelson et al., 2009). These systems typically extend for several kilometres (Fig. 1.1a) from the shelf (water depth <200 m) to the basin floor (up to water depths of 4800 m). For example, the Amazon Fan has a total length of up to 700 km, and the Zaire Fan is approximately 1200 km long (Damuth and Flood, 1984, 1985; Damuth et al., 1988; Babonneau et al., 2002; Savoye et al., 2009; Nelson et al., 2009; Talling et al., 2013). A typical passive margin is characterised by deltaic/fluvial systems on the shelf, and major canyons that link the deltaic systems to the deepwater channels located on the slope (Fig. 1.1a; Babonneau et al., 2002; Savoye et al., 2009; Nelson et al., 2009). These feeder canyons can be > 15 km in width and have a relative relief of up to 1 km (Fig. 1.1b, Table 1.1; Damuth and Flood, 1984; Shanmugam and Moiola, 1988; Babonneau et al., 2002; Pirmez and Imran, 2003; Savoye et al., 2009). They are characterised by V-shaped geometries because of active incision (Fig. 1.1b,c; see also Stow and Mayall, 2000); and they serve as the conduit for sediment supply, through turbidity currents to the channel system located down-slope (e.g., Damuth et al., 1988; Babonneau et al., 2002; Babonneau et al., 2010; Covault and Graham, 2010; Covault, 2011; Nelson et al., 2009). However, most canyons are disconnected from their sediment source during sea level high-stands, which is typically manifested in a slow growth of the associated fan (e.g., the Amazon Fan, Table 1.1; Damuth et al., 1988). Notable exceptions do exist where the canyon remains connected to the sediment source during sea level highstand, such as the Congo/Zaire Fan and the Mississippi Fan, (Table 1.1; Shanmugam and Moiola, 1988; Babonneau et al., 2002; Babonneau et al., 2010; Covault and Graham, 2010). Between the upper fan-valley and middle fan-valley, the upper channel-levee systems occur, and are characterised by erosionally V-shaped to less erosionally U-shaped geometries (Fig. 1.1d; see Stow and Mayall, 2000; Babonneau et al., 2002, 2004; Savoye et al., 2009). This zone is characterised by submarine channels whose relief is typically a few hundred metres, with widths that are less than 4 kilometres (Babonneau et al., 2002, 2004; Mayall et al., 2006; Savoye et al., 2009). Between the middle fan and the lower fan zones, lower channel-levee systems dominate (Babonneau et al., 2002, 2004; Savoye et al., 2009), and are characterised by well-developed channel-levee systems with typical channel relief and width of up to 150 m and 1.5 km respectively (Fig. 1.1e; Stow and Mayall, 2000; Savoye et al., 2009). In the seaward, distal-end of the system (lower fan areas), terminal fan-lobe complexes occur on the basin floor. This marks the most basinward limit of deposition for any turbidity current. The lobes in these regions are characterised

by compensationally stacked, small-scale distributary channels/lobe systems (Fig. 1.1a; see also Straub et al., 2009). Overall, these seismic sections (sections b, c and d) from Babonneau et al. (2004) down-system of the Congo/Zaire Fan, and a schematic representation (section e) from Stow and Mayall (2000) show a typical example of the systematic variation in submarine channel system geometry from the canyon areas to the basin floor lobe areas. In essence, there is a general decrease in channel width and depth of incision down-system which is partly a function of the change in the regional gradient. Higher gradients of up to 0.8^{o} occur in the upper slope close to the sources of the turbidity currents (e.g., Savoye et al., 2009). However, the presence of actively growing structures such as faults and folds on the slope also contribute to the down-system evolution of channel geometries as the channels interact with these structures over time (see also Pirmez et al., 2000; Huyghe et al., 2004; Ferry et al., 2005; Gee and Gawthorpe, 2006 amongst many). This study focuses on the channel – structure interaction on the lower slope/toe-thrust region of the submarine channel system, using the deepwater Niger Delta as a case study.

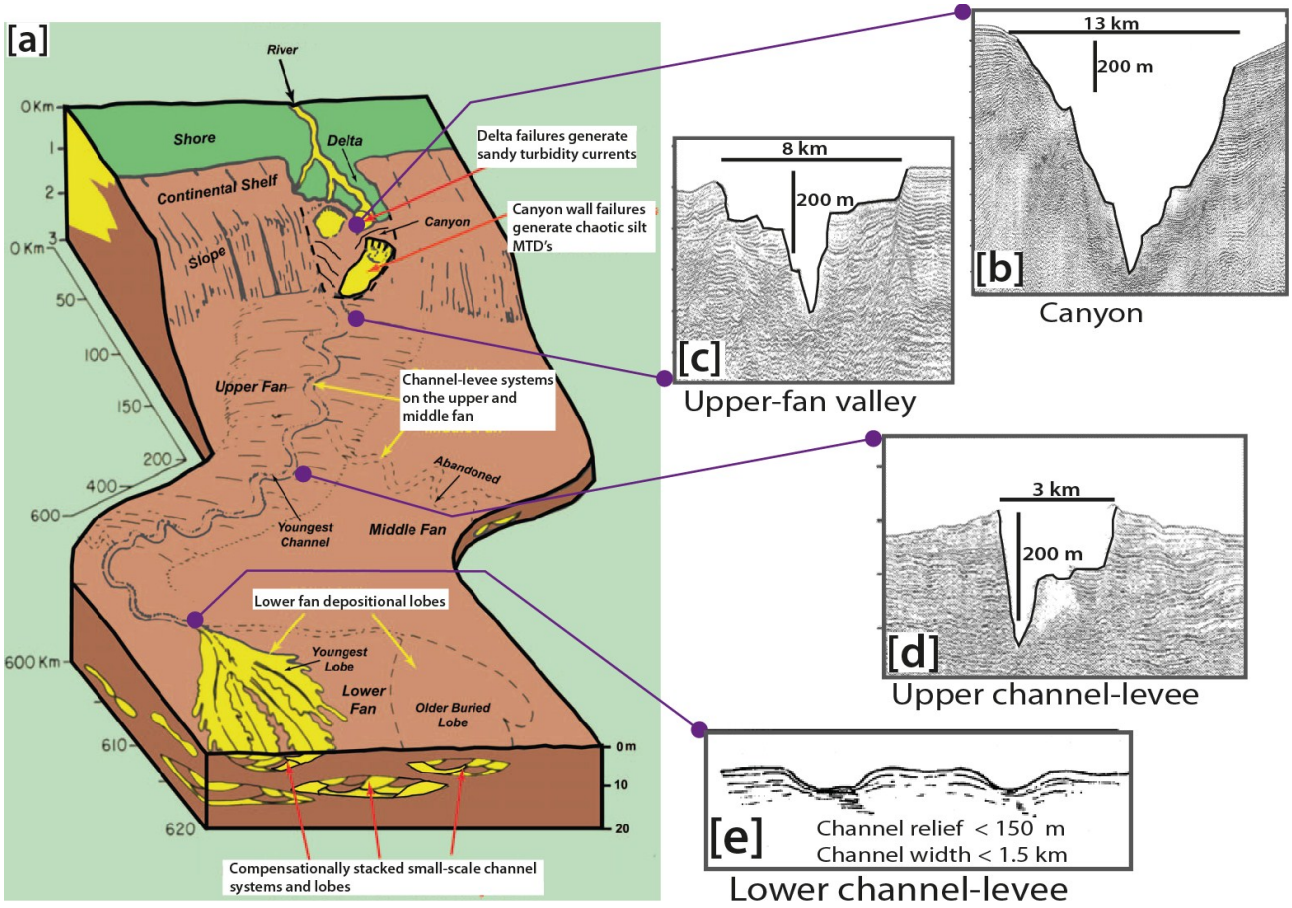


Figure 1.1: (a) 3D sketch of a passive margin setting (after Nelson et al., 2009) showing a submarine channel system – starting from the shelf/delta area, to the canyon system on the slope, to sinuous channels on the upper – middle fan area, and a depositional lobe on the basin floor/lower fan area. Seismic sections (b), (c) and (d) are from Babonneau et al. (2004); and the schematic representation (e) is from Stow and Mayall (2000). These sections show the typical down-system variation in submarine channel geometry from the canyon areas to the lower fan areas.

Fan/Location	Characteristics	
Amazon Fan/Equatorial Atlantic	**Tectonic settings**	Mature passive margin
	Associated sea-level state	Maximum Growth during sea-level low stand and disconnected from river mouth during Holocene sea-level high stand
	Maximum thickness of fan (m)	Up to 4200
	Length of canyon (km)	About 250
	Width of canyon (km)	3-15
	Depth of canyon (m)	250-600
	Levee width (km)	50
	Passive margin type	Atlantic type
Mississippi Fan/Gulf of Mexico	**Tectonic settings**	Mature passive margin
	Associated sea-level state	Maximum growth during transgression
	Maximum thickness of fan (m)	Up to 4000
	Length of canyon (km)	About 400
	Width of canyon (km)	2-15
	Depth of canyon (m)	150-450
	Levee width (km)	50
	Passive margin type	Atlantic type
Congo (Zaire) Fan/ equatorial atlantic	**Tectonic settings**	Mature passive margin
	Associated sea-level state	Maximum growth during sea-level high stand and connected to river mouth during Holocene (still active today)
	Maximum thickness of fan (m)	-
	Length of canyon (km)	About 135
	Width of canyon (km)	0-15
	Depth of canyon (m)	0-1300
	Levee width (km)	10-15
	Passive margin type	Atlantic type
sources: Damuth and Flood, 1984, 1985; Shanmugam & Moiola, 1988; Babonneau et al., 2002, 2010; Savoye et al., 2009; Covault and Graham, 2010.		

Table 1.1: Showing the dimensions of some modern fan/channel systems associated with different sea-level states.

1.3 TURBIDITY CURRENT SOURCES AND FLOW EVOLUTION

The process of turbidity current flow initiation, transport/evolution and deposition are varied and complex (e.g., Middleton and Hampton, 1973; Hampton et al., 1996; Stow and Mayall, 2000; Nelson et al., 2009; Covault, 2011; McHargue et al., 2011). Sediment failures on the shelf-edge are in various forms (e.g., Fig. 1.1a), and are often triggered by different factors which may include; instability of earlier sediments as a result of over-steepening, storm wave-induced failure, seismically induced failure as a result of an earthquake amongst others (e.g., Shepard et al., 1977; Prior et al., 1989; Piper et al., 1985; Friedman et al., 1992; Nelson et al., 2009). The product of these failure can be in the form of a slide – where a coherent mass of sediments bounded on all sides by distinct failure plane occurs, and the internal structure of the removed material is largely undisturbed during transportation (Fig. 1.2a; Middleton and Hampton, 1973; Shanmugam, 2006; Covault, 2011; Nelson et al., 2009); or a slump – where the detached sediments may break up into smaller blocks that exhibit some internal deformation during transportation (Fig. 1.2b; Middleton and Hampton, 1973; Shanmugam, 2006; Covault, 2011; Nelson et al., 2009). If the internal deformation is high, in situations where the entire body of sediments is thoroughly mixed with ambient fluid (i.e., sea water), the sediments become fluidised and flow rather than slide or slump, thereby forming what is known as a turbidity current (Fig. 1.2c; Shanmugam, 2006; Covault, 2011; Nelson et al., 2009). Therefore, subaqueous gravity-driven processes that initiate either by sliding, slumping or debris flow (Nelson et al., 2009), may transform dynamically during transport between the shelf-edge and the basin floor where they are deposited (Fig. 1.2d; Hampton et al., 1996; Stow and Mayall, 2000; Covault, 2011). For example, on reaching a steeper slope, the moving mass is accelerated due to enhanced gravitational pull, and the flow tends to become turbulent, and increasingly incorporates entrained sea water into the sediment-fluid mixture and becomes a turbidity current (Fig. 1.2d; Bagnold, 1962, Middleton and Hampton 1973; Piper et al., 1985). Deposits from these currents are known as turbidites (Fig. 1.2d; see also Bouma, 1985). These turbidites are not only deposited at the basin floor (Fig. 1.2d), but can also be deposited on the slope as the turbidity current interact with structures on the slope (e.g., Normark et al., 1980; Hackbath and Shaw, 1994; Mayall and Stewart, 2000; Wynn et al., 2000a, 2000b; Posamentier and Kolla, 2003; Mayall et al., 2006; Cross et al., 2009). Modelling of flows within submarine channels has provided some insight into the evolution of turbiditic flows, the vertical velocity distribution, and how they distribute sediments along their paths (e.g., Imran et al., 1999; Peakall et al., 2000; Kneller, 2003; Das et al., 2004; Corney et al., 2006; Straub et al., 2008 and many more). However, the main challenge in understanding turbiditic flow processes and evolution, including their erosivity and how they disperse sediments comes from our

inability to fully constrain the variations in turbiditic flow parameters such as sediment concentration, flow velocity, and bed-shear stress, and relate them to channel behaviour in response to tectonic perturbations. Moreover, only a few direct measurements of these parameters have been reported (e.g., Pirmez and Imran, 2003; Meiburg and Kneller, 2010; Xu et al., 2004, 2010; Xu, 2011; Talling et al., 2012, 2013). For example, the velocities of submarine flows that run beyond the continental slope to the basin floor have only been documented accurately by cable breaks or instruments at 5 locations worldwide since 1929 Grand Banks event, while their sediment concentration has yet to be directly measured (Meiburg and Kneller, 2010; Talling et al., 2012). Sediment concentration of real turbiditic flows has only been measured twice using monitoring instruments on the Monterey Canyon – with limited success because of the current's destructive nature (Xu et al., 2004; Xu, 2011; Talling et al., 2012). Moreover, very few studies have directly measure turbiditic flow velocities at different heights above bed (i.e., velocity profile; see Xu et al., 2004, 2010; Xu, 2011). Consequently, much of the current understanding of real turbiditic flows behaviour comes from rock record and from observations on the modern sea floor (Talling et al., 2012, 2013).

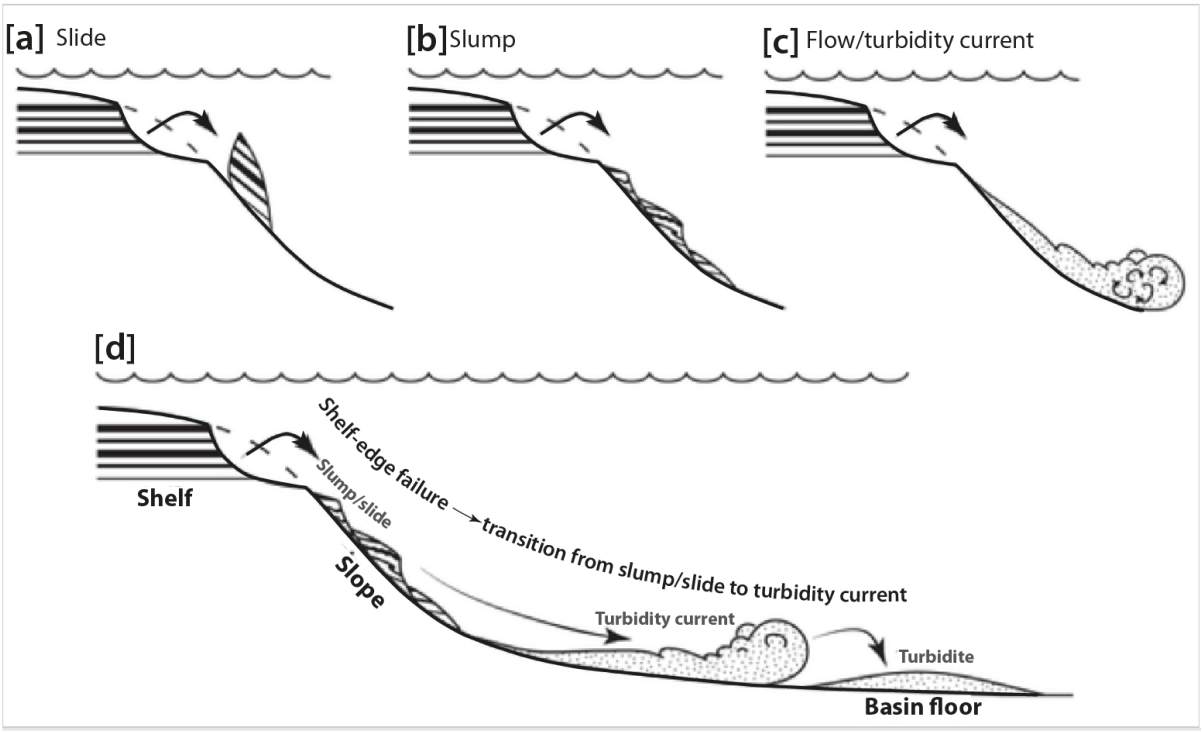


Figure 1.2: Types of submarine mass flows [a], [b] and [c], which are generally distinguished based on the degree of internal deformation and sediment-fluid mixture; and [d] shows flow transformation/evolution from shelf-edge slump/slide to turbidity current on the slope and basin floor (Figure from Covault, 2011).

1.4 STRUCTURAL IMPACT ON SUBMARINE CHANNEL GEOMETRY AND LONGITUDINAL PROFILE

Submarine channels geometry in deepwater slopes are generally U-shaped with relatively high aspect ratios (e.g., Clark and Pickering, 1996; Stow and Mayall, 2000; Deptuck et al., 2003, 2007); however, tectonic perturbations produced by structures growing on the slope cause these channels to respond by changing their shapes to a more V-shaped geometry as they increase their incision in structurally active domains (e.g., Pirmez et al., 2000; Huyghe et al., 2004; Ferry et al., 2005; Heinio and Davies, 2007; Gee and Gawthorpe, 2006). The changes in channel geometry in these structural domains also affect the longitudinal profiles of these channels. Moreover, at a basin-scale, the longitudinal profiles of submarine channels have been reported to vary from setting to setting (e.g., Covault et al., 2011). For example, some systems have profiles that are concave-up (e.g., the Amazon Fan and the Congo/Zaire Fan). However, studies have shown that the Niger Delta submarine channels have linear to quasi-linear shapes (Pirmez et al., 2000; Covault et al., 2011). Some studies suggest that this is related to the type of continental margin and the dominant tectonic setting (e.g., Goff, 2001; Gerber et al., 2009; Covault et al., 2011). However, we know that the overall geometry and shape of a submarine channel also depends on the channel erosional dynamics, and how the channel responds to tectonic perturbations on the slope over long periods of time (Pirmez et al., 2000). Consequently, simple erosion laws that define the shape(s) of submarine channel longitudinal profiles do not exist. Although, some authors have derived power-law equations for different deepwater systems that are in many ways analogous to the governing equations developed for rivers, however, these are not easily applicable to submarine channels in different settings (e.g., Mitchell, 2006; Gerber et al., 2009; Konsoer et al., 2013). In contrast, there are well-established power-law relationships between river catchment area, A, channel gradient, S, and down-system length, L, that neatly accounts for the ubiquity of concave-up longitudinal profiles in typical river systems at topographic steady-state (e.g., Hack et al., 1953; Howard, 1994; Whipple and Tucker, 2002; Tucker and Bras, 1998).

Most of our understanding about submarine channel response to tectonic perturbations, and to a large extent, how the channels attempt to reach topographic steady-state as they continually erode over areas of uplift and depositing in topographic lows, is that over time, the channel profile become relatively linear to concave-up ('equilibrium profile'), but with no unified governing equation. The concept of 'equilibrium profile' in submarine channels has been described qualitatively by many authors. For example, studies have shown that submarine channels that are capable of incising

across active structures often do so by exploiting low areas that developed between the structures (e.g., Huyghe et al., 2004; Ferry et al., 2005; Morley, 2009; Mayall et al., 2010). In these areas, underlying faulting or folding along the channel pathway causes localised increase in slope which is often referred to as a 'knickpoint' (Fig. 1.3). Over these knickpoints, submarine channels respond by decreasing channel sinuosity and increasing channel incision, so as to achieve 'topographic equilibrium' in those locations (Pirmez et al., 2000; Huyghe et al., 2004; Ferry et al., 2005). Thus, the interplay between channel processes and structural deformation over several thousands of years will result in a channel long-profile that is in 'equilibrium' (i.e., smooth and concave) relative to the overall slope profile which is normally irregular due to tectonic perturbations (Fig. 1.3; Pirmez et al., 2000; Ferry et al., 2005; Mitchell, 2006). Generally, the magnitude of the accommodation space is defined by the difference between the depositional profile (slope) and a hypothetical 'equilibrium profile' (Fig. 1.3). Neither erosion nor deposition occurs on this hypothetical 'equilibrium profile' surface (Pirmez et al., 2000; Kneller, 2003). For example, the area highlighted red in Figure 1.3 represents a region above the equilibrium profile where channel erosion over a knickpoint occurs, and the width-to-depth ratio of the channel will be low due to high incision and overall channel width narrowing. In contrast, the area highlighted in blue is below the hypothetical equilibrium profile and in this case, channel deposition dominates over channel erosion resulting in high channel width-to-depth ratio (Fig. 1.3).

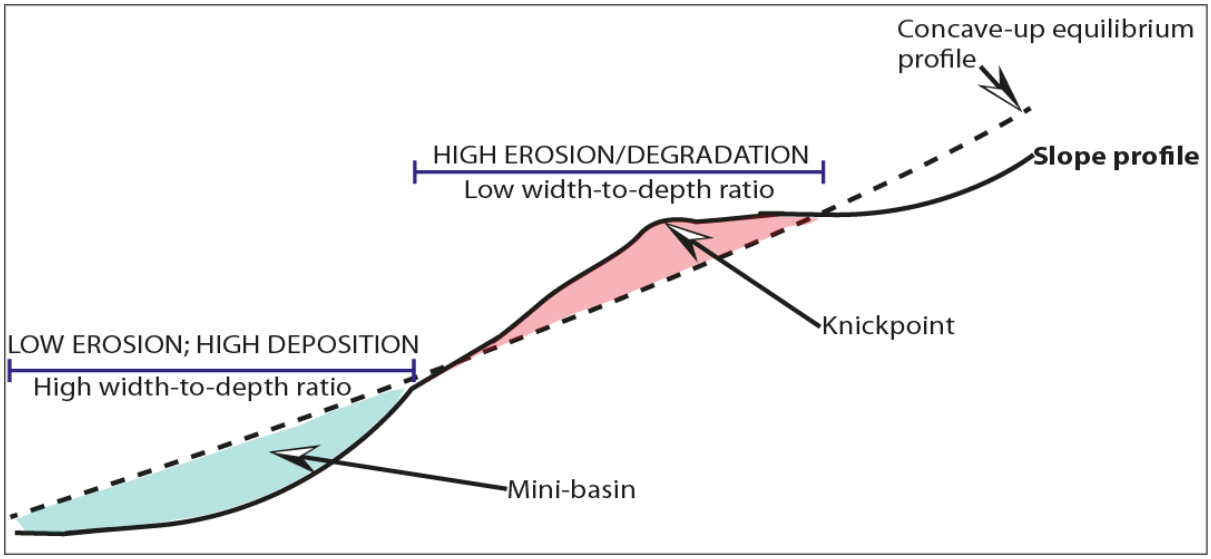


Figure 1.3: Shows a schematic diagram of the equilibrium profile model for slope and deepwater settings modified from Ferry et al. (2005).

1.5 STRUCTURAL GROWTH, ACCOMMODATION SPACE AND CONTROLS ON SLOPE DEPOSITION MODELS

Key controls on the depositional architecture produced by turbidity currents are the growth of structures at or near the seabed, the accommodation space produced by the growing structures, and sediment supply (see Pirmez et al., 2000; Prather et al., 1998; Prather, 2000; Beaubouef and Freidman, 2000; Hooper et al., 2002). Due to the deep water depths, eustatic sea level variations are not considered to have any significantly control on accommodation space in these setting, but may still influence the long-term regional variations in sediment supply. The long-term morphodynamic equilibrium between depositional and erosional processes on one hand, and the growth of structures on the other hand determines how accommodation space is created and filled in deepwater slope environment (Beaubouef and Freidman, 2000; Hooper et al., 2002). Growing folds on deepwater slopes for example, create accommodation space in their footwall or hangingwall synclines. This accommodation space is often filled by sediments, termed growth sequences, because they developed coevally with structural growth, and are characterised by wedge-shaped geometries that expands into the synclines (Suppe et al., 1992; Burbank and Verges, 1994; Rowan, 1997). In deepwater submarine channel systems, these growth sequences are typically comprised of channel-levee complexes, pelagic – hemi-pelagic deposits and mass transport deposits (Deptuck et al., 2003; Morley and Leong, 2008; Morley, 2009; Clark and Cartwright, 2012). The history of structural deformation can be determined by the geometries of the growth sequences associated with the growing structures (Suppe et al., 1992; Burbank and Verges, 1994). This means that, in principle, growth sequence geometries serve as excellent indicators of how variations in sedimentation and structural growth evolution have varied over time (e.g., Suppe et al., 1992; Burbank and Verges, 1994; Poblet and Hardy, 1995; Burbank et al., 1996). In general, growth sequences can be used to; (a) record the onset of fold growth via the first occurrence of onlap and/or thinning onto the fold limb or crest (Suppe et al., 1992), (b) determine the relative rates of uplift of the crest of the fold versus sediment accumulation over time, and (c) determine absolute fault-slip rates if key beds can be dated (Suppe et al., 1992; Burbank and Verges, 1994). However, a significant challenge for seismically-constrained folds is how to accurately convert fold growth (shortening plus slip) into absolute uplift rates at and close to the fold culmination due to lack of biostratigraphic resolution for closely-spaced dates through time, poor seismic quality at structural zones, and the often lack of robust velocity profiles for accurate conversion of seismic two-way-time to depth (Bergen and Shaw, 2010). A number of studies in the deepwater Niger Delta for example, have analysed how structures grow and create accommodation space, and how the accommodation

is filled with deepwater sediments through time (e.g., Hooper et al., 2002; Morgan, 2004; Heinio and Davies, 2006, 2007; Higgins et al., 2009; Maloney et al., 2010; Clark and Cartwright, 2012). However, there are no studies that have used 3D seismic data to quantify the growth of deepwater folds in the Niger Delta, and analyse the effects on the positioning of submarine channels pathways developing coevally with structural deformation.

1.5.1 Deepwater slope sedimentation models

The growth of structures in deepwater settings (such as the Gulf of Mexico and the Niger Delta) can create varying accommodation styles which also control the distribution of sediments (Prather, 2000; Beaubouef and Friedmann, 2000; Smith, 2004; Gee and Gawthorpe, 2006; Gee et al. 2007; Mayall et al., 2010). Generally, two end-member models exist which can be influenced by the presence, or absence of salt. These models are (i) the cascade of silled sub-basins, known as the "Fill and Spill' model, which was originally developed for the Gulf of Mexico slope (Prather, 2000; Beaubouef and Friedmann, 2000) and (ii) the connected tortuous corridor model (Smith, 2004). For example, in deepwater slope settings where salt occurs, enclosed mini-basins formed in response to salt withdrawal (e.g., Gulf of Mexico slope – Beaubouef and Friedmann, 2000; Angolan slope – Gee and Gawthorpe, 2006). Sedimentation in these areas is structurally controlled so that sediments have filled mini-basins upslope first before progressively filling mini-basins downslope. Each successive mini-basin will be completely filled to its spill point and incoming submarine channels will then by-pass this to the next mini-basin downslope.

However, the interaction between sedimentation and growing structures creating accommodation in deepwater settings that do not have salt (e.g., the Niger Delta) is slightly different. Here, the sedimentation model (the connected tortuous model) describes a progressive basin fill through a 'tortuous route' created by seabed structures (Smith, 2004). The tortuous path of the channels down-slope is made of both areas of erosion and deposition depending on the topographic relief created by folding or faulting and the overall slope gradient (e.g., Huyghe et al., 2004; Ferry et al., 2005; Pirmez et al., 2000; Geogiopoulou and Cartwright, 2013). Structural growth can create topographic lows that serve as depocentres, and topographic highs which are areas of erosion by channels (Pirmez et al., 2000; Hooper et al., 2002; Huyghe et al., 2004; Ferry et al., 2005; Heinio and Davies, 2006). The age of the sediments filling the accommodation space does not systematically young downslope as the case with the fill and spill model. The age is mostly affected by channel deflection and subsequent avulsion due to the impact of growing structures (Pirmez et al., 2000;

Hooper et al., 2002; Kolla, 2007; Deptuck et al., 2007). The growth of extensional faults (such as normal faults and growth faults) and folds (such as detachment and fault-propagation folds) cause the flow pathways of submarine channels to deflect to the fault-tips (Ferry et al., 2005; Morley, 2009, Clark and Cartwright, 2009). However, in some scenarios, these channels are capable of incising across active structures, and hence behaving counter-intuitively. Moreover, we have yet to fully understand, and constrain the conditions that allow these channels to cut-through actively growing structures (e.g., Mayall et al., 2010). In addition to channel deflection by faults and folds, channels may be ponded in areas of lowest topography created by shale withdrawal in a similar way to salt withdrawal, or in hanging and footwall-synclines (piggyback basins) associated with fault-propagation and detachment folds (e.g., Hooper et al., 2002; Heinio and Davies, 2006; Higgins et al., 2009; Clark and Cartwright, 2012).

1.6 QUESTIONS ARISING FROM THE LITERATURE AND RESEARCH OBJECTIVES

Several research questions emerge from the overview of existing literature on the interaction of submarine channels and actively growing structures in deep water settings which are addressed in this thesis:

1. A number of studies using seismic data have addressed submarine channel geometries (e.g., Mayall and Stewart, 2000; Babonneau et al., 2002; Fonnesu, 2003; Deptuck et al., 2003; Abreu et al., 2003) or the growth and interaction of structures in passive margin settings (e.g., Rowan et al., 2004; Morley and Guerin, 1996; Cohen and McClay, 1996; Corredor et al., 2005; Higgins et al., 2007, 2009; Maloney et al., 2010); but there is no study that systematically quantifies the spatial and temporal variation in structural growth rate, and investigates how this affects the pathways of submarine channels interacting with actively growing structures. Consequently, the analysis in chapter 3 is aimed at addressing this challenge in the Niger Delta study area, with the specific objective of quantifying the temporal and spatial variation in the strain rate of folds with seabed expression and investigating how the variation in structural growth rate affects the positioning of channel pathways.

2. At present the spatial and temporal variation in submarine channel erosional dynamics, and the effect this has on channel pathways, is poorly constrained and mostly only estimated from modelling (e.g., Imran et al., 1999; Peakall et al., 2000; Kneller, 2003; Das et al., 2004; Corney et al., 2006; Straub et al., 2008; Konsoer et al. 2013). Consequently, we have yet to fully understand the circumstances under which submarine channels identified from seismic data are capable of incising

across active structures on the slope. This problem is addressed in chapter 4 where measurements of channel long-profile responses and down-stream variations of morphometric parameters of modern (recently active) channels are used to make estimates of bed-shear stresses and flow velocities. The variation in flow velocity, and bed-shear stress is then coupled to down-system variation in tectonic perturbations in order to estimate modern channel erosivity and circumstances in which submarine channels are capable of cutting across growing structures.

3. Submarine slope channel systems consisting of several cut-and-fill sequences confined by a time-integrated erosion surface (e.g., Mayall et al., 2006; Deptuck et al., 2007; Janocko et al., 2013) have been extensively studied from a sedimentological perspective using seismic datasets and well data and much is now known about their fill, geometry and how they develop over time. However an outstanding question is how the cut-and-fill channel sequences themselves, and not just the most recent channel thalweg-profile, evolve through time in response to structural growth. While this has been addressed in a descriptive way (e.g., Clark and Cartwright, 2009, 2011; Gee and Gawthorpe, 2006, Gee et al., 2007; Mayall et al., 2010), there is potential to investigate the problem with more quantitative approaches. This is attempted in chapter 5 by applying similar geomorphic techniques to those used in chapter 4. The long-profiles of the erosive bases of the channel complexes are analysed and the results are linked to quantified values of fold growth to investigate how the time-integrated Pleistocene-recent channels have responded to tectonic perturbation.

4. There is a need to continue to improve our understanding of how deepwater slope channel systems distribute sediments across actively growing structures in time and space; chapter 6 aims to contribute to this understanding by investigating the factors that control the deposition of the Pleistocene to recent channel-related facies (such as channel-axis sands, levees and sheet sands/splays) in the study area, and integrating this with the structural analysis of the fold growth.

The toe-thrust region of the Niger Delta is an excellent natural laboratory to answer these questions because of the good quality 3D seismic data that has revealed structures at a resolution that is good enough to carry out linked structural and sedimentological investigations. Scientifically, the study area provide an ideal place for the study of a wide variety of structural and sedimentological processes involving large-scale interactions between growing structures and growth sequences to more detailed small-scale interactions between submarine channel-levee systems and fold growth.

1.7 THESIS AIM AND STRUCTURE

The main aim of this thesis is to quantitatively investigate the linked structural and sedimentological relationship between the Plio-Pleistocene channel systems and actively growing folds and thrusts in the toe-thrust region of the deepwater Niger Delta. To achieve this goal, the thesis is organised into seven chapters.

Chapter 2 presents the geological background to the study area, and the dataset used. Chapters 3 to 5 comprise the main body of the thesis, and present methods, literature and results appropriate to each chapter. Specifically, Chapter 3 addresses the growth histories of fold-thrust structures having seabed relief from the Miocene – Present in the study area. The spatial and temporal variation in fold shortening along major structures is identified and constrained from the 3D seismic data, and the chapter quantitatively addresses how these variations have affected the pathways of channels that developed coevally with structural deformation.

Chapter 4 applies geomorphic techniques, often used in fluvial studies, to quantify the geometry and long profile responses of the modern (active) seabed channels to Pleistocene to Recent displacement generated by the growing structures, which were constrained in chapter 3 of the thesis. In particular, the modern seabed channels are mapped from seismic data, and their down-system variation in morphometric parameters constrained. Changes in the down-system channel geometry and bathymetric long profile generated by active structures are used to infer the morphodyanamic processes that sculpted the channel systems through time, and down-system estimates of bed-shear stress are used to constrain the extent to which these channels can reach a topographic steady state.

Chapter 5 builds on the results of chapter 4 (which was based only on the study of the modern channel thalweg geometry) by extending the geomorphic analysis to cover the channels that constitute the entire Pleistocene to Recent system (including abandoned, buried channel systems). In this chapter the lowermost erosive surface of the channel cut-and-fill sequences (known as the 'container' in this study) in both the active channel systems and the buried systems were mapped from seismic data and the down-system variation in the morphometric parameters were also constrained. The long-profile of these erosive surfaces (known as 'container profiles') were generated, and the analysis of the down-system variation of these profiles in response to time-integrated fold growth was carried out. The variations in the overall geometry of the cut-and-fill sequences (container), and the shape of the containers profiles were compared to those of the

modern channels (reported in chapter 4) in order to gain a better insight into the time-integrated evolution of the Pleistocene to Recent channels in the study area.

Chapter 6 analyses the overall structural controls on seismic facies distribution in the study area. The specific objectives were to investigate the spatial and temporal distribution of seismically recognisable facies, and hence the distribution of reservoir sands based on seismic reflections characteristics and calculation of seismic attributes maps such as the root-mean-square (RMS) amplitudes. The focus is on the distribution of sand bodies such as channel axis sands, sand sheets (crevasse splays), and the impact fold growth has on the initiation/deposition of these sands. The chapter also analyses how the variation in fold growth observed in different parts of the study area affects the style of sand deposition.

A discussion section (chapter 7) integrates these key findings and addresses the implications of the results for our understanding of the coupled structural-geomorphic evolution of submarine channels in deep water systems. Areas for future work are highlighted. Finally the key conclusions of the thesis are given in chapter 8.

CHAPTER 2

GEOLOGICAL SETTING AND DATASET

This section gives the regional overview of the geological setting, structures and stratigraphy of the Niger Delta region as a whole; and ends with a description of the datasets used for this research. The methods used for this research are documented in chapters 3 – 6 where they have been adapted to fit with specific aims and objectives presented in those chapters.

2.1 Location of Niger Delta and study area

The Niger Delta is located along the western margin of Africa, and it forms a symmetrical protrusion into the Gulf of Guinea (Fig. 2.1 – inset). Spatially, the delta is bounded to the east by the Cameroon Volcanic Zone, to the west by the Dahomey Basin, and to the south (seaward) by the 4000 m bathymetry contour – making it one of the largest modern-day deltas (Fig. 2.1; Doust and Omatsola, 1990; Hooper et al., 2002; Corredor et al., 2005). The delta covers an approximate area of 140,000 km^2 both in subaerial exposure and the associated deepwater slope to basin-floor depositional systems (Whiteman, 1982; Damuth, 1994). The delta extends more than 300 km from apex (landward) to the mouth (seaward), and the maximum vertical thickness of the clastic sediments wedge is up to 12 km (Doust and Omatsola, 1990; Damuth, 1994, Morgan, 2004). Generally, the Niger Delta forms the seaward-end of a NE – SW oriented failed arm of a rift triple junction called the Benue Trough (Fig. 2.1) which was formed during the opening of South Atlantic following the separation of Equatorial Africa from South America in Early Cretaceous times (Whiteman, 1982; Mascle et al., 1986; Fairhead and Binks, 1991). The trough was progressively filled with younger post-rift deposits and by Late Eocene times a delta had begun to build across the continental margin (Burke, 1972; Damuth, 1994). The study area is located in the eastern lobe of the toe-thrust system in water depths between 2000 m and 4000 m, and covers an area of 75 km by 35 km (Fig. 2.1).

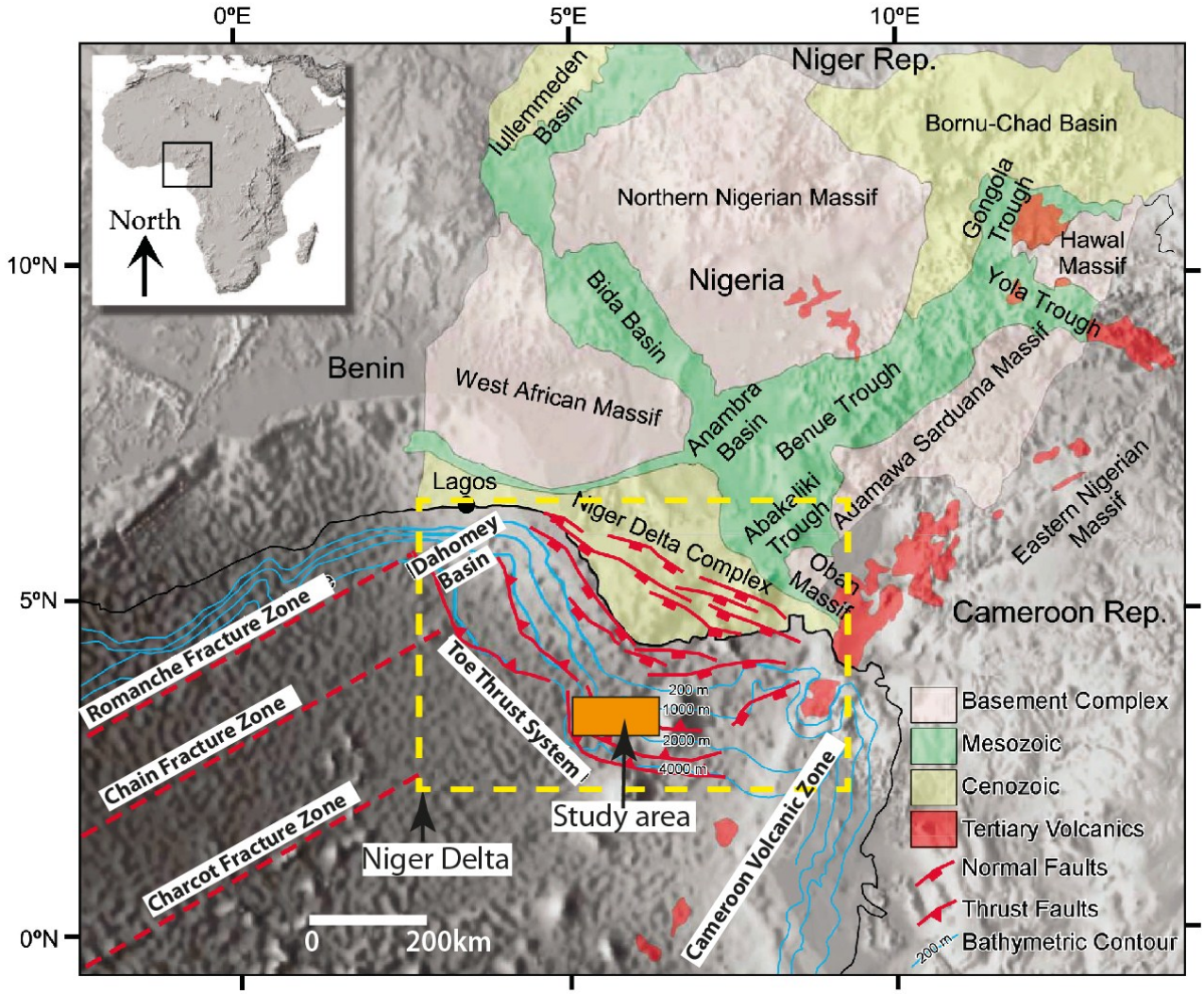


Figure 2.1: Map showing the location of the Niger Delta region and associated sedimentary basins and tectonic features (After Corredor et al., 2005). Inset shows the location of Niger Delta in the Gulf of Guinea (black square box).

2.2 REGIONAL STRUCTURAL SETTING

Regional fracture zones along the oceanic crust (e.g., the Charcot, Chain and Romanche Fracture Zones; *cf.* Fig. 2.1) also controlled the shape and internal structure of the Niger Delta (Corredor et al., 2005). These fracture zones comprised dominantly of strike-slip faults, ridges and trenches, were formed during the opening of the South Atlantic in the Early Cretaceous times (Whiteman, 1982; Mascle et al., 1986; Fairhead and Binks, 1991; Corredor et al., 2005). After the cessation of rifting, and the progressive filling of the delta by younger post-rift deposits from the Eocene times, thin-skin gravitational tectonics takes over (e.g., Morley and Guerin, 1996; Cohen and McClay, 1996; Wu and Bally, 2000; Rowan et al., 2004; Billoti and Shaw, 2005). Thus, continued deformation of the delta is driven by differential loading of the advancing delta, and resulting in downslope translation of the delta front and slope deposits on major detachment levels within the pro-delta marine shales of the Akata Formation (Bilotti and Shaw, 2005; Briggs et al 2006). Consequently, major structural zones developed on the delta, and were first sub-divided into three zones by Damuth (1994); and subsequently, Corredor et al. (2005) sub-divided them into five zones (Fig. 2.2a, b). These zones include; (1) the extensional province on the shelf – characterised by both basinward-dipping and counter-regional extensional normal faults with associated rollovers and depocenters; (2) a mud diapir zone located beneath the upper continental slope – characterised by passive, active and reactive mud diapirs (Morley and Guerin, 1996); (3) an inner fold and thrust belt – characterised by basinward-verging imbricate thrust belt and associated folds including some detachment folds; (4) a transitional detachment fold zone beneath the lower continental slope – characterised by little or no deformation and interspersed with large, broad detachment folds over a deep shale detachment layer; and (5) an outer fold and thrust belt in the deepwater end – characterised by both basinward and landward verging thrusts and associated folds.

2.3 REGIONAL STRATIGRAPHY

Stratigraphically, the Tertiary Niger Delta is divided into three diachronous units of Eocene to Recent age that form a major regressive, offlap sequences named the Akata, Agbada and Benin Formations (Fig. 2.2c; Short and Stauble, 1967; Avbovbo, 1978; Evamy et al., 1978; Whiteman, 1982; Knox and Omatsola, 1989; Doust and Omatsola, 1990; Damuth, 1994; Morgan, 2004). These units overlie the continental and oceanic crust (Fig. 2.2b, c). The Cretaceous section that lie beneath the Niger delta basin has not been penetrated, and can only be extrapolated from the exposed sections in the Anambra Basin located inland and northeast of the delta (*cf.* Fig. 2.1a; Nwachukwu, 1972; Reijers et al, 1997). The Akata Formation directly overlies the continental and oceanic crust, and is comprised of Paleocene to Recent marine clays with silty and sandy interbeds that range in thickness from 2000 m at the most distal part of the delta to 6500 m beneath the continental shelf (Whiteman, 1982; Doust and Omatsola, 1990; Reijers et al., 1997; Corredor et al., 2005). The traditional/original definition of the Akata Formation was based on the stratigraphy of the shallow water part of the delta where the Akata Formation is deltaic-shallow marine facies. However in the offshore - fold and thrust belt areas (where the study area is located), the stratigraphic equivalent of the Akata Formation is pro-delta slope and deep-water facies since at least Miocene. Overlying the Akata Formation is the Agbada Formation which is the major petroleum-bearing unit in the Niger delta. This formation is Eocene to Recent in age and consists of paralic, brackish to marine, coastal and fluvio-marine deposits that are up to 3500 m in vertical thickness (Reijers et al., 1997; Corredor et al., 2005). However, in slope regions and basin floor, the Agbada Formation consists of slope deepwater channel-levee systems, mass transport deposits (MTD) and hemi-pelagic mudstones. Onshore and in some coastal regions, the Agbada Formation is overlain by the Benin Formation which consists of Late Eocene to Recent continental deposits that can be up to 2000 m thick (Avbovbo, 1978). The Benin Formation is absent in offshore deepwater Niger Delta, and hence, the Benin Formation is not present in the study area (Fig. 2.2b; see also Corredor et al., 2005; Maloney et al., 2010). The main source of sediment supply to the delta is through the Niger River, which today has a mean water discharge of approximately 6140 m^3s^{-1} and a sediment load of 1270 kgs^{-1} (Mulder and Syvitski, 1995). It has the capacity to transport bedload sediments up to coarse-grained sand and gravel size fractions during flood events (Allen, 1965). It is inferred that sediments from the Niger River and other sediment sources (including fine-medium sands from barrier islands, tidal channel mouth bars amongst others) can all make their way to the shelf-edge during periods of low Pleistocene sea level, these sediments could ultimately reach deepwater environments through submarine canyons (Deptuck et al., 2007).

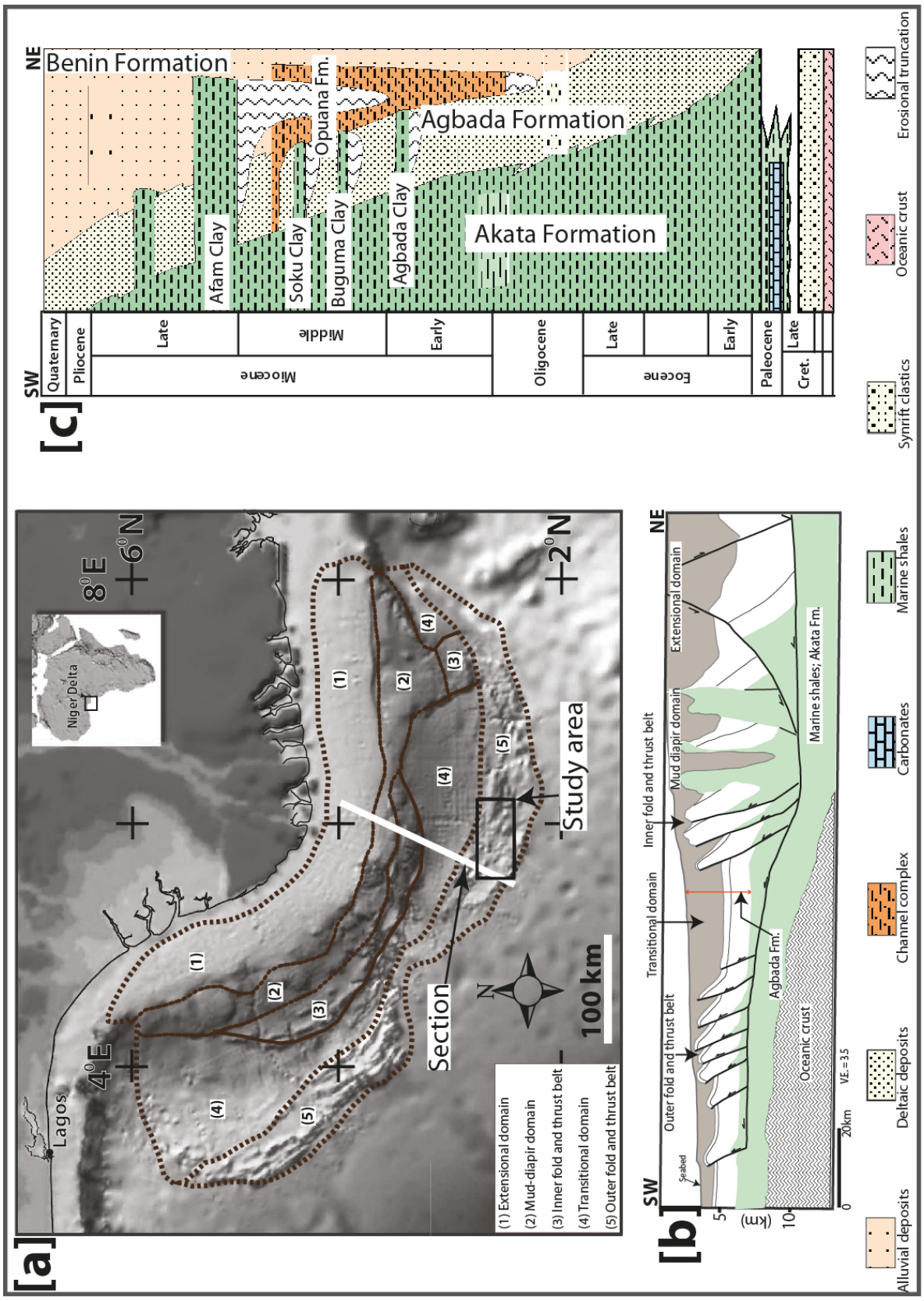


Figure 2.2: (a) Map of the Niger Delta region showing structural zonation (modified from Corredor et al., 2005). Inset shows the location of Niger Delta in the Gulf of Guinea; (b) Regional seismic profile across the Niger Delta (modified from Corredor et al., 2005) showing the structural styles from the shelf (extensional province) to the contractional toe-thrust in the deepwater-end. (c) Regional stratigraphy of the Niger Delta showing delta progradation from the NE to the NW (from Corredor et al, 2005).

2.4 3D SEISMIC VOLUME AND AGE DATA

A time-migrated 3D seismic reflection dataset was provided by Petroleum Geo-Services (PGS) for the study. The seismic data volume is part of the PGS Nigerian deepwater megasurvey, and covers OPL block 256 which is the study area (Fig. 2.3a). The data was processed to near zero-phase and is displayed using SEG-Normal polarity where an increase in acoustic impedance is represented by a peak (positive amplitude on seismic sections). The data was migrated using Kirchhoff pre-stack migration and bending ray post-stack migration to generate a 12.5 m by 12.5 m grid with a 4 ms sampling interval and was displayed every 4-inlines and cross-lines giving it a bin-size of 50 m which corresponds to the maximum horizontal resolution. The recorded length of the seismic data volume is 9.5 s with a velocity grid of 250 m. Based on the frequency content and assuming an average interval velocity of 2000 ms^{-1}, the data has a vertical resolution of approximately 10 – 12 m in the shallow Plio-Pleistocene section, and decreases to ~30 m in the deepest parts of the section where seismic velocities are also expected to increase. A tie-line X – Y across two wells (one close to the study area and the other to the north of the study area; Fig. 2.3a, b) was provided by Shell (Pers. Com. Shell Nigeria, 2011). This tie-line with the ages constrained by biostratigraphy data from Shell was used to constrain the stratigraphic ages in this study (Fig. 2.3b).

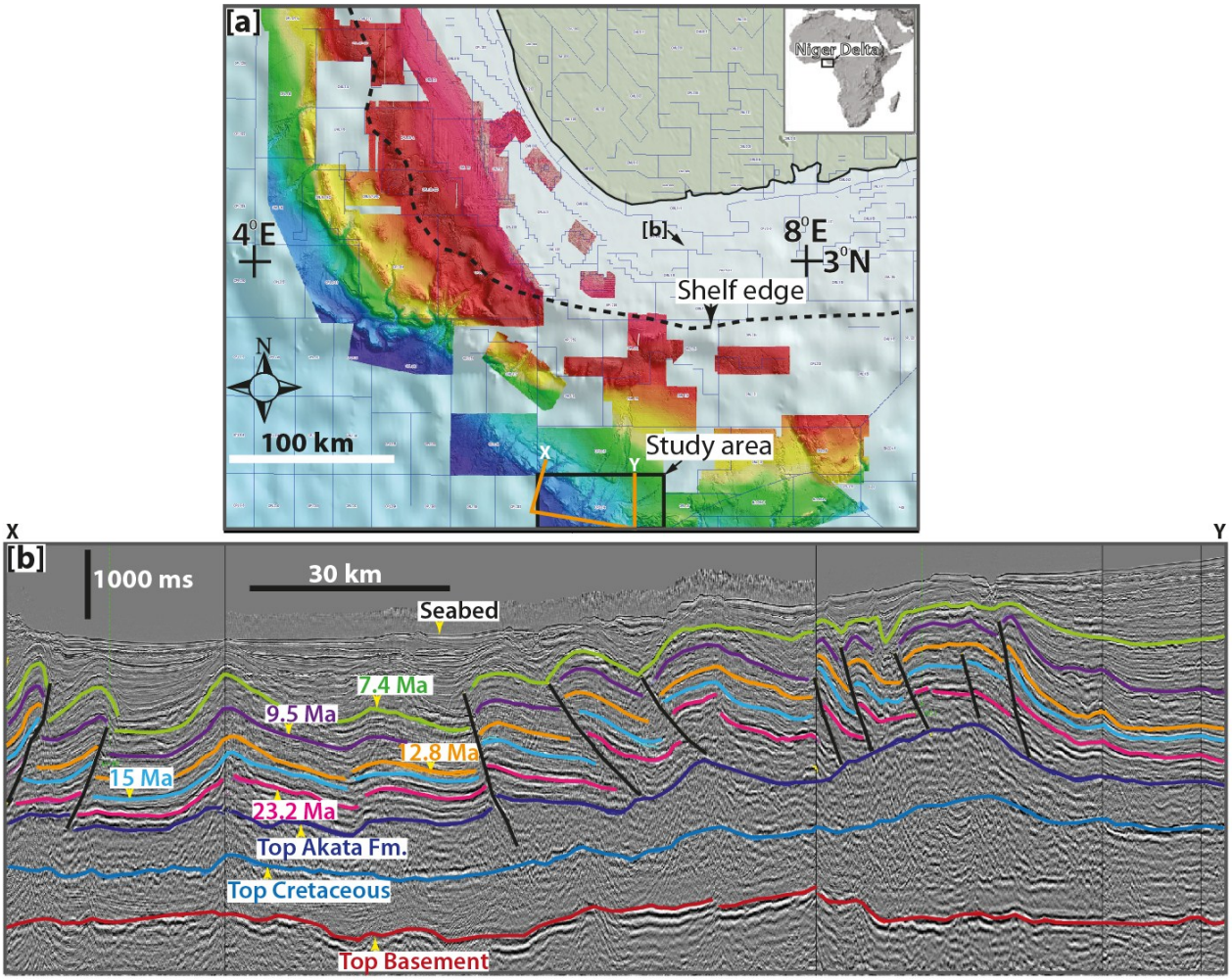


Figure 2.3: (a) Map of the Niger Delta mega-survey (by PGS) showing the study area located in OPL block 256. Inset shows the map of Africa and the outline of the Niger Delta. (b) Is a confidential tie-line X – Y (provided by Shell-Nigeria) showing stratigraphic ages that were used to calibrate seismic reflections in the 3D survey (tie-line location is shown in Fig. 2.2a).

CHAPTER 3

GROWTH HISTORY OF FAULT-PROPAGATION FOLDS AND INTERACTION WITH SEABED CHANNELS IN THE TOE-THRUST REGION OF THE DEEPWATER NIGER DELTA

3.1 INTRODUCTION

Deepwater fold and thrust belts, such as the Niger Delta toe-thrust region, represent areas of tectonic shortening in which the main driving force is the thin-skinned gravitational collapse of large deltaic sediment wedges above a ductile substrate, such as overpressured shale in the Niger Delta (e.g., Morley and Guerin, 1996; Cohen and McClay, 1996; Wu and Bally, 2000; Rowan et al., 2004; Billoti and Shaw, 2005) or mobile salt on the Angolan passive margin and the Gulf of Mexico (Cramez and Jackson, 2000; Anderson et al., 2000; Wu and Bally, 2000; Rowan et al., 2004). Contractional deformation within these fold and thrust belts is generally associated with the development of sedimentary growth sequences, deposited coevally with deformation. The growth sequences synchronously fill the accommodation space created by the growing structures and are characterized by stratal thinning or onlap onto the fold crest, and the development of a wedge-shaped geometry, due to the expansion of the sedimentary packages into the accommodation space created on both the forelimb and backlimb of folds.

In deepwater slope settings, submarine channel-levee systems are an integral part of the growth sequences which also include pelagic – hemi-pelagic deposits and mass transport deposits (Morley and Leong, 2008; Morley, 2009; Deptuck et al., 2003; Clark and Cartwright, 2012). Consequently, the pathways of these submarine channels are often influenced by the growth of structures at, or near the seabed (e.g., Morley, 2009; Clark and Cartwright, 2009; Mayall et al., 2010). The history of structural deformation can be determined by the geometries of the growth sequences associated

with the growing structures. This means that, in principle, growth sequence geometries serve as excellent indicators of how variations in sedimentation and structural growth evolution have varied over time (e.g., Suppe et al., 1992; Burbank and Verges, 1994; Poblet and Hardy; 1995; Burbank et al., 1996). However, it is difficult to constrain the detailed geometry of growth sequences associated with deepwater folds without good quality 3D seismic data (e.g., Hooper et al., 2002; Heinio and Davies, 2006; Morley, 2009). Consequently, the increasing availability of high quality 2D and 3D reflection seismic data coming from hydrocarbon exploration in deepwater settings has led to a renewed focus on fold-related thrusting in deepwater gravitational systems (e.g., Corredor et al., 2005; Briggs et al. 2006; Higgins et al., 2007, 2009; Morley and Leong, 2008; Morley, 2009; Maloney et al., 2010 Clark and Cartwright, 2012). The availability of such seismic data means that individual growth sequences can be measured, and the shortening accumulated during the growth of the fold/thrust can be quantified. This information can therefore help to determine how strain varies through time in such settings, and how it may affect the sedimentary depositional systems which interact with the growing structures. Here we focus on the toe-thrust area of the Niger Delta, which is an excellent natural laboratory to study the coeval development of thrusts/folds and submarine channels because the structures are well-developed and well-preserved, without the problems of sub-aerial exposure and degradation found in terrestrial settings (*cf.* Morley, 2009; Clark and Cartwright, 2012).

Previous studies of folding and thrusting in the deepwater Niger Delta have focused on the evolution of the structures as a whole (e.g., Higgins et al., 2009; Maloney et al., 2010). For example, Higgins et al. (2009) described the spatial and temporal evolution of a major fault-propagation fold in the deepwater Niger Delta. These authors use evidence of transfer of fault-displacement within the structure as it changes vergence along strike, to argue that numerous thrust faults, initially growing separately, eventually linked into a single structural culmination. Maloney et al. (2010) reported that in some cases, an early phase of fault-propagation folding is followed by a second phase of fold growth caused mainly by thickness changes (lateral redistribution of shale) within the basal shale detachment. There has been more limited work (mainly qualitative) on the related depositional systems. Hooper et al. (2002) for example, discuss at a broad scale how the structural evolution controls the evolution of accommodation space in the form of ponded-slope basins that are closely linked to the evolution of the associated thrusts. Degradation of emergent anticline crests was investigated by Heinio and Davies (2006) and the response of deep water channels to growing structures has been documented by Morgan (2004) and Heinio and Davies (2007). Moreover, a recent study in deepwater fold belt of the western Niger Delta by Clark and Cartwright (2012)

showed that a good understanding of the interaction between sediment (growth sequence architecture) and growing folds can provide insight into the creation, and filing of accommodation space as folds grow through time. These authors also described the evolution of paleao-seafloor relief using growth sequence architecture, and how the seafloor relief affected the primary sediment pathways through time.

A number of attempts have been made to quantitatively understand the relationship between the structural elevation of the fold crest and the amount of fold shortening in fault-propagation folds in general (e.g., Storti and Poblet, 1997; Poblet et al., 2004). These studies suggest a simple linear relationship between fold crest uplift rate and fold shortening/strain. For example, Poblet et al. (2004) show that for syn-kinematic strata, when crestal-structural-relief and fold area are plotted against the amount of shortening, fault-propagation folds tend to show a linear relationship between crestal structural relief and fold shortening. These studies allow the conversion of shortening into vertical component of uplift. However, the results are highly dependent on the kinematic model chosen, and many natural folds do not necessarily comply with simple end-member fault-propagation or detachment fold models.

Despite the growing number of studies addressing the interaction between active structures and submarine channels (e.g., Morley, 2009; Clark and Cartwright, 2009, 2011, 2012; Mayall et al., 2010), there is no study that systematically quantifies the spatial and temporal variation in strain rate, and how it affects the pathways of submarine channels. In this paper, we tackle this problem. We use 3D seismic reflection data to map age-constrained stratigraphic horizons, in both the pre- and syn-kinematic strata, across actively growing thrust-related folds with seabed relief in the gravitational toe-thrust region of the deepwater Niger Delta. We use simple line-length balancing methods (Dahlstrom, 1969) to calculate the spatial (along-strike) and temporal variation in the cumulative strain that the horizons have accumulated in response to the continual growth of the folds. We also examine the effect of strain variations on modern seabed channels pathways through time. We found that this method of measuring fold growth and the impact on sediment pathways is simple and robust.

3.2 METHODS

3.2.1 Seismic interpretation

The seabed seismic reflection was mapped throughout the 3D seismic volume and a seawater seismic velocity of 1490 ms^{-1} was used to convert the two-way travel time seabed map to bathymetry (Fig. 3.1a). From the seabed bathymetry map, the edge-attribute map of the seabed (Fig. 3.1b), and the seismic data, we identified modern seabed channels flowing down-slope from NE to SW (channel 1, 2, 3 & 4); and actively growing structures with seabed relief (Fold A, B, C & D), which can be traced for up to 35 km along strike, and are also associated with seabed scarps and slumps (Fig. 3.1b; Fig. 3.2b). We interpreted and analysed the seismic data (e.g., the seismic section in Figure 3.2a) to evaluate the structure and growth history of folds and thrusts in the study area through time. A tie-line across two wells (one close to the study area and the other to the north of the study area) was used to constrain the stratigraphic ages for 7 seismic horizons between 23.2 Ma and the seabed. The age data for the horizons between 23.2 and 7.4 Ma was provided by Shell based on biostratigraphy (Pers. Com. Shell Nigeria; 2011). However, a younger age of 3.7 Ma was extrapolated by assuming a constant sedimentation rate in the main piggyback basin behind a major detachment fold in the east of the study area. I constrained the onset of fold growth by mapping the syn-growth strata. For example, the growth of Folds A and D in Figure 3.2b has created accommodation space on the both the back-limb and fore-limb of the structures. This accommodation space is filled with the syn-growth sequences which were identified from onlapping and overlapping reflector geometries, unconformities and thickness changes in the vicinity of the folds with thinning towards the fold crest and stratigraphic expansion in the inter-fold synclines (Fig. 3.2). The onset of seismically-visible growth, where we see thickening and the first evidence for onlapping reflectors, occurs between the 12.8 and 9.5 Ma horizons (Fig. 3.2). The 12.8 is seismically within the pre-growth strata, but first evidence of thinning of strata on some fold flanks can be seen before the 9.5 horizon (e.g. Fold D, Fig. 3.2). However, for the purpose of mapping the 9.5 surface was used as a proxy for the base of the growth sequence (see Fig. 3.2) though I recognise that in places, structures started to grow somewhat earlier. In this study seven mapped seismic horizons (that is, the 23.2, 15, and 12.8 Ma horizons within the pre-growth sequence; and the 9.5, 7.4, 3.7 and the seabed (0 Ma) within the syn-growth sequences). I chose the 3.7 Ma horizon within the syn-growth interval because it is a surface that divides the syn-growth unit into approximately two major packages (Fig. 3.2). A thickness map (Isochron map) of the study area was derived to quantify the distribution and structural control on the syn-growth sequence in the study area. The traces of the major structures identified are shown in plan-view in Figure 3.1.

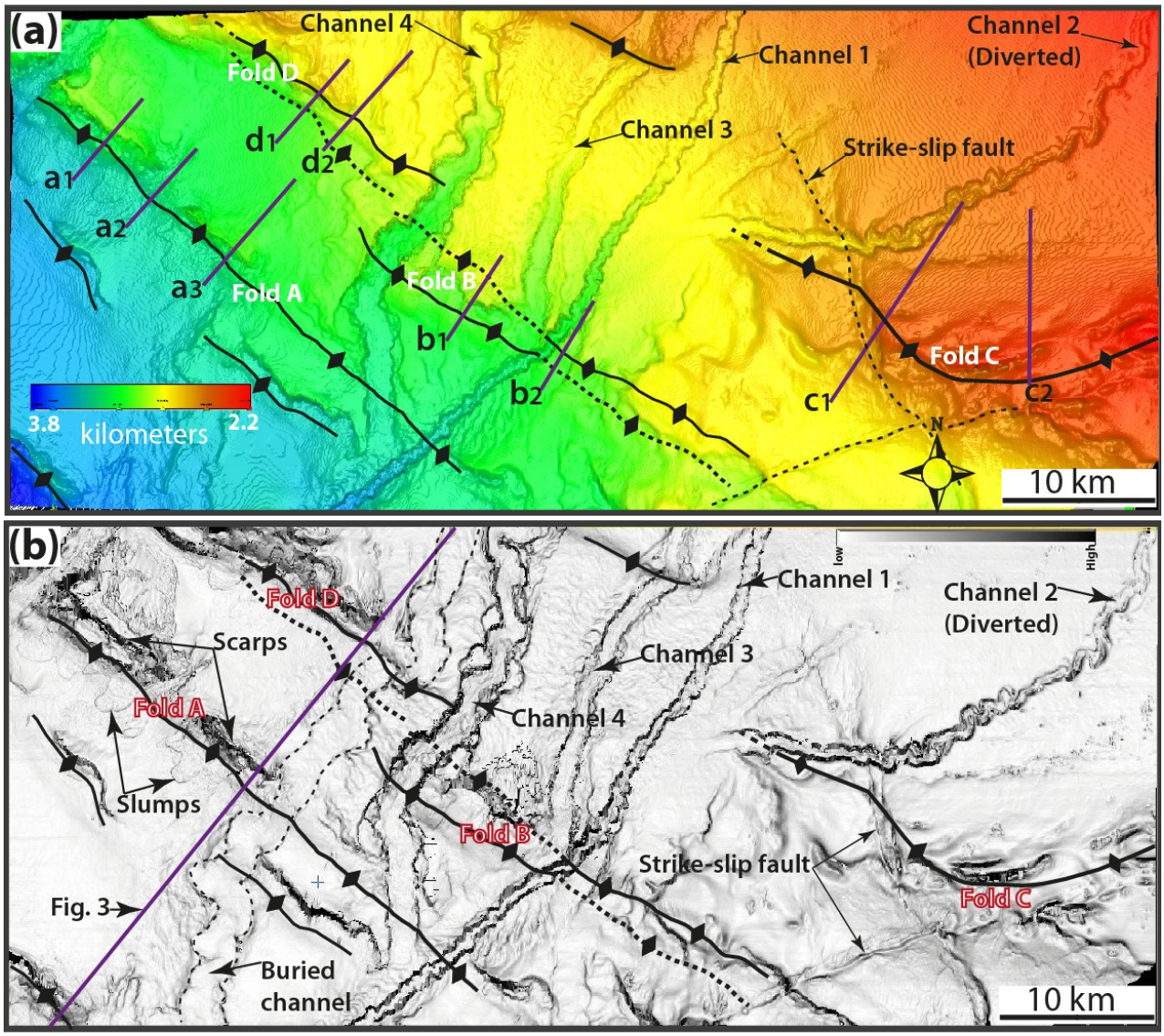


Figure 3.1: (a) 3D bathymetry map; and (b) edge-attribute map of the seabed over the study area. The maps show modern, seabed channel systems (1, 2, 3 and 4) and growing folds with seabed relief (Folds A, B, C and D). The trace of the fold axes at the seabed is shown as sold black lines with diamonds; the dashed fold axes are folds that do not have bathymetric expression at the modern sea floor. Section lines, a1, a2, a3, b1, b2, c1, c2 and d1, d2 across folds are shown in Figures 3.7, 3.8, 3.9, and 3.15.

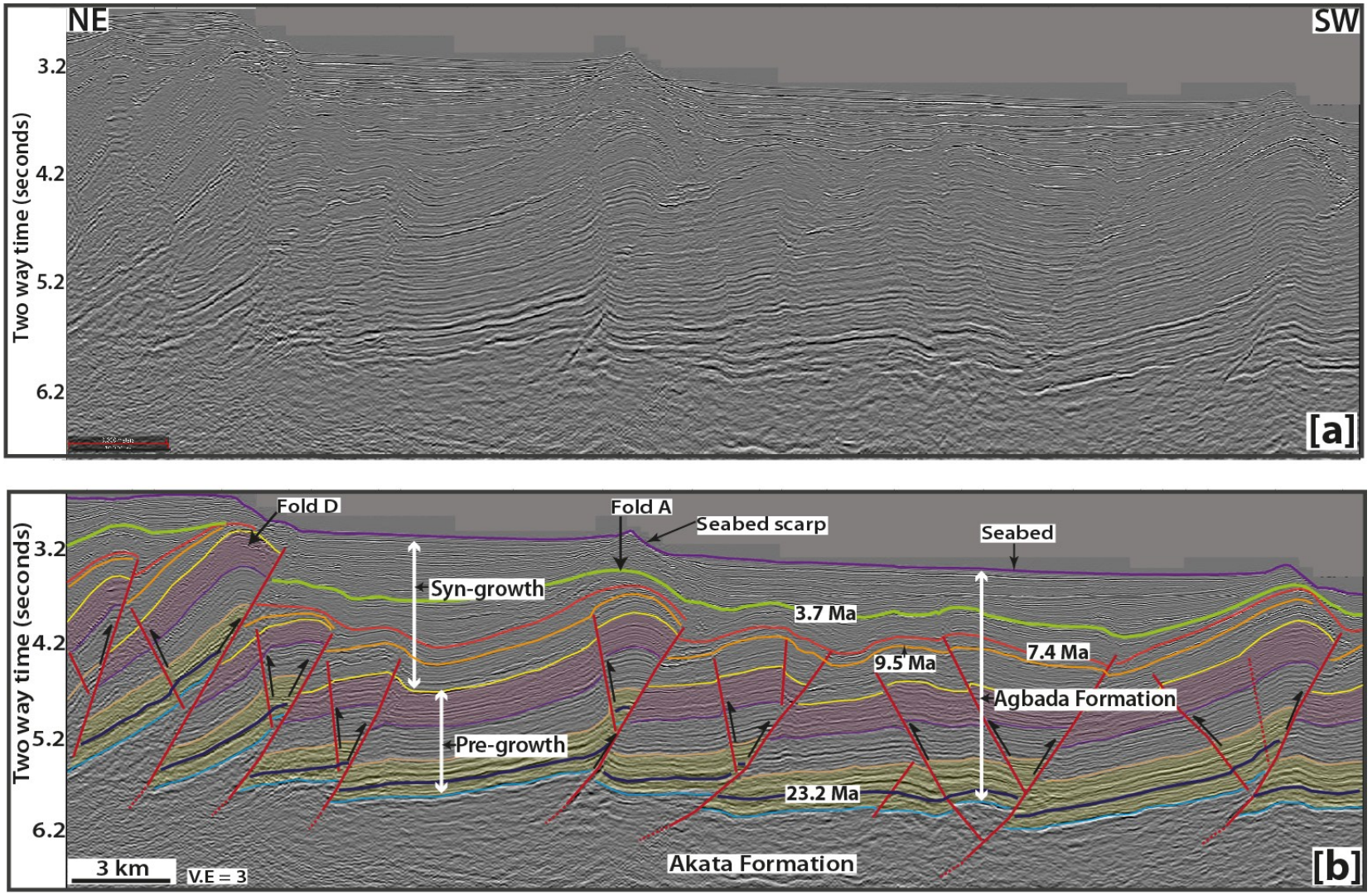


Figure 3.2: A dip-orientated section across the study area (see location on Figure 3.1b) showing the general structural style. The structures are made up of fore-thrusts that detach within the Akata Formation shales, and back-thrusts that mostly intersect the fore-thrusts. Syn-growth units are characterised by thickness changes over growing structures having seabed relief.

3.2.2 Measurement of fold shortening

In this study, shortening was measured by line-length balancing (Dahlstrom, 1969) on a series of dip sections spaced at approximately 2 km intervals along the fault-related folds of interest. The sections were pinned away from the structure at the point where the strata become horizontal, or pinned midway between two closely spaced structures. For pre-growth strata, a simple measure of shortening, s_h, can be defined as the summed length of the folded and faulted horizon measured between the section pin points (($\mathbf{L_o} = \mathbf{P_1} + \mathbf{P_2}$) in Figure 3.3), minus the present-day length, $\mathbf{L_f}$, between the same pin points. However as the absolute value of shortening is dependent on the line-length chosen for the measurement, which may change along the length of the fold, where the fold changes in width for example, strain (**e**) was considered to be a more useful measure, where:

$$\mathbf{e} = (\mathbf{L_f} - \mathbf{L_o})/\mathbf{L_o} \quad \text{(Eq. 1)}$$

I note that the strain can easily be converted to a shortening factor, $\mathbf{S_f}$, where

$$\mathbf{S_f} = Lf/\mathbf{L_o} = \mathbf{1} + \mathbf{e} \quad \text{(Eq. 2)}$$

hence a strain of -0.8 is the equivalent of a shortening factor of 0.2, or, in other words, the section has undergone 80% shortening. The syn-growth surfaces for which strain was measured are predominantly overlapping strata so, $\mathbf{L_o} = \mathbf{S}$ (Fig. 3.3). However, in cases where the syn-growth strata onlap the growing structure, a modification of methodology is required (see Poblet et al., 2004). Erosion due to slumping is common on the front limb of the folds and forms significant scarps (Figs. 3.1b, 3.2b). Where a palaeo-scarp is buried by younger sediments, for any syn-growth horizon truncated by the scarp such as horizon h_3 in Figure 3.4a, the length was measured by projecting the horizon across the palaeo-scarp and over the structure while maintaining the overall shape of the structure (Fig. 3.4b). For modern seabed scarps I employ a similar approach by visually reconstructing the seabed and extrapolating it across the scarp (Fig. 3.4c, 3.4d). Where modern seabed channels have incised across a growing fold, I also applied the same method by extrapolating the stratigraphic horizon, over the growing structure(s), and into the channel fill as per horizon h_3 in Fig. 3.4(e, f). This method allows me to estimate the likely strain accumulated by the horizon assuming it had not been affected by any form of degradation such as slumping or channel incision.

Strain measurements were made for the seven seismic horizons I mapped within the pre-growth and syn-growth strata on sections across the structures (e.g., section a2 across Fold A; Fig. 3.5a). From this, the cumulative strain through time was determined – that is the cumulative summed difference

in strain recorded between adjacent stratigraphic layers (Fig. 3.5b). The maximum cumulative shortening occurs at the present day (0 Ma) and this represents the total shortening recorded on the pre-growth strata. If there has been no ductile thickening of the beds then the shortening calculated on any pre-growth surface should be constant for each pre-growth layer. From the cumulative strain it is simple to calculate an average interval strain rate between dated seismic horizons (Fig. 3.5c). Shortening of folded layers has to be measured on sections where the horizontal and vertical scales are the same. This requires depth-converting the data; in the absence of velocity data I have assumed that the velocities in the depth range under consideration are likely to vary between 2100 ms^{-1} (near seabed) and increasing to 2500 ms^{-1} at depth and I used a mid-point velocity of 2300 ms^{-1}. A test of the dependence of the results on changes in velocity is shown in Figure 3.5 for Fold A. Increasing the velocity to 2500 m s^{-1} changes the measurements by about 1–10 % at high values of shortening, and makes little difference to the cumulative shortening through time (Fig. 3.5b). The interval shortening rates are also similar regardless of seismic velocity used, although the percentage error is greater at smaller values of strain, normally within the younger syn-growth strata (Fig. 3.5c).

To view the variation in shortening along the length of each structure I plot the shortening for each surface against distance along the structure to produce a strain-distance diagram as is routinely done for extensional fault systems (i.e., displacement-distance plot). This was done using transects taken at approximately 1.5 km intervals along the strike of the structures. Similar diagrams have been constructed for displacement on active thrusts in New Zealand (Davis et al. 2005); and subsurface thrusts imaged on seismic data from the Niger Delta, Sichuan Basin – China, and the Magdalena Basin – Colombia (Higgins at al. 2009; Bergen and Shaw, 2010).

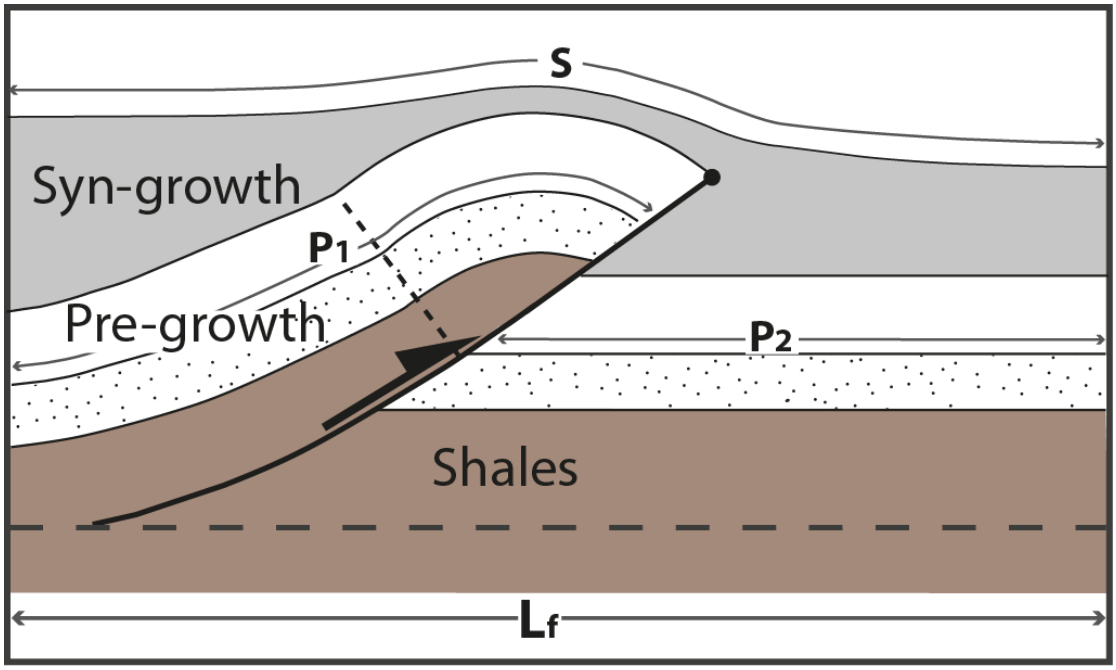


Figure 3.3: Diagram showing the methodology for measuring strain based on the concept of line-length balancing. **L_f =** length of the section while **L_0** = original bed length. For example, **L_0** for the pre-growth horizon will be **$P_1 + P_2$.**

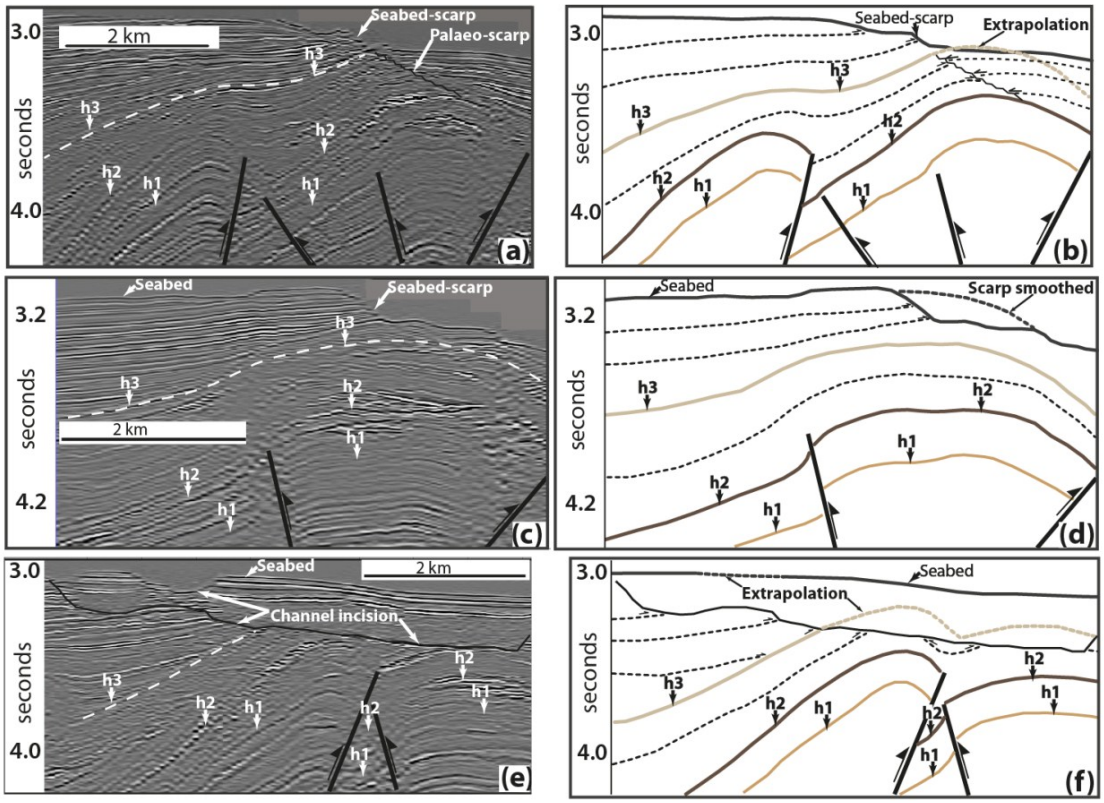


Figure 3.4: Representative sections across Folds A and Fold B, illustrating potential seismic interpretation problems and how they are treated. Section a, shows a palaeo-scarp and the interpretation b, shows the extrapolation of h3 – horizon across the palaeo-scarp in order to measure strain; section c, shows a seabed scarp and the interpretation d, shows how the scarp is smoothed in order to measure strain on the seabed; section e, shows channel incision across growing folds and the interpretation f, shows extrapolation of h3 – horizon across the erosive base of the channel in order to measure strain.

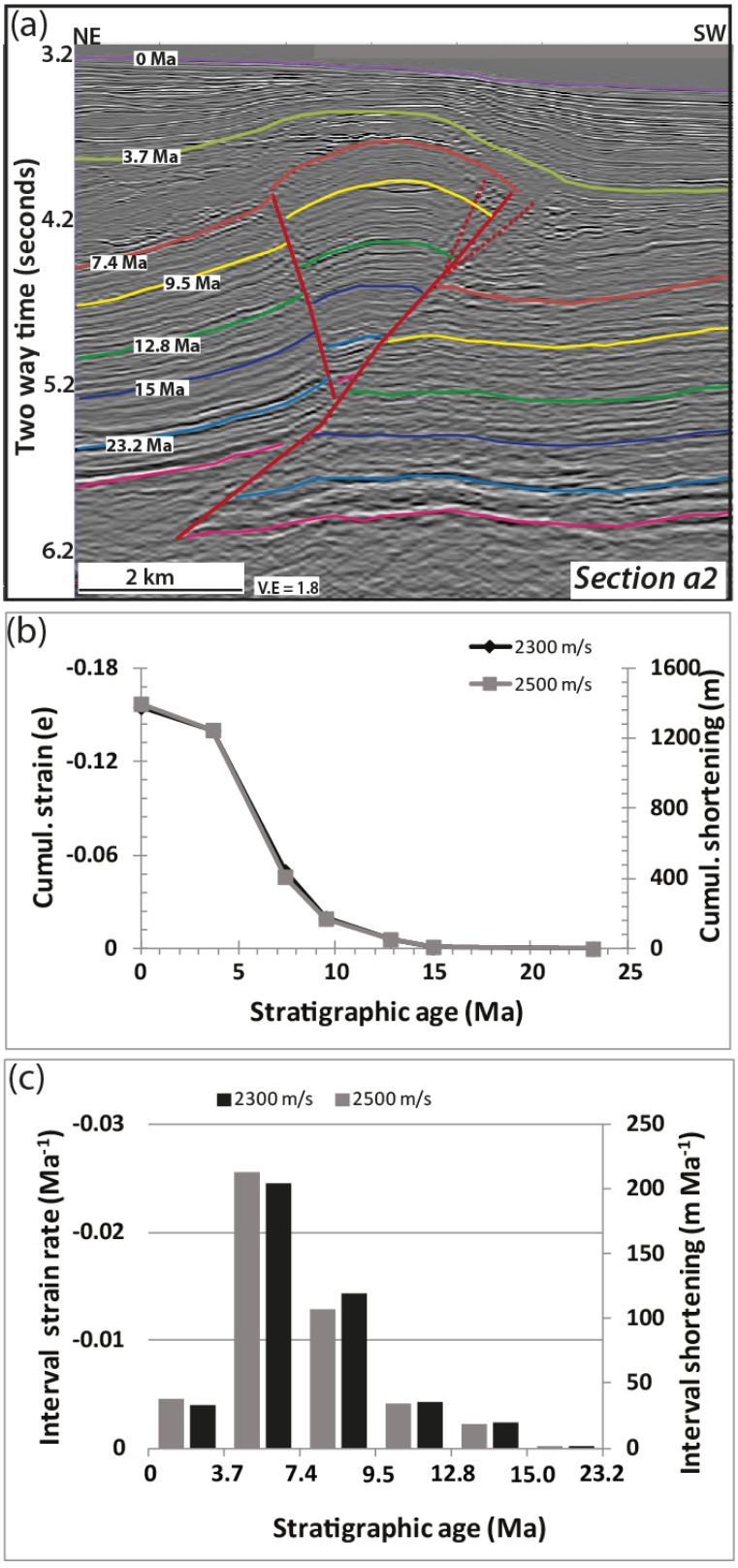


Figure 3.5: (a) Seismic section across Fold A (section a2 in Figure 3.1a) with stratigraphic horizons used for strain measurement labelled. (b) Plot of cumulative strain measured from stratigraphic horizons shown in Figure 3.5a; for two different depth conversion seismic velocities of 2300 and 2500 m/s; (c) is the interval strain rates derived from Figure 3.5b.

Limitations of the line-length balancing approach have been discussed in the literature in some depth (e.g., Hossack, 1979; Chapman and Williams, 1984). For example, any ductile thickening of the units during deformation where strain is accommodated by layer-parallel shortening will introduce errors. However our measurements typically show that strain for all horizons pre 15 Ma is approximately the same within measurement error which suggests that ductile thickening was not significant in the lower parts of the sedimentary units in the area. However Figure 3.5b suggests that some reduction in total strain is observed for the 12.8 Ma horizon in Fold A, which occurs before any significant growth strata are observed in the seismic data (Fig. 3.2). There are two possible explanations; (1) there may be some ductile thickening of the 12.8 – 9.5 Ma interval or (2) It may reflect some uncertainty in the location of the thrust fault (Fig. 3.5a). The seismic signal is often degraded in the vicinity of the thrust faults towards the top of the pre-growth package which introduces uncertainty in the location of fault plane (see Bergen and Shaw, 2010) and hence position of cut-offs (Fig. 3.5a). A single fault-plane was normally interpreted in such zones by positioning the cut-off through the middle of the zone of poor data quality. Error can also arise from the digitization of the horizon upon which strain is measured either by slightly increasing or decreasing the original length ($\mathbf{L_o}$). Errors arising as a result of digitization are very small in absolute terms, and reach up to 0.5 % for higher strain values on the pre-kinematic units. However, they become relatively more significant when the absolute strain measurements themselves are very small, such as the younger syn-growth strata or older pre-growth strata with very low strain. In these cases the very low absolute strain values have error bars of comparable magnitude to the strain itself. Errors may also arise from the reconstruction of the seismic horizons that have been degraded on the fold crest (e.g., scarps and channel incision; Fig. 3.4). There is no information on any errors associated with stratigraphic ages which may impact on the plots of strain against stratigraphic age. The majority of these limitations will affect the absolute value of shortening derived, but as this chapter focuses on the relative variation in shortening both through time and along the strike length of the structures, the approach used is considered robust enough for the purpose of the study.

3.3 Results and observations

3.3.1 Structures and fold geometries

The western half of the area is dominated by closely-spaced, fault-propagation folds with a linear NW-SE trend (Figs. 3.1b, 3.2b, 3.6). Many fold crests are separated by only 2 – 3 km. In the east, a 10 km wide, arcuate, fold (Fold C) dominates; it forms the southern boundary to a synclinal, piggyback basin which is at least 20 km wide (see Isochron map, Fig. 3.6). Generally, Figure 3.6 shows thick synclinal basins up to 2000 ms TWTT thick, which are located between the folds and thrusts, with significant thinning of the syn-growth strata onto the crests of the structures. The faults within the fault-propagation fold structures in the area terminate within the lower parts of the syn-growth strata, and rarely intersect the 3.7 Ma horizon, with no faults extending to the seabed (Fig. 3.2). Many of the structures in the area are buried (Figs. 3.2b, 3.6). I focus, however, on four folds (A – D; Figs. 3.1a and 3.6) which can be traced for up to 35 km along strike, have seabed expression and deform the seabed, or very near seabed strata, and hence demonstrate evidence of ongoing growth. Although the folds have relatively simple expression at the seabed, with associated seabed scarps where the structural relief is highest (Figs. 3.1b, 3.2b), some are more complex structures at depth.

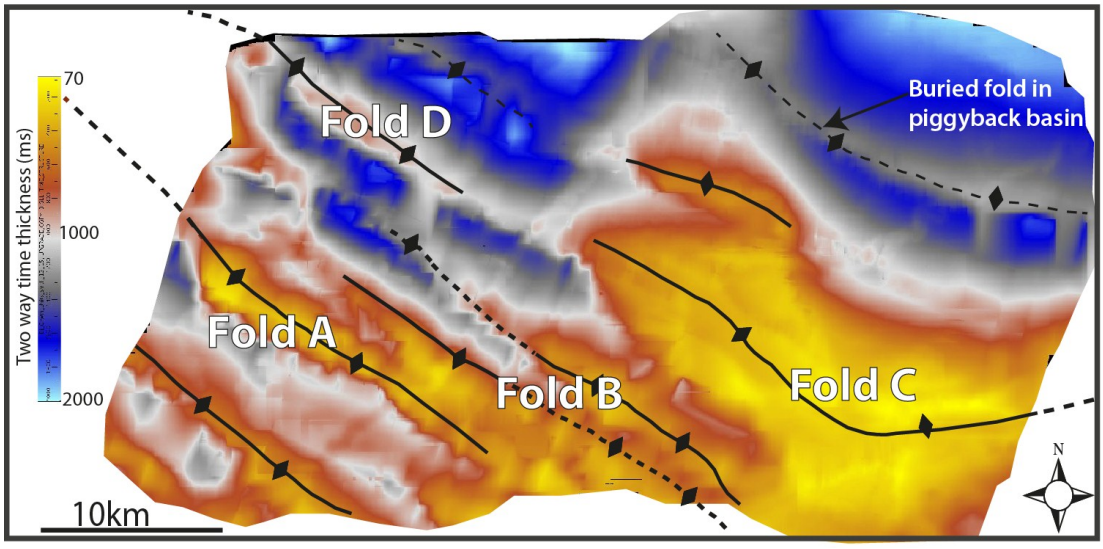


Figure 3.6: Isochron map of the growth sequence interval over the study area showing a series of NW – SE orientated depocentres (blue areas) and growing folds (yellow areas). The depocentres correspond to the footwall and hangingwall synclines of the actively growing structures. The gross depositional pattern can be seen clearly because where the growth units overlap growing structures, it thins over fold crests (yellow colours) and thickens adjacent to the fold limbs (blue colours). Fold with axes labelled are those studied in detail.

Fold A is a relatively simple structure, which extends for at least 35 km along strike, continuing outside the study dataset. It is linear in plan-view and formed above a seaward-verging forethrust dipping at c. 28 – 31° which detaches within the Akata shales (Fig. 3.7b and Fig. 3.7d). An antithetic backthrust, which intersects the main thrust, deforms the back limb of the fold. The faults die out upward within the folded syn-growth strata and deform, but apparently do not offset the 3.7 Ma horizon. Seabed scarps (up to 250 m high) occur along the fold in regions of higher structural relief (e.g., Fig. 3.1b; Fig. 3.7b). It appears that slumping on the front limb of the structure is responsible for the formation of the scarps and has caused degradation of the fold crest. Small lobate slump deposits visible on the seabed dip map (Fig. 3.1b) at the base of the scarps testify to this. I interpret Fold A to be a fault propagation fold associated with on-going shortening in the toe region of the Niger Delta.

Fold B is defined as a composite structure consisting of two, closely spaced thrusts. Along the north-western half of the mapped fold trace (solid line Figs. 3.1a, 3.6) the seaward thrust dominates the structure and has the highest structural relief (Fig 3.8b). Seabed scarps form on the frontal side of the associated fold. A second thrust cuts the backlimb of the frontal thrust and is buried at the present day but was active until at least 3.7 Ma. In contrast, on the south-eastern half of Fold B, the more landward of the two thrusts takes over as the dominant structure, with highest structural relief (Fig. 3.8d) and the frontal thrust is buried (dashed line on Figs. 3.1a, 3.7). Because the two thrusts are so closely spaced, for the purposes of calculating the shortening it is necessary to calculate the strain across both structures to allow a consistent pin-point for the line-length measurements on both flanks of the overall fold.

Fold D is also a composite structure, where the more landward of the two folds is the one with seabed expression, while the frontal fold has been buried since at least 3.7 Ma (Fig. 3.8f). In contrast to Fold B the relationship between the two structures remains consistent along the fold length (Fig. 3.1a). Again, to get consistent shortening estimates I consider the two structures together. In the same way as Folds A and B, Fold D also has well-developed seabed scarps, with a seabed relief of up to 280 m (*cf.* Fig. 3.1b).

In contrast, Fold C, in the east of the area (Figs. 3.1a, 3.6), has a very different geometry. It is a much broader, longer wavelength anticline (>5 km), with low displacement planar thrusts on the front and back limbs, and in places in the fold core (Fig. 3.9b). A key difference between Fold C and the other folds is the thickening of the Akata shale observed under the fold crest. Some of the thickening is due to imbrication within parts of the Akata shale itself (Fig. 3.9b). In the core of this fold, the top of the Akata shale is approximately 800 ms TWTT shallower than in the fault-related folds in the west

of the area. The first-order geometry of this anticline is similar to a detachment fold (Jamison, 1987) where the folding is driven by thickening at the detachment level. Fold C may be the along strike continuation of a similar structure documented by Maloney et al. (2010), from an area just to the east of our study.

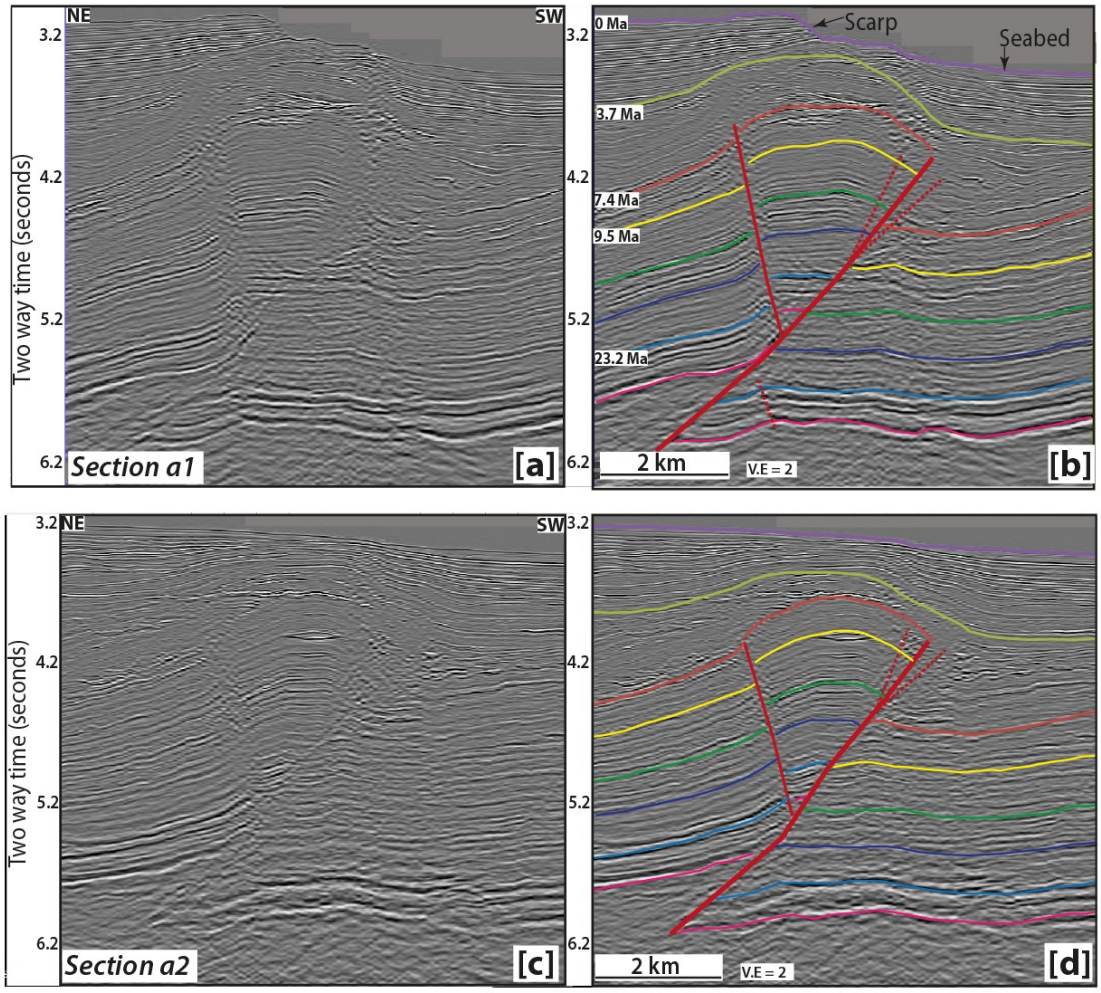


Figure 3.7: (a) and (c) are un-interpreted, and (b) and (d) are interpreted sections across Fold A respectively (sections are located in Figure 3.1a). These sections reveal the structural style of the fold which is made up of a forethrust that detached within the Akata shales, and a backthrust that intersects the forethrust. Note the presence of a seabed scarp in the section (see also Fig. 3.1b).

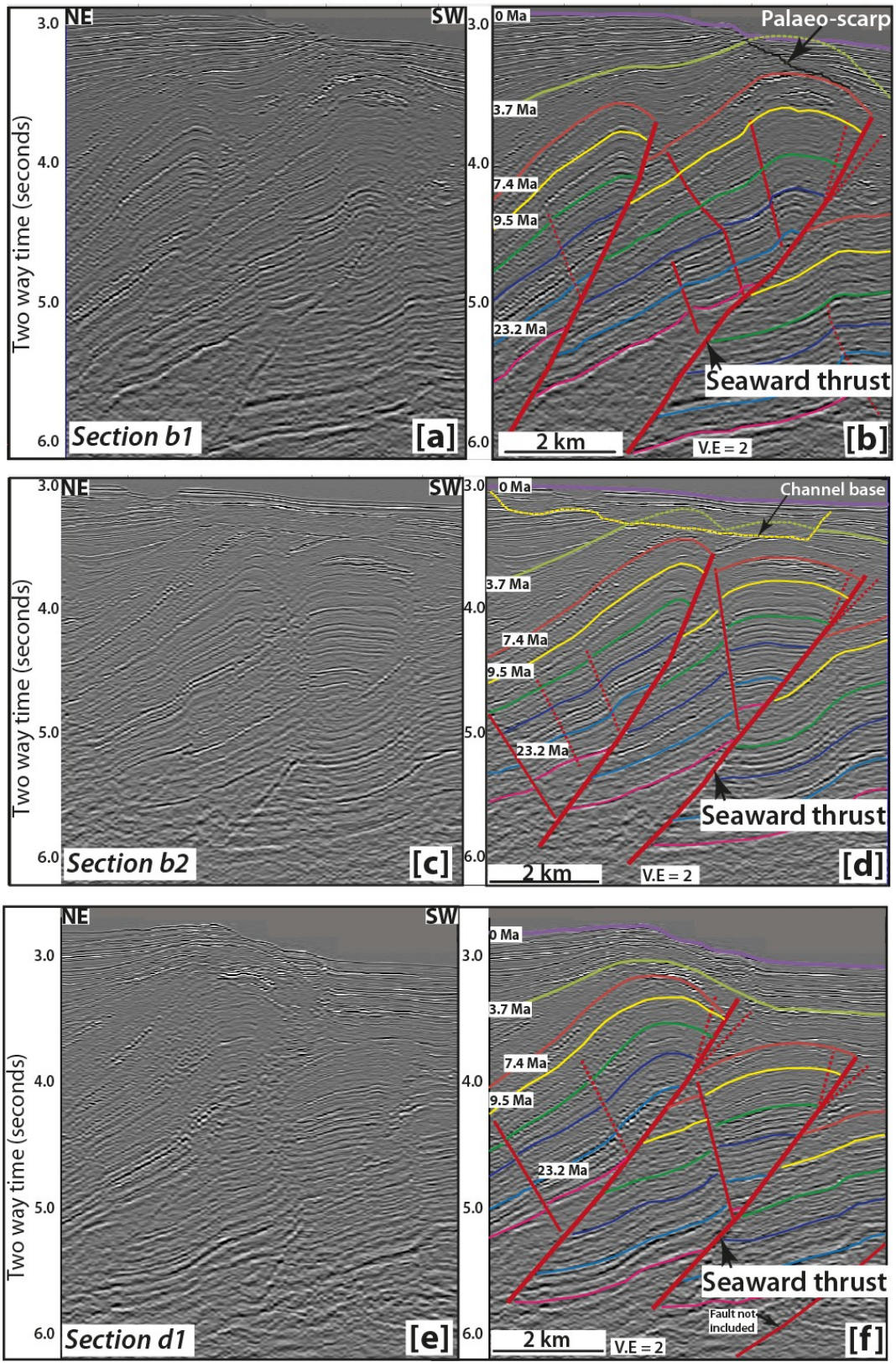


Figure 3.8: (a) and (c) un-interpreted, and (b) and (d) interpreted sections across Fold B respectively; (e) and (f) un-interpreted and interpreted section across Fold D (see sections location in Figure 3.1a) . These sections all show composite thrust-related folds each with two synthetic forethrusts where one of the thrust/fold carries the other on a piggy-back. Note that only one of the folds has a significant influence on the seabed and the other is buried. Note also that there is a palaeo-scarp in (a, b); and the folds in (c, d) have been cut-through by active seabed channel.

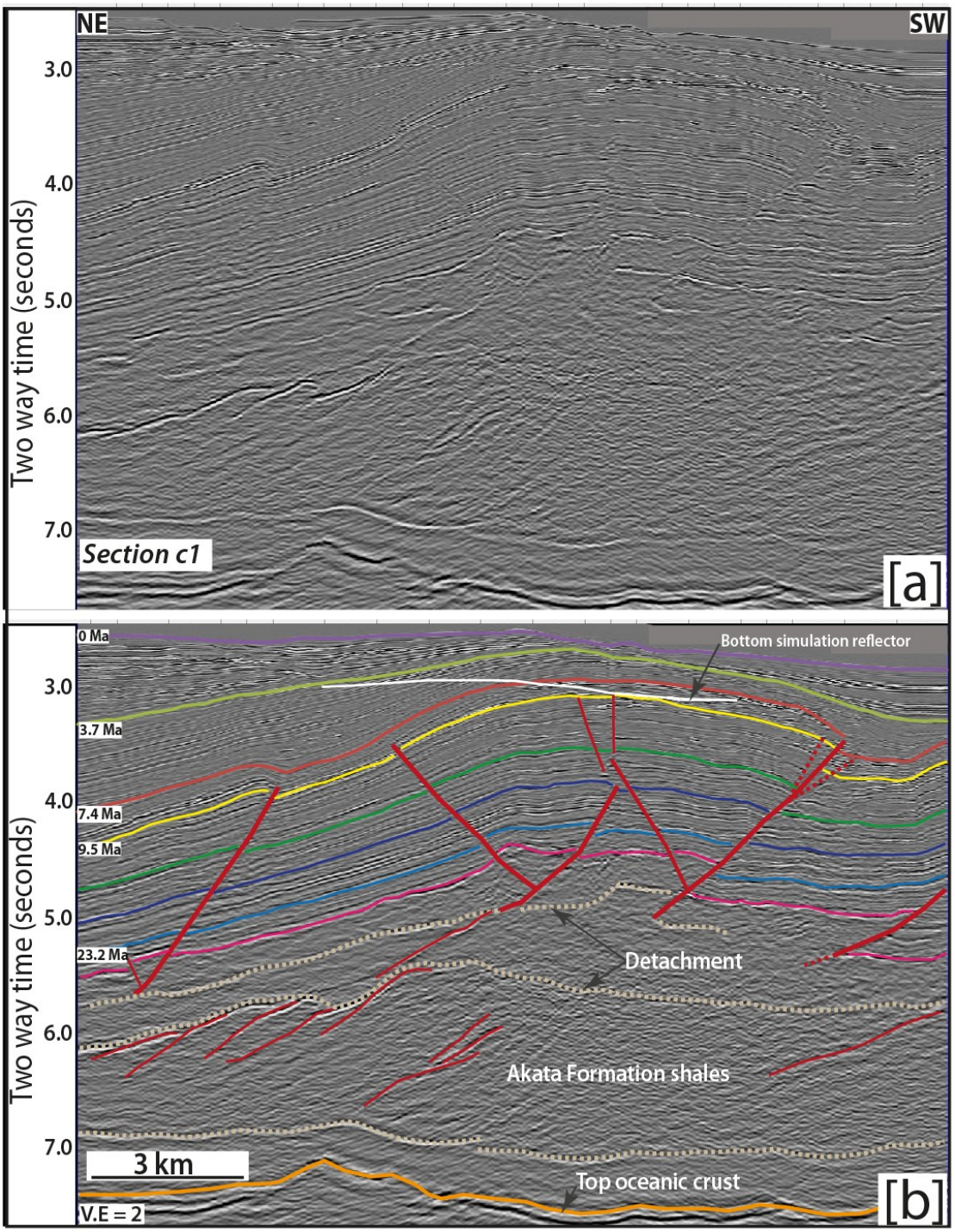


Figure 3.9: (a) and (b) represent un-interpreted section, and interpreted versions of section c1 across Fold C (located in Figure 3.1a). This section shows the seismic expression of fold C which is a very broad (up to 10 km wide) structure with low displacement planar thrusts. The structure is cored by a thrust duplex that developed within the Akata shales.

3.3.2 Channels and interaction with structures

From the seismic analysis, four Pleistocene – Recent active channels were identified (labelled 1 – 4) and four main fold structures (A – D), which are the focus of the study (*cf.* Fig. 3.1a). The channels can be identified clearly on the seabed bathymetry and edge map together with a buried channel which is not considered in this study (Fig. 3.10c). A map of the seabed compiled from 3D seismic datasets (provided by PGS – *cf.* Fig. 2.3a) shows that these channels largely originate from the shelf edge region of the Niger Delta (see also Mitchum and Wach, 2002). A section across the buried channel and channel 4 reveals the general nature of channels in the study area (Fig. 3.10a, b). The channel facies are made up of a channel axis fill that is characterized by medium to high amplitude, discontinuous, chaotic seismic reflections and usually contained within an erosional base (labelled 'container' – Fig. 3.10b). The channels are also characterised by well-developed levees (outer levees) and possible internal levees in situations where a channel complex develops (Fig. 3.10b; see also Deptuck et al., 2007; Janocko et al., 2013). These levees (up to 4 km in lateral extent) are characterised by relatively low to high amplitude, continuous seismic reflections that thin laterally away from the main channel axis, defining a wedge-shaped geometry. Most of the Pleistocene – Recent channel levees appear to downlap onto a seismic surface that is estimated to be approximately 1.2 – 1.3 Ma (Fig. 3.10b) which implies that the channels are approximately of that age and younger.

These channels display a range of interactions with the active structures having seabed relief (Fig. 3.10c). These interactions include deflection around fold tips (e.g., channel 4 deflection at the tip of Fold B, and the deflection of the buried channel at the tip of Fold D); diversion parallel to a structure (e.g., channel 2 diversion by Fold C) and incision across the centre of growing structures (e.g., channel 1 incision across Fold B). These channels are generally transverse to structures and predominantly run in an approximately NW-SE direction parallel to the slope gradient except where they interact with active structures (Fig. 3.10c). Channel 4 which is deflected at the lateral tips of Folds D and B, is then diverted to a more southerly path as it approaches Fold A, before cutting through Fold A where it then joins, or is captured by channel 1 (Fig. 3.10c; Fig. 3.1b). Channel 1, in contrast cuts through Fold B, but channel 3, is deflected slightly to the south prior to joining channel 1 where channel 1 cuts across the fold (Fig. 3.10c). Channel 2 exhibits a somewhat different behaviour; It flows down through the piggyback basin where the underlying thrusts are buried (*cf.* Fig. 3.6) and it is diverted by approximately 25 km in a SW direction to end up running almost perpendicular to the regional seabed slope behind Fold C. Beyond the tip of Fold C it too joins channel 1.

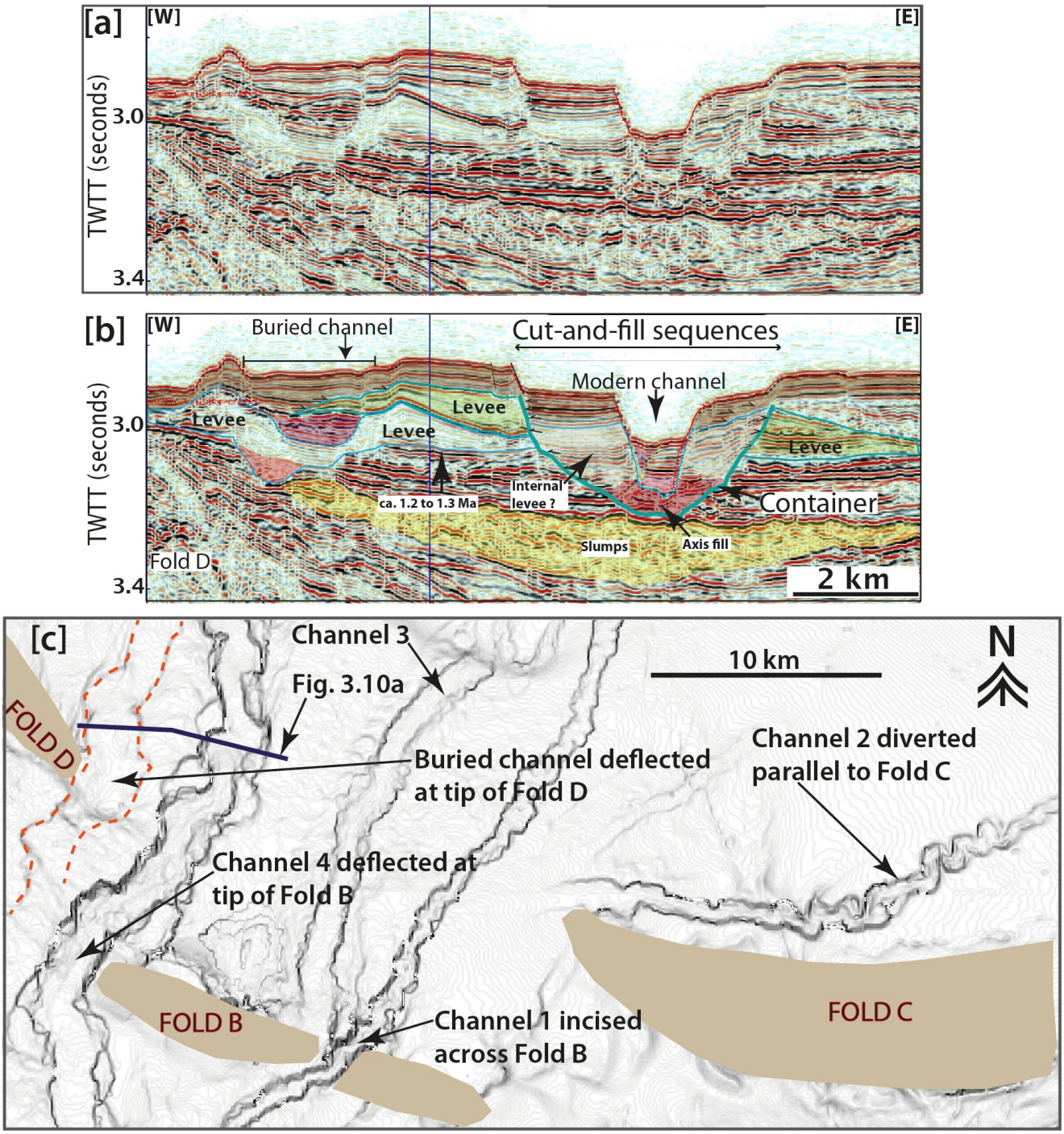


Figure 3.10: (a) uninterpreted; (b) interpreted seismic section across a buried channel and channel 4 (see section location in Figure 3.10c) illustrating the geometry of studied channels, and how the downlap surface of channels levees is used as a proxy to estimate channel age; (c) is a geomorphic map of the seabed showing modern channels and a buried channel (dash-red line) interaction with structures having seabed relief (Folds B, C and D).

3.3.3 Temporal and spatial variation in fold shortening

The calculated shortening through time, expressed as strain, is shown for four representative sections, a1, b1, c2, and d1 across each fold (Fig. 3.11a). The total (maximum) shortening is the strain recorded on the pre-growth strata at the present day and hence is the intercept on the y-axis in the cumulative strain graph. The sections chosen for this calculation are at strain maxima. Folds D and B, which each include two fault-related, fold structures (*cf*. Fig. 3.8) have shortened by 3810 m and 3430 m respectively. This equates to a strain of -0.35 and -0.32.

The shortening of Fold A is lower (1470 m) with a strain of -0.15. The maximum shortening recorded on Fold C from a representative section (section c2; Fig. 3.1a) is significantly lower than the other structures at 1027 m or a strain of -0.06 (Fig. 3.11a). For this study I am particularly interested in the variation in the shortening through time. The analysis shows that shortening started at 12.8 and 9.5 Ma for all structures investigated (Fig. 3.11a), and for Folds A, B and D continued at a similar rate from 9.5 until 3.7 Ma. Moreover, Folds B and D exhibit the highest strain rates in this time interval. Fold C appears to have behaved somewhat differently to the fault-propagation folds exhibiting a low, constant growth rate until 7.4 Ma when its growth rate accelerated. The growth rates for all structures slowed down in the last 3.7 Ma (Fig. 3.11a). The interval strain rates can be calculated explicitly by considering the discrete accumulation of strain between each time line mapped on the seismic data set (Fig. 3.11b). Generally, the highest interval strain rates, between -0.02 and -0.06 Ma^{-1} or (-1E-16 and -15 s^{-1}), are recorded for Folds A, B and D within the 9.5 – 7.4 and 7.4 – 3.7 Ma time intervals (Fig. 3.11b). For Fold C, the strain rate values are very low (< -0.01 Ma^{-1}), although it does appear to increase between 7.4 and 3.7 Ma time interval (Fig. 3.11b). In detail, Fold B has had the fastest rate between 9.5 and 7.4 Ma, followed by Fold D; however, the rate for Fold D is higher than that of Fold B between 7.4 and 3.7 Ma. These strain analysis results are broadly in line with the seismic observations of the Miocene to Recent sedimentary units.

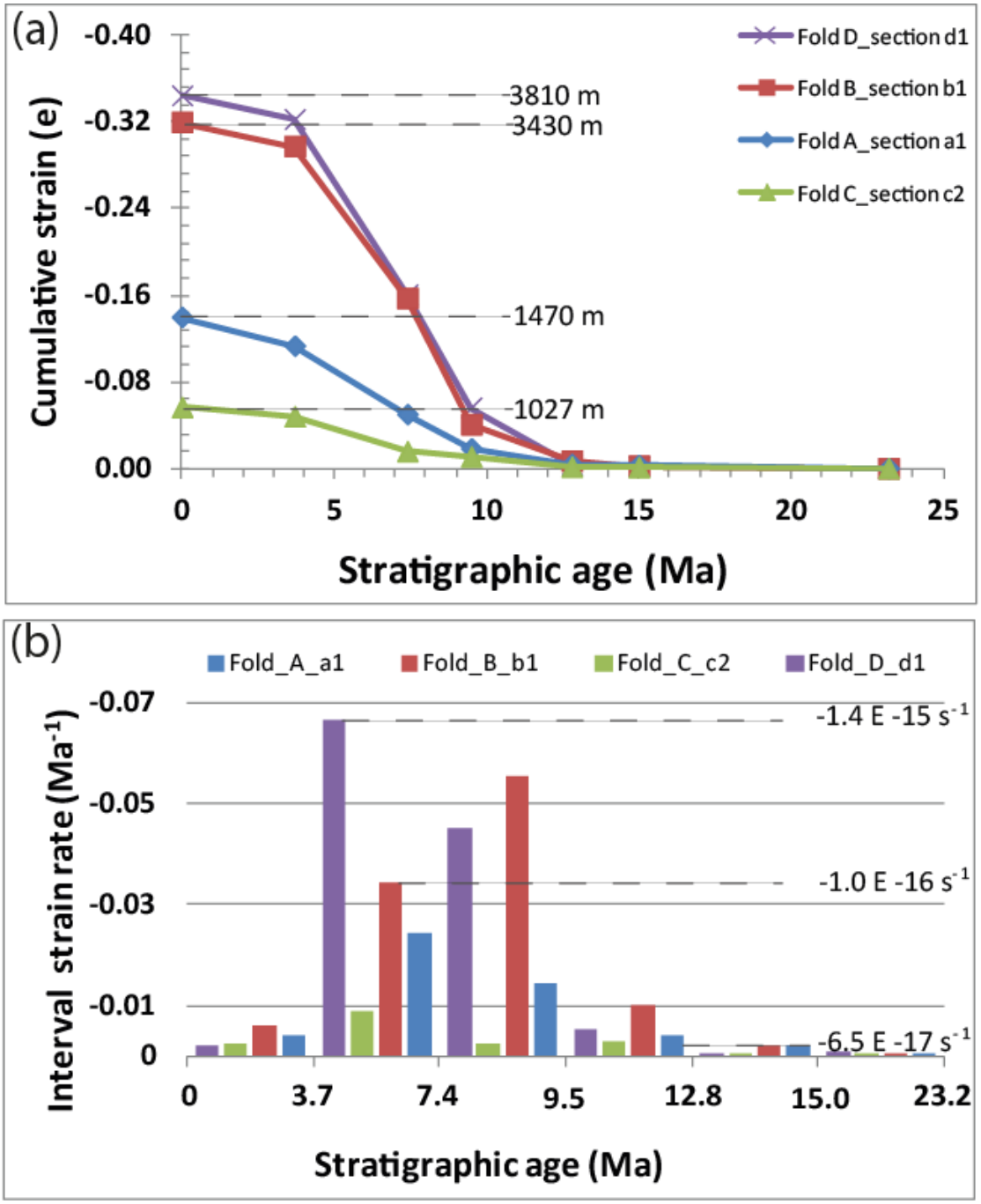


Figure 3.11: (a) Plots of cumulative strain against stratigraphic age determined from representative sections (a1, b1, c2 & d1) shown in Figure 3.1a. The pattern of strain is the same for all folds but the absolute cumulative strain varies from structure to structure; (b) plots of interval strain rate against stratigraphic age (i.e., the gradient of curves shown in Figure 3.11a). These plots show variations in the interval strain rate through time. The maximum interval strain rate for all folds occurred between 9.5 Ma and 3.7 Ma; and all folds show a significant reduction in interval strain rate in the last 3.7 million years.

The truncation of seismic reflections by the 3.7 Ma surface (Fig. 3.2b) coupled with the fact that this surface can easily be traced across major structures in the seismic volume is notable. It may mean that there was a pause or hiatus in deformation during that time thereby explaining the slowdown in interval growth rate since 3.7 Ma (Fig. 3.11). The larger maximum strains measured for Folds B and D are not surprising when compared with Fold A, because Folds B and D represent two structures (composite folds). The results are interesting in that if we assume equal contribution of both structures in B and D to the total strain, to a first approximation individual fault-propagation fold structures in this part of the Niger Delta have almost the same maximum cumulative strain and it has apparently accumulated at relatively similar rates (-0.02 to – 0.06 Ma^{-1}), at least within the temporal resolution of our data.

The pattern of strain distribution along the strike of the folds is shown in Figure 3.12 for a single pre-kinematic horizon (23.2 Ma) and three other horizons (7.4 Ma, 3.7 Ma and the seabed). For Folds B and D we see strain reduction towards the fold tips, while for Folds A and C, the folds continue outside of the survey area for which we have seismic data, so the lateral tips are not observed. Folds B and D have typical 'bell'-shaped shortening profiles, which is characteristic of structures that grow by lateral propagation. Strain is highest on the oldest pre-kinematic horizons and declines over time, consistent with the data in Figure 3.11. For all three of the folds, local minima are seen between regions of higher strain. Such local minima in both thrust and normal fault systems are typically interpreted as the signature of segment linkage (e.g., Davis et al. 2005; Higgins et al., 2009; Cartwright et al., 1995; Gawthorpe and Leeder, 2000; Bergen and Shaw, 2010 amongst many others) although there is a possibility along strike variation in strain could also be due to growth partitioning and not just structural linkages. Significantly, the minimum in the strain profile for the composite Fold B at 18 km along strike distance occurs at the position where the main switch occurs in dominant thrust out of the two mapped (Fig. 3.1a). So although neither fault-propagation fold tips out at this position, the cumulative shortening is at a minimum at this position at all times during the formation of the fold, including at the present day. However, in detail the along-strike, strain-distribution maxima and minima are not always in the same location for each stratigraphic horizon. At the 10 km position along Fold A for example, maxima or relative highs in the 23.2 and 7.4 Ma horizons actually correlate with strain minima at the 3.7 Ma and seabed surfaces. At a position of 15 km along this fold the opposite occurs, and again at 30 km a broad minimum in the older two horizons corresponds with a high in the 3.7 Ma surface. In Fold C, the strain variations in along strike distance, also show possible fold segments identified in the older horizons, but the youngest syn-growth strata (seabed) does not show the same number of segments. This may suggest early linkage between fold segments and once linked, younger growth strata record shortening of a single

structure, and that linkage points do not necessarily remain the location of persistent low displacement. For Fold C, which behaves more like a detachment structure (*cf.* Fig. 3.9), the accumulated strain is low compared to the other structures (Fig. 3.11). The maximum strain recorded by this structure is less than -0.06, which is only approximately 30 % of the maximum in Fold A (strain of -0.15) which is also a single structure and not a composite structure as are Folds B and D. These data suggest that whilst a first-order generalization of the accumulation of strain on the structures since Miocene can be deduced, an understanding of the accumulation of strain at any one point in time or space depends on the detailed history of the fault/fold interaction through time. It also appears that the kinematics, or mechanics, of the deformation through time may also have influenced the strain history because the fault propagation folds seem to have a different strain history than that of the nearby detachment fold; and on the overall behavior of the structure – either as a fault-propagation, or a fold detachment structure.

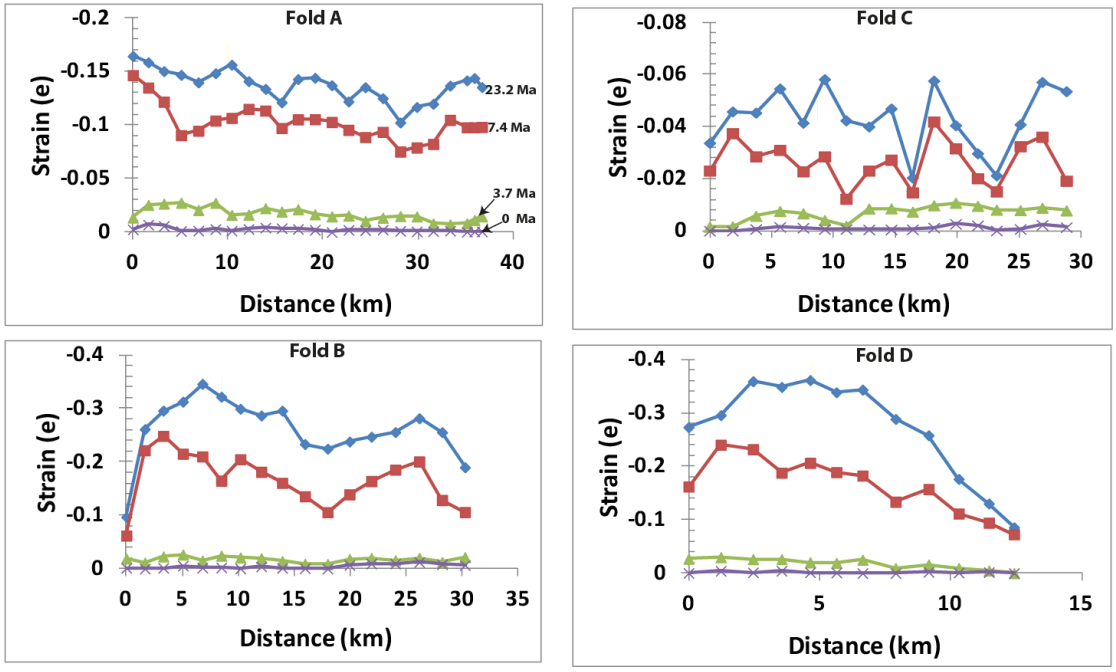


Figure 3.12: Shows the plots of cumulative strain for horizons at 23.2, 7.4, 3.7 Ma and present day seabed along the strike of Folds A to D. The strain decreases as the horizons become younger, reflecting the growth of the structures through time.

3.3.4 Strain variation and submarine channel response

Using the temporal and spatial evolution of strain through time, we can evaluate how the Miocene to Recent shortening in the toe-region of the Niger Delta wedge affected pathways of submarine channels in the area. Starting in the north of the study area, channel 4 is deflected around the tip of Fold D, where there is a minimum in the present day topographic expression of the fold. When the position of channel 4 is plotted on the strain-distance graph, the channel has been, as might be qualitatively expected, deflected to the region of lowest cumulative strain corresponding to the tip of the fold (Fig. 3.13 – D1). In addition, if the interval strain rates calculated at two positions [1], at 4 km along the fold, and [2], at 10 km along the fold are examined, we see that the interval strain rate at location [2] (close to the fold tip) is always lower compared to that at location [1] throughout the growth of the structure, and is significantly reduced to approximately -0.0023 Ma^{-1} (-7 x 10^{-17} s^{-1}) in the last 3.7 million years (Fig. 3.13 – D3). These data strongly suggest that channel 4 is exploiting this region to cross Fold D because it has been a local strain minimum throughout the life time of the channel.

However down-system to the south, both channel 4 and channel 1 cross Fold A in an area where the total cumulative strain since the Miocene is high (ca. -0.15), and close to a maximum for this structure (Fig. 3.13 – A1 and A2). However the strain on the younger 3.7 Ma and seabed horizons is low at this position (Fig. 3.13 – A1). The interval strain rate calculated for the last 3.7 Ma in this area is approximately -0.0016 Ma^{-1} (-5 x 10^{-17} s^{-1}; Fig. 3.13 – A3). The calculated rate for the same time interval at position 29 km along the fold, where there is a broad minima in the older horizons (23.2 and 7.4 Ma), is approximately -0.004 Ma^{-1} (-1.2 x 10^{-16} s^{-1}). Nevertheless this strain difference was enough to cause channel 4 to deflect and flow southward before eventually crossing the fold (Fig. 3.13 – A2) at a position where the interval strain rate in the younger horizons is low (-5 x 10^{-17} s^{-1}). The interval strain rate where this channel crosses Fold A, is similar to the interval strain rate in the younger horizons where channel 4 also crosses Fold D (*cf.* Fig. 3.13 – D1 and D3). Fold B, in the center of the study area, is incised by channels 4, 3 and 1. The seabed map shows that channel 4 is deflected to the fold tip, crossing in a region characterized by low cumulative strain values on the older stratigraphic horizons, and also low strain for the younger stratigraphic horizons, where the interval strain rate from 3.7 Ma to present is -0.0026 Ma^{-1} (-8.4 x 10^{-17} s^{-1}) (Fig. 3.13 – B1, and B2).

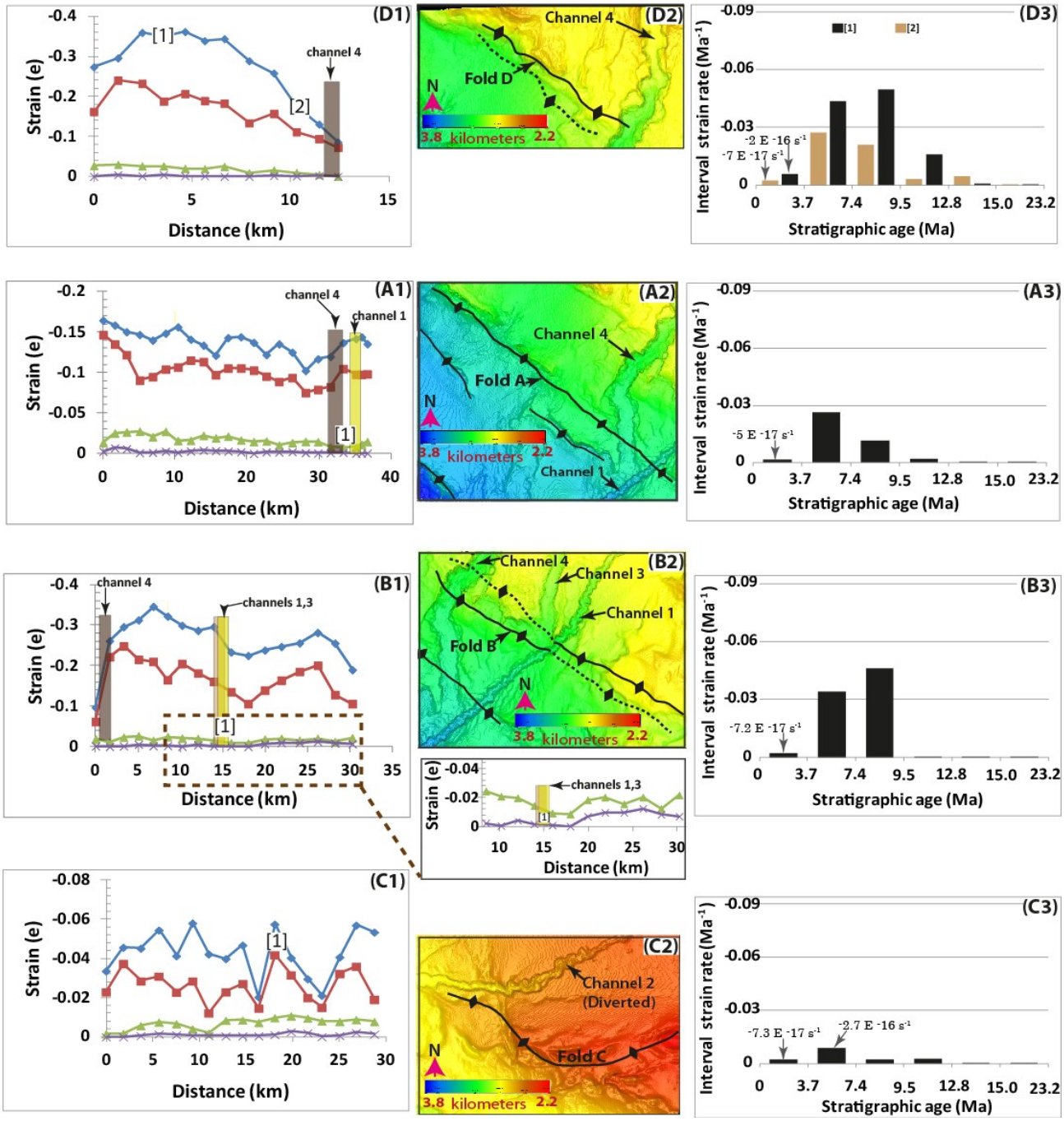


Figure 3.13: (D1) Cumulative strain of stratigraphic horizons in Fold D, (D2) seabed map showing the outline of Fold D and relative position of Channel 4, (D3) interval strain rates measured at locations [1] and [2] shown in D1, and represented by the black and brown bars respectively; (A1) Cumulative strain of stratigraphic horizons in Fold A, (A2) seabed map showing the outline of Fold A and relative positions of seabed channels, (A3) interval strain rates measured at location [1] shown in A1; (B1) Cumulative strain of stratigraphic horizons in Fold B, (B2) seabed map showing the outline of the composite Fold B and relative position of seabed channels, (B3) interval strain rates measured at locations [1] shown in B1; (C1) Cumulative strain of stratigraphic horizons in Fold C, (C2) seabed map showing the outline of Fold C and relative position of Channel 2, (C3) interval strain rates measured at location [1] shown in C1.

Similarly, channels 1 and 3 also cross close to the local strain minimum along strike on Fold B where displacement is transferred between the two structures that form the composite structure (Fig. 3.13 – B2). Nevertheless the cumulative strain of the older horizons at -0.16 and -0.28 is still relatively high at this position (> 75 % of the maximum at which the channels can keep pace). However, the cumulative strain for the 3.7 Ma – Recent interval is very low where the two channels cross, with an interval strain rate of approximately -0.0022 Ma^{-1} (-7.2 x 10^{-17} s^{-1}) which again is similar to the values calculated for the same interval where channel 4 crosses Fold D and channels 1 and 4 cross Fold A. This likely explains why the channels cross at this location, and the clear deflection of channel 3 to join channel 1 upstream of this location.

The detachment fold (Fold C) in comparison has a much lower cumulative strain over its entire history than the other three folds examined (Fig. 3.13 – C1). The maximum cumulative strain is about 15 % that of Folds D and B and 30 % that of Fold A. The interval strain rates for the time of channel development are consequently also very low, at approximately -0.0023 Ma^{-1} (-7.3 x 10^{-17} s^{-1}; Fig. 3.13 – C3). Nevertheless, this structure is still able to cause the diversion of channel 2 for up to 25 km before the channel finally deflects around the fold tip and joins with the other channel systems (Fig. 3.13 – C2, Fig. 3.1a). Despite the low strain in this fold, the positive topographic relief, coupled with an uphill slope that extends for up to 5 km due to the broad nature of the fold (*cf.* Fig. 3.6) likely caused the channel diversion.

In summary, the seabed channels in this part of the Niger Delta can keep pace with the growth of fault-propagation folds whose interval strain rates are between -0.002 to -0.0022 Ma^{-1} (-5 and -7.2 x 10^{-17} s^{-1}) for the time period from 3.7 – 0 Ma (*cf.* Fig. 3.13). For the broad, detachment fold with a longer wavelength of uplift field, even lower maximum strain rates -0.0023 Ma^{-1} (-7.3 x 10^{-17} s^{-1}) have caused enough tilting of the seabed to force the channel to be diverted around the tip of the fault.

3.4 DISCUSSION

3.4.1 Strain rate reduction in the last 3.7 Ma

The results in in this chapter show that the growth of the thrust-related folds in the study area has taken place since 12.8 Ma and although some of the thrusts stopped growing within the 3.7 Ma to Recent interval, those with seabed expression are still actively growing (see Fig. 3.2b), but that the shortening rate has reduced significantly since 3.7 Ma. Another observation is that across this ca. 40 km wide transect through the outer fold and thrust belt there is no evidence for simple forward-propagating thrusting and that the four thrust-related folds studied have grown at the same time, at least within the constraints of the available stratigraphic data (Fig. 3.11).

This slowdown in growth during the later stages of fold growth may be due to the fact that; (i) faster growth is now being taken up by the younger thrusts/folds which have formed further basinward at the down-dip toe of the outer fold and thrust belt (e.g., Corredor et al., 2005; Morley, 2007, 2009;); or (ii) there has been an overall reduction in deformation rate on the entire Niger Delta gravitational system in the Plio-Pleistocene. Corredor et al. (2005) used growth strata and palinspastic sequential restoration of regional sections through the inner and outer fold and thrust belts to demonstrate that the youngest thrust is the most frontal (located ca. 10 km basinward of our study area), and that the inner fold and thrust belt formed before the outer fold and thrust belt. However they also show that at a more local scale, a complex sequence of thrusting can be observed which can include coeval thrusting, and not just piggy-back forward propagation. The observation of synchronous growth on the four structures studied for our work is consistent with the Corredor et al. (2005) results.

Recent work by Rouby et al. (2011) suggests that second reason given above for the slow down in growth is more plausible. Using a detailed stratigraphic framework at high temporal resolution, they demonstrate very clearly a slow down of both the amount and rate of deformation in the upslope extensional domain in the Plio-Pleistocene of the eastern Niger Delta in the last 4 Ma. Their work also shows that deformation slowed down in the compressional domain within the same time-frame, indicating a strong coupling between the deformation in the extensional and compressional domains, as is expected in a gravity-driven system. They attribute the slowdown in the extension to a decrease in sediment supply reaching the delta. The reduction in sedimentary load, leads to a reduction in strain rate on the extensional faults, which then translates down-slope to lower rates of shortening. The reduction in sedimentary load is supported by the work of Jermannaud et al. (2010)

who reported a general reduction in sediment supply to the Niger Delta during the Plio-Pleistocene which they suggest may have been in response to the aridification of the East Atlantic region.

3.4.2 Fold growth

Where fold growth is associated with the deposition of syn-growth units, two conceptual end-member models can be used to describe the relationship between sediment accumulation rate and structural uplift rate (Fig. 3.14; see also Burbank et al., 1996; Shaw et al., 2004). For example, when the sediment accumulation rate is greater than the uplift rate, the syn-growth sediments (pink) albeit thinning over the crest of the structure will overlap the growing structure (Fig. 3.14a). In this situation, seabed channels would be expected to keep pace with the growth of the structure by cutting through as shown in Figure 3.14b because there wouldn't be a significant positive bathymetric relief. However, when the structural uplift rate is higher than the sediment accumulation rate (Fig. 3.14c), the syn-growth sediments cannot overlap the growing structure and therefore, will largely onlap the structure (Burbank et al., 1996). Consequently, seabed channels would be expected to divert to the lateral tips of the structure (Fig. 3.14d) as a result of the development of positive bathymetric relief.

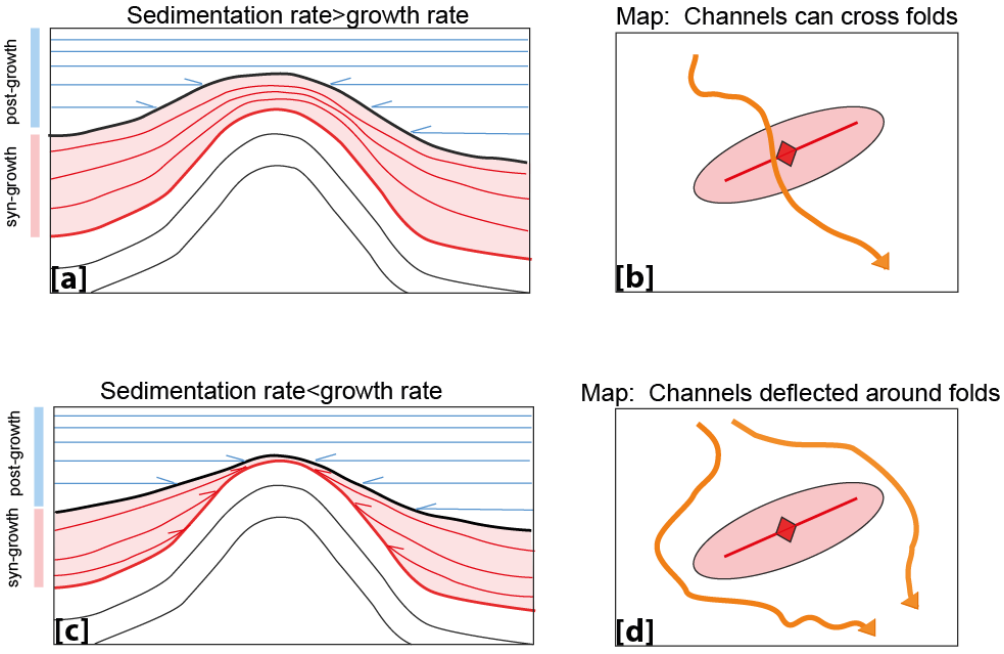


Figure 3.14: Simple diagrams to illustrate the end-member relationship between structural uplift rate and sediment accumulation rate: (a) Higher sediment accumulation rate relative to uplift rate where the syn-growth sediments (pink) overlap the growing structure, and a seabed channel that keeps pace with growth of structure is illustrated in (b); (c) Higher uplift rate relative to sediment accumulation rate with the syn-growth sediments (pink) onlapping the growing structure, and related channel diversion in (d).

In reality, many natural examples of growing structures are expected to lie somewhere between these two end-members. In this study for example, two groups of structures were identified – the fault-propagation folds that largely occur in the central and western parts of the study area, and the broad detachment fold that occurs in the eastern part of the study area. At the resolution of the seismic data, the syn-growth sediments in the fault-propagation folds largely overlap the crest of the growing structures since 3.7 Ma as shown in representative sections across Folds A and D in Figure 3.15 (a, b). However they are still associated with a tilt of the present day seabed and there is an 'uphill' slope on both of these folds (Fig. 3.15a, b) of between 1.5^{o} and 2^{o} on the up-dip, north-easterly dipping limb of the respective anticline. The 'uphill' slope is limited in lateral extent to a maximum of 2 km. The presence of this 'uphill' slope, coupled with the overall thinning of the growth sequences at the structural culmination of the fault-propagation folds, does suggest the presence of a slight positive bathymetric relief for most of the recent growth histories albeit showing an overall higher sediment accumulation rate relative to structural uplift rate. Consequently, the fault-propagation folds in the central parts of our study area lie somewhere close to the end-member model (a) in Figure 3.14.

On the other hand, the detachment fold in the east of the study area, lie somewhere close to the end-member model (c) in Figure 3.14 because the syn-growth sequences associated with this structure since 3.7 Ma, largely onlap the fold (Fig. 3.15c). On close examination, these syn-growth units show periods of minor offlap (continuous white lines, Fig. 3.15c) within overall onlapping geometry. These discrete, alternating packages of onlap, offlap within overall onlapping geometry, suggest variation (or pulses) in growth rate of Fold C through time and not just a uniform growth rate. Other studies with either good stratigraphic resolution or seismic resolution have also documented non-uniform growth rate for other folds (e.g., Butler et al., 1995a; Shaw et al., 2004). Fold C also has a similar 'uphill' slope of between 1.5^{o} and 2^{o}, on its northerly dipping limb, but it has a longer wavelength 'uphill' slope of up to 5 km when compared to the fault-propagation folds (Fig. 3.15c). In addition to the difference in uphill slope length, the fault-propagation folds are only 2 to 3 km wide whereas Fold C is characteristically very broad (up to 10 km wide, *cf.* Fig. 3.6).

In summary, both the fault-propagation folds and the detachment fold show variation in their pattern of fold shortening along strike; and typical 'bell'-shaped shortening profiles which are characteristic of structures that grow by lateral propagation (e.g., Davis et al. 2005; Higgins et al., 2009; Gawthorpe and Leeder, 2000) are observed in all structures (*cf.* Fig. 3.12). The detachment fold however, shows an overall lower cumulative strain (shortening) compared to the fault-propagation folds. The interval growth rate also differs in the two sets of structures; however, all

structures show a similar pattern of growth through time with the maximum period of growth occurring between 9.5 Ma and 3.7 Ma, and slowing significantly from 3.7 Ma (*cf.* Fig. 3.11). The fault-propagation folds have the highest interval growth rate (-0.02 and -0.06 Ma^{-1}) and in contrast, the growth rate is very low in the detachment structure (< -0.01 Ma^{-1}) over the same period of time.

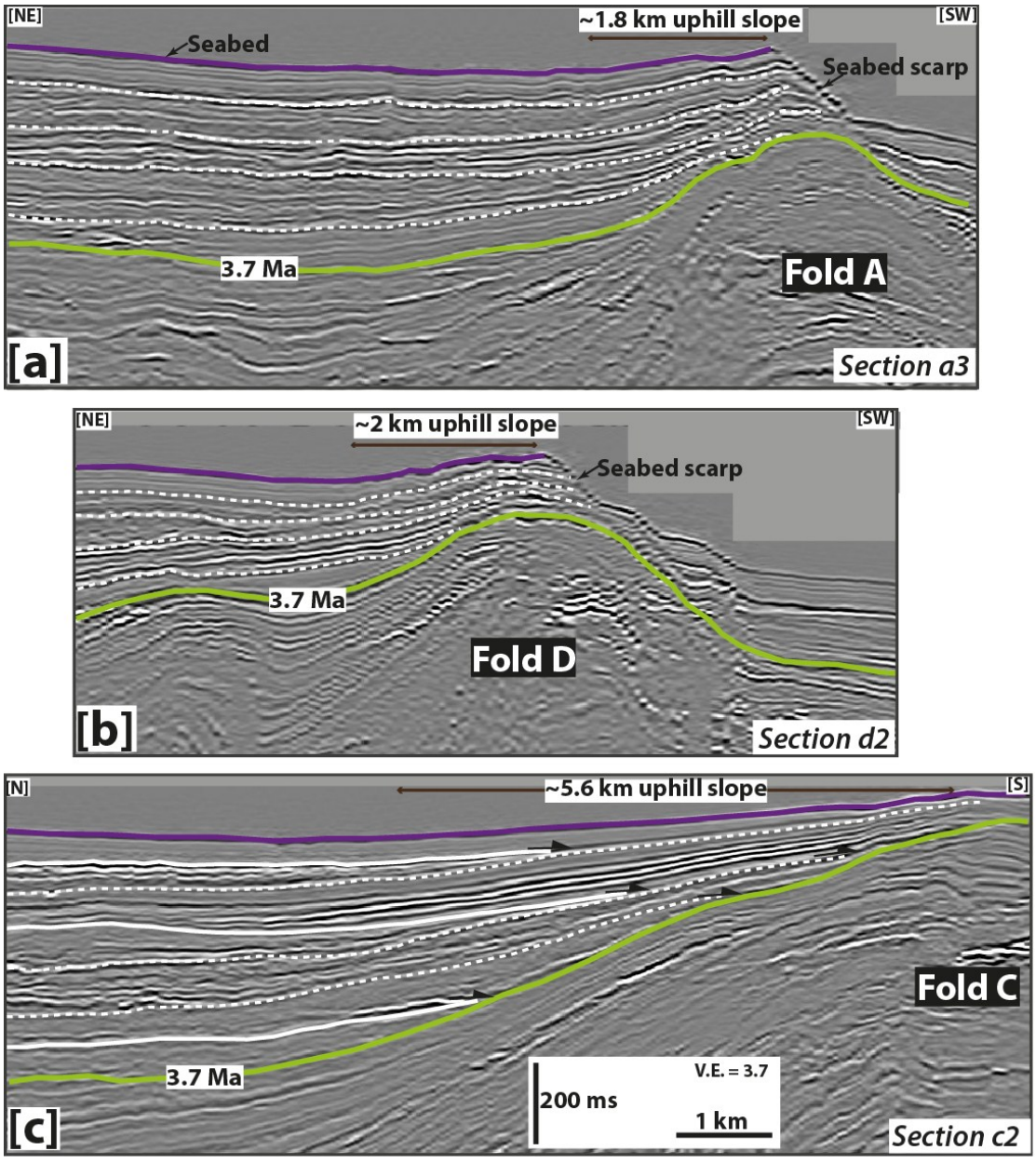


Figure 3.15: (a) Section across Fold A (section a3 in Figure 3.1a) showing mainly overlapping seismic horizons over the structure since 3.7 Ma (although these horizons have been truncated by the seabed scarp); this indicates a slightly lower uplift rate relative to sedimentation rate. Note that the uphill slope is 1.8 km in lateral extent. (b) Section across Fold D (section d2 in Figure 3.1a) also showing the same geometric relationship as in (a). Note also that the uphill slope is ~ 2 km in lateral extent and the overlapping horizons have been truncated by a scarp. (c) Section across Fold C (section c2 in Figure 3.1a) showing seismic horizons which largely onlap the growing structure since 3.7 Ma – although there are periods of minor offlap (continuous white lines) which indicate variation in growth rate through time. The overall onlapping geometry indicates a slightly higher uplift rate relative to sedimentation rate. Note that the uphill slope is ~ 5.6 km in lateral extent.

3.4.3 Channel response to active deformation

Analyses in this study show that all structures affecting channel pathways are associated with some bathymetric relief, but the length of the 'uphill' slope varies (approximately 2 km for the fault-propagation folds and up to 5 km for the detachment fold). And while the syn-growth sediments largely overlap the fault-propagation folds, the presence of the local 'uphill' slopes on the up-dip flanks of the anticlines suggests that sedimentation does not completely keep pace with the structural growth. If the sediment accumulation rate were to fully keep up with fold growth then the fold would never develop bathymetric relief and would be continuously covered with sediment; hence incoming channels would not 'see' the fold.

These results help us to elucidate the detailed interaction between the time-integrated history of deformation in this part of the Niger Delta fold and thrust belt, and the submarine channels which convey sediment from the shelf edge to the deep sea. In general, the quantitative results support the qualitative conclusions that workers have drawn from previous studies – namely that submarine channels tend to seek out points of lowest relief and lowest relative uplift rate to make their way down slope (e.g., Huyghe et al., 2004; Ferry et al., 2005; Clark and Cartwright, 2009; Morley, 2009; Mayall et al., 2010 amongst others).

In addition, I find that fault-propagation folds with very little positive bathymetric relief – associated with 'uphill' slope of no more than 2 km long (Fig. 3.15a, b); and whose contemporary interval strain rates is between -0.002 to -0.0022 Ma^{-1} (-5 and -7.2 x 10^{-17} s^{-1}) can be incised by modern seabed channels that are active at the same time. However, for the detachment fold whose positive bathymetric relief is associated with a longer wavelength of 'uphill' slope (up to 5 km); even at a comparatively lower maximum strain rates of -0.0023 Ma^{-1} (-7.3 x 10^{-17} s^{-1}), can cause enough tilting of the seabed and force channels to be diverted around the tip of the fold. These results suggest that where channels have already developed, and are cutting through a growing structure, they are likely able to keep pace with growth rates on the order of 0.0022 Ma^{-1} once the 'uphill' slope length is not more than 2 km as seen in the fault-propagation folds. However, these channels could be diverted if the 'uphill' slope was already in place (no matter its length) prior to channel development. Secondly, broad structures with longer wavelength of 'uphill' slope will automatically cause channels to divert (such as the diversion of channel 2 by Fold C, Fig. 3.1a). But if the channel was already in place, it might be forced to abandon its original path, or migrate laterally as a response to continued seabed tilting as the structure widens through time. However another factor that is likely to play an important role in channel incision through growing structures is the erosive power of the sediment

gravity flows that flow down the channels. Channels with lower erosive power will be forced to divert and those with higher erosive power may be able to continue to incise and maintain a pathway through a growing structure (see also Morley, 2009; Mayall et al., 2010). Quantifying the erosive power of sediment gravity flows is not a trivial matter; an approach based on calculating turbidity current shear stresses is covered in chapter 4.

While variation in strain measured both spatially and through time can be important in determining channel response to growing structures as demonstrated in this study, it is important to note that using displacement – distance plots to identify strain minima for prediction of sediment pathways can be misleading if these displacement measurements are not made for strata that actually bracket the time interval of channel system activity. In this study I have found that fold growth rates have not been constant through time, and that areas with high cumulative displacement may nonetheless have accumulated relatively small amount of strain in the recent geological past. In a number of examples, positions of fold/thrust linkage remain persistent regions of low displacement during the life of fold growth (e.g., Fold B, Fig. 3.12). However, for some folds (e.g., Folds A, C), the regions of low displacement may vary during the life of fold growth (*cf.* Fig. 3.12). Therefore, without knowing that the channels investigated started to form in the last 1.3 Ma for example; and not measuring the interval strain rate of stratigraphic horizons that actually bracket the time interval of channel system activity (in this case, from 3.7 Ma to present-day), we might have assumed that the channels were capable of keeping pace with higher structural growth rates of up to -0.06 Ma^{-1} (-1E -15 s^{-1}) which in this study, are associated with the older 9.5 – 7.4 Ma intervals.

3.4.4 Shortening versus vertical uplift

A remaining question is how the horizontal fold shortening and strain rate, translates into a vertical component of growth. To be able to quantify the amount of vertical rock uplift, and more specifically the amount of bathymetric relief associated with a certain amount of fold shortening would arguably be more useful than quantifying the horizontal shortening. In general, all cases of fault-related-folding generate vertical uplift associated with shortening. Uplift continues as shortening progresses except for the case of a simple fault bend fold, where once the lowest unit in hanging-wall reaches the upper footwall flat, the fold broadens (increases in width) without generating any further vertical relief. To convert shortening into a vertical component of uplift requires knowledge of an appropriate geometrical and kinematic model for the fault-fold type. The results are highly dependent on the kinematic model chosen and it is not trivial to derive uplift from shortening or slip.

Some of the simplest relationships exist for detachment folds, but even these kinematic models for a single fold type predict different amounts of vertical uplift for the same amount of slip or shortening. For example if one uses the De Sitter (1956) model for detachment fold growth, where the fold grows by increase in limb dip, or progressive limb rotation, then the relationship between uplift and slip is non-linear with more uplift at lower slip values, and uplift decreasing as slip increases (e.g., Hardy and Poblet, 1994; Poblet and Hardy, 1995; Storti and Poblet, 1997). In comparison with the Dahlstrom (1990) model, where fold limbs lengthen as dip increases and folds grow, the relationship between uplift and slip is linear (Poblet and Hardy, 1995).

Likewise for fault-propagation folds there are many kinematic models and the final shape of the fold will depend on whether flexural slip (e.g., Suppe and Medwedeff, 1990) or a trishear model (e.g., Allmendinger, 1998) is assumed. Within the flexural-slip suite of models, two cases often considered are that of a constant limb thickness, or a fixed axial surface that allows for thickening or thinning in the frontal limb of the fold (Suppe and Medwedeff, 1990; Hardy and Poblet, 2005). For simple geometries both of these models predict an almost linear relationship between uplift and shortening (e.g., Storti and Poblet, 1997). More recently Hardy and Poblet (2005) have investigated the relationship between uplift rate, fault geometry and slip rate using a velocity description of deformation for both fault-propagation and trishear folds. Their results show that the velocity field varies in the back-limb, crest and forelimb of the structure and hence the relationship between slip, fault geometry and uplift rate is non-trivial. When they compare velocity models of a trishear fold versus a fault-propagation fold they show that the uplift rate above trishear fold crests is significantly smaller than for fault-propagation fold models. A method proposed by Bernard et al. (2007) and subsequently applied to emergent growing folds in the Tienshan, Taiwan and the Chinese Pamir (Daeron et al. 2007; Simoes et al. 2007; Li et al. 2013) uses another analytical, velocity-based model, derived from an analogue sandbox model of a growing fault-tip fold to relate fault slip to vertical rock uplift. This model likewise shows that uplift rate varies within domains with separate axial surfaces defined for the fault-related fold. In essence, all these kinematic approaches are entirely dependent on the application of an appropriate fault-fold model and fault geometry, being able to estimate fault slip from shortening, and do not take into account any change in fault-folding mechanics through time, and as such have significant limitations. Furthermore recent numerical studies based on geomechanics show that key parameters of a growing fold, such as crestal uplift, can vary significantly from results based on kinematic reconstructions (Vidal-Royo et al. 2012).

Despite the limitations of a kinematic approach, in an attempt to obtain an indication of the magnitude of the vertical uplift in the fold crestal area, I use the Hardy and Poblet (2005)

relationship for a single-step flexural-slip fault propagation fold where the uplift rate at the fold crest is given by:

$$\text{Uplift rate} = 2\,\dot{s}\,\text{Sin}\,\emptyset \qquad \text{(Eq. 3)}$$

Where $\dot{s}$ = slip rate, and $\emptyset$ is the fault dip.

To apply this relationship requires the conversion of our fold shortening to a slip rate, which we do using the relationship:

$$\dot{s} = (\text{shortening}/\text{Cos}(\emptyset))/\text{shortening time} \qquad \text{(Eq. 4)}$$

Therefore, using the measured strain and dip angle, the resultant uplift rates (m/Myr) for the fault-propagation folds (A, B and D) over a period of 3.7 million years, and the absolute uplift in meters are shown in Table 3.1. The maximum shortening measured across Folds A, B, and D in this study, is -216 m, -198 m, and - 204 m respectively. These translate to approximate uplift of 217.5 m, 201.7 m, and 216 m respectively. And the uplift rates are 58.8 m Ma^{-1}, 54.5 m Ma^{-1}, and 58.4 m Ma^{-1} respectively (Table 3.1). Overall, these calculated values of uplift rate are similar to the measured shortening rates for the fault-propagation folds (Table 3.1). This suggests an almost linear relationship between uplift and shortening with a gradient of approximately 1. This is not surprising as a similar relationship was reported by Storti and Poblet (1997) for fault-propagation folds.

Applying this method on Fold C (which has a lower shortening, Table 3.1) will produce an uplift value that is significantly lower compared to the fault-propagation folds. However, seismic analysis showed that Fold C has a relatively high uplift rate compared to the fault-propagation folds in the last 3.7 million years (*cf.* Fig. 3.15). For different kinematic models of detachment folds, the amount of uplift can vary by a factor of 2 (see Figure 2a in Poblet et al., 1997); hence, I don't attempt to estimate an equivalent uplift for Fold C. This shows that the conversion of fold shortening/strain to vertical uplift will produce results that largely depend on the model chosen. However, I think that shortening is easier to measure for subsurface seismically imaged examples. And when used in conjunction with the analysis of syn-growth strata relationship to growing structures, gives a model-independent strain estimate that can be relatively easily be applied, and use to judge large-scale channel – structure relationships as seen in this study.

Maximum uplift and uplift rate; shortening and shortening rate; strain and strain rate since 3.7 Ma								
Fold		**Uplift (m)**	**Uplift rate (m/Myr)**	**Shortening (m)**	**Shortening rate (m/Myr)**	**strain**	**Strain rate (Ma/Ma)**	**Strain rate (s^{-1})**
Fault-propagation	**A**	217.5	58.8	-216	-58	-0.0266	-0.00719	2.3E-16
	B	201.7	54.5	-198	-54	-0.0265	-0.00716	2.3E-16
	D	216	58.4	-204	-55	-0.0298	-0.00805	2.6E-16
Detachment								
C		-	-	-169	-46	-0.0107	-0.00289	9.2E-17

Table 3.1: Shows the measurements of maximum shortening and shortening rate; strain and strain rate since 3.7 Ma across the fault-propagation folds (A, B and C) and the detachment fold (Fold C). The equivalent maximum vertical uplift and uplift rate in the fold crest area of the fault-propagation folds is based on the Hardy and Poblet (2005) model.

3.4.5 Limitations

Most of the limitations in this study relate to the measurements of strain as already documented in section 3.2.2 (see also Hossack, 1979; Chapman and Williams, 1984). However, the resolution of the seismic data, which in this case, is approximately 10 – 13 m in the shallower levels that bracket the period of channel development, only allow us to fully constrain fold shortening and strain of the 3.7 Ma and the seabed (0 Ma) horizons in this younger syn-growth strata. This is a limitation because of inadequate temporal scale of structural growth; real variation may be stepped due to pulses in growth as seen in Figure 3.15c for example. Patterns of onlap and offlap in the seismic volume suggest that there may be a more pulsed growth rate at a finer temporal resolution. Consequently, this may affect the rate of growth that we associate with channel response in this study. For example, the uniform interval strain rates we associate with the time of channel development may actually vary through time if the resolution of the seismic data were to allow us map individual growth sequences deposited between 3.7 – 0 Ma across the seismic volume. Although there is no information about the absolute age of the channels, but estimate of the age using the dowlap-surface of the most recent channels levees (Fig. 3.10) suggests channel age that range from ca. 1.2 to 1.3 Ma; this period lies within the bracket of stratigraphic ages whose interval strain rate (growth rate) was used to analyse channel response. Therefore, the absolute age of the channel is not necessarily important for judging large scale channel response to structural growth and does not affect the results. In this study, I am only concerned with the large scale channel – structure

interactions such as channel deflection, diversion or incision across growing structures. The consideration of other important factors in understanding channel response to growing structures, such as flow shear stress and erosivity are found in chapter 4.

3.5 CONCLUSIONS

In this study area, the 3D bathymetry map of the seabed reveals modern seabed channels flowing downslope and perpendicular to growing thrusts/folds that act as barriers to the channels. These structures either cause the channels to deflect towards relay or lateral tips of folds. One structure causes channel diversion such that the channel flows parallel to the fold axis. However, some channels continue to incise through the growing structures.

I have reconstructed the temporal and spatial variations in cumulative strain and strain rates for four of the thrusts/folds having seabed relief in the study area. This work reveals that strain varies spatially along-strike of the structures, and from structure to structure. Cumulative strain also varies through time, and the maximum interval strain rate occurred between 9.5 Ma and 3.7 Ma, and has reduced significantly in the last 3.7 million years. Over this period, the highest interval strain rates for the fault-propagation folds documented in this study are between 0.02 and 0.06 Ma^{-1} (equivalent to 1E-16 and -15 s^{-1}). The detachment fold studied, Fold C, has much lower maximum interval strain rate values (< -0.01 Ma^{-1}). The total shortening for the structures varies from 3810 m (Fold D) to 1072 m Fold (C); giving a time-averaged maximum shortening rate of between 350 $\pm$50 and 90 $\pm$10 m/Myr (0.4 and 0.1 mm/yr) and then 50 $\pm$5 and 40 $\pm$5 m/Myr (0.05 and 0.04 mm/yr) in the last 3.7 Ma when the channels studied were active.

Displacement – distance plot relationships show that the fault/thrust structures have linked laterally over time. However, while points of fold linkage (recognised from minima in displacement-strike graphs) may remain persistent in regions of low displacement during the life of fold growth (e.g., Fold B), the locations of fold strain minima observed in older horizons may not necessarily coincide with regions of strain minima in younger syn-growth horizons for some folds (e.g., Fold A). Consequently, identification of strain minima for prediction of sediment pathways can be misleading if these displacement measurements are not made for strata that bracket the time interval of the channel systems.

Seismic evidence reveals that both the fault-propagation and detachment folds have positive bathymetric relief at the culmination of structural growth, with an associated uphill slope of

between 1.5^{o} and 2^{o}. However, whilst the uphill slope of the fault-propagation folds is approximately 2 km in lateral extent, that of the detachment fold is up to 5 km long. Where submarine channels developed coevally with structural growth, and are capable of crossing the structures, such as those in the central and western parts of the study area, they do so in positions of recent strain minima and at interval strain rates that are generally less than -0.02 Ma^{-1} (i.e., -15 m per million years which is ca. -1 x 10^{-16} s^{-1}) or at cut-off rate of approximately -0.001 to -0.002 Ma^{-1} (-5 to -7 x 10^{-17} s^{-1}). The study shows that a fold with similar uphill slope, but over a broader area (longer wavelength fold) (e.g., Fold C), may cause channel diversion even at very low strain rate of -0.002 Ma^{-1} (-7 x 10^{-17} s^{-1}). Therefore, a good understanding of the variations in spatial and temporal cumulative strain accommodated by growing structures in deepwater settings can help us predict the response of submarine channels which are the conduits for the transport of coarse-grained sediments that form hydrocarbon reservoirs in deepwater settings.

CHAPTER 4

QUANTIFYING GEOMORPHIC RESPONSE OF MODERN SUBMARINE CHANNELS TO ACTIVELY GROWING FOLDS AND THRUSTS, DEEPWATER NIGER DELTA

4.1 STUDY AIMS

How submarine channels behave in response to tectonic perturbation depends on their erosional dynamics. Channel erosivity over long periods of time will determine the overall channel morphology and long profile form. Consequently, the hydraulic geometry and shape of submarine channel longitudinal profiles are a manifestation of the competing processes of sedimentation, erosion and deformation (e.g., Pirmez et al., 2000; Huyghe et al., 2004; Ferry et al., 2005; Henio and Davies, 2007; Covault et al., 2011). This implies that, in principle, anomalies observed from along-channel profiles can be used to decode the long-term sedimentation history and responses to on-going deformation (Gerber et al., 2009; Amblas et al., 2011). However, our ability to do this is currently hampered by the fact that we have (i) a limited understanding of the time-integrated (as opposed to event-based) erosivity of submarine channels (Talling et al., 2012; Clark and Pickering, 1996a); and (ii) there are limited data sets which document the geomorphic response of submarine channels to tectonic perturbation where the timing, magnitude and locus of deformation can be constrained independently (e.g., Pirmez et al., 2000; Gee and Gawthorpe, 2006; Gee et al., 2007; Clark and Cartwright, 2009; Geogiopoulou and Cartwright, 2013). Moreover, our understanding of modern submarine channel systems is still in its infancy because we also have very few direct observations of turbiditic flow processes, and it is not clear how to upscale such data to geologic time periods in any case (e.g., Mitchell, 2006; Talling et al., 2012; Konsoer et al., 2013). Fundamentally, therefore, improved constraints on the response of submarine channels to tectonic perturbation over geological time periods is likely to require the use of high quality seismic datasets

and seabed digital elevation models that will allow us to resolve the time-integrated rate and distribution of deformation with respect to channel form at a high spatial resolution.

Some progress has been made in this issue; for example, Clark and Pickering (1996) used detailed bathymetric charts, 3.5 kHz and precision echo sounder profiles to carry out quantitative analysis for many submarine channel parameters and concluded that the planform geometry of submarine channels is generally similar to those of large rivers. However, they noted that there is less of a correlation in trends in submarine channels compared to fluvial systems. Moreover, many other studies have used 3D seismic datasets to study the planform geometry of modern submarine channels in different tectonic settings (e.g., Pirmez et al., 2000; Pirmez and Imran, 2003; Gee et al., 2007; Clark and Cartwright, 2009; Geogiopoulou and Cartwright, 2013 amongst others). However, uncertainties from all of these studies have led many authors to report that submarine channels show a great diversity of form and morphology (e.g., Clark and Pickering, 1996a; Mitchell, 2006). In addition, some of these studies have, necessarily, been qualitative in nature while some are limited by poor quality datasets. Consequently, our understanding of submarine channel form and how it reflects long-term erosional dynamics is limited compared to what we already know in fluvial settings (e.g., Hack et al., 1953; Howard, 1994; Whipple and Tucker, 2002; Tucker and Bras, 1998; Whittaker et al., 2008; Yanites et al., 2011, amongst many other studies).

This chapter addresses these important research challenges by constraining the spatial interactions between deepwater channels and growing structures using 3D seismic reflection data from the toe-thrust region of the deepwater Niger Delta. Here, I have analysed the longitudinal profiles and channel geometries of four modern seabed channel systems that have been active within the last million years. I also document how these channel systems respond to tectonic perturbation caused by growing structures at, or near the seabed; and estimate changes in the dimensional shear stress and flow velocities down-system.

4.2 PREVIOUS WORK

Recent studies on submarine channels have focused on their geomorphology, particularly with respect to their long profile shapes and their relationship to different tectonic settings (e.g., Pirmez et al., 2000; Goff, 2001; Gerber et al., 2009; Covault et al., 2011); and on how these channel profiles respond to tectonic perturbation (e.g., Pirmez et al., 2000; Huyghe et al., 2004; Ferry et al., 2005; Henio and Davies, 2007; Geogiopoulou and Cartwright, 2013 amongst many). These studies address

the relationship of submarine channel geometry, such as widths and depths, to active geological structures at, or near, the seabed in deepwater settings such as the Nile Delta (e.g., Cross et al., 2009; Clark and Cartwright, 2009, 2011; Georgiopoulou and Cartwright, 2013); the southern Barbados accretionary prism (e.g., Huyghe et al., 2004); the West African margin (e.g., Fennesu, 2003; Ferry et al., 2005; Gee and Gawthorpe, 2006; Gee et al., 2007; Hadler-Jacobsen et al., 2007) and the Niger Delta (e.g., Damuth, 1994; Pirmez et al., 2000; Deptuck et al., 2003, 2007; Morgan, 2004; Heinio and Davies, 2006; Clark and Cartwright, 2012).

The concept of "equilibrium" profiles in submarine channels, in a manner comparable to their fluvial counterparts, and their relationships to seafloor deformation has been emphasised in several studies. For example, Huyghe et al. (2004) and Ferry et al. (2005) showed that submarine channels respond to a local increase in slope (gradient) due to underlying faulting or folding by decreasing sinuosity and increasing incision, so as to achieve equilibrium slope at that location. In particular, studies from the western Niger Delta by Pirmez et al. (2000) shows that channel incision reaches a localized maximum where the channel profile shows the greatest increase in gradient – normally in regions corresponding to the transition between intra-slope basins or where the channels cross faults. Heinio and Davies (2006) used evidence of erosion of coarse-grained sediments deposited up-dip of knickpoints, to argue that the dominant mechanism by which these channels readjust to an increase in gradient is through upslope retreat of the knickpoint generated, thereby gradually smoothing the profile until it approaches the equilibrium profile.

On a longer time scale, Pirmez et al. (2000) argued that the mechanism by which an equilibrium profile of submarine channels is achieved is fundamentally governed by the interplay between sedimentary processes and tectonic deformation over several thousands of years, and that could lead to a quasi-linear long-channel profile where sedimentary processes are comparable to tectonic deformation. They also argued that where sedimentary processes dominate over tectonic deformation, the channel profiles will adopt a concave-up shape (e.g., submarine channels on the modern Amazon Fan). Moreover, the equilibrium profile will be disrupted if tectonic deformation exceeds the sedimentary processes. In contrast, Goff (2001) reported that submarine channel profiles are related to the overall background slope curvature of the continental margin (see also Gerber et al., 2009) while Covault et al. (2011) contend that the convexity or concavity of submarine channel longitudinal profile is also determined by the type of continental margin and the dominant tectonic setting. For example, channels from mature passive margins have slightly-concave profiles (e.g., the Amazon, Mississippi and Zaire); channels in passive margins subject to gravity tectonics or those in convergent margins have convex-up profiles (e.g., Nigeria, Barbados); and channels in young

margins have very-concave profiles (e.g., La Jolla, Ascension). More recently, Georgiopoulou and Cartwright (2013) tested the concept of equilibrium profile in submarine channels affected by ongoing normal faulting on the slope of the Nile Delta and reported that in areas where the total fault displacement is relatively small, the combined process of channel erosion and aggradation (even when sediment supply is episodic) results in a relatively linear profile and as expected, the change in channel geometry (width and depth) in those regions can easily be predicted.

It is clear from the above research that no single theory underpins the form or evolution of a steady-state or 'equilibrium' submarine channel profiles, which are likely to be eroded by turbidite flows with a temporal and spatial range of incision dynamics. Consequently, we do not actually have a predictive or quantitative model of 'equilibrium' submarine channel form over the long term, in the way that concave-up river long profiles, and stream power driven incision are understood in fluvial settings (e.g., Howard, 1994; Whipple and Tucker, 2002; Tucker and Bras, 1998; Whittaker et al., 2007a; Yanites et al., 2011). In fluvial catchments, the existence of well-documented and well-understood relationships between river catchment area, *A*, channel gradient, *S,* and down-system length, *L*, neatly accounts for the ubiquity of concave-up longitudinal profiles in typical river systems at topographic steady-state (e.g., Hack et al., 1953; Howard, 1994; Whipple and Tucker, 2002; Tucker and Bras, 1998). Moreover, recent work has significantly-improved insights into channel response to tectonic perturbation from both theoretical and field perspectives, particularly with respect to the timescale and mechanisms of knickpoint (steep gradient between lower gradient sections) retreat upstream of active faults (e.g., Tucker and Whipple, 2002; Whipple and Tucker, 2002, Whittaker et al., 2007a; Whittaker, 2012 amongst many others). In contrast, simple power-law relationships between upstream catchment area (as a proxy for discharge) and channel gradient may not apply to submarine channels for obvious reasons; while we know that many show a great diversity in form and morphology (e.g., Clark and Pickering, 1996a; Mitchell, 2006).

Nevertheless, some progress has been made on understanding the long-term (rather than event-based) erosional dynamics of submarine systems. For example, numerical modelling by Mitchell (2006) suggests that simple bed erosion models analogous to both detachment-limited and transport-limited models of fluvial system (Howard, 1994; Whipple and Tucker, 2002) can also apply to submarine canyons if the total load of eroding turbidite currents does not change much during passage down-canyon. The simple bed erosion models presented by Mitchell (2006) are (1) 'advective' – where erosion rate, *E*, is a power-law function of bed gradient and (2) 'diffusive' – where erosion rate is governed by variation in transport flux of the channel and therefore, directly related to the degree of long-profile curvature. When applying this model on the southern Barbados

accretionary prism, Mitchell (2006) showed that both 'advective' and 'diffusive' components are well represented if the erosion rules are applied continuously. Mitchell however noted some anomalies when applying thresholds which he attributed to factors that cannot be fully-constrained due to limited data on gravity flow systems such as differing sediment flux, differing threshold stress, changes in flow acceleration and depth-varying substrate resistance to erosion. While necessarily simplified, this kind of approach does provides one means of trying to estimate the long term incisisional capacity of submarine channels, because we presently have no means to upscale individual erosional events to geological time periods.

More recently, Konsoer et al. (2013) carried out an extensive review and compared morphometric parameters including slopes of approximately 170 submarine channels and 230 rivers. These authors, like Gerber et al. (2009), reported that submarine channels and rivers do follow comparable power-law and trends in width, depth and flow velocity as a function of bankfull discharge. These authors reported that the cross-sectional dimensions of submarine channels exceed those of the largest rivers on earth by an order of magnitude, and that the slope of submarine channels can be up to two orders of magnitude greater than the slope of rivers with similar dimensions. Konsoer et al. (2013) also used a combination of equations and published data on submarine channels and rivers to estimate the unit driving force, *F*, of a turbidity current as:

$$F = \rho_w RCgS \qquad \text{[Eq. 1]}$$

where ρ_w = density of seawater; *R* is the excess sediment density and size; *C* = percentage sediment concentration (typically in the range of 0.2 % to 0.6 %; *g* = force of gravity and *S* is the channel slope. They also estimated the mean bankfull flow velocity, *U*, for turbidity currents by modifying the Chezy equation (Komar, 1977) to include the effect of the interface between turbidity current and the ambient seawater above, and the force of buoyancy as shown in the equation below, i.e.

$$U^2 = \left(\frac{1}{1+r} \right) \frac{RCgHS}{C_{fb}} \qquad \text{[Eq. 2]}$$

where H is the bankfull channel depth measured from the levee crest to the channel floor (a proxy for the effective hydraulic radius of the flow) and $r = \frac{C_{fi}}{C_{fb}}$ where C_{fb} is the bed friction coefficient and C_{fi} is the coefficient of friction at the interface between the turbidity current and the ambient fluid above (seawater). If used to estimate the erosive power of a turbidite, such an approach is, in

essence, equivalent to the 'advective' slope dependent models of Mitchell (2006), where erosion is modelled simply as being proportional to bed slope or shear stress.

These equations for turbidity currents, and their associated hydraulic geometry, are in many ways analogous to the governing equations developed for rivers (e.g., Leopold and Maddock, 1953). Ideally therefore, their application to submarine channel system would be calibrated using turbidity flow data obtained through direct measurement and observations. However, these data sets are mostly lacking (e.g., Talling et al., 2012, 2013). Consequently, these studies imply that another way to improve our understanding of submarine channel behaviour, characteristics and incisional capacity is to quantify their long profiles, hydraulic geometry and potential erosivity where we have independent data on the long-term tectonic boundary conditions in a manner analogous to many recent fluvial studies (e.g., Whittaker et al., 2008; Yanites et al., 2011, amongst many). This chapter addresses this research opportunity by considering how submarine channels respond to displacement across actively deforming structures in the toe-thrust region of the deepwater Niger Delta using high quality 3D seismic data, where rates of shortening have already been constrained independently (chapter 3).

4.3 EXISTING CONSTRAINTS BASED ON ANALYSIS IN CHAPTER 3

Here, the focus is on four modern seabed channels (channels 1 to 4; Fig. 4.1a) whose interaction with growing structures associated with seabed relief (Folds A, B, C and D; Fig. 4.1a), have resulted in a range of channel behaviours. Importantly, the thrusts and folds in the study area have developed perpendicular to the regional slope, thereby acting as barrier to the down-slope flow of the modern seabed channels (Fig. 4.1a). The detailed analysis of how these folds and how they have affected the positioning of the channel pathways has been documented in chapter 3. The structural evolution of this area, including the shortening and cumulative strain across the folds and thrusts is also described in detail in chapter 3; where key seismic horizons were mapped across the four major structures and the cumulative strain on these individual seismic horizons was measured using the principle of line-length balancing (Dahlstrom, 1969). The cumulative strain *e,* was measured on a series of sections across the structures (e.g., section lines a1, a2, b1, b2, b3, c1, c2, d1 and d2 located in Figure 4.1a), and defined as the total shortening (original length minus present-day length) undergone by a horizon from the time it was deposited to date, and divided by the original length of the horizon. Documented results in chapter 3 show how the cumulative strain and interval strain

rates vary through time for the different stratigraphic horizons. For example, the variation in cumulative strain measured through time is shown in Figure 4.1b. Using Fold A as an example, the recorded total cumulative shortening of the pre-growth horizons in Fold A, measured from section a1 (Fig. 4.1a), is 1470 m (square box, Fig. 4.1b). This shortening is equivalent to a strain value of -0.156 at the present-day (Fig. 4.1b). This represents the shortening recorded over a period of growth of approximately 12.8 – 9.5 million years. The shortening accumulated by the syn-growth horizons (since ~12.8 Ma) is lower compared to the pre-growth horizons and decreases through younger syn-growth horizons to a minimum at the present-day seabed horizon. In essence, this same pattern of growth is observed in all structures in the study area (Fig. 4.1b), and the period of reduced structural growth (from 3.7 Ma to present-day) is important because it broadly brackets the period of channel development (see chapter 3). Figure 4.1c shows the maximum and minimum estimates of strain rates/shortening since 3.7 Ma at position of channel incision and close to incision across structures (Fig. 4.1a). This is different for Fold C because modern channels are unable to incise across this structure (Fig. 4.1a). These interval strain rates represent the possible range for each structure in regions where channels cross the structure. The lowest rates measured at channel positions, are likely to be underestimated or overestimated because of the degradation of stratigraphic horizons by channels (see chapter 3). Overall, the strain and associated tectonic deformation accumulated from the late Pliocene onwards by the growing structures, determines the tectonic boundary conditions to which the submarine channels have to respond. I therefore use this structural background to quantify how the geometry, profile and bed-shear stress of channels in the study area varies as the channel systems interact with growing structures.

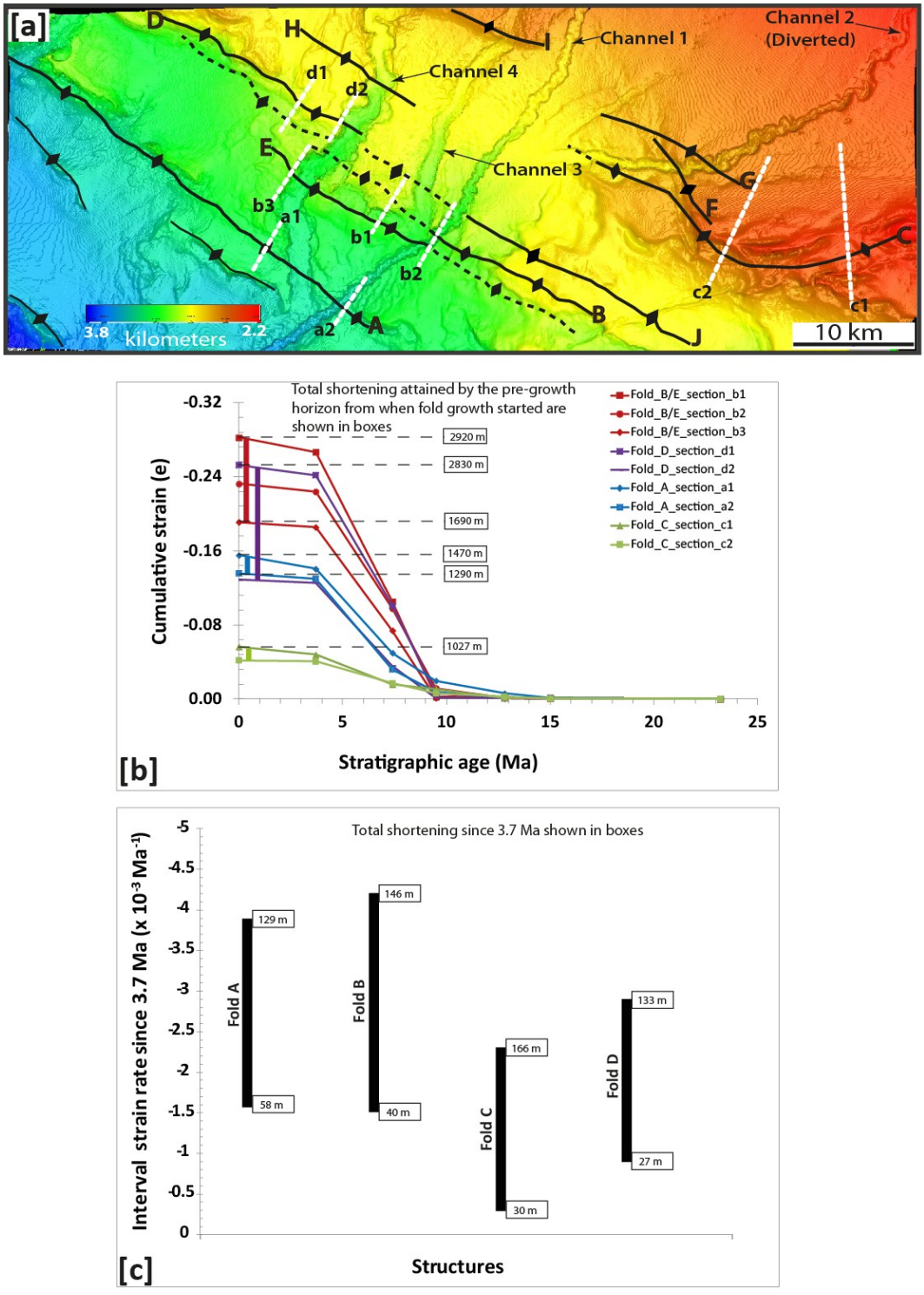


Figure 4.1: (a) 3D depth-structure map of the seabed over the study area (from chapter 3) showing the modern, seabed channel systems (channels 1, 2, 3 and 4) and growing structures at, or near the seabed (Folds A – J). Section lines a1 – d2 (white dotted lines) indicate the positions of section used to measured cumulative strain of horizons through time, and shown in Figure 4.1b, c. (b) A graph of cumulative strain through time for the four folds (Fold A – D) measured using section lines a1, a2, b1, b2, b3, c1, c2, d1 and d2 (location in Figure 4.1a). Note that the values in square boxes represent the total shortening attained by the pre-growth horizon from when structural deformation stated (~12.8 – 9.5 Ma) to date. (c) Shows the interval strain rates over the last 3.7 Ma derived from Figure 4.1b, and the values in square boxes – represent the total shortening of the 3.7 Ma horizon from when it was deposited to date. Note that the interval strain rates represent a range in each structure: from the lowest values (measured at channel incision positions) to the highest values (measured adjacent to the channel incision positions), and for Fold C, the sections were taken close to the fold tip (section c2) and at the position of maximum growth on the structure (section c1).

4.4 METHODS

4.4.1 Seismic interpretation and DEM derivation

From the 3D seismic volume (see chapter 2), the seabed horizon was mapped using Landmark's 3D seismic interpretation software, and was depth-converted using seismic velocities of 1490 ms^{-1} and exported it to Arc-GIS where it was geo-referenced and used to build a 50 m resolution Digital Elevation Model (DEM). The resolution of the DEM was determined by the bin-size of the seismic data which is 50 m by 50 m. The DEM was processed to produce a flow network of submarine channels, defined stream orders and turn them into vector coverage. Submarine channel long-profile data were obtained using the stream order vector coverage to run 'cost-paths' that follow the lines of successive lowest values in the DEM elevation and flow accumulation rasters, starting from a user-defined source point located upstream (Fig. 4.2a; see section 4.4.2 for more details). Using the 3D seismic volume, I also mapped the 3.7 Ma horizon and an intermediate continuous horizon that occurs closest to the incisional base of the Pleistocene – Recent channel systems. The age of this intermediate horizon was estimated to be ca. 1.7 Ma based on the average sediment accumulation rate determined in a piggyback basin in the northeast of the study area (see Fig. 3.6 in chapter 3). Using vertical seismic profiles along the channels pathways, the vertical sediment thicknesses between the seabed and the 1.7 Ma horizon that is closest to the incisional base of the channels were measured. These sediment thicknesses were used as proxy for measuring the distribution of structural uplift along the pathways of individual channel systems (see section 4.4.3 for details). The existing seismic data was also used to constrain major structures having seabed relief and thereby affecting the modern channels profiles by generating knickpoints (Fig. 4.1a).

4.4.2 Channel morphometric parameters and long-profiles

From the DEM and the mapped channel networks, the following channel parameters were extracted and measured:

a) Channel longitudinal profiles – the bathymetric depth from sea level to the floor of the modern seabed channels, Z_m, against down-system channel distance, L. To remove noise and smooth steps in the data, the long-profiles were fitted with a high-order polynomial.

b) Modern channel width, W_m – the width measured horizontally between levee crests of active seabed channels, at approximately every 1 km downstream (Fig. 4.2a, b).

c) Modern channel incision, H_m – the incisional depth of active seabed channels, measured vertically from levee crest to the channel floor (Fig. 4.2b). These measurements were carried out on sections perpendicular to the seabed channel systems at the same places as the channel width measurements.

d) Channel slope, S, which was smoothed and obtained explicitly as a function of downstream distance by differentiating a high order polynomial fit to the channel long-profiles.

e) The cross-sectional areas of the modern channels, A_m, were calculated by integrating the incised channel depth, (ΔH_m) as a function of channel width, W_m. For submarine channels, the estimated cross-sectional area measured as the area within the channel and below a horizontal line between levee crests (labelled modern channel width; Fig. 4.2b), is likely to be a minimum estimate of the flow cross-sectional area as direct observation of turbidity flows on the slope offshore of the Congo (e.g., Meiburg and Kneller, 2010) suggests that flows in channels of order 100 m depth often have vertical flow depths 50 % greater than this. The presence of levees at the tops of the incised channels, which can be seen to grade to the modern seabed, supports this assumption (see also chapter 5, Figure 5.2a).

The cross-sectional area was then use to estimate the hydraulic radius, h^r in each of the transect using the approximation,

$$h^r = \frac{A_m}{W_m + 2H_m} \qquad \text{[Eq. 3]}$$

which is appropriate for wide channels. These data were used to evaluate both how channel geometry evolved as the turbidite systems interacted with the geological structure, and also to help constrain the channels incision across growing fold and thrusts. Clearly, the erosivity of every flow that has come down these channels is impossible to constrain. However, the likely distribution of bed-shear stress in these channels (based on the present-day channels geometries) was estimated using these morphological measurements and appropriate assumptions, in an analogous way to the distribution of channel stream power downstream in fluvial settings (*cf.* Whittaker et al., 2007). To do this using equation 2, I make the assumption that for turbidity currents, the interfacial friction

between the current and the ambient fluid is not negligible, and was assumed to be 1. Therefore, a minimum fluid velocity, derived from the modified Chezy equation [Eq. 2] can be written as:

$$u^2 \sim \left(\frac{1}{2}\right)\frac{RCgHS}{C_{fb}} \qquad \text{[Eq. 4]}$$

Thus, multiplying the unit driving force, [Eq. 1] by the hydraulic radius, h^r [Eq. 3] – which was calculated using the seismically-constrained channel geomorphic parameters, also assumed to be the minimum for these channel systems; a measure of the bed shear stress, τ_b for each submarine channel was obtained, i.e.:

$$\tau_b = \rho_w RCgh^r S \qquad \text{[Eq. 5]}$$

Combining equations 4 and 5, and recognising that channel depth is typically taken as a proxy for flow depth (Whittaker et al., 2007; Konesoer et al, 2013); the fluid velocity can be written as:

$$u = \sqrt{\frac{\tau_b}{2\rho_w C_{fb}}} \qquad \text{[Eq. 6]}$$

Additional assumptions were made which include; an initial sediment concentration value, *C*, of 0.6 % as reported by Pirmez and Imran (2003) and Konsoer et al. (2013), and coefficient of bed friction, C_{fb} = 0.005, as reported by Konsoer et al. (2013). For the Niger Delta, where the sediments are predominantly siliciclastic, *R,* the excess sediment density [$(\rho_s - \rho_w)/\rho_w$], will be a constant 1.65 (for quartz grains with a density of 2650 kgm^{-3}) if we assume seawater density ρ_w, of 1000 kgm $^{-3}$; or 1.57 for seawater density of 1030 kgm^{-3}.

Equations [Eq. 5] and [Eq. 6] were used to estimate the down-system variation in bed-shear stress and flow velocities respectively for the four modern channels in this study. Flow density obviously varies down-system, so only two end-member solutions were calculated. In the first end-member, the initial sediment concentration was assumed to remain constant down-system, regardless of changing cross-sectional area of the flow – in effect this simplifying assumption implicitly allows the flow to 'bulk' where channel cross-sectional areas are large. In the second end-member, we make the assumption that the concentration of the flow is related to the cross-sectional area of the channel. We therefore allow the sediment concentration to increase proportionally when the cross-sectional area decreases and vice versa, conserving mass. The bulk concentration of real turbidite flows likely lies somewhere between these two end-members. Because the bed-shear stress and

flow velocities were calculated at approximately 1 km intervals (i.e., at the location of transects), and because the results are partially dependent on the average gradient in those locations, the mean gradient 250 m up-stream and down-stream of each location was also determined; and used in the calculation of shear stress, velocity and in the plot of width-to-depth ratios versus gradient. We predict sub-critical flows for > 90 % of locations, which is consistent with this being a deep-water system. The standard deviation in gradient at each transect location was also determined and used to estimate the errors in the results.

It is emphasised that these results aim to approximate what the down-system distribution of bed-shear stresses and flow velocities would be for a typical turbidite flow assuming a starting sediment concentration of 0.6 %, given the measured channel geometries and documented geologic structures. Our approach is therefore directly analogous to the way in which downstream distribution of specific stream powers or bed shear stresses are routinely calculated for fluvial systems incising across active faults or growing structures (e.g., Whittaker et al., 2007a). In particular we do not seek to reproduce the specific hydrodynamics of each flow. We adopt this methodology because a detailed knowledge of the shear stress and time-integrated erosivity of these channels, which will necessarily have varied over their Pliestocene to recent history, would require knowledge of the evolution of sediment concentrations and flow properties, weighted for flow frequency and size over periods longer than 1 Myr. Constraints on such parameters are, self-evidently, impossible to obtain. (*cf.* Xu, 2011; Talling et al., 2012).

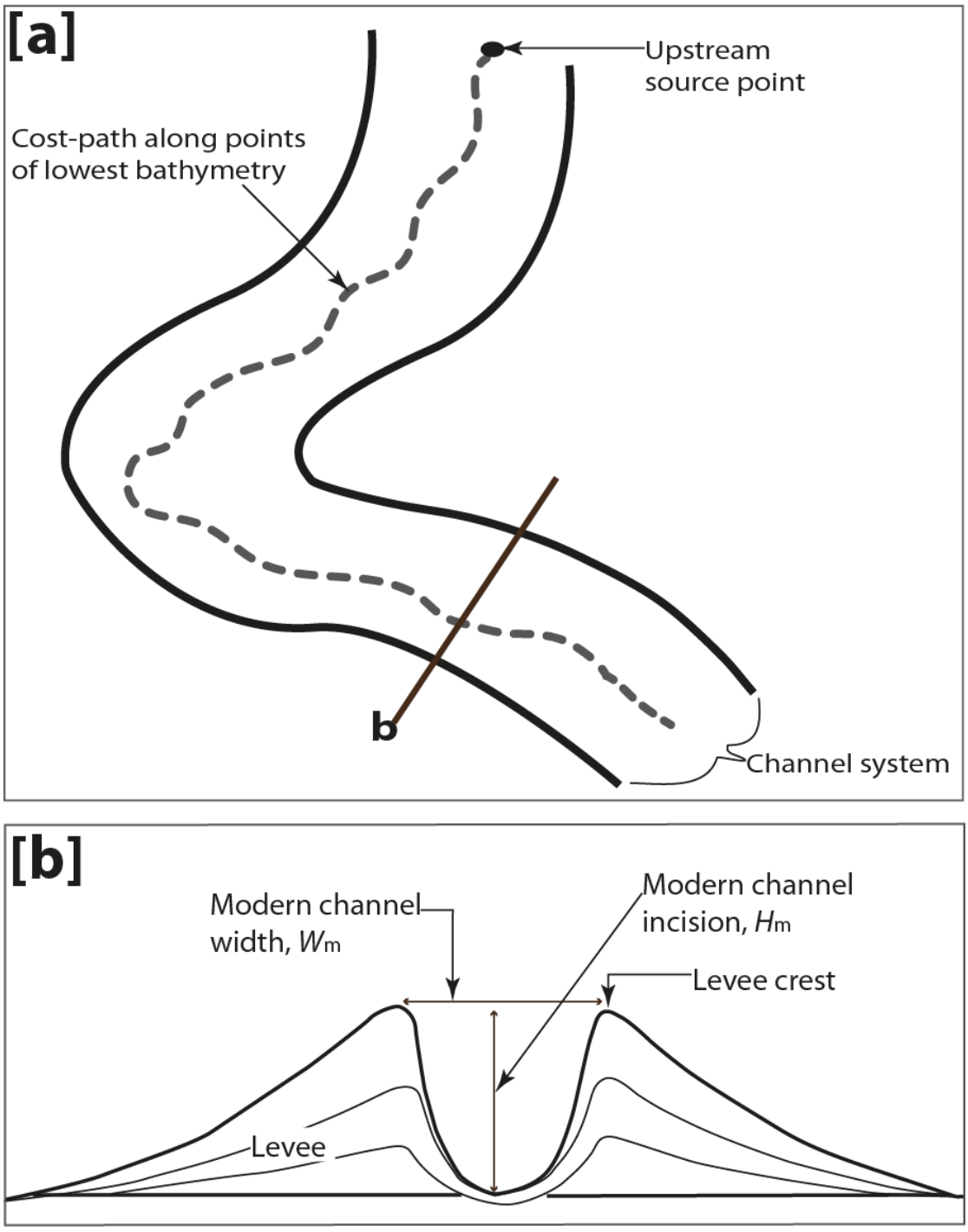


Figure 4.2: (a) Shows the plan-view sketch of a channel system and the method for extracting bathymetry long profile; (b) is a sketched section across the channel system in (a) showing the method for measuring channel morphometric parameters.

4.4.3 Distribution of structural uplift down-channel system

To measure the relative distribution of structural uplift of horizons along the path of channels, the distribution of sediment thickness along the channel pathway was used as a proxy. For example, to measure the distribution of the relative structural elevation on horizon c (Fig. 4.3a), I simply measure the vertical sediment thickness from the seabed to the top of horizon c at regular intervals along the channel pathway. Where the maximum elevation of horizon c, coincides with the elevation of the seabed horizon (e.g., continuous-line, Fig. 4.3a); then the vertical sediment thickness measured from the seabed to the top of that horizon at any location *x*, along the channel pathway is represented by *t* (Fig. 4.3a). Otherwise, in the situation where additional sediments (dash-line, Fig. 4.3a) have buried the horizon in question at the point of maximum elevation, then the sediment thickness is measured as shown in equation 7.

$$t = t_x - t_{\min} \qquad \text{[Eq. 7]}$$

Here, t_x is the sediment thickness measured at any location *x* from the seabed to the top of the horizon whose structural elevation is being quantified; and t_{min} is the sediment thickness measured above the same horizon at the point of maximum crestal structural elevation (Fig. 4.3a).

To convert the measured sediment thickness into normalised relative uplift, the maximum sediment thickness t_{max}, was first determined from the measured thicknesses *t*, along the channel pathway and then the relative structural uplift *E,* was computed as:

$$E = \frac{(t_{\max} - t)}{t_{\max}} \qquad \text{[Eq. 8]}$$

Based on equation 8, the normalised relative uplift of horizon c will be 1 where the sediment thickness is at minimum and approaches zero when the sediment thickness is large. Note that the normalised relative uplift is often measured by simply determining the sediment expansion factor, which can be calculated by dividing t_{min} by t_x at each location (see Higgins et al., 2009). However, this will only work when the sediment column thickness, t_{min}, is large whereas t_{min} is approximately zero for the four channels, meaning this method is inappropriate for the study purposes (e.g., Fig. 4.3b).

Figure 4.3b demonstrates how this method works along the path of channel 1 (*cf.* Fig. 4.1a). Here, the maximum relative uplift of the 3.7 Ma horizon (dark brown) and the red horizon (ca. 1.7 Ma) mapped close to the base of the channel incision surface (dash-red line) coincides with the position

of underlying Folds B/E. The distribution of the relative structural elevation of these two horizons is shown in Figure 4.3c, where the distribution of uplift reveals underlying thrusts and folds including those that are buried. The maximum relative uplift for the two horizons is 1 (Fig. 4.3c), which also coincides with the position of underlying Folds B/E (Fig. 4.3b). However, results of relative structural uplift presented in this chapter (see section 4.5.3) are based on sediment thickness measurements carried out on the red horizon (ca. 1.7 Ma) because it is close to the channel base and therefore serves as a more realistic surface with which to judge channel response to structural growth.

Figure 4.3d shows the position of channel 1 across Folds B/E in relation to the along strike variation in cumulative strain for the 3.7 Ma horizon (taken from chapter 3) and the 1.7 Ma horizon derived in this study using identical methodologies. The position at which channel 1 has incised through these folds is indicated by an arrow, where the strain for both the 3.7 Ma and the 1.7 Ma horizons is low. As already described in section 4.3, both the minimum strain (at channel position) and the maximum strain (adjacent to channel position) were calculated (*cf.* Fig. 4.1a). For example, the maximum strain recorded by the 3.7 Ma horizon adjacent to channel 1 location in Figure 4.3d is -0.019, which is equivalent to 146 m of cumulative shortening. The interval shortening rate is approximately 39 m/Myr over 3.7 million years, which is equivalent to interval strain rate of approximately - 0.004 per million years (*cf.* Fig. 4.1c). Moreover, the period of channel development (ca. 1.2 Ma) can be approximately related to the strain regime recorded between the 3.7 Ma and the 1.7 Ma seismic horizons (Fig. 4.3d). Note how the strain reduces through time so that the strain values recorded by the 1.7 Ma horizon is approximately half that of the 3.7 Ma horizon, and approaches zero on the modern seabed (see chapter 3 for details). Within the limit of the seismic resolution, the strain recorded on the 1.7 Ma horizon, which occurred just prior to channel development, is assumed to be robust enough for analysing channel response to tectonic perturbation in this study.

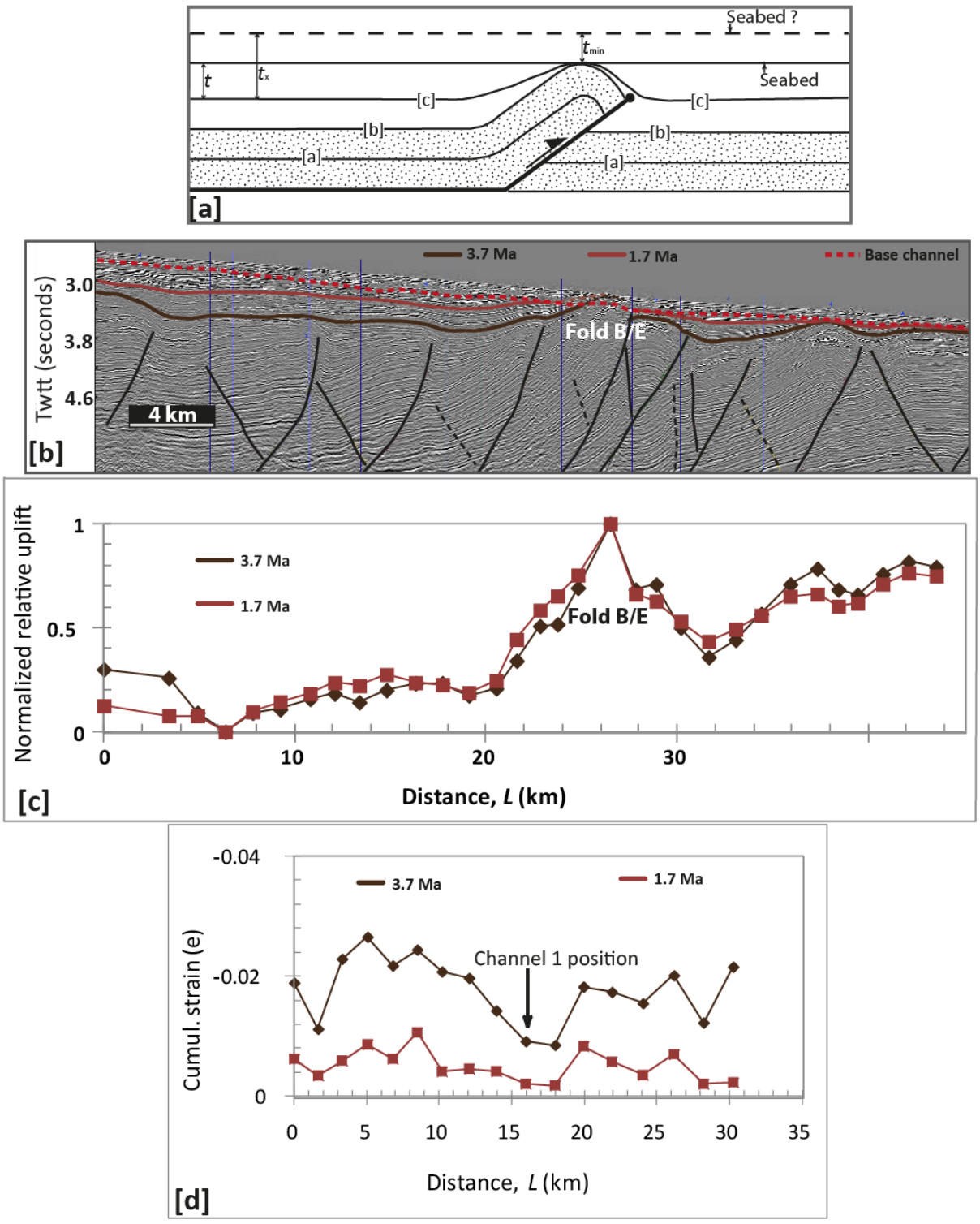


Figure 4.3: (a) A diagram describing how to measure, and use sediment thickness as a proxy for the relative structural elevation of horizons from long channel profiles. (b) Seismic section taken along channel 1 (Fig. 4.4) showing relative structural elevation of the 3.7 Ma and the 1.7 Ma horizons. The maximum relative elevation of these horizons is on the crest of Fold B/E. The red dash line represents the base of channel 1 incision. (c) Shows the result of the relative uplift of the 3.7 Ma and the 1.7 Ma horizons measured using the seismic section shown in Figure 4.3b. The normalized relative uplift of the 1.7 Ma horizon is used to analyse channel incisional response in this study. (d) Shows the result of cumulative strain along the strike of Fold B/E (Fig. 4.4), measured on the 3.7 Ma horizon (from chapter 3) and on the 1.7 Ma horizon in this study. Note the low displacement point on the cumulative strain curves where channel 1 incised across the structure.

4.5 RESULTS

4.5.1 Modern seabed channels

Figure 4.4 shows the 3D depth-structure map of the seabed in the study area, together with selected transects across the four modern channels. The map shows the spatial distribution of the four channels with three of them all located in the west of the map (channels 1, 3 and 4) and only one of the channels (channel 2) located in the east, where it has been deflected to the west behind Fold C. Structures with seabed relief that have affected channel geometry or orientation are labelled on the map. Structures A, B/E, C and D have been analysed in detail in chapter 3. Channel 4, in the west, is apparently the most established of the four channels with an overall width that is three times the average width of the other channels. Transects perpendicular to the channels show the channels generally have high aspect (width-to-depth) ratios (Fig. 4.4). Nevertheless, they clearly reveal the impact of the underlying thrusts/folds as shown in the graphs of water depth versus transect distance below the map. For example, the plot of transects along channel 1 shows an area of increased channel incision between transect 6 and 8 which also coincides with the position of Folds J, B and E. Channel 2 also shows an increase in incision when crossing Folds G and F as revealed by transects 5 to 7, and transect 3 to 6 for channel 4 clearly reveal a large area of increased channel incision because of the channel interaction with a number of structures (Folds D, E and H).

These graphs give a good overview of the impact of active structures with seabed relief on the channel geometry. The range of widths and depths are described using normalised frequency density plots in Figure 4.5. For example, channels 1 and 2 have a similar width-frequency distribution, which ranges from 900 m to 1900 m, with means of approximately 1100 m and 1200 m respectively (Fig. 4.5a, c). However, the depth-frequency distribution varies in these two channels. Channel 1 has a distribution that can be described as broadly mono-modal with a mean of 65 m (though there is a wide spread from 30 m to 140 m; Fig. 4.5b). Channel 2 shows a strong bi-modal distribution in depths with approximate means of 25 m and 70 m respectively (with an overall mean of 42 m; Fig. 4.5d). Channel 3 also shows a mono-modal distribution in channel width (range from 1500 – 2500 m) with a mean of 1800 m (Fig. 4.5e). But the smallest width (1500 m) is almost equivalent to the largest widths in channels 1 and 2. However, channel 3 has reduced channel depth-distribution because it crosses only one major structure (Fold I, Fig. 4.4), although, the depths are skewed towards higher values (Fig. 4.5f). In contrast to the three channels already described, channel 4 shows a much larger width range (from 1700 m to 3100 m) with a mean width of approximately 2480 m (Fig. 4.5g). However, the frequency distribution is bi-modal, unlike the other

channels. Moreover, there is a wide range of incisional depth distribution (from as low as 10 m to as high as 140 m) with an overall mean of approximately 95 m (Fig. 4.5h). The wide spread in the depth values for channel 4 further underlines the impact of seabed structures on channel incision because this channel crosses a number of structures along its path (*cf.* Fig. 4.4). The standard deviation in channels width ranges from 178 in channel 1 to 498 in channel 4; and the standard deviation in channels depth ranges from 9 in channel 3 to 40 in channel 4 (Fig. 4.5).

These range of widths and depths in the Niger Delta are similar to values reported by Clark and Pickering (1996) based on the studies of modern submarine channels in different settings including the Mississippi fan channels, the Indus fan channels and the Rhone fan channels amongst many others. For example, the Mississippi fan has channels with widths that range from 1 – 5 km (average of 2 km) and depths that range from 5 – 50 m. The Indus fan has channels with widths that range from 0.6 – 1.5 km and depths that range from 10 – 190 m. Similar values on the Rhone fan are widths of 0.5 – 1.2 km and depths that range from 10 – 200 m. Note that Clark and Pickering (1996) studied these channels over distances of up to 500 km from the canyon heads to the fan regions (compared to channel lengths of 30 – 60 km in our study). While comparable to these findings in broad terms, our results demonstrate that channel geometry can actually be extremely variable over short distances of < 10 km, due to the interaction of tectonics and submarine channel erosion.

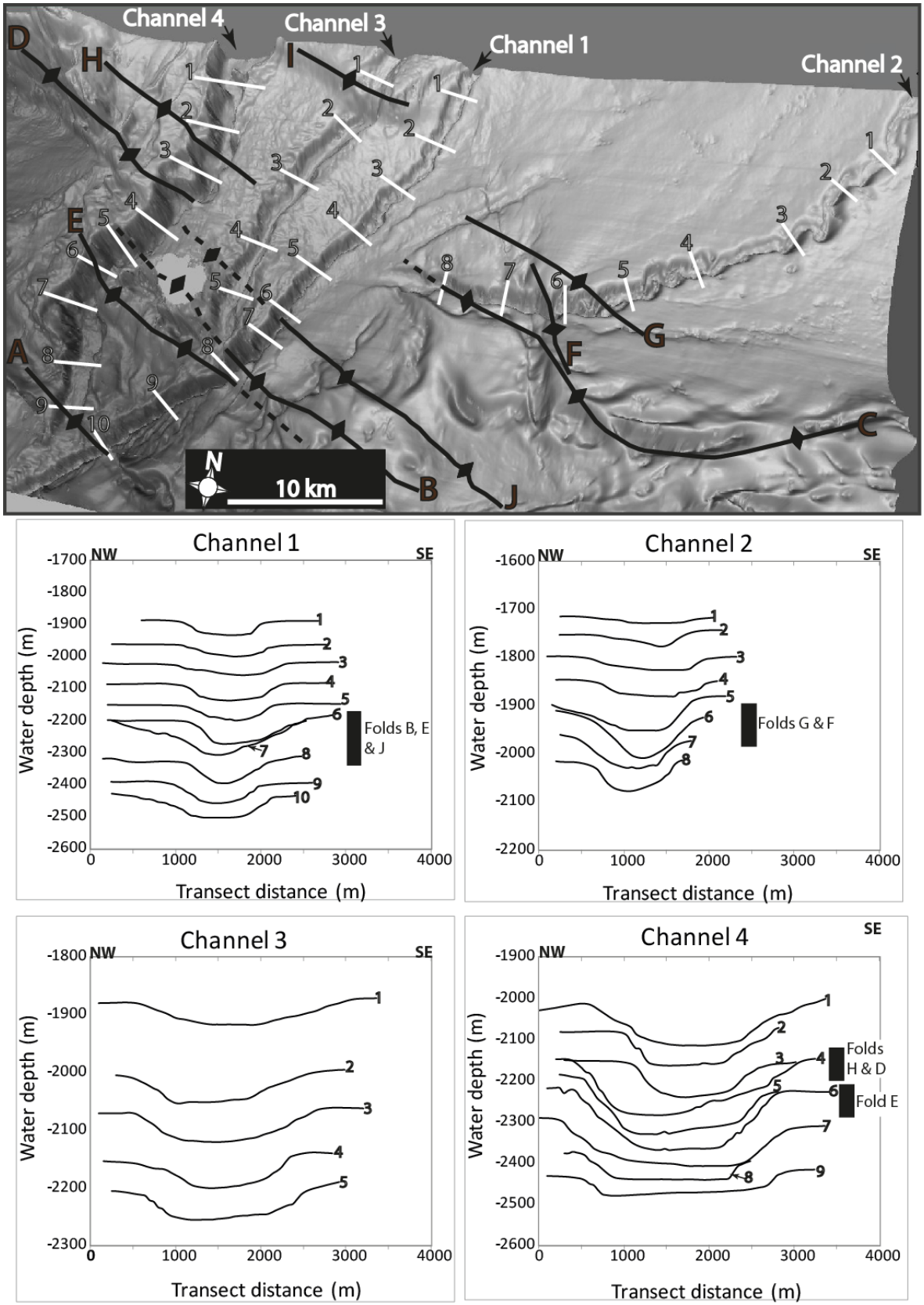


Figure 4.4: Top panel, is a 3D depth-structure map of the seabed in the study area showing the four modern channels (1, 2, 3 and 4), and structures that occur at, or near the seabed (labelled A – J). The white lines are transects across the four channels from left to right looking north, and shown in the graphs below the map. These graphs show plots of water depth against transect distance for the four channels shown on the map. The channel transects generally have high aspect ratio but clearly reveal the effect of the underlying thrusts/folds on channel incision.

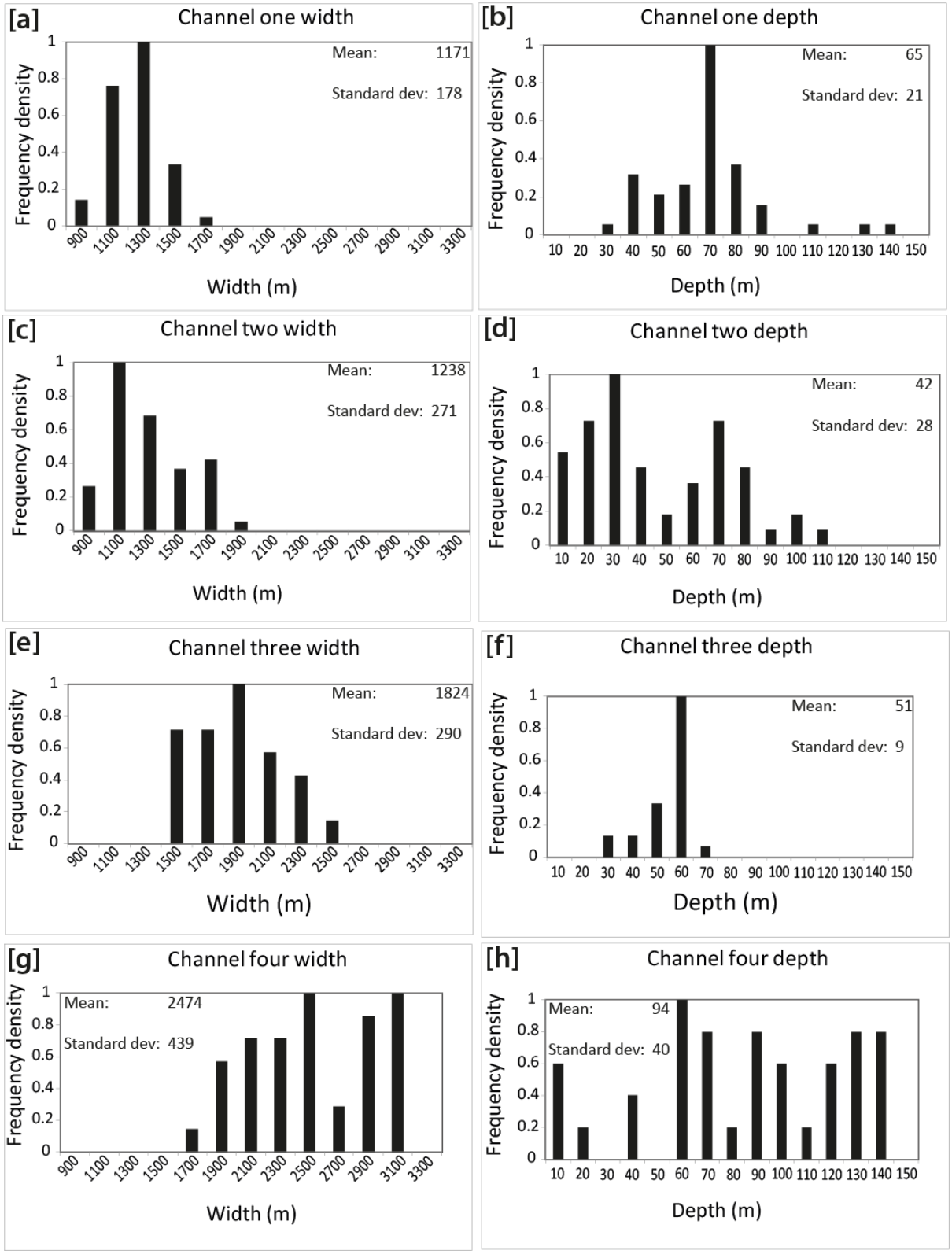


Figure 4.5: Shows the frequency distribution of channel depths and widths in the study area: (a) channel 1 width, and (b) channel 1 depth; (c) channel 2 width, and (d) channel 2 depth; (e) channel 3 width, and (f) channel 3 depth; (g) channel 4 width, and (h) channel 4 depth. Channels 1, 2 and 3 have mono-modal width-distributions with the exception of channel 4 that is bi-modal. All the channels show wide spread depth-distribution with the exception of channel 3 whose depth is skewed towards higher values.

4.5.2 Modern seabed channels profiles

The long-profiles of seabed channels are relatively linear with some local scale steepening that is apparent near mapped structures (Fig. 4.6a). Because the profiles vary in length, and to facilitate comparison between profiles with differing bathymetric distributions, channels are normalised by their depth range and maximum downstream distance (Fig. 4.6b; see also Covault et al., 2011). From the normalised profiles, it is obvious that the profiles are linear to sub-linear with a concavity that ranges from -0.08 in channels 1 and 2, to -0.2 and -0.34 in channels 3 and 4 respectively. The shapes of these profiles are similar to those described by other workers in deepwater settings of the Niger Delta (e.g., Pirmez et al., 2000; Covault et al., 2011). However, this study finds that some of the channels have profiles that are essentially more linear (e.g., channels 1 and 2) than others (e.g., channels 3 and 4) which are slightly concave-up (Fig. 4.6b). The average gradient of the channel profiles is 0.9^{o} to 1^{o} (y/x slope of 0.015 to 0.017). However, the profiles are also characterised by small-scale variations in down-system gradient (knickpoints) which often coincide with the position of underlying folds and thrusts (labelled Fold A to J, Fig. 4.6a) and implicitly therefore, variations in substrate uplift rate. These data suggest that knickpoints of varying scales develop along the channel profiles, which may relate to on-going deformation due to the gravitational collapse of the delta (*cf.* Morley and Guerin, 1996; Cohen and McClay, 1996; Wu and Bally, 2000; Rowan et al., 2004; Billoti and Shaw, 2005). Nevertheless, the general linear nature of the profiles suggests that any substantial profile convexities generated by active tectonics tend to be smoothed-out by the turbidity current erosion over time (e.g., Pirmez et al., 2000; Georgiopoulou and Cartwright, 2013).

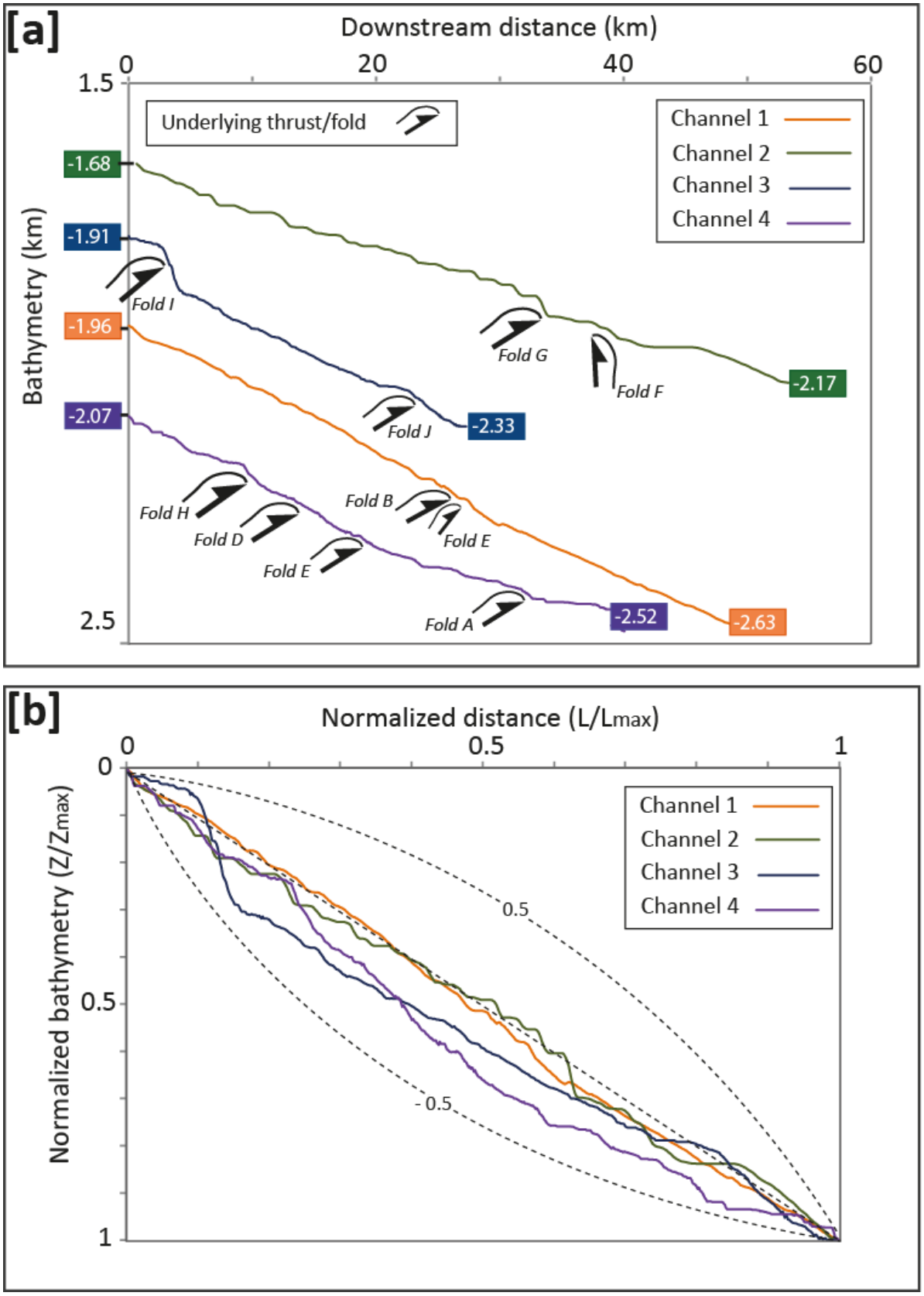


Figure 4.6: (a) Shows modern seabed long-profiles of channels 1, 2, 3 and 4, and characteristic small scale variations in down-system gradient which coincide with the position of underlying faults and thrusts (labelled A – J, see Fig. 4.4). (b) Shows the overall linear to sub-linear nature of the four channel profiles when normalised. Note that channel 1 and channel 2 are much linear (with concavity of ca. -0.08) compared to channels 3 and 4 with concavity that is up to -0.34.

4.5.3 Relationship between profile shape, structural uplift and channel geometry

This section compares the relative uplift of structures along the channels pathways from ca. 1.7 Ma to date by examining geomorphic parameters measured down-system. In channel 1 the overall background slope (y/x) is approximately 0.01 (Fig. 4.7a). However, the slope value can increase significantly in areas where knickpoints have developed along the channel profile because of underlying thrusts (see Fig. 4.6a). For example, at 28 – 30 km down-system distance, the slope of channel 1 (middle panel, Fig. 4.7a) increases by a factor of 2 from 0.01 to 0.02 because of the time-integrated uplift of Folds B and E which is clearly reflected in the normalised relative uplift of the 1.7 Ma surface (upper panel, Fig. 4.7a). This area of higher, time-integrated uplift is accompanied by a more than 70 % increase in channel incision to 140 m, from a background incision of about 80 m (lower panel, Fig. 4.7a). However channel width remains virtually constant at approximately 1100 m throughout the channel reach (*cf.* Fig. 4.5a). In a similar manner, channel 2 has an overall background slope of approximately 0.01 but increases to > 0.02 between 32 km and 38 km downstream (Fig. 4.7b) as the channel incise across the flank of Fold C (see Fig. 4.4). This increase in gradient correlates spatially with the time-integrated uplift of Folds G and F that intersect the northern flank of Fold C, and is also reflected in the normalised relative uplift of the 1.7 Ma surface over that region (upper panel, Fig. 4.7b). Channel 2 also responds to the gradient change in that region by increasing incision depth from 45 m to 100 m (lower panel, Fig. 4.7b) while the channel width maintains an average of approximately 1200 m down-system (see also Fig. 4.5c).

For the slightly concave channels (channels 3 and 4) with a concavity of - 0.2 and - 0.34 respectively, there is a difference in the channel geometry response when compared with channels 1 and 2. For example, channel 3 has a background gradient (approximately 0.01) which is similar to those in channels 1 and 2 (Fig. 4.7 – a, b, c). There is a gradient increase from 0.01 to > 0.07 (up to a factor of 7) created by a knickpoint in the vicinity of Fold I along channel 3 (middle panel, Fig. 4.7c). However, the normalised relative uplift in that area (upper panel, Fig. 4.7c) is only a quarter of the maximum documented in the area affected by Fold J, which is here characterised by a more muted increase in slope. Moreover, the incision depth in channel 3 remains fairly constant at approximately 50 m down-system and the channel width also remains constant at an average of 1800 m (see also Fig. 4.5 – e, f). Consequently, it appears that the high channel gradients in the vicinity of Fold I (from 0.01 to > 0.07), where time-integrated uplift is relatively low, are not coupled to enhanced channel incision. This is not consistent with the channel response we see in channels 1 and 2. Hence, there is

a need to analyse the erosivity of these channels in order to understand whether this is a transient effect.

Channel 4 behaves like channels 1 and 2 in terms of channel incisional response to actively growing structures with an overall increase in incision from ~ 80 m to 160 m (lower panel, Fig. 4.7d) while maintaining a relatively constant channel width (~2400 m; see also Fig. 4.5g) in areas characterised by structural growth of Folds D, E and H. However, this channel shows a higher overall variation in gradient down-system with highest gradient (up to 0.025) observed between 8 km and 14 km down-system in an area affected by Folds H and D (middle panel, Fig. 4.7d). In this area, the normalised uplift on the 1.7 Ma surface (upper panel, Fig. 4.7d) is only a quarter of that at Fold E (between 16 km and 22 km) where the gradient is also lower than 0.02. However, unlike the channel 3 example, channel 4 has responded by increasing incision in that area (lower panel, Fig. 4.7d). The gradient at 30 km down-system within channel 4 is the same as the average in other channels (0.01) but the time-integrated uplift of the structure in that area (caused by Fold A, Fig. 4.7d) is approximately two-thirds that of Fold E. In summary, channel 4 differs from the rest of the channels not only because it has a largely concave-up profile (*cf.* Fig. 4.6b), but also because the broad area of increased channel incision (from 10 km to 22 km down-system) is not co-located with the region of maximum relative structural uplift since 1.7 Ma (i.e., from 12 km to 22 km, upper panel, Fig. 4.7d). Consequently, channel 4 shows a much longer wavelength of incision compared to the wavelength of the time-integrated structural uplift since 1.7 Ma.

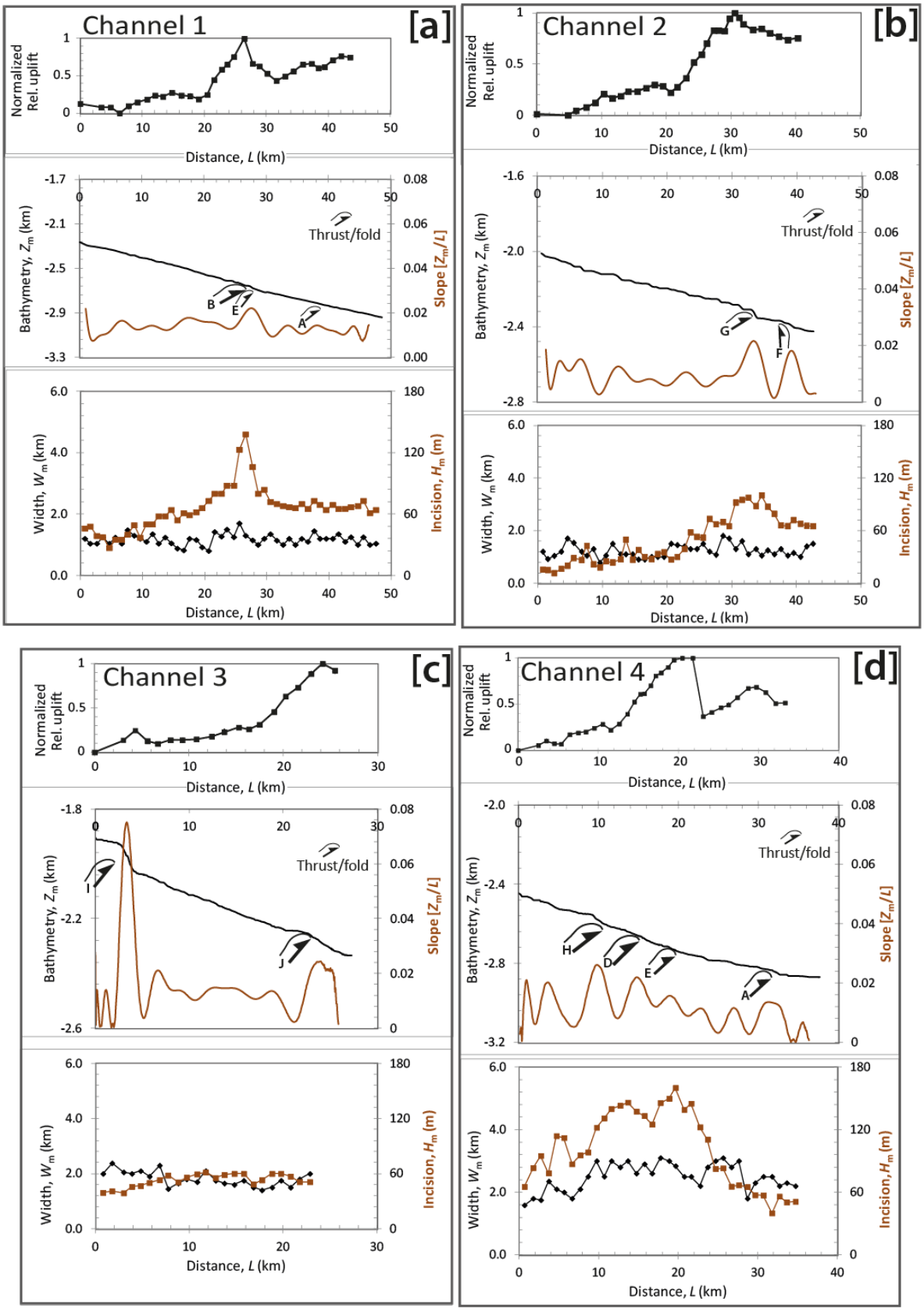


Figure 4.7 (see caption in next page)

Figure 4.7 (overpage): (a) Shows the time-integrated uplift of the 1.7 Ma horizon (upper panel) by structures along the path of channel 1; the middle panel shows the long profile of channel 1, and the channel slope (red); the lower panel shows channel 1 incision (red) and width (black). Note that the gradient (slope) along channel 1 increases where the channel crosses Folds B/E – also indicated by the high relative uplift of the 1.7 Ma surface (upper panel), and the channel incision also increases without a significant change in width. (b) Shows the time-integrated uplift of the 1.7 Ma horizon (upper - panel) by structures G and F along the path of channel 2 which have incised on the flank of Fold C in that area (see Fig. 4.4); the middle panel shows the long profile of channel 2, and the channel slope (red); the lower panel shows channel 2 incision (red) and width (black). Note that the gradient along this channel increases where the channel crosses Folds G and F – also indicated by the high relative uplift of the 1.7 Ma surface (upper panel), and the channel incision also increases without a significant change in width. (c) Shows the time-integrated uplift of the 1.7 Ma horizon (upper panel) by structures along the path of channel 3; the middle panel shows the long profile of channel 3, and the channel slope (red); the lower panel shows channel 3 incision (red) and width (black). The high gradient increase caused by the uplift of Fold I, represents only a quarter of the time-integrated uplift of the 1.7 Ma surface in that location (upper panel) compared to the maximum documented at Fold J location, whose gradient increase is low. Note that both the channel incision and width do not show significant changes downstream. (d) Shows the time-integrated uplift of the 1.7 Ma horizon (upper panel) by structures along the path of channel 4; the middle panel shows the long profile of channel 4, and the channel slope (red); the lower panel shows channel 4 incision (red) and width (black). Just like in channel 3, the high gradient at Folds H and D locations, represent only a quarter of the time-integrated uplift of the 1.7 Ma surface in that location compared to the maximum documented at Fold E location.

The plot of width-to-depth ratio (aspect ratio) versus channel gradient (slope) shows a large degree of scatter in data points (Fig. 4.8). This is in contrast to the aspect ratios of rivers crossing active structures which show a clear trend of decreasing width for increasing channel slope (e.g., Whittaker et al., 2007a). Studies of buried submarine channel systems showed that as they incise across structures, their widths get narrower (e.g., Mayall et al., 2010), hence, modern channels are expected to show a decreasing trend of aspect ratio with increasing gradient. The outliers labelled on Figure 4.8 are from the plot of the aspect ratios of channel 3 from measurements obtained on the knickpoint generated by Fold I (Fig. 4.7c), and indicating the anomalously high gradient at that location. Because these points plot separately from other data, one explanation is recent movement by Fold I, thus amplifying the knickpoint in this location. Clark and Pickering (1996) also reported a large scatter of data points for modern submarine channel aspect ratios, and showed that this is in contrast to aspect ratios of ancient (buried) submarine channels (normally obtained from outcrop or subsurface data) which tend to plot in a field of smaller dimensions. These authors suggested that this may be because the dimensions of ancient submarine channels are often underestimated because they are often mapped on the basis of the presence of sand. These results highlight the diversity of submarine channel form (e.g., Clark and Pickering, 1996a; Mitchell, 2006; Meiburg and Kneller, 2010) and our current inability to fully constrain factors controlling submarine channel development in a manner equivalent to their fluvial counterparts because of the lack of sufficient data from direct measurements of turbiditic flows (e.g., Talling et al., 2012, 2013). But in general terms, the channels in this study are responding to tectonics by increasing their slope and depth. However, the channel widths tend to remain constant down-system, regardless of on-going tectonic deformation (*cf.* Figs. 4.5, 4.7). This result suggests that channel depth and slopes are more sensitive indicators of channel response to tectonic perturbation than widths, unlike their fluvial counterparts (e.g., Hack et al., 1953; Howard, 1994; Whipple and Tucker, 2002; Tucker and Bras, 1998; Whittaker et al., 2007; Yanites et al., 2011).

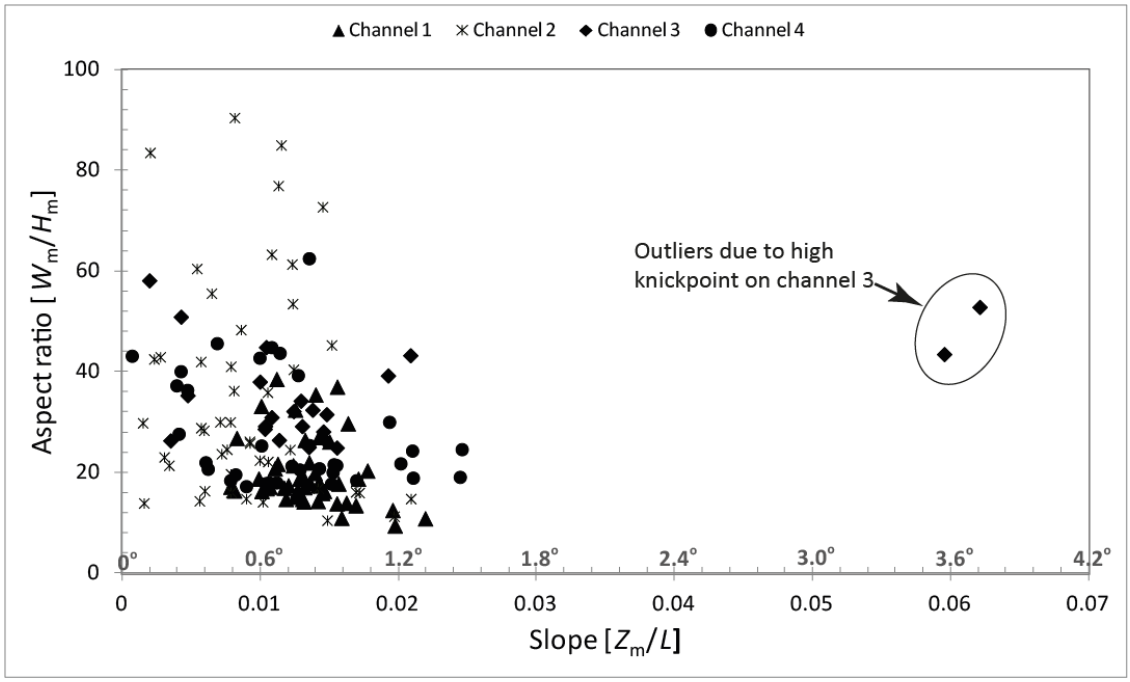


Figure 4.8: Shows the plot of aspect ratio of the four channels in the study area, against channel slope indicated in y/x, and in degrees. Note that the aspect ratios show a large scatter in data points, and the outliers, are from the plot of aspect ratio of channel 3 derived at the location where Fold I caused a large increase in slope (see Fig. 4.7c).

4.5.4 Down-system evolution of channel shear stress and flow velocity

A key question is whether the channel morphologies we see represent the transient responses of the submarine channels to on-going deformation since 1.7 Ma, or whether the channels are in a topographic steady-state with respect to the tectonic boundary conditions. To evaluate this, I use estimates of the downstream distribution of channel shear stress and flow velocity as a proxy for the potential erosivity of turbidite flows in the study channels (Fig. 4.9). Because it is impossible to reconstruct the erosivity of each flow that has come down a submarine channel in the last 1 to 2 million years, an approach similar to that used by the fluvial geomorphology community was adopted. This approach was used to quantify the distribution of shear stress, τ_b and flow velocity, u, where both τ_b and u are represented by two end-members; (1) based on constant sediment concentration (black curves, Fig. 4.9) and (2) based on varying sediment concentration (red curves, Fig. 4.9) modelled to be inversely proportional to the cross-sectional area of the channel (as described in section 4.4.2). The latter predicts lower shear stresses and flow velocities because the flow is more dilute when the cross sectional area of the channel increases. The calculations demonstrate that variations in measured channel geometry and channel gradient are likely to be very important in determining turbidity flow velocities and bed shear stresses.

The results of shear stress in channel 1 (Fig. 4.9a) show a peak shear stress of 130 Pa for constant sediment concentration (black curve, middle panel) between 23 km and 28 km down-system. But the peak shear stress for the varied sediment concentration (red curve) is less than 100 Pa. The flow velocity in channel 1 (lower panel, Fig. 4.9a) ranges from as low as 1.6 ms^{-1} to as high as 3.6 ms^{-1} between 26 km and 28 km down-system which coincides with an area of significant increase in channel gradient (see Fig. 4.7a). Real flows are expected to lie somewhere within the range of these curves, so potential maximum shear stresses increase is between 10 and 28 km down-system particularly in the region where the normalised relative uplift rate of the 1.7 Ma surface is high (upper panel, Fig. 4.9a). So in first order terms, assuming that erosivity is proportional to bed shear stress τ_b, then the increase in τ_b does correspond to areas of structural uplift since 1.7 Ma, and this channel may have reached a topographic steady state with respect to structural uplift since this time.

Channel 2 shows similar results to channel 1 with a peak shear stress of ~125 Pa (middle panel, Fig. 4.9b), and peak velocity of 3.6 ms^{-1} for the constant sediment concentration model (lower panel, Fig. 4.9b), and overall lower bed shear stress and flow velocity for the varied sediment concentration. Moreover, the region of overall increase in bed shear stresses (from 28 – 40 km down-system) also

corresponds to the area where the normalised uplift of the 1.7 Ma surface (upper panel, Fig. 4.9b), the channel gradient and channel incision is high (see Figs. 4.7b, 4.9b) even though this channel has been forced to divert by Fold C (*cf.* Fig. 4.4). However, while channel 1 shows an overall average shear stress of ~ 50 Pa, the average is low in channel 2 (~ 20 Pa); and the average velocity in channel 1 is ~ 2 ms^{-1} while that of channel 2 is ~ 1 ms^{-1} (Fig. 4.9 – a, b). Overall, channels 1 and 2 have almost linear profiles and the areas of larger increase in bed-shear stresses for these two channels occurred in regions where both the normalised relative uplift of the 1.7 Ma surface (Fig. 4.9 – a, b) and the channel erosivity (Fig. 4.7 – a, b) is high. Consequently, both these channels may have achieved long-term topographic steady-state.

Channel 3 shows a very high bed-shear stress and flow velocity for both the constant sediment concentration and the varied sediment concentration between 2 km and 5 km down-system (middle and lower panels, Fig. 4.9c). The bed-shear stress in this area is 220 Pa and 160 Pa and the flow velocity is 4.6 ms^{-1} and 4 ms^{-1} for constant and varied sediment concentration respectively. The overall average bed shear stresses and velocities for channel 3 are similar to the averages in channel 1. However, the area with the highest bed shear stress in channel 3 does not correspond to the region of higher time-integrated uplift of the 1.7 Ma surface (upper panel, Fig. 4.9c). This high value of shear stress (~220 Pa) in an area where the time-integrated uplift of the 1.7 Ma surface is only a quarter of the maximum documented, and the absence of any increase in incision depth at this point (*cf.* Fig. 4.7c), suggests that the high present-day gradient is a direct result of relatively recent on-going uplift, to which the channel has not yet fully adjusted.

Channel 4 shows considerable variation down-system for both shear stress and flow velocity derived from constant sediment concentration (middle and lower panels, Fig. 4.9d). However, the peak bed-shear stress (~ 200 Pa) and flow velocity (~4.4 ms^{-1}) are modelled to occur at approximately 10 km down-system. Just like channel 3, these peaks occurred where the time-integrated uplift of the 1.7 Ma surface (upper panel, Fig. 4.9d) is also a quarter of the maximum documented. But unlike in channel 3, channel 4 responded by enhancing incision in this area (*cf.* Fig. 4.7d). This suggests that not only has channel 4 experienced enhanced uplift in this area post 1.7 Ma, but that it is already responding by increasing shear-stress driven incision. Moreover, the region of longer, time-integrated uplift of the 1.7 Ma surface (from 12 to 22 km, Fig. 4.9d) does approximately correspond to an overall increase in bed shear stress (middle panel, Fig. 4.9d) and channel incision (*cf.* Fig. 4.7d). This shows that channel 4 has likely been responding to structural growth of Fold E (Fig. 4.7d) since 1.7 Ma in an attempt to regain topographic steady state.

Generally, the low time-integrated uplift of the 1.7 Ma surface in channels 3 and 4 in areas where the channel gradient is very high (Fig. 4.7 – c, d) may suggest that this steepening is likely to be recent. And while channel 3 has yet to respond to this recent change in gradient, channel 4 has responded by increasing shear-stress-driven incision to keep pace with the enhanced recent uplift on structures H and D whose amplitude represents only 25 % of the normalised uplift along the channel since 1.7 Ma relative to Fold E (Fig. 4.7d).

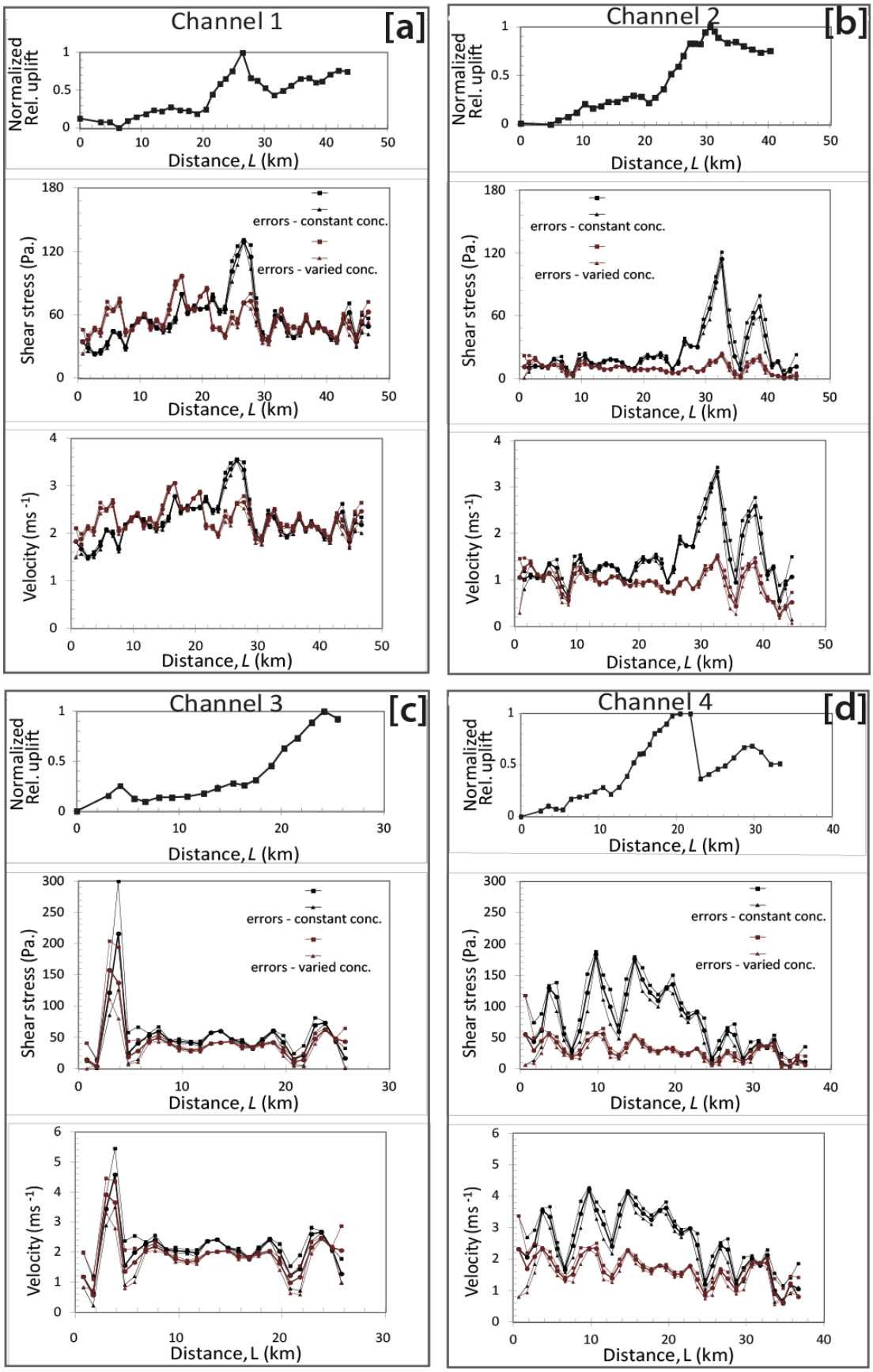


Figure 4.9 (see caption in next page)

Figure 4.9 (overpage): (a) Shows the time-integrated uplift of the 1.7 Ma horizon (upper panel) along the path of channel 1; the middle panel shows the variation in shear stress (black curve – from constant sediment concentration; red curve – from - varied sediment concentration) along channel 1; and the lower panel shows variation in flow velocity for both the constant, and the varied sediment concentration down-system of channel 1. Note a shear stress increase of up to 130 Pa, and flow velocity increase of up to 3.6 m s^{-1} in response to the high relative uplift of the 1.7 Ma horizon by growing Folds B/E (Fig. 4.7a). (b) Shows the time-integrated uplift of the 1.7 Ma horizon (upper panel) along the path of channel 2; the middle panel shows the variation in shear stress (black curve – from constant sediment concentration; red curve – from varied sediment concentration) along channel 2; and the lower panel shows variation in flow velocity for both the constant, and the varied sediment concentration down-system of channel 2. Note a shear stress increase of up to 120 Pa, and flow velocity increase of up to 3.6 m s^{-1} in response to the high relative uplift of the 1.7 Ma horizon by growing Folds G (Fig. 4.7b). (c) Shows the time-integrated uplift of the 1.7 Ma horizon (upper panel) along the path of channel 3; the middle panel shows the variation in shear stress (black curve – from constant sediment concentration; red curve – from varied sediment concentration) along channel 3; and the lower panel shows variation in flow velocity for both the constant, and the varied sediment concentration down-system of channel 3. Note a shear stress increase of up to 215 Pa, and flow velocity increase of up to 4.6 m s^{-1} in the location of Fold I (Fig. 4.7c) where the relative uplift of the 1.7 Ma horizon is only 25 % of the maximum. (d) Shows the time-integrated uplift of the 1.7 Ma horizon (upper panel) along the path of channel 4; the middle panel shows the variation in shear stress (black curve – from constant sediment concentration; red curve – from varied sediment concentration) along channel 4; and the lower panel shows variation in flow velocity for both the constant, and the varied sediment concentration down-system of channel 4. Note the overall higher variation in shear stress and flow velocity, and the highest shear stress increase of up to 180 Pa, and flow velocity of up to 4.2 m s^{-1} also occur where the relative uplift of the 1.7 Ma horizon is only 25 % of the maximum. However, the values are also high in the location of long time-integrated uplift of the 1.7 Ma surface by Fold E (Fig. 4.7d).

4.6 DISCUSSION

4.6.1 Channel response to seabed structures: morphology

This study shows that while the mean channel width varies from channel to channel, the frequency distribution tends to be mono-modal with relatively little systematic variation as a function of downstream distance even when channels cross actively growing structures (Figs. 4.4, 4.5). There is a much more varied distribution in channel depths, because of the effect of growing folds, most of which have seabed relief. In general, average channel widths range from as low as 1100 m in channels 1 and 2, to as high as 2400 m in channel 4. Typical incisional depths vary from as low as 10 m to as high as 140 m. Studies of modern submarine channels in different settings including the Mississippi fan, the Indus fan and the Rhone fan, amongst others, shows that they exhibit similar width and depth characteristics (e.g., Clark and Pickering, 1996a).

The normalised profiles of the modern channels (Fig. 4.6b) show that the profiles are generally linear to sub-linear, though some channels (e.g., channels 1 and 2) whose concavity is approximately -0.08, are linear, while channels 3 and 4 are slightly concave with concavity that is approximately -0.2 and -0.34 respectively. The average gradient of these channel profiles is 0.9^{o} to 1^{o} (or y/x slope of 0.015 – 0.017). However, the profiles are also characterised by small-scale variations in down-system gradient forming knickpoints which often coincide with the position of underlying folds and thrusts and implicitly therefore, variations in substrate uplift rate (Fig. 4.6a).

Analysis of the geomorphic response of channels to tectonic perturbation shows that the channels in this study are responding by increasing their slope and depth of incision. However, channel widths appear to be insensitive to on-going tectonic deformation (Figs. 4.5, 4.7). For example, in channels 1 and 2, areas of significant increase in channel gradient, generated by the time-integrated structural uplift of the 1.7 Ma surface are associated with more than 70 % increase in channel incision but the average width (ca. 1100 m) remains fairly constant downstream (Fig. 4.6b). Channel 4 also shows similar response to channels 1 and 2. However, both this channel, and channel 3, are characterised with areas of recent uplift – where the time-integrated uplift of the 1.7 Ma surface by growing structures is only approximately 25 % of the maximum documented uplift along the path of each channel. However, only in channel 4 does channel incision correlate with these areas, whereas channel 3 is yet to fully adjust to this recent structural growth.

These results suggest that submarine channel depths and slopes are far more sensitive indicators of channel response to tectonic perturbation than widths, unlike their fluvial counterparts (e.g.,

Howard, 1994; Whipple and Tucker, 2002; Whittaker et al., 2007; Yanites et al., 2011). The insensitivity of submarine channel width to tectonic perturbation is in stark contrast to river systems which show a clear trend of decreasing channel width as local gradient increases (e.g., Whittaker et al., 2007). In these cases, channel narrowing acts to increase unit shear stresses on the base of the river, and also increases bankfull flow depth. I suggest that the reason why turbidity current channels do not behave in the same way as fluvial systems is likely due to flow stratification and structure of typical turbidite flows, where the higher concentration of sediment is within the channel and a low concentration plume usually overflows the channel bank. For example, direct observation of a modern turbidite flow by Meiburg and Kneller (2010) at water depth of ca.4000 m in Zaire/Congo; showed that the low concentration plume overflows the channel bank for up to 18 km away from the main channel axis and that the total flow thickness (including the low concentration plume) was up to 150 m. Based on these observations, I suggest that channel steepening driven by the growth of submarine structures leads to channel incisional depths increasing, rather than channel width narrowing because (i) the concentration of coarse-grained sands in the bottom of these flows will increase shear-stress driven incision in the deepest part of the channel only (ii) the channel banks are mostly affected by the low concentration plumes and implicitly therefore, low shear stress, which is probably why the channel banks are less susceptible to width changes even at points of large gradient increase. This may explain why the plot of aspect ratio against channel slope tends to show large scatter in data points (Fig. 4.8). Moreover, channel systems that are still adjusting to recent structural uplift that created a very large gradient increase (e.g., channel 3, Fig. 4.7c) can result in aspect ratio data point outliers because the channel is yet to fully adjust to this recent gradient change which may take some time (Fig. 4.8).

4.6.2 Channel response to seabed structures: deflection/diversion and incision

Seabed channels in this study display a range of interactions with seabed structures such as channel deflection and diversion (e.g., channel 2, Fig. 4.4) and incision across folds at displacement low points (e.g., channel 1, Fold B/E, Figs. 4.3d and 4.4). Clark and Cartwright (2009) have previously reported four end-member channel interactions with structures (folds/faults) in the deepwater Nile Delta. These include deflection to fold tips, diversion by folds, confinement between two parallel folds and blocking of channels by folds. Whether submarine channels are diverted by growing structures, or incise across them, is the result of a number of factors including: the erosive power of the channel relative to the rate of growth of the structure (e.g., Morley, 2009; Mayall et al., 2010);

any variation in bedrock resistance to erosion (e.g., Mitchell, 2006); the width of the structure, which controls the wavelength of the uplift field (chapter 3); and the existence of high relief paleao-structures which act as a barrier to flow. Not all of these controls are easy to quantify, such as the variation in bedrock resistance to erosion and the variation in bed-shear stress that allows channel incision (e.g., Mitchell, 2006).

However, using data obtained from the geomorphic response of channels to tectonic perturbation in this study and assuming sediment concentrations of ~ 0.6 % (as reported in Pirmez and Imran, 2003; Konsoer et al., 2013), I predict a range of channel shear stresses between 50 – 200 Pa, and flow velocity varies from as low as 0.8 ms^{-1} to as high as 5 ms^{-1} (Fig. 4.9). These range of flow velocities are consistent with reported values of turbidite flow velocities from rare direct field observations previously reported (e.g., Meiburg and Kneller, 2010; Xu, 2011; Talling et al., 2012, 2013). It is also important to remember that the plots shown in Figure 4.9 represent only end-members of a possible large continuum of submarine channels bed-shear stress and flow velocity behaviours. Deviation is expected from the proposed models because of the following reasons: (1) increase in channel discharge down-system due to flow evolution (Gerber et al., 2009) as a result of entrainment of clear ambient water into the flow which can further dilute the sediment concentration; (2) variation in the erodibility of the underlying substrate (Mitchell, 2006); (3) variation in threshold shear stress for incision (Mitchell, 2006) and (4) the influence of background sedimentation (Gerber et al., 2009).

Nevertheless, this study illustrates how the erosive power of flows can be a major factor in determining channel incision across folds/thrusts with on-going structural deformation since 1.7 Ma. That is, channels continue to incise across growing structures at displacement low points. Moreover, where the normalised relative uplift rate of the 1.7 Ma surface is high, the bed shear stress and flow velocity of the channels is also high. This suggests that channel flow power (shear stress and velocity) partly determines whether the channel can keep pace with fold growth. For example, the average bed-shear stress and flow velocity (~20 Pa and 1 ms^{-1} respectively) of channel 2 is low compared to averages in channel 1 (~50 Pa and 2 ms^{-1}). This may partly explain why channel 2 has been diverted by Fold C (Fig. 4.4). Although in chapter 3, I documented that Fold C is a broad detachment structure, and is associated with a longer wavelength (~5 km) of slope whose dip direction is opposite to that of the regional slope. This counter-regional slope might be enough to cause channel diversion if it is already in-place prior to channel development. The counter-regional slopes associated with structures traversed by channels is less than 2 km long (see chapter 3).

Along channel 3, the uplift of the 1.7 Ma horizon by Fold I has generated a major knickpoint on the modern seabed – indicated by high channel gradient (~0.07). But the normalised uplift of the 1.7 Ma

surface in that area, is only 25 % of the maximum (upper panel, Fig. 4.9c). Furthermore, the calculated bed-shear tress in that area (middle panel, Fig. 4.9c) is high (up to 220 Pa) and the flow velocity is up to 4.6 ms^{-1}, but the channel incision in that area is very low (Fig. 4.7c). This suggests that this uplift is relatively recent, and the increase in predicted bed-shear stress and flow velocity is an indication that subsequent turbidite flows, given the present channel geometry, will lead to enhanced channel incision over time, as demonstrated by channels 1 and 2. The peak bed shear stress (~ 200 Pa) and flow velocity (~4.4 ms^{-1}) in channel 4, just like in channel 3, are modelled to occur where the time-integrated uplift of the 1.7 Ma surface is also a quarter of the maximum documented (upper panel, Fig. 4.9d). But unlike in channel 3, channel 4 has responded by enhancing incision in this area (Fig. 4.7d). Thus, the region of time-integrated uplift of the 1.7 Ma surface in channel 4 does approximately correspond to an overall increase in bed-shear stress (middle panel, Fig. 4.9d) and channel incision (Fig. 4.7d). This shows that channel 4 has likely been incising in response to structural growth of Fold E since 1.7 Ma and to active growth of Folds D and H more recently in an attempt to regain topographic (bathymetric) steady-state (Fig. 4.7d).

This process of increased bed-shear stress/incision following an increase in channel gradient is the geomorphic expression of having steeper slopes, but in most cases, the channel width remains largely insensitive to these changes in gradient (Fig. 4.7). I therefore suggest that the enhanced channel incision in knickpoint areas is a way of restoring topographic steady-state and allowing the channel to keep pace with the growing structure. Similar observations have been reported by authors working on submarine channels in different settings. For example, Ferry et al. (2005) and Heinio and Davies (2007) reported that the dominant mechanism by which submarine channels readjust to an increase in gradient (knickpoint) is through the upslope retreat of the knickpoint as a result of channel erosion which will gradually smooth the profile in order to restore equilibrium in those locations. Pirmez et al. (2000) reported that the linear nature of submarine channel profiles in the Niger Delta (e.g., channels 1 and 2, Fig. 4.6b) suggest that they are in a state of equilibrium where the channel sedimentation/erosional processes, are comparable to tectonic deformation, and this is normally achieved over thousands of years.

4.6.3 Are these channels in topographic steady-state?

A full understanding of how, and in what circumstances, submarine channels cut across actively growing structures and how they keep pace with structural growth has remained elusive (Shaw et al., 2004; Morley, 2009; Mayall et al. 2010; Georgiopoulou and Cartwright, 2013). However, using 3D seismic data, coupled with techniques more commonly used in land-based tectonic geomorphology studies, we can effectively compare the magnitude of the relative uplift rate, the width of growing folds (chapter 3) and estimates of down-system erosivity. Thus, I used the results in this study, and the Hardy and Poblet (2005) method for measuring the vertical uplift in the fold crestal area of fault-propagation folds (see chapter 3) to test whether these channels are in topographic steady-state. The focus is on channels 1 and 4 crossing folds B/E and D (Fig. 4.4), which have a seafloor expression, because existing work has carefully constrained the shortening on these structures through time (*cf.* Fig. 4.1).

In areas where channel 1 crosses Fold B/E (Figs. 4.3d, 4.4), the maximum cumulative shortening of the 3.7 Ma horizon, measured adjacent to the channel in this structure is 146 m (Fig. 4.1c). This value of shortening translates to 143 m of vertical uplift if we use the relationship of Hardy and Poblet (2005) to relate shortening to uplift for fault-propagation folds. This vertical uplift of Fold B/E can be compared with channel incision in that area as a proxy to determine whether this channel is in topographic (bathymetric) steady-state. Therefore, if we assume a constant sedimentation rate between 3.7 Ma and now, the maximum uplift of the 1.7 Ma surface in areas adjacent to where channel 1 cuts-across fold B/E is 66 m. Significantly, the results presented in this chapter show a total increase in 'excess' channel 1 incision of ~60 m above the background incision (~ 65 m, Fig. 4.5b) in response to Fold B/E uplift since 1.7 Ma (Fig. 4.7a). This channel incision is almost identical to the maximum uplift since 1.7 Ma, and strongly suggests the channel is capable of keeping pace with the structural uplift. If we apply the same method to channel 4, where it crosses Fold D, the maximum cumulative shortening of the 3.7 Ma horizon in this structure, is 133 m (Fig. 4.1c). This value translates to a vertical uplift of approximately 132 m, which gives a maximum uplift of 61 m over 1.7 Ma. From the analysis of channel 4 incision, the 'excess' channel incision above the background incision (~94 m, Fig. 4.5h) is ~45 m in the region affected by Fold D (Fig. 4.7d). This value is 26 % less than the maximum uplift (61 m) calculated adjacent to channel 4, but as this channel has been deflected to the tip of Fold D (Fig. 4.1a) where the uplift is certainly lower than 61 m, this also suggests the channel is in an approximate bathymetric steady-state. In like manner, a maximum increase in channel 4 incision (~56 m above the background incision), occurred at the location of

Fold E (Fig. 4.7d) where the channel is also deflected to the tip of Fold E (Fig. 4.4). This increase in channel incision is also slightly less than the maximum uplift (~66 m) calculated for Fold E because of channel deflection to the fold tip (Fig. 4.1a). Therefore, making the reasonable assumption that the documented excess channel incision is in response to the maximum uplift since of 1.7 Ma (even though average channel age is ~1.2 Ma; see chapter 3); then channel 1 and channel 4 may have reached topographic steady-state, or are more than capable of keeping pace with fold growth (if we used the minimum estimates of uplift since 3.7 Ma, or if we take into account that the channels are likely younger than the 1.7 Ma reflector, as they do not cut across it).

A similar story emerges for the other two channels. For instance, channel 2 has increased its incision by approximately 50 m above a background incision of ~42 m (Fig. 4.5d) across structures G and F (*Cf.* Fig. 4.7b). Estimate of uplift from a single seismic section across Fold G gives a maximum uplift value of approximately 60 m which suggest that this channel is also approaching a steady-state. Based on a similar section across Fold I, an estimate of vertical uplift of the 1.7 Ma surface just adjacent to channel 3, is ~38 m which is comparably low even though this structure is associated with a steep slope on the modern seabed (see Fig. 4.7c – upper panel). And because the uplift observed on Fold I along channel 3 is not coupled to significant change in channel 3 incision, this channel is likely not to have reached topographic steady-state (lower panel, Fig. 4.7c).

These data of maximum uplift and excess channel incision measured along the paths of the studied channels are plotted on a graph of maximum structural uplift since 1.7 Ma versus channel excess incision in response to those uplift (Fig. 4.10). However, because this is 'excess' channel incision above the background mean incision, the channel incision coupled to fold uplift might have been underestimated. Nevertheless, the line of bathymetric steady-state in which channel incision equals structural uplift is very close to the maximum predicted uplift for each of the channels, apart from channel 3 (Fig. 4.10). Taking into account that the minimum uplift for these horizons could be substantially less than the maximum, given the shortening constraints we have (chapter 3, and above); Figure 4.10 demonstrates clearly that these submarine channels are likely to be keeping pace with the growth of structures since 1.7 Ma. The only exception is in channel 3 in which the ~38 m uplift measured on Fold I since 1.7 Ma, is not coupled to any increase in channel incision (Fig. 4.10). This may suggests a sequence of firstly, structural growth – creating knickpoints, then followed by increase in channel incision during the next phase of turbidite flows in order to reestablish equilibrium (see McHargue et al., 2011). If that happens, then the data point-plot for this channel will move up the graph, towards the steady-state line (Fig. 4.10).

Of course, it is important to note that the erosivity of submarine channels, and hence whether they have reached topographic steady-state also depends on the frequency of turbidity currents and the sediment supply to them. Both of these are difficult to predict over million year timescales (see Pirmez and Imran, 2003, Xu et al., 2011; Talling et al., 2012). However, it is possible that the seabed channels considered in this study may predominantly reflect the last glacial period (120 ka – 18 ka; see Damuth, 1994) when low-stand depo-centres were shifted seaward and sediment could be fed directly to deepwater regions by rivers (see Posamentier and Kolla, 2003; Jermannaud et al. 2010). In contrast, during the periods of maximum sea-level in interglacials (e.g., during the Holocene; Damuth et al., 1988; Damuth, 1994), the locus of river sedimentation was shifted landward across the wide shelf of the Niger Delta which likely reduces the terrigenous sediment supply to the deep sea (Damuth, 1994). We know that low-stand conditions represent up to 90 % of the last million years when the channels have been incising. Nevertheless, Burke (1972) demonstrated that major submarine canyons at the flanks of the Niger Delta (e.g., the Calabar Canyon and its associated fans down-slope) are presently active. This author argued that prevailing north-easterly setting surface currents create strong long-shore drifts eastward and westward along the inner shelf toward the delta flanks; and that large amounts of sediments are transported to the heads of these canyons, and subsequently reaching the deepwater fan areas. Several studies of submarine fan systems (e.g., Damuth and Flood, 1984, 1985; Shanmugam and Moiola, 1988; Babonneau et al., 2002, 2010; Savoye et al., 2009; Covault and Graham, 2010) have also showed that the period of maximum fan growth is not necessarily related to periods of sea-level lowstand as some fans have grown faster during periods of sea-level transgression (e.g., Mississippi Fan; Table 1.1) and sea-level highstand (e.g., Zaire Fan; Table 1.1).

There is no data about current or past flow frequency of the channels studied here. However, regardless of whether the 'modern' sea-bed channels currently do receive fewer turbidite flows, due to suppressed sediment supply, than during previous glacial low stand periods, our predicted shear-stress results reflect time-integrated erosional geometry of the channels to structural growth in the last 1. 7 My. This erosional geometry is unlikely to have been significantly altered in the last 10 Kyrs, because sedimentation rates and turbidite flow frequency are lower, while rates of structural shortening (tens of metres per million years) are too small to significantly affect channel geometry during the Holocene.

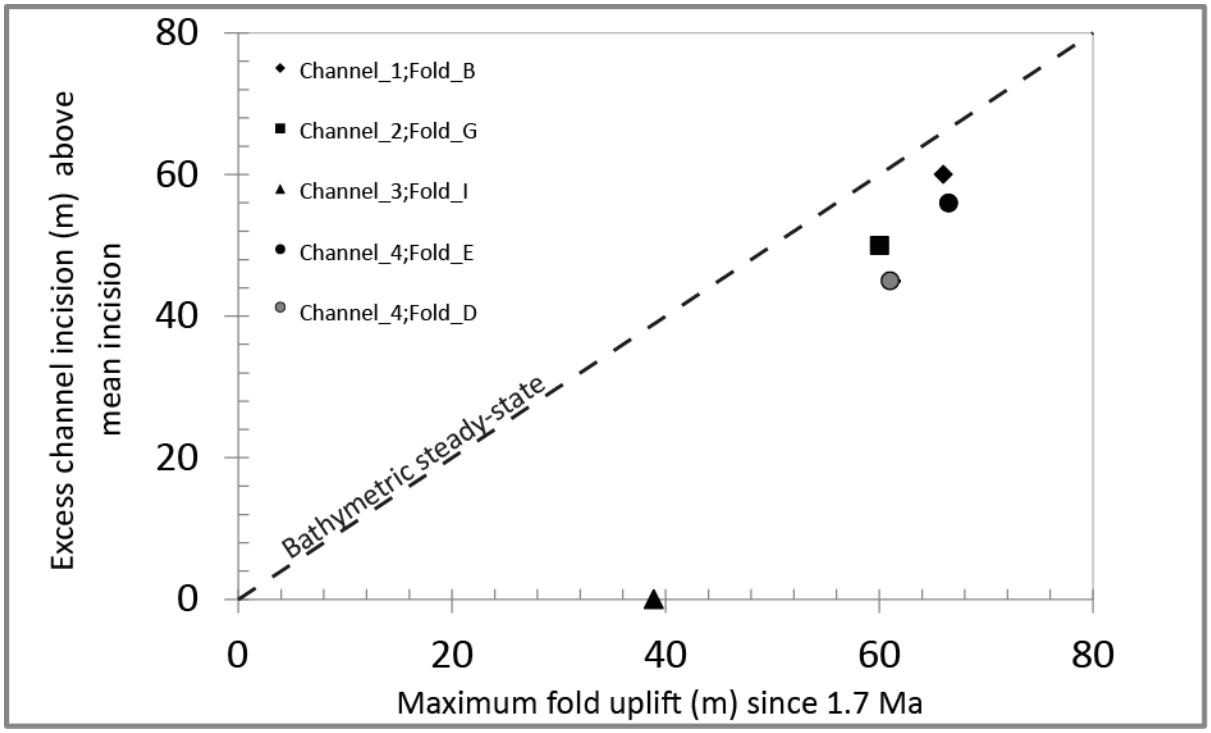


Figure 4.10: A graph showing plots of maximum fold uplift since 1.7 Ma versus excess channel incision. The dash line represents a topographic (bathymetric) steady-state. All plots with the exception of channel 3 – Fold I plot, are close to the steady-state line. Note that channel 3 plots further away from the steady-state line because this channel is yet to respond to a recent growth on Fold I.

4.7 CONCLUSIONS

Four main active seabed channels that are interacting with growing thrust-related folds in the toe-thrust region of the Niger Delta have been studied. The study showed that average channel widths range from as low as 1100 m to as high as 2400 m, and that typical incisional depths vary from as low as 10 m to as high as 140 m. Channel widths are characterised by mostly mono-modal distribution and are insensitive to active folds affecting channel pathways while channel depths tend to show a large spread in frequency distribution because of the impact of seabed structures.

The long profiles of these channels are relatively linear with concavity that ranges from -0.08 to -0.34 with an average gradient of $0.9^{o} – 1^{o}$. Local scale steepenings (knickpoints) are apparent near mapped structures and implicitly therefore, variations in substrate uplift rate. Areas of significant increase in channel gradient caused by long time-integrated structural uplift of the 1.7 Ma surface (e.g., channels 1, 2 and 4), are associated with more than 70 % increase in channel incision. However, in channel 3, recent channel steepening in response to Fold I, which has only a small time-integrated uplift component, is not matched by a comparable increase in channel incision.

As submarine channels interact with seabed structures, they can be forced to deflect to the lateral tips or relay areas of growing structures, or they must incise across them. Channel diversion is caused by a combination of factors which include; wide folds with longer wavelength of uplift field, the presence of positive topographic relief as a result of high structural uplift rate relative to sediment accumulation rate, and lower bed-shear stress and flow velocity amongst others.

For channels in this study area, I model channel bed-shear stresses between 50 – 200 Pa for flows with a sediment concentration of 0.6 %, and flow velocities from 0.8 ms^{-1} to as high as 5 ms^{-1}. These range of flow velocities are consistent with reported values of turbidite flow velocities from rare direct field observations reported by others (e.g., Meiburg and Kneller, 2010; Talling et al., 2012, 2013).

Analysis of structural uplift since 1.7 Ma, and excess channel incision showed that some of the channels are able to keep pace with the time-integrated uplift of the 1.7 Ma horizon, and may have reached a topographic steady-state with respect to structural uplift since 1.7 Ma. However, one of the channels (channel 3) is unlikely to be in topographic steady-state because of recent structural uplift not coupled to significant channel incision. I show that submarine channels can adjust to growing folds and thrusts by changing their slope and incisional depth, and shear stresses of approximately 130 Pa are sufficient to keep pace with structural strain rates of ~4.2×10^{-3} per Ma.

CHAPTER 5

EVOLUTION OF PLEISTOCENE SUBMARINE CHANNELS IN RESPONSE TO THE GROWTH OF ACTIVE STRUCTURES FROM 3D SEISMIC ANALYSIS, NIGER DELTA

5.1 INTRODUCTION AND PREVIOUS WORK

A number of studies have analysed the overall geometry of submarine channel complexes and how they develop and fill over time (Mayall and Stewart, 2000; Mayall et al., 2006; Deptuck et al., 2003, 2007, among others). For example, Mayall and Stewart (2000) reported that the main components of many channel-fill systems comprise sands and gravel bypass lags, typically at the bottom of the fill; slumps and debris flows; high net-to-gross stacked channel fill; and low net-to-gross channel-levee complexes at the top of the system. Consequently, the channel system fill is made up of several cut-and-fill sequences that are stacked both laterally and vertically through time, and confined by an erosional surface (e.g., Mayall and Stewart, 2000; Mayall et al., 2006; Deptuck et al., 2003, 2007; Kolla et al., 2007; Janocko et al., 2013). Confined cut-and-fill sequences documented by Janocko et al. (2013) range from those that are purely erosionally-confined or levee-confined, to those that are a combination of both (e.g., Fig. 5.1a). These authors also referred to fully-developed systems made up of several superimposed channel belts (cut-and-fill) as valley-fill complexes (e.g., Fig. 5.1b). Mayall et al. (2006) referred to these valley-filled complexes as '3rd order' channel complex systems (up to 4 km wide and 150 m thick), and the individual channel belts within the '3rd order' system as '4rd order' channel complexes (up to 1500 m wide and 50 m thick) that also have within them the individual channels that are generally less than 400 m wide and 10 m thick (Fig. 5.1c). These channel systems are sometimes characterised by large-scale 'gull-wing' levees that flank the system (referred to as external or outer levees) whereas the smaller-scale levees flanking individual channels within the channel complex are referred to as internal levees (e.g., Fig. 5.1a, b; see also Babonneau et al., 2004; Deptuck et al., 2007; Kane and Hodgson, 2011). In the Benin

Canyon, located in the offshore Niger Delta, Deptuck et al. (2007) also documented the evolution of similar systems where they showed that they develop from a combined process of cut-and-fill, and overall aggradation through time.

In each of these studies the documented channel system evolved through a combined process of channel re-incision, migration and aggradation. However, one key limitation of these studies is that they do not explicitly analyse the impact of tectonic perturbations on the time-evolution of the channel cut-and-fill sequence, which is essential for understanding the overall evolution of the submarine channel systems, and how they attain topographic (bathymetric) steady-state in areas of on-going deformation. Although some progress has been made in describing how active submarine channels interact spatially with growing structures in deepwater settings (e.g., Gee and Gawthorpe, 2006; Gee et al., 2007; Clark and Cartwright, 2009, 2011, 2012; Pirmez et al., 2000; Mayall et al., 2010; Geogiopoulou and Cartwright, 2013 amongst others), none of these studies have explicitly constrained the geometric evolution of channel cut-and-fill sequences in response to growing structures. To-date, a number of recent studies have shown that tectonic perturbations produced by growing structures also affect the shapes of submarine channel longitudinal profiles (e.g., Huyghe et al., 2004; Ferry et al., 2005; Pirmez et al., 2000). As a consequence, active submarine channel longitudinal profiles are expected to reflect in part, the channel processes and the history of channel responses to tectonic perturbations (e.g., Pirmez et al., 2000; Huyghe et al., 2004; Ferry et al., 2005; Henio and Davies, 2007, chapter 4). Therefore, morphologic perturbations in submarine channel geometry should not only give information on the tectonic and sedimentary evolution of the active channel system, and any deviations from steady-state conditions (e.g., Amblas et al., 2011; chapter 4), but should also help determine the time-integrated geometry and aggradation history of the wider cut-and-fill channel system. Spatially, submarine channels have been documented both to be deflected and diverted by growing structures (Clark and Cartwright, 2009; Mayall et al., 2010; chapter 3, 4). Therefore, the lateral and vertical shifts in submarine channel location on the slope may result in lateral and vertical aggradation in submarine channels through time (Gee and Gawthorpe, 2006; Deptuck et al., 2003, 2007; Mayall et al., 2006; Kolla et al., 2007). In contrast, the absence of any structural control, depositional systems tend to preferentially fill a topographic low and then migrate laterally to fill the next available low. In these cases, the channels often organise in a manner which is increasingly referred to as compensational stacking (e.g., Straub et al., 2009). However, the combination of structural deformation and repeated turbiditic flows can generate channel cut-and-fill sequences over time, which will be preserved or partially preserved if channel aggradation dominates (Mayall et al 2006; Deptuck et al., 2007; McHargue et al., 2011). Consequently, the channel system fill and the channel system geometry should record the history of

tectonic perturbation *if* the resolution of the seismic data is good enough to allow the mapping and analysis of these systems.

In the Niger Delta study area that this PhD addresses, a detailed quantitative study of the responses of four recently-active seabed channels to tectonic perturbation is documented in chapter 4 (e.g., Fig. 5.1d). The data presented in chapter 4 shows that these active seabed channels have profiles that are generally linear to slightly concave and the average gradient in all channels is ~1^{o}. However in many cases a local increase in gradient corresponds to the positions of underlying thrusts and folds. Additionally, the overall linear nature of the modern channel profiles, the distribution of down-system bed-shear stress, coupled with the fact that the excess channel incision at thrust and fold locations matches the estimated magnitude of structural uplift over a period equivalent to the time of channel development, suggested that these submarine channel systems are capable of maintaining 'topographic steady-state' (see also Pirmez et al., 2000). However, an outstanding question is how the cut-and-fill channel sequences themselves evolve through time in response to structural growth, and whether this steady-state situation also applies when considering the entire cut-and-fill sequence, and not just the most recent channel thalweg-profile (i.e., the depth from the sea level to the channel floor measured down-channel). The results presented in chapter 4, as well as studies by other authors on the longitudinal profiles and geometry of channels in Niger Delta and similar deepwater settings fundamentally involve the active channel thalweg only. Only one study on the Benin Canyon by Deptuck et al. (2007) analyses both the lowermost erosive surface (which they referred to as the 'canyon thalweg') and the modern channel thalweg. Consequently, most studies on deepwater channel systems do not fully account for the coupled sedimentological and structural evolution of submarine channel systems in deepwater over million-year timescales.

To gain a more complete picture of longer-term channel response to on-going deformation, it is therefore important to analyse the geometry and nature of channel cut-and-fill sequences that record the time-integrated behaviour of the channel system. This study is therefore aimed at elucidating the findings reported in chapter 4 of this thesis by extending the analyses carried out on the most recently active (modern) seabed channels to cover the subsurface parts of modern channels and those recently buried within the Pleistocene to Recent strata. Here, I have analysed the cut-and-fill sequences of the active channel system and those of the buried channel systems (e.g., buried channel 5, Fig. 5.1d, e). Subsequently, the evolution of the cut-and-fill sequences are related to the time-integrated growth of structures affecting the channel systems in the study area (e.g., Folds A, B, C and D; Fig. 5.1d, e).

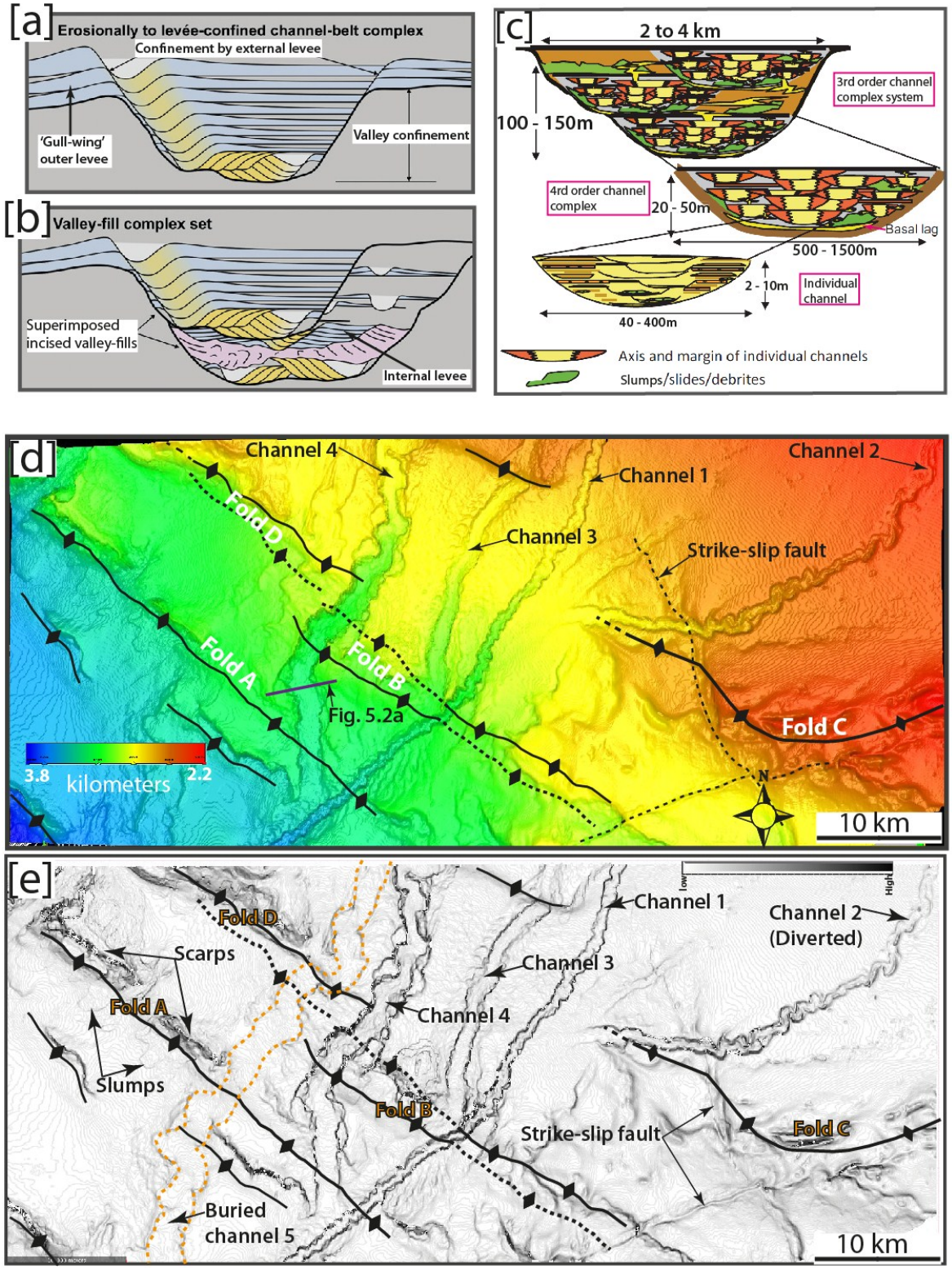


Figure 5.1: Schematic diagram of an erosionally-confined to valley-confined channel belt complex (a), and a valley-fill complex set (b) all from Janocko et al. (2013). (c) Shows a 3rd order channel complex system and sub-division of the complex into a 4rd order complex and an individual channel system from Jones et al. (2012) – originally modified from Mayall et al. (2006). (d) Is a 3D bathymetry map; and (e) is an edge-attribute map of the seabed over the study area. The maps show modern, seabed channel systems (1, 2, 3 and 4) and the outline of a buried channel still having seabed expression (buried channel 5, in Figure 5.1e). Growing folds with seabed relief (Folds A, B, C and D) are also shown on the maps. The trace of the fold axes at the seabed is shown as sold black lines with diamonds; the dashed fold axes are folds that do not have bathymetric expression at the modern sea floor.

5.2 METHODS

In order to analyse the evolution of channel systems through time, 3D seismic data (*cf.* chapter 2) is used to map the base and outer-margins of each of the main channel complexes including the buried channels which are no longer active. These margins are surfaces that have developed through a process of: (1) channel erosion into the pre-channel substrate which is clearly identifiable from the erosional truncations of the pre-channel substrate; and (2) outer levee build-up through time so that the upper part of the channel system is confined by outer levees (Fig. 5.2a). Through time, multiple channel 'cut-and-fill' sequences (including internal levees) can occur broadly in the same place forming a channel complex (e.g., Mayall et al. 2006). Hence the erosional surface, which is here called the channel container, represents a time-transgressive bounding surface, formed by multiple channelizing flows, with or without associated levees. For most of the examples studied in this research the lower part of the container is predominantly erosional and levees appear to be better defined in the upper parts of the confined channel system. The erosive surface (yellow line; Fig. 5.2a) was clearly recognised from the truncation of seismic horizons against the channel fill (which may in turn be made up of multiple smaller erosion channels with their fill) and possible internal levees as the system widens (Fig. 5.2a; Deptuck et al., 2003). In the example shown in Figure 5.2a the upper-levee defined part of the container, and is shown with dash-red lines.

For convenience, the erosive surface (made of both the yellow line and the dash-red line; Fig. 5.2a) bounding each of the mapped cut-and-fill sequences is here referred to as a 'channel container' and can be mapped down-system of individual channels. However it is important to stress that the base of the channel system – i.e. the container base, may be a composite erosive surface that formed through alternating periods of erosion and partial fill in the initial stage of development (see Deptuck et al., 2007). The container mapping was conducted using Landmark's 3D seismic interpretation software, using sections taken perpendicular to and along the channel, in order to manually map the erosive surface. For each channel system, the container was mapped down-system and across growing structures (e.g., Fig. 5.2b). The channel container bases lie just above the continuous 1.7 Ma seismic horizon that was used for the shortening and uplift calculations in chapter 4. Based on the approximate age of the downlap surface of the earliest, outer levees, associated with these established channel systems, onto the stratigraphy into which the channels are incised (e.g., Fig. 5.2a) the base container ages are tentatively estimated to be 1.2 – 1.3 million years old. However it is important to stress that there is considerable uncertainty on these age estimates, as they are based on the assumption of average sedimentation over a period from 3.7 Ma to now, since there is no biostratigraphic data to date the age of seismic horizons precisely in the

interval dominated by the Plio-Pleistocene channels (see Fig. 2.3; chapter 2). Consequently, the absolute container ages will vary depending on the variation in actual sedimentation rates. Relatively younger systems such as the modern channels 1 to 3 (Fig. 5.1d) may be less than 1 million years old. Deptuck et al. (2007) reported container age estimates for the relatively older Benin Canyon offshore Niger Delta to be up to 1.8 Ma.

With the aid of Landmark's interpolation algorithm, continuous container horizons were produced using the manually-picked horizons as seed points. These container horizons were depth-converted using an average seismic velocity of 1700 ms^{-1} as representative for the channel fill. A thickness map of the container fill in each of the channel systems could then be estimated. For containers whose modern channel is still active (e.g., active container 4, Fig. 5.2a), the fill thickness along the container centreline is calculated as the container depth minus the modern channel incision (Fig. 5.2b, c). However, for each buried system, the thickness of the fill is the same as the container depth because the accommodation space created by last period of channel incision prior to abandonment is now filled with abandonment/post-channel deposits (Fig. 5.2d). Consequently, the container width measured directly from the thickness map of the buried container will be the same as the maximum width measured between levee crest in a section across the buried container (Fig. 5.2d). However, it is important to realise that the width measured directly from the thickness map of the active container will be slightly lower because it will represent width measured at a depth just above the preserved container fill (Fig. 5.2c). A key limitation of this method of thickness calculation comes from the use of a constant velocity (in this case 1700 ms^{-1}) to calculate thickness of the container fill. Variation of velocity within thicknesses of 300 – 400 m maximum is likely to be small in comparison to the value of velocity of 1700 ms^{-1} (maximum error may be up to 9%; see Deptuck et al., 2007). Another error source may be due to lateral facies variation in container fill (i.e., sands versus shales). The different lithologies will have different velocities which may introduce error into container depth profiles; so higher frequency undulations in container thalweg profiles should be treated with caution; long profiles have therefore been smoothed using polynomial interpolation in order to address this problem (see below). Container thicknesses shown in this study are considered robust enough for the purpose of describing thickness variations within the container, since the priority is the maximum thickness (i.e., thickness along the container axis, Fig. 5.2b). Structures already identified and mapped in chapter 3 and 4 (including those not having seabed relief but affecting the channel system geometry) were used in this study to examine how they affect the evolution of the channel containers. In particular, buried structures and channel systems were identified and mapped using Root-Mean-Square (RMS) amplitude maps and seismic sections. The RMS amplitude was

extracted in a 100 ms window shifted c.150 m (~180 ms) from the mapped seabed horizon allowing edges of buried channels and outlines of buried structures to be mapped in plan-view.

The depth-converted horizon for each container (with depth measured from the sea-level) was exported in *text file (x,y,z)* format to Arc-GIS, and geo-referenced to build a 50 m resolution Digital Elevation Model (DEM) whose resolution was determined by the bin-size of the seismic data. These DEMs were then processed to get a flow network of channels by building separate flow networks for each channel container. From the flow networks, stream orders were defined and turned into vectors. To extract channel long profiles, the stream order vector coverage was used to run 'cost-paths' that follow the lines of the lowest values in the DEM along a channel system, starting from a user-defined point upstream (*cf.* chapter 4). From the DEMs, and the mapped channel networks, the following key variables were extracted and measured:

a. The container longitudinal profiles, *Zc* (measured as the elevation of the container centreline from sea level, against down-system distance, *L*) for each channel system (Fig. 5.2b). The down-system paths, along which the container profiles were extracted, were defined automatically by the cost-path algorithm in Arc-GIS. To remove noise and smooth steps in the data, the long profiles were fitted with a high-order polynomial, which could be differentiated to obtain the downstream evolution of the along-channel gradient. These profiles were compared with the associated modern channel thalweg-profiles already documented in chapter 4.

b. Container morphometric parameters which include (i) container width, *Wc* – the width measured horizontally between outer levee crests bounding the entire cut-and-fill sequences (Fig. 5.2a, c); and (ii) container depth, *Hc* – the maximum depth of the entire cut-and-fill sequences measured vertically from the outer levee crests to the base of the container (Fig. 5.2c); (iii) container fill thickness, *Hf* – the thickness of the preserved fill measured by subtracting the depth of modern channel incision, *Hm* from the container depth (Fig. 5.2c). Note that the container fill thickness, *Hf* of the buried systems is the same as the container depth, *Hc* (Fig. 5.2d). All morphometric parameters were measured at approximately 1 km intervals along the individual channels in order to capture as much detail as possible.

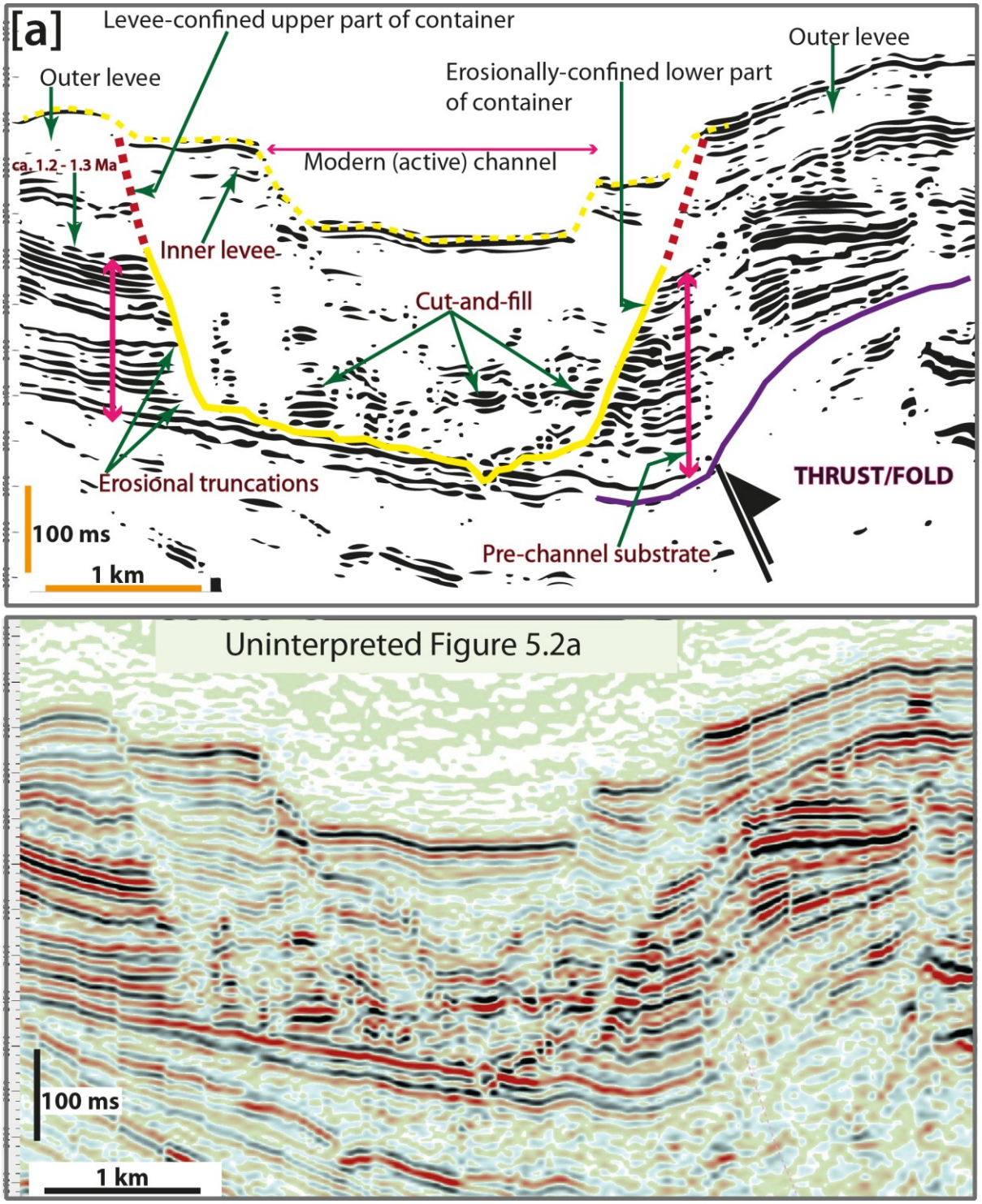


Figure 5.2: (a) Transect across active channel 4 (see section position in Figure 5.1d) showing channel geometry in the study area, and how the several cut-and-fill sequences are bounded within an erosionally-confined to levee-confined surface called the "container". The modern channel is the active or recently active channel forming the modern seabed thalweg within the system. Note that 5.2b, c and d are shown in the next page.

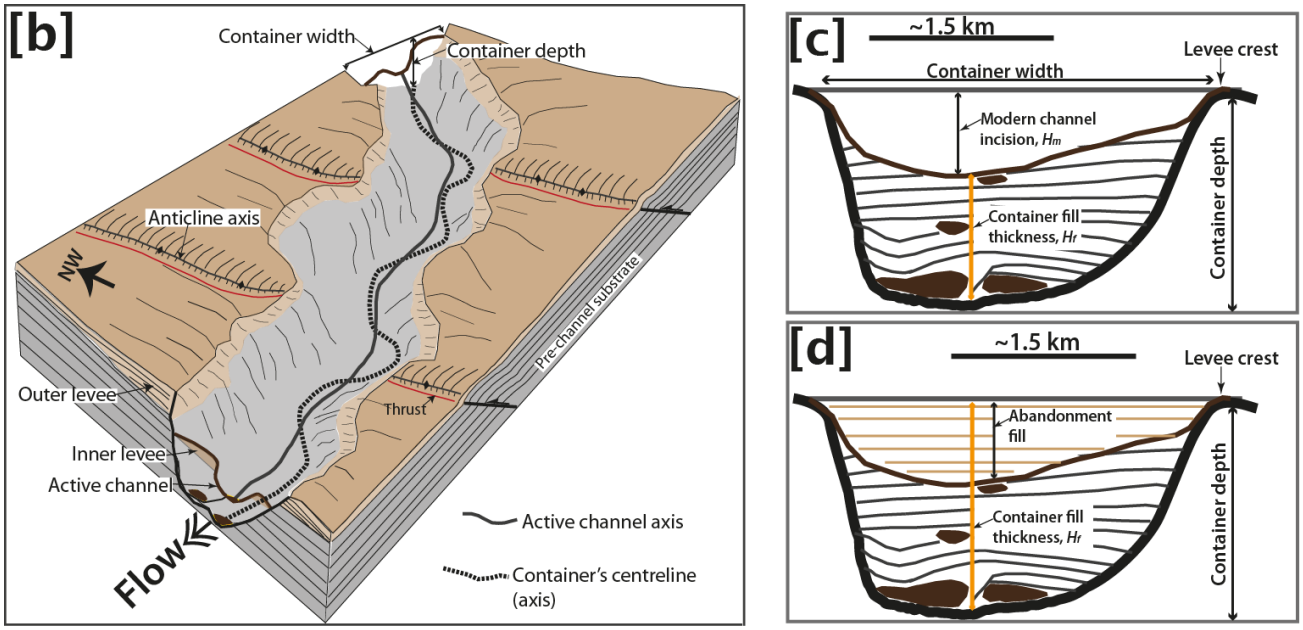


Figure 5.2: (b) Shows a 3D sketch representing the channel container across growing structures. The container centreline is an arbitrary line defining the central axis of the container and represents the locus along which the container profile was extracted. (c) and (d) Illustrate the methodology of measuring channel system parameters which include; the container depth, the modern channel incision depth and the preserved container fill thickness.

5.3 RESULTS

In this section, I present the results of the container mapping, followed by the container fill thickness maps and their spatial relationship to major seabed structures in order to analyse the structural effect on container geometry. I then present the results of the container longitudinal profiles and that of their associated modern channels in order to facilitate comparison. The longitudinal profile section is further divided into two sub-sections, the first of which concerns the containers whose associated modern channels are still active. Here the profiles were directly compared in order to analyse the effect of underlying growing folds to changes in both the container and the modern channel profiles, and the knock-on effect on the evolution of the preserved container fill at locations where structural growth has occurred. Secondly, an analysis of buried containers whose associated modern channels are no longer active is presented.

5.3.1 Container interaction with growing structures

A 3D view of the mapped channel containers is shown in Figure 5.3a, and their spatial relationship to major structures with seabed relief (Folds A – D), can be observed in the RMS amplitude extraction depicted in Figure 5.3b. These containers comprise those in which the modern channel is still active and open at the seabed (active containers 1 – 4), and those that are buried with no modern channel at the present-day seabed (buried containers 1, 2 and 5). Active containers 1 and 2 are related to the buried containers 1 and 2 because for the majority of their extent, they are contained within the equivalent buried containers and were clearly part of those composite cut-and-fill channel systems (Fig. 5.3b). Therefore, these containers have been mapped largely as 'sub-containers' within buried containers 1 and 2. In the northern part of the map, active container 1 (initially a separate container) joins with buried container 1 (Fig. 5.3b). Likewise, at the tip of Fold C, active container 2 separates from its buried counterpart, and flows into active container 1 (Fig. 5.3b). Active container 4 and buried containers 1, 2 and 5 are relatively older, and based on the position and estimated age of the downlap surface of the earliest levees associated with these containers (see Fig. 5.2a), it is estimated that these containers started to develop between 1.2 and 1.3 Ma. However, active containers 1, 2 and 3 are relatively younger with age of development that may be less than 1 Ma. The overall flow direction of these containers is from northeast to southwest.

The details of the interaction of these channel containers with structures affecting channels pathways and/or geometry is illustrated in Figure 5.4. This shows the contoured-thickness map of the channel containers with respect to folds and thrusts that have seabed relief (red colour

structures), or folds and thrusts that have been truncated by the channel containers (black colour structures). Figure 5.4a shows only the active channel containers, while Figure 5.4b shows all containers, including those that are buried. The white dotted lines in Figure 5.4b show the outline of the active containers 1 and 2 with respect to their buried counterparts. Section lines a, b, c and d cross the active container 4 (Fig. 5.4a), and are shown in Figure 5.5. Section lines i, ii, iii and iv cross buried container 2 (Fig. 5.4b), and are shown in Figure 5.6. In this section, a qualitative spatial description of the thickness maps is presented. A quantitative description of the variation of down-system container thicknesses as a function of down-system distance is presented in section 5.3.4.

A key point from Figure 5.4 is that the overall thickness distribution within the individual containers varies markedly, both across each of the containers, and down-system as the channels cross structures. For instance, fill depth varies from 0 m on the container edges (yellow colours) to about 400 m in the centre of the containers (dark purple colours). Active containers 1 and 2 have overall lower thicknesses (red hues); and the highest thickness is observed in buried container 2 (purple hue). In detail, active containers 1 and 2 have average container fill thickness, H_f of about 75 m and 80 m respectively (Fig. 5.4a) and they have relatively narrow widths (<1000 m) because they represent the younger flow paths of active submarine channels. For active container 3, which initiated in relative terms earlier than active containers 1 and 2, the average width and thickness is ~1800 m and 120 m respectively. Generally, for the younger containers (active containers 1, 2 and 3), the width remains relatively constant down-system, and there is often a slight decrease in the average thickness (the quantitative details are shown in section 5.3.4) where these containers cross active structures (Fig. 5.4a). This lack of systematic change in width is a common characteristic that was also observed in the recently active (modern) seabed channels in the study area (see chapter 4). However, for the older, active container 4, there is a much clearer relationship between the time-integrated container fill thickness and the container width. In this case, where this channel cuts across active structures, the container map shows both a decrease in the width of the container and a reduction in the time-integrated thickness of the container fill (Fig. 5.4b). For example, the most obvious change occurs in an area where the channel crosses over Fold E (Fig. 5.4b). Here the container narrows its width from an upstream-average of 2500 m to a width of less than 1600 m; the thickness also decreases from ~250 m (light-blue to blue hues) in the upstream and downstream parts of Fold E to greenish hues (~160 m) over the fold where the container narrows.

For the buried systems (buried containers 1, 2 and 5), a similar decrease in container width and fill thickness is also observed over active structures (Fig. 5.4b). For example, in buried container 1, the width decreases from an average of 1400 – 1600 m to 900 m over Folds B and J (Fig. 5.4b). In the

same area, the thickness decreases from an average of 180 – 200 m to less than 100 m (reddish colours). Buried container 2, which has been diverted for about 20 km parallel to the axis of the growing Fold C, eventually cuts through this broad fold close to its tip where other minor structures (Fold G, F and a strike-slip fault) also occur (Fig. 5.4b). Over this area, the channel width and the container fill thickness shows an obvious decrease. The average width of container 2 prior to incising across Fold C is ~5000 m but it reduces to ≤2000 m over the structure, and widens again to more than 4000 m in the downstream part of Fold C as it bends round the structure (Fig. 5.4b). Moreover, the average fill thickness upstream of Fold C is 300 – 320 m (dark blue hues), but reduces to 180 – 200 m over the structures (light blue-green hues). Further downstream, buried container 2 also narrows its width to 2800 m, and thins its fill (from an average of 380 m to approximately 320 m) on crossing Folds J, B and E towards the southern part of the map (Fig. 5.4b). For buried container 5, the average width is 2100 – 2200 m but this decreases to an average of 1100 – 1300 m between Fold D and Fold B, and over Folds A and H (Fig. 5.4b). In addition, the fill thickness also decreases from an average of 200 m (light blue colours) to a minimum of ~160 m (greenish colours) over Fold A (Fig. 5.4b). These results demonstrate that long-lived but buried submarine channel systems show obvious width narrowing and a decrease in container fill thickness in response to on-going structural growth since the Pleistocene.

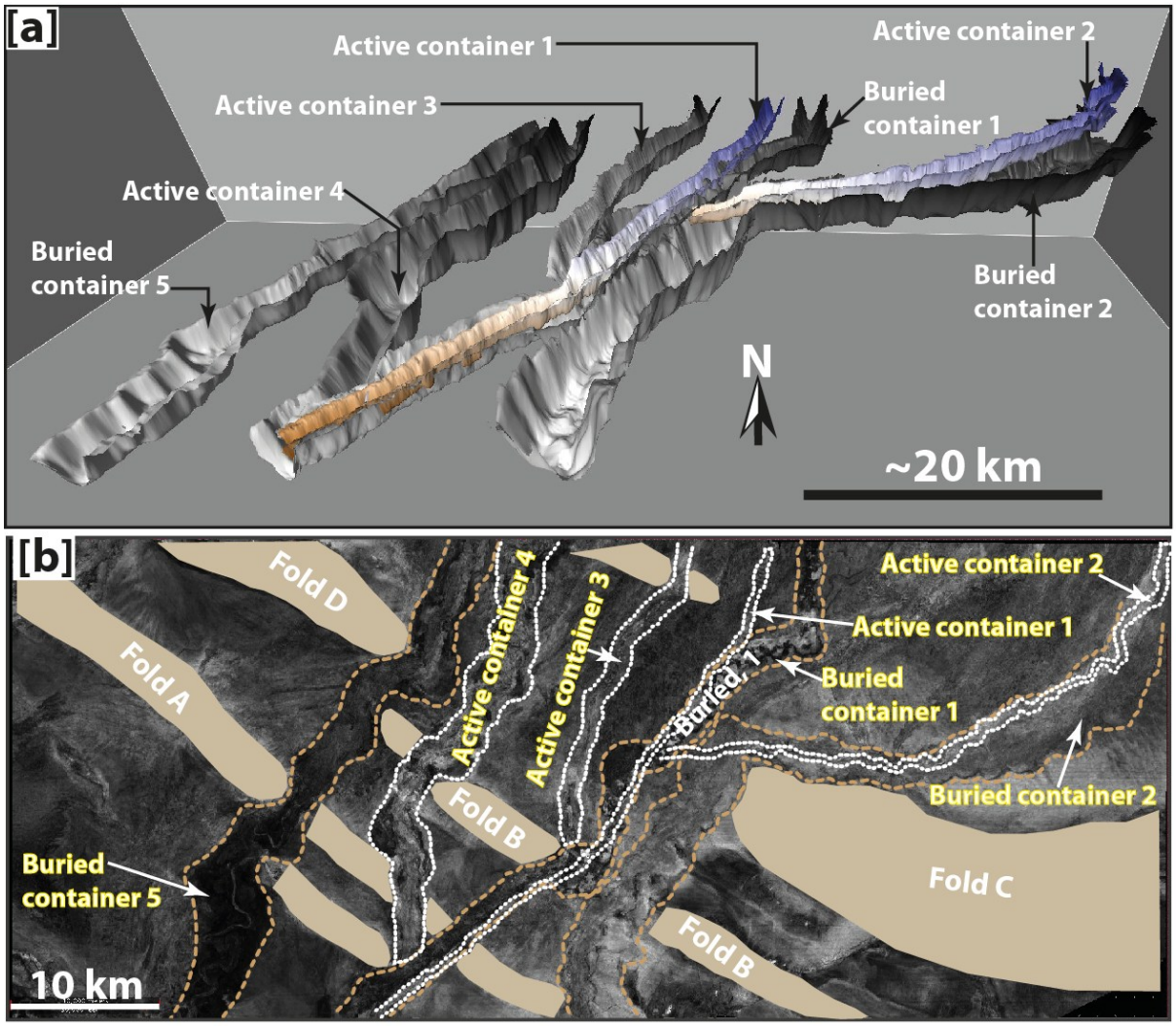


Figure 5.3: (a) Shows the 3D perspective view of all the mapped channel containers including those that are buried (buried 1, 2 and 5); (b) shows an RMS amplitude map calculated using a 100 ms window, shifted from the seabed by approximately 150 m. The RMS map cross-cuts stratigraphy and structures; which make it easier to see both the buried channels and structural trends. Note how 'active; containers 1 and 2 are largely coincident with their buried counterparts.

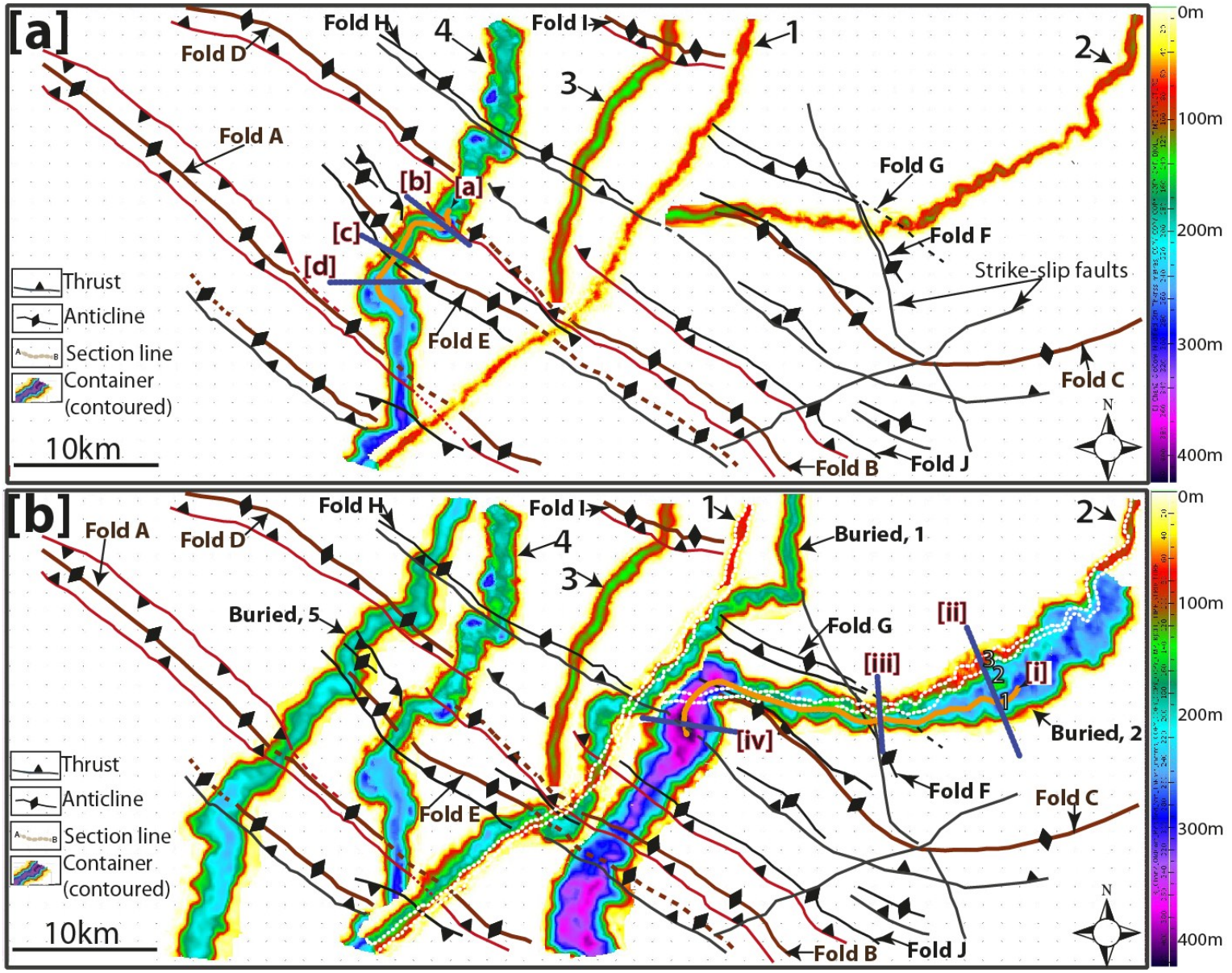


Figure 5.4a: Map showing growing structures (folds/thrusts) with seabed relief (red) or, truncated by submarine channels (black). Also shown on this map are the time-integrated container fill thickness maps of active channel containers (active containers 1, 2, 3 and 4). Note the presence of oblique strike-slip faults in the east of the map across Fold C. Section line [a], [b], [c] and [d] across container 4 are shown in Figure 5.5.

Figure 5.4b: The same map and structures as in Figure 5.4a, but with the thickness maps of the buried containers (buried 1, 2 and 5) added. The white-dotted lines represent the outlines of active containers 1 and 2 shown in Figure 5.4a. Section line [i] [ii], [iii] and [iv], across the buried container 2 are shown in Figure 5.6. Note the obvious narrowing of containers width and the decrease in the fill thickness of containers over active structures.

5.3.2 Seismic expression of channel containers

Seismic sections across the channel containers illustrate the geometric changes in both the active and buried containers, and the relationship of these responses to the underlying structure (Figs. 5.5 and 5.6). Figure 5.5 shows section line [a] along active container 4 where it crosses Fold E, along with three transects, across the same container (sections [b], [c], [d]; plan-view locations of these shown in Figure 5.4a). Figure 5.6 shows section line [i] along buried container 2 where it crosses Fold C, and three transects, [ii], [ii] and [iii] across the same channel (section locations in Figure 5.4b). The along-channel section reveals a generally linear to slightly convex profile for active container 4, represented by the yellow line (container profile, Fig. 5.5a). In Figure 5.5a, the stratigraphic horizons that occur below the container profile represent the pre-channel substrate, and have been clearly truncated at the base of the container profile due to the time-integrated channel incision over Fold E. The stratigraphic horizons that occur above the container profile represent the preserved container fill (Fig. 5.5a). The discontinuous high amplitude reflections within the fill are parallel to the container profile (indicated by the red arrow-heads), and represent the erosional surfaces of successive cut-and-fill sequences through time (Fig. 5.5a). The presence of buried erosive surfaces suggests that there is, overall, a down-system tendency for channel-fill aggradation, including over fold crest areas where there is high relative channel incision today. Transects upstream [b], and downstream [d] of fold E, reveal active channel widths of approximately ~2600 m and 3000 m respectively, measured within these containers at the top of the preserved fill (Fig. 5.5b, d). However, the middle transect [c], lying over Fold E shows a narrower width of approximately 1700 m (Fig. 5.5c). These widths measured from seismic sections, are similar to the averages revealed along-container 4 in Figure 5.4. Similar width narrowing has been reported by Mayall et al. (2010) for buried channels that cross an active structure in the Gulf of Mexico.

The along-container section does show a decrease in the time-integrated thickness of the container fill over Fold E as modern channel incision continues (Fig. 5.5a). Moreover, high time-integrated channel incision into the underlying pre-channel substrate, coupled to structural growth is clearly seen in the vicinity of Fold E. This is shown by the truncation of horizons HA and HB (green and orange reflectors, Fig. 5.5a) against the base container profile (yellow, Fig. 5.5a). Nevertheless, despite this on-going channel incision and erosion, it is important to stress that the overall depositional sequence within the container is broadly aggradational over time (Fig. 5.5a; see Mayall et al., 2006 and Kolla et al., 2007).

For the buried containers, similar channel responses to tectonic perturbation are also observed in seismic sections. Figure 5.6(i) shows a transect along buried container 2, where it interacts with fold C, including three transects [ii], [ii], [iv], the locations of which are shown in Figure 5.4b. It is notable that the base of this older buried container system has a longitudinal profile that is convex in the vicinity of fold C (Fig. 5.6 – i). There is also an obvious increase in the time-integrated channel incision into the pre-channel substrate over the crest of Fold C, which has resulted in deep incision into the pre-channel substrate and the complete removal of horizons H1 and H2 over the fold crest (Fig. 5.5). Just like in active container 4, the container fill shows a reduction in thickness over the fold crest in areas affected by modern channel incision; and the container fill is also characterised by high amplitude reflections, sub-parallel to the container profile (arrowed on Fig 5.6 – i), representing the surfaces of successive cut-and-fill sequences, some of which are unconformable with each other, as the system aggrades through time. There is considerable variation in the container geometry down-system. Transects [ii] and [iv] which are located off the crest of Fold C (Fig. 5.6 – i), have large widths (~4900 m), but the container width is narrowed by a factor > 2 (~2150 m) in transect [iii] which is positioned on the flank of Fold C where modern channels cut-through (Fig. 5.4b). At this position of transect [iii], the individual channel cut-and-fill events have largely remained in the same position through time, and younger channels re-incising in the same position (Fig. 5.6 – iii). It appears that the container widening visible in transects [ii] and [iv], is due to continued channel migration. For example, in transect [ii], the shift is in a northwest direction (from position 1 to position 3 where the present-day active channel 2 is also located (Fig. 5.4b; Fig. 5.6 (ii)). Significantly, this process has resulted in a larger container width, relative to depth, through time.

More evidence for channel deflection and lateral migration in buried container 2 is shown in Figures 5.7 and 5.8. In Figure 5.7, the edges of buried channels and buried structures can be seen in the RMS amplitude map. For example the edges of buried container 2 depicted by the brown, yellow and white dotted lines (Ea, Eb and Ec), and the structural trend of Folds B and J (which are also shown in Figure 5.4) are very clear on the map (Fig. 5.7b). Two sections across buried container 2 are used to demonstrate gradual shift in buried channel 2 as it responds to fold growth through time (Fig 5.8). The section in Figure 5.8a is located where the buried container bends around the tip of Fold C. In this area, the container develops off the crest of Fold C, and in the early phase of its development (lower part), the channel migrates laterally from east to west (i.e., from position 1 to 5, Fig. 5.8b). As the channel reached position 5, which is away from the structure it aggraded vertically (dotted yellow lines) before migrating eastwards. During this time of migration to the east, the channel system developed by both lateral and vertical aggradation, and was also associated with the development of levees that appear to offlap each other as the channel migrates (Fig. 5.8b). The

channel was temporarily abandoned and draped with low amplitude, continuous, uniform thickness seismic reflections that are likely to be pelagic drapes (see Droz et al., 2003; Possamentier and Kolla, 2003). Channels that developed after this temporal abandonment were largely unconfined (Fig. 5.8b).

In a similar way, for the section further south along the buried container (marked in Fig. 5.7 and shown in Fig. 5.8c, d), more evidence of westward shift away from the tips of growing structures (e.g., Folds B and J; Fig. 5.7b) can be discerned. Here, the eastern edge of the container is clearly imaged and labelled [Ea] in Figures 5.7b and 5.8d. Over time, this container edge appears to have migrated westward to positions [Eb] and subsequently to position [Ec] (depicted by yellow and white dotted lines in Figure 5.7b). Away from these active structures, the channel remained in the same position and developed dominantly by vertical aggradation. Successive levee offlap is also seen as the channel migrates in a westward direction. In both sections, levees on the eastern side of the channels have been uplifted, as structures to the east of the channel continued to grow (Fig. 5.8b, d; see also Clark and Cartwright, 2011). However, the levees to the west of the channel, which were deposited away from the growing structures, are not deformed and appear to downlap onto a horizontal surface (e.g., Fig. 5.8b). In summary, these two sections show that the process of gradual and continued channel shift away from growing structures over periods of approximately 1 – 1.3 Ma (based on age estimates of the downlap surface of the earliest levees; Fig. 5.8, and Fig. 5.2a), may lead to container widening and aggradation through time. However, where the channel continues to cross over an active structure, then channel incision and narrowing will dominate, and the preserved time-integrated container fill will be relatively thinner (e.g., Figs. 5.5 and 5.6).

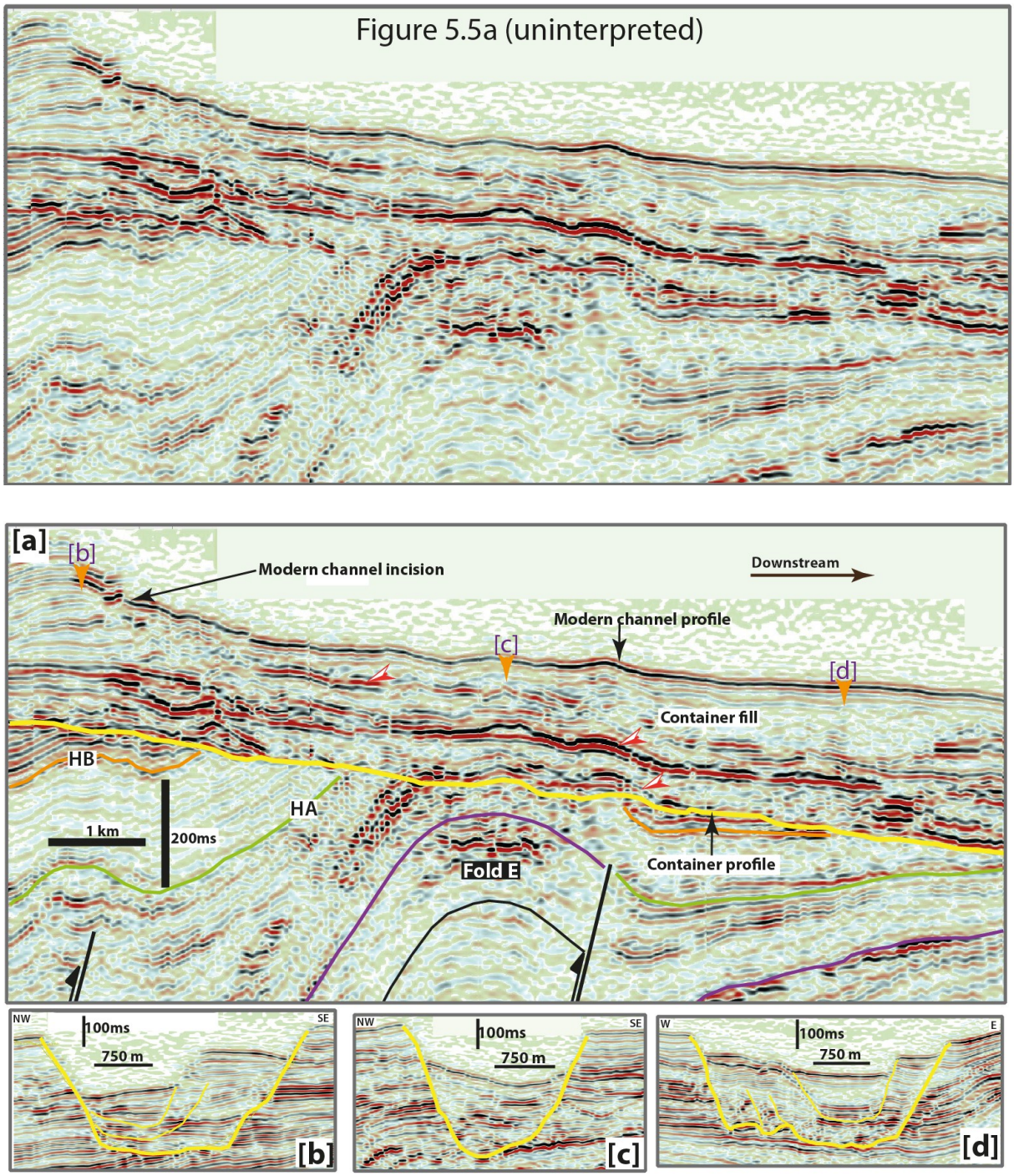


Figure 5.5: (a) Seismic section along-active container 4; (b), (c) and (d) are transects across the same container (see section locations in Fig. 5.4a). The along-channel section shows deep incision (yellow line – container profile) into the pre-channel substrate and across growing Fold E. The section also reveals slight thinning of the time integrated container fill over Fold E. Transects [b] and [d] located upstream and downstream of Fold E reveal much wider container geometry compared to a more narrowed container revealed by transect [c] located on the crest of the fold. Note the presence of high amplitude seismic reflections (erosional surfaces) parallel to the container profile.

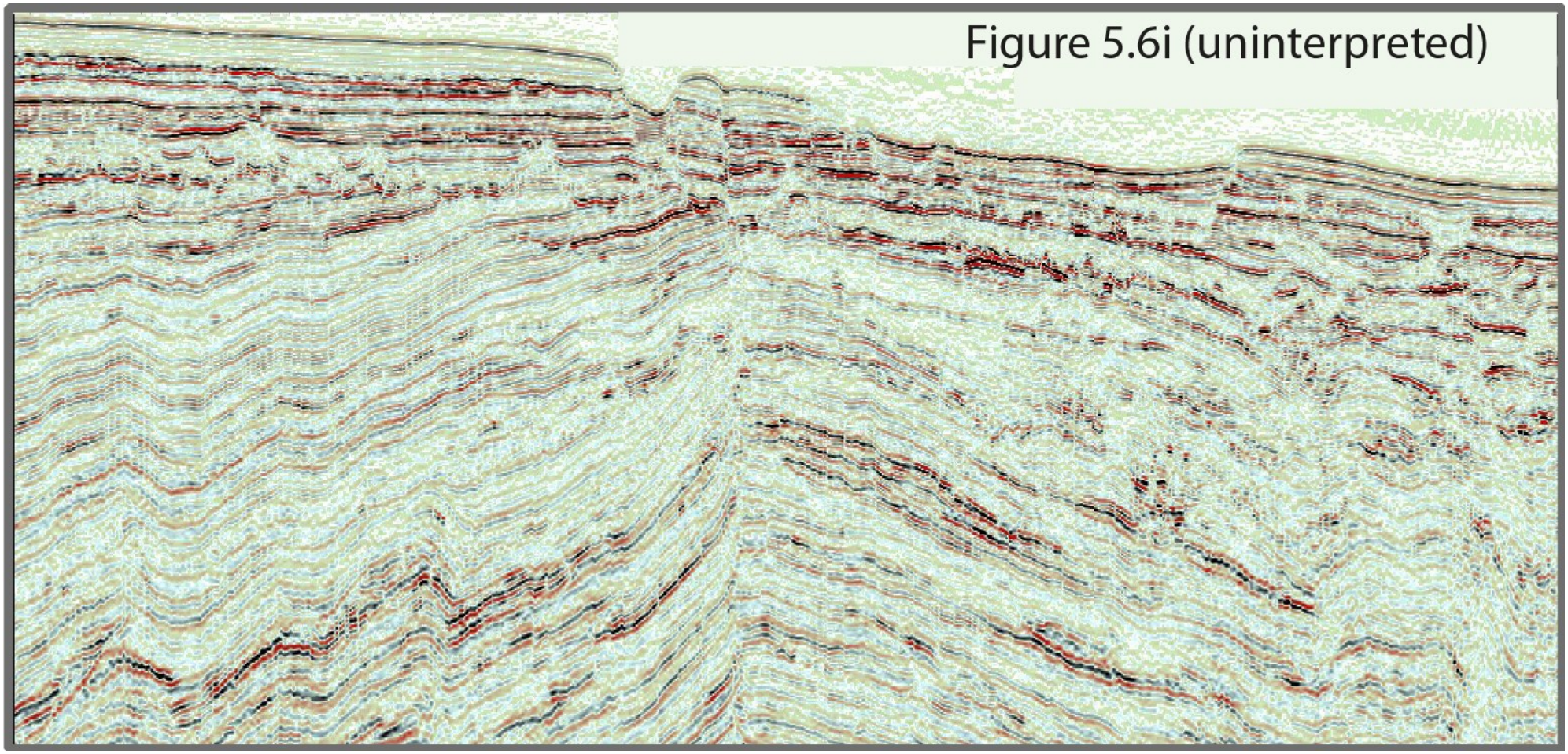


Figure 5.6i: Uninterpreted seismic section along-buried container 2. (Interpretation and transects are shown in next page)

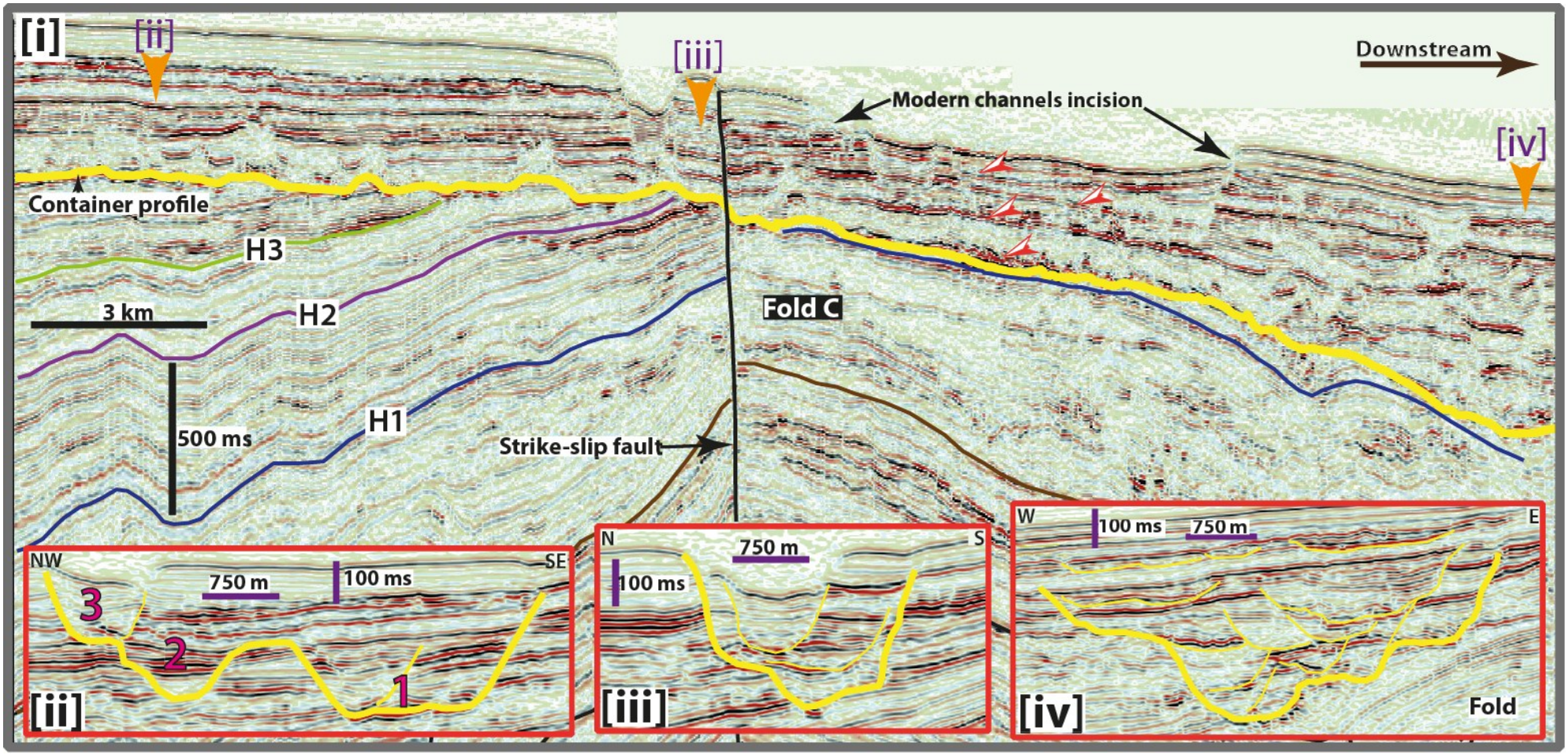


Figure 5.6: (i) Seismic section along-buried container 2; (ii), (iii) and (iv) are transects across the same container (see section locations in Fig. 5.4b). The along-container section shows deep incision (yellow line – container profile) into the pre-channel substrate over the flanks of Fold C. The section also reveals clear thinning of the time-integrated container fill over the flanks of Fold C because of continued incision and erosion by modern channels. Transects [ii] and [iv] located upstream and downstream of Fold C reveal much wider container geometry compared to a more narrowed container revealed by transect [iii] located on the flanks of the fold. Note the convex nature of the container profile and the high amplitude reflections of the preserved erosive surfaces of previous flows which are parallel to the container profile.

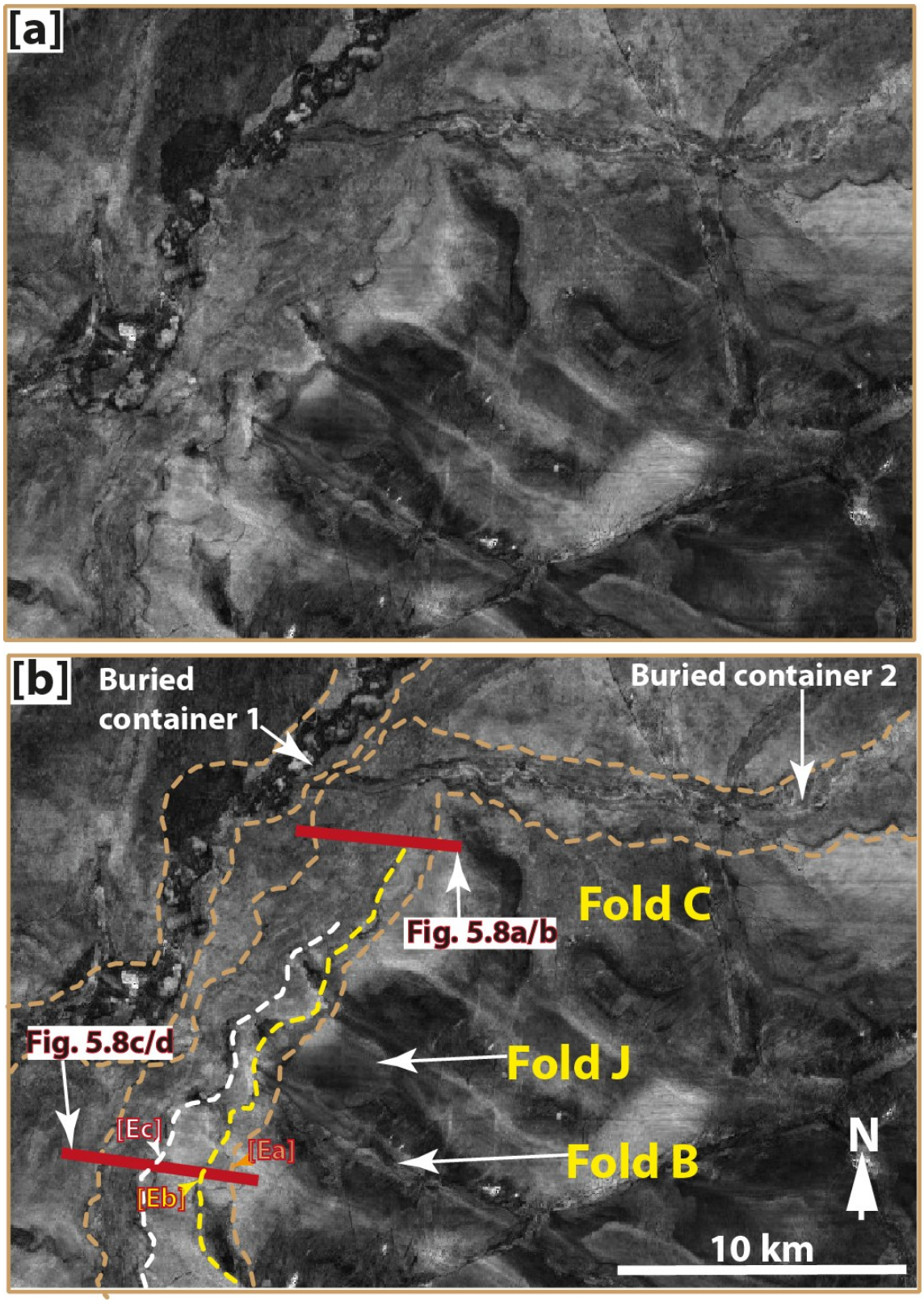


Figure 5.7: (a) and (b) Un-interpreted and interpreted version of a part of the RMS amplitude map shown in Figure 5.3b (see amplitude window in Figure 5.8c). Location of buried containers 1 and 2 shown and two sections located along buried container 2. The dotted yellow and white lines represent the westward shifts of the channel eastern edge through time.

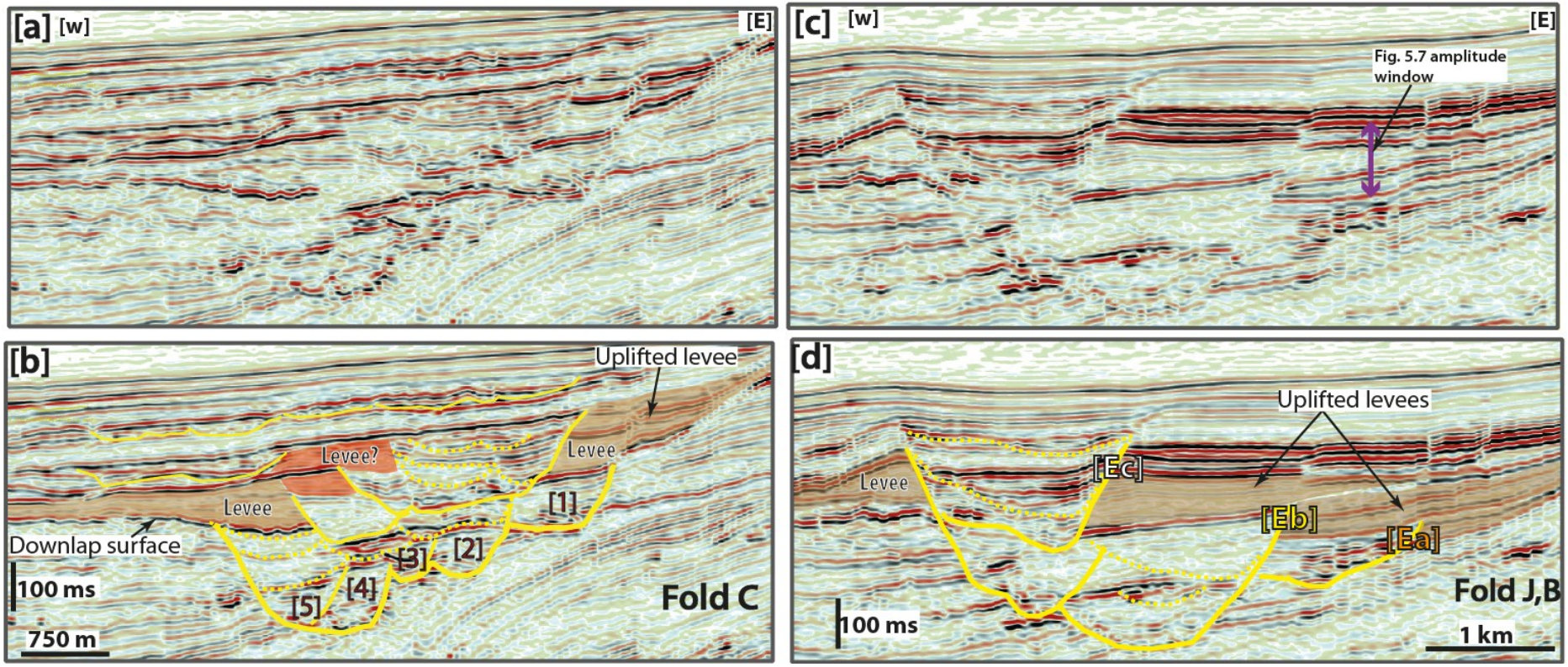


Figure 5.8: (a); (b) Un-interpreted and interpreted seismic section across buried container 2 (see location in Figure 5.7b). Note that this section shows channel migration from the east to the west from position 1 to 5 in its lower part, and overall lateral/vertical aggradation in the middle to upper part. (c); (d) Un-interpreted, and interpreted version of the section located in the southern part of buried container 2 (Fig. 5.7b). Note that this section shows channel migration from the east to the west as structures located east of the channel grow, followed by vertical channel aggradation.

5.3.3 Comparison of container and modern channel profiles

The results presented in chapter 4 show that the modern channel thalweg-profiles (Z_m) in the study area are linear to slightly concave, observations which complement previous studies of submarine channel profiles in the Niger Delta and elsewhere (e.g., Pirmez et al., 2000; Deptuck et al., 2007; Covault et al., 2011). However, a key question is how the time-integrated geometry of the container thalweg profiles compares to recent channels in the Niger Delta toe-thrust zone. In Figure 5.9, modern channel profiles, Z_m (labelled M1 to M4) have been plotted together with the profiles, Z_c of both active containers (labelled A1 to A4) and buried containers (labelled B1, B2, B3) for the purpose of comparison. Because these profiles differ in their depth range and down-system lengths, to facilitate comparison, they are normalised by their depth range and maximum down-system distance (Fig. 5.9). The shapes of the normalised profiles are distinct, and are clearly differentiated between the modern (active) channel profiles (dashed purple colour), the active container profiles (green) and the buried container profiles (black).

The modern channel profiles are generally linear to slightly concave-up, while the active channel container profiles are generally linear to slightly convex in nature (Fig. 5.9). The only exception is the active container 3 profile, *A3* which has a concave shape similar to its modern channel profile, *M3* (see Fig. 5.10a). This relatively young container has been affected by recent structural deformation without a commensurate incisional response (*cf*. chapter 4). In contrast, all the buried containers have profiles that are much more convex and also irregular (e.g., buried container 2 profile, *B2;* Fig. 5.9). Overall, these profiles have average gradients that are approximately 0.9^{o} to 1^{o}, and variations in gradient along individual profiles (up to maximum of 5^{o}) occur at underlying thrust and fold locations (*cf.* chapter 4; Deptuck et al., 2007).

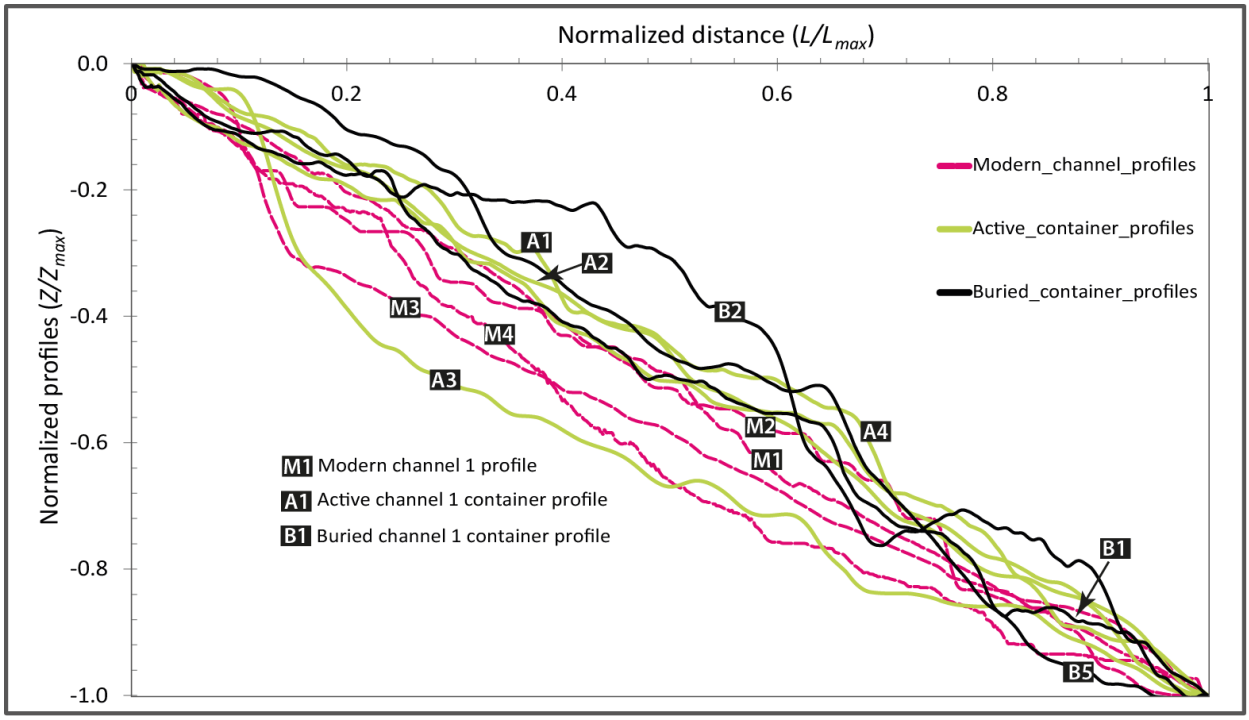


Figure 5.9: Normalised modern channel profiles; and the active container, and buried container profiles. The modern channel profiles are linear to slightly concave. The active container profiles are linear to slightly convex, except one – that of active container 3 which is concave because it is relatively younger and have been recently deformation (see chapter 4). The buried container profiles are more convex due to continued deformation even after abandonment.

5.3.4 Active containers: profile, gradient, width and depth

Here the cut-and-fill systems associated with channels 3 and 4 are used to describe quantitatively, the responses of active containers to on-going structural deformation (Fig. 5.10). The choice of channel 3 (Fig. 5.10a, c, e) and channel 4 (Fig. 5.10b, d, f) allows a direct comparison of the responses of the containers to tectonic perturbation to those of the associated modern channels, since these container systems still have modern channels within them that are active (*cf*. Fig. 5.2a). The modern channel bathymetry, Z_m and the container bathymetry, Z_c are shown in blue and red colours respectively as a function of downstream distance, and their respective gradients are shown in black and green (Fig. 5.10a, b). The container widths, W_c and depths, H_c are shown in black and pink (Fig. 5.10c, d). The modern channel widths, W_m (black) and modern channel incision, H_m (green) are shown in Figure 5.10e and Figure 5.10f. As described above, both the modern channel profile and the container profile in the younger channel 3 have very similar shapes, and their respective gradients are broadly similar except for the increase in the container gradient over Fold H (Fig. 5.10a). In comparison, the two profiles in the older (~1.2 – 1.3 Ma) channel 4 system are different (Fig. 5.10b). Here, the modern channel profile, Z_m is slightly concave while the container profile, Z_c is linear to slightly convex (*cf.* Fig. 5.9). Likewise, their gradients also differ, although they are similar in the first 20 km of the channel reach. However, the gradient of the container profile increases to approximately 2.4^{o} at 24 km and 32 km down-system near Fold E (representing a change of up to 200 %), while the modern channel gradient remains low at approximately 0.9^{o}. In all channels, localised steepening of the container gradient occurs in areas underlain by active thrusts and folds (Fig. 5.10a, b; Fig. 5.4). Moreover, the relative separation between the modern channel profile and the container profile in channel 4 shows a clear reduction over the zone of active structures (Folds H, D, B, E). However, immediately upslope and downslope of these active structural zones, the separation between the container and the modern channel profiles increases (Fig. 5.10b).

Channel 3 container width and depths do not show much variation down-system (Fig. 5.10c). However in channel 4, there is considerable variation in the container width relative to depth down-system with a pattern of clear width reduction at the location of active structures (Fig. 5.10d). However, the container depth shows little variation, maintaining a fairly uniform depth (~300 m) down-system. If the modern channel incision and width (Fig. 5.10e, f), are compared to the container depth and width (Fig. 5.10c, e), we see that in channel 3, the modern channel incision and width mimics the container depth and width. For example, there is an overall increase in container depth and modern channel incision in response to Fold I growth at ~5 km along-channel distance,

though this incisional response is not commensurate with the big gradient change at Fold I location (*cf.* chapter 4). In contrast, the modern channel incision and channel width in channel 4 do not mimic the associated container depth and width (Fig. 5.10d, f). Here, there is much greater sensitivity in modern channel incision to the time-integrated growth of Folds H, D, B and E. This has resulted in a high increase in modern channel incision (Fig. 5.10f). However, the change in container depth in the same areas is relatively small (Fig. 5.10d). The overall increase in modern channel incision is also clear in seismic sections where the modern channels appear to cut into the preserved container fill at locations of active structures (e.g., Fig. 5.5 and 5.6). This suggests that over longer periods, the system is broadly aggradational such that the modern channel is often only able to incise through the preserved container fill without necessarily reaching the container base. However, this process necessarily leads to the overall reduction of the preserved container fill thickness over active structures, thereby narrowing the gap between the modern channel long profile and the container long profile (e.g., Fig. 5.10b). The difference between the modern channel long-profile relative to the container long profile in channel 4, suggests that this channel system continues to be sensitive to structural growth of Folds H, D, B and E by increasing the modern channel incision and erosion over the actively growing structures, and resulting in lower preserved time-integrated container fill thickness.

The differences between the ca. 1.3 Ma container long-profiles and the modern long-profiles could be explained by the fact that (i) the initial container long-profiles were actually much steeper in some places than the modern day channels; (ii) that the container long-profiles have been deformed by on-going structural uplift since they were formed more than a million years ago, and/or (iii) that the container thalweg is a composite of more than one channel incision event (see deptuck et al., 2007). While (iii) may play a role, the evidence suggests that explanation (ii) is important: The folds have continued to grow since 1.7 Ma (chapters 3 and 4), and I have documented that the time-integrated container fill is lower on the fold crest, despite the fact that the modern day channel incision depths are actually greater here. Moreover, the fact that successively preserved unconformities or erosive surfaces within the container fill have shapes that reflect or partially reflect the container profile (*cf.* Fig. 5.5a), further suggests that the convex nature of the container base in channel 4 is the result of long term uplift by underlying structures. Therefore, the presence of a sustained higher container profile gradient (up to 200 % change) downstream of growing Folds H, D, B and E, in channel 4 is interpreted to be a consequence of time-integrated structural uplift which has deformed the container long profile.

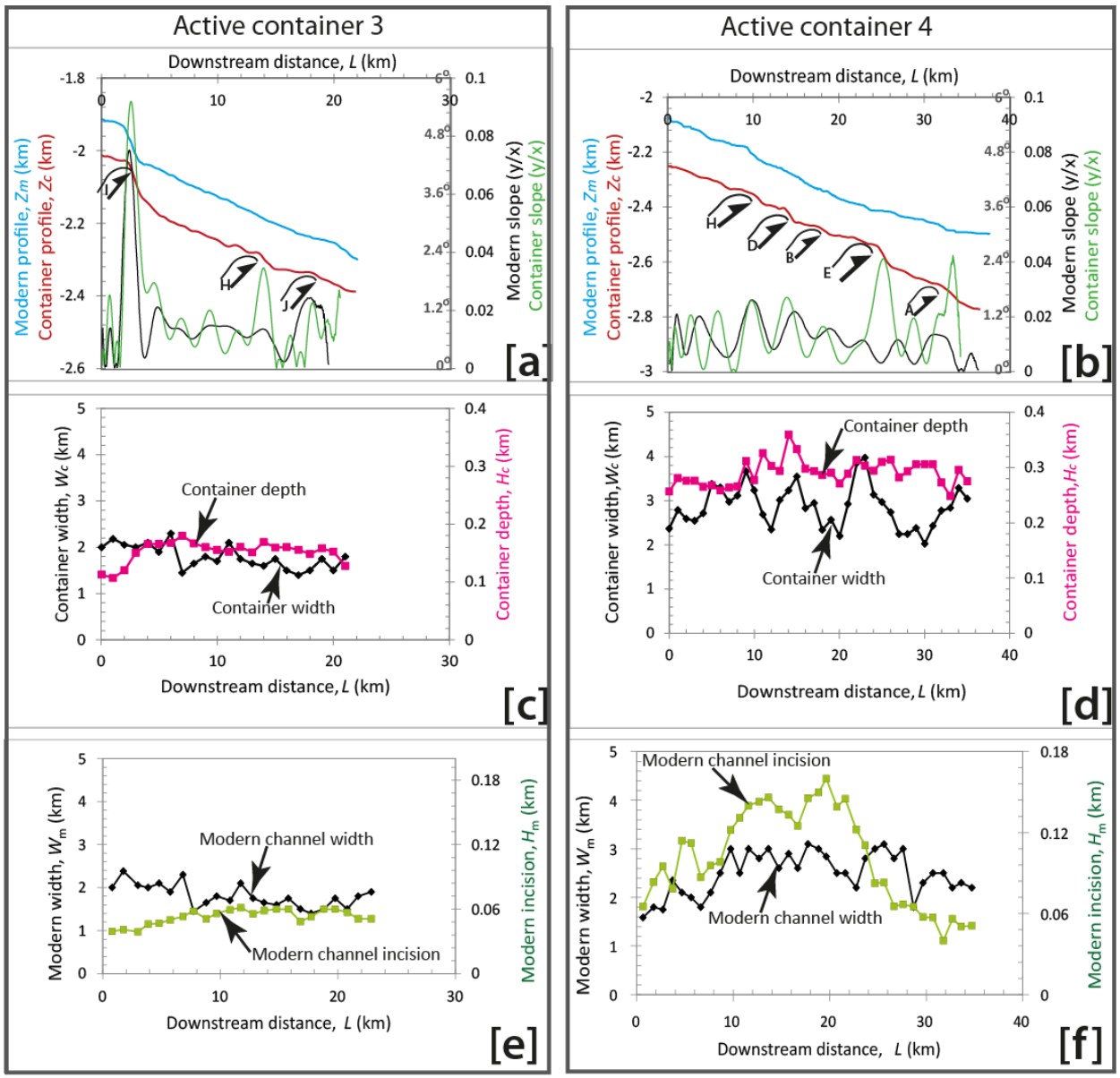


Figure 5.10: (a); (b) Graphs of modern channel profiles (blue) and their associated container profiles (red) along channels 3 and 4 respectively. The black curve is the modern channel slope and the green curve is the associated container slope in both (a) and (b). Note that variations in along-channel profiles are due to growth of underlying thrust and folds. Where channel 4 crosses active seabed structures (Folds H, D, B & E), the separation between the container profile and the modern channel profile is narrowed. (c); (d) Are graphs of container width (black) and container depth (pink) for containers 3 and 4 respectively. (e); (f) Are graphs of modern channel width (black) and modern channel incision (green) for channels 3 and 4 respectively. Note that modern channel 4 incision shows a large change over Folds H, D, B and E areas relative to the channel width.

The down-system variations in the preserved container fill, together with the container depths and modern channel incision for the active containers (1 – 4) are shown in Figure 5.11. The upper panel in Figure 5.11a shows the container depth (pink curve) and the modern channel incision (green curve) along active container 1; and the lower panel shows the same container depth (pink) and the preserved container fill (black) along the same channel. The upper and lower panels in Figures 5.11b, 5.11c and 5.11d show the same morphometric measurements along active containers 2, 3 and 4 respectively. These plots show a general trend where the container depth, H_c and modern (active) channel incision, H_m are coupled – i.e. the modern channel incision increases as the active container depth increases (continuous arrows in the upper panels, Fig. 5.11a, b, c and d). In contrast, the fill thickness of these containers decreases (dashed arrows, lower panels) as the container depth, and the modern channel incision increases. The increase in modern channel incision and the corresponding decrease in the preserved container fill in these active containers, correspond to the locations where these channels cross active structures (*cf.* Fig. 5.4). For example, the obvious change along active container 1 occurs where this channel crosses Folds B and E (Fig. 5.11a). Likewise the obvious change along active container 2 occurs where the channel crosses Folds C, F and G (Fig. 5.11b). A major structure affecting the upstream end of active container 3 is Fold I (Fig. 5.11c). However, there is no significant change in the container fill thickness in the location of this fold (between 2 and 4 km of along channel distance) because the uplift in this area is very recent (see chapter 4), and the modern channel incision in that area is still very low (Fig. 5.11c). However, there is a slight decrease in the container fill thickness (from the average of ~120 m to ≤100 m) between 10 and 12 km of along-channel distance where the channel crosses Fold H (Fig. 5.11c). The obvious change in container fill thickness and modern channel incision along active container 4 occurs between 0 km and 22 km of along-channel distance where the channel crosses Folds H, D, B and E (Fig. 5.4b). In this area, the average container fill thickness is ≤150 m (Fig. 5.11d). However, the thickness of the preserved fill increases significantly after 22 km as the channel crosses Fold E into an area with no seabed structures (Fig. 5.4b). In essence, the thickness of the fill in all active containers is approximately 50 % or less over active structures where the modern channel incision is at maximum. This suggests that areas of active structural growth are characterised by long term incision and erosion by the active channels – leading to lower preserved container fill over the crests of growing structures, despite the overall aggradational nature of this systems. As a consequence of the long term channel incision and erosion in response to continued tectonic perturbations over growing folds, the bathymetric profiles of the modern (active) channels have shapes that are linear to concave (Figs. 5.9 and 5.10b). This suggests that the linear to concave shapes of the modern channel profiles are more typical of a topographic steady-state (*cf.* chapter 4).

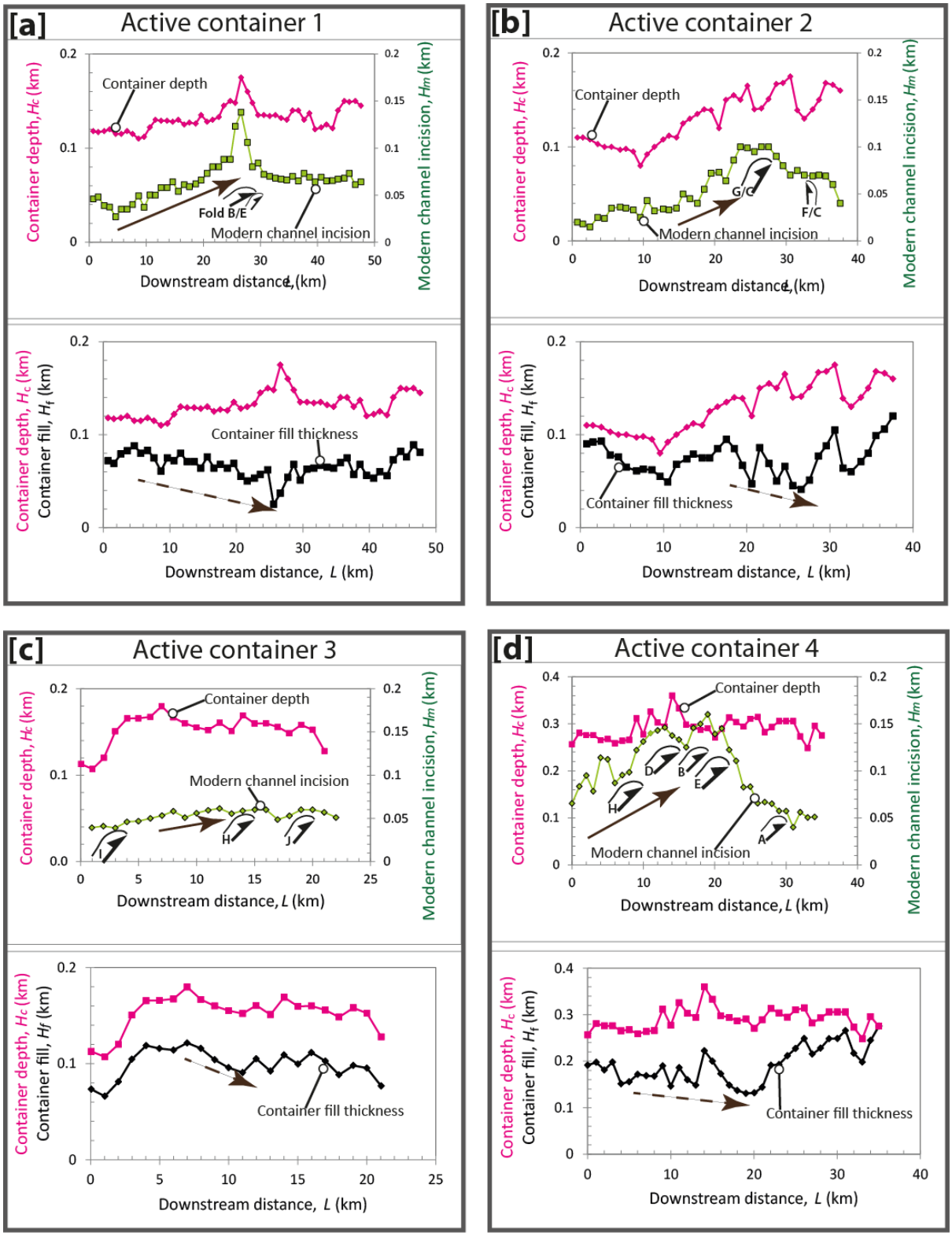


Figure 5.11: Graphs of container depth (pink) versus modern channel incision (green) down-system of active containers 1 – 4 (upper panel in a, b, c and d); and the graphs of container depth versus preserved container fill thickness (black) measured along the centre of the active containers (lower panel in a, b, c and d).

5.3.5 Buried containers: profile, gradient, width and depth

As described in section 5.3.3, the bathymetric profile, *Zc* of the older buried channel containers as a function of down-system distance, is much more convex and to some extent irregular than the active channel containers (*cf.* Fig. 5.9). For example, the profile of buried container 1 in Figure 5.12a is more irregular than that of active container 4, whose associated modern channel is still active (Fig. 5.10b). Buried container 1 gradient shows a major increase (up to 0.034 or 2.2^{o} from the background gradient that is generally less than 0.018 or 1.2^{o}) immediately downstream of fold locations downstream, which represents a change of up to 200 % (Fig. 5.12a). The first increase occurs at 12 km (downstream of the strike-slip fault and Fold G), the second major change occurs downstream of Folds H and J at 36 km and so on. Both the container width, W_c and container depth, H_c (the depth, H_c is the same as the preserved fill thickness, H_f in buried systems) of buried container 1 show an overall increase at approximately 26 km down-system where the channel crosses over Fold H, and subsequently Folds J, B and E (Figs. 5.5.12a). The channel maintains a relatively constant width and depth prior to crossing into this structural zone where both the width and depth show some degree of variation (Fig. 5.12b). This variation is partly the result of channel deflection away from growing structures, together with the fact that active container 1 continues to cut through this buried container at certain locations – leading to further width narrowing (*cf.* Fig. 5.4b). In buried container 2, the profile, Z_c shows high degree of convexity in two regions: (a) on the flanks of Fold C where Fold F and the strike-slip fault are located, and (b) over growing Folds J, B and E (Fig. 5.12c, d and Fig. 5.4b). In like manner to the active channel containers, and buried container 1, a major gradient change occurs just downstream of these structures, however, the gradient change (up to 400 %) in this container is higher than the change in buried container 1 by a factor of 2 (Fig. 5.12c). The gradient changes in buried container 5, are similar to those observed in buried container 1 (Fig. 5.12e).

There is a large increase in the width of buried container 2 over the first 20 km of the along-channel distance, and again at approximately 40 km down-system (Fig. 5.12d). Moreover, the container depth, H_c increases as the width increases from approximately 40 km onwards. However, the depth remains constant at approximately 250 m in the first 20 km where there is significant width increase (up to 5 km), and between 20 km and 35 km where the width decrease significantly in the vicinity of the Fold C structures (Fig. 5.12d). These changes in width and depths along buried container 2 are related to both channel processes and the effect of the long-term growth of Fold C (*cf.* Figs. 5.7 and 5.8). In the first 20 km of the container reach, the diverted channel has been shifted generally

northwards as Fold C has grown and expanded (this is evident by the current position of modern channel 2 indicated by white dotted lines in Figure 5.4b). This process has led to channel container widening (up to 5 km) but without necessarily increasing the overall container depth – since the channel is hardly entrenched in one position for a very long time. Between 20 km and 35 km, the channels continue to incise across the flank of Fold C which has resulted in overall width narrowing due to the increased shear-stress driven incision (Fig. 5.4b; see chapter 4). However, because channel incision (including the modern-day channel in this area) has persisted, even when this container has been abandoned and buried, the container depth does not change that much because of continued uplift by Fold C (i.e., convex container profile in Figures 5.6 – I and 5.12c). In contrast, from 35 km down-system, where the channel is truly buried (now abandoned), the channel moved westwards in a series of gradual shifts before it finally became entrenched and aggradational in a position away from the growing structure which caused the channel migration (*cf.* Figs. 5.7 and 5.8). Therefore, this gradual shift of the channel to the west, allows for both an increase in width as well as depth through time (Fig. 5.8 and Fig. 5.12d), and hence both the container width and depth from approximately 35 km down-system of buried container 2, seem to respond in tandem (Fig. 5.12d). A similar relationship between container width and depth seen in buried container 1, is observed in buried container 5 as it deflects to the tip of Fold A (Fig. 5.4b and Fig. 5.12e, f), and where it crosses Folds H, D, and E, there is variation in container width, and little variation in the overall container depth (Fig. 5.12f).

Generally, channel containers, while still active, preferentially tend to deflect to the tip of growing folds and only cut across folds if they cannot find their way around. In all containers (both active and buried) major increases in container gradient occur immediately downstream of growing thrusts and folds, and this change may be up to 200 %. However, in buried systems affected by large-scale structures (e.g., Fold C) that continue to grow even after the channel system has been abandoned (e.g., container 2), the magnitude of deformation of the channel profiles is likely to be much higher. In essence, the maximum documented change in gradient of the modern channels over growing structures is less than half of the maximum observed in the associated containers (see chapter 4). This suggests that the modern channels continue to be sensitive to tectonic perturbations and responding by increasing channel incision and hence acquiring relatively linear to concave profiles through time. On the other hand, the overall aggradation of the container systems through time means that continued fold uplift, will gradually deform the container profiles thereby making them more convex and irregular.

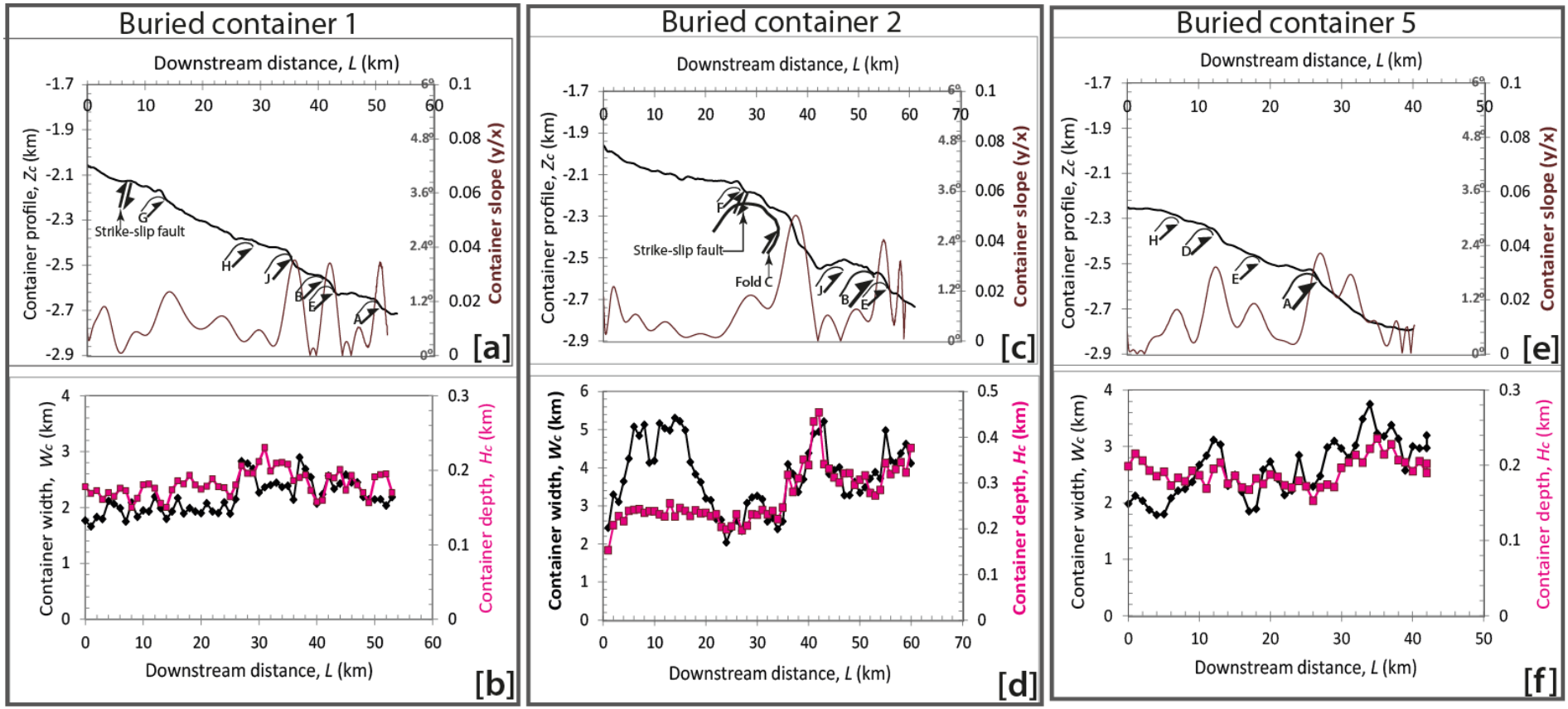


Figure 5.12: (a) Buried container 1 profile (black) and its slope (red). The profile is relatively convex to irregular due to the growth of underlying folds and thrusts; and major gradient change occurs immediately downstream of folds; (b) graph of container width (black) and container depth (pink). Note the increase, and variation in both width and depth after the channel crosses Folds H, J, B, E. (c) Container profiles (black) and slope (red) in buried container 2. Note the very convex nature of the profile over the broad Fold C; (d) Container width (black) and container depth (pink) for buried container 2. Note the high variation in container width relative to depth. (e) Shows buried container 5 profile (black) and its slope (red). The profile is relatively convex to irregular due to the growth of underlying folds and thrusts; and major gradient change also occurs immediately downstream of folds; (f) is the graph of container width (black) and container depth (pink).

5.4 DISCUSSION

5.4.1 Container evolution: a combination of tectonic perturbations and channel processes

The results presented in this chapter demonstrate that variation in container width and fill thickness is caused generally by (1) the time-integrated channel incision/erosion over growing folds – causing the container to narrow its width with an overall lower deposition/preservation of container fill over time; and (2) the process of continued channel deflection/migration away from the tip of growing structures – causing the width to increase with an overall higher deposition/preservation of container fill. Consequently, the preserved container fill is thickest off the crest of folds where the width is also larger (e.g., Fig. 5.8). This suggests that the evolution of the container system is related to both the effect of tectonic perturbation and channel incisional and depositional processes through time. For example, in Figure 5.8b, we see a trend of dominantly lateral migration to the west in the lower part of buried container 2 without levee development. This lateral migration is in response to the growth of Fold C, which means that channel widening in this lower part is mainly due to tectonic perturbations. However, as the channel moves further away from the growing fold, deposition/aggradation and levee development became dominant. These observations suggest that the development of these channel containers (valley-fill complex – Janocko et al., 2013) is due to a combination of channel processes and the effect of tectonic perturbations. Lateral migration versus vertical aggradation (Fig. 5.13a from Kolla et al., 2007) is observed in many parts of submarine channel systems, and can be attributed to different causes; in this study the response of channel 2 to the growth of Fold C shows how such a channel stacking pattern can evolve, where a channel is subjected to a tectonic perturbation.

For example, in the first 20 km along-buried container 2, the container width increased significantly but the container depth remains constant (Fig. 5.12d). This suggests that the growth of Fold C causes the diverting channel to shift continuously in a northward direction as indicated by the current position of the modern channel (dotted white line, Fig. 5.4b). This continuous shift means the channel was never entrenched in one position for a long time, and lateral migration dominates resulting in a larger container width while maintaining a constant thickness (e.g., the lower part of Fig. 5.8b; and (i), (ii) in Fig. 5.13a). However, from 35 km down-system of the along-container distance, both the width and depth increase as the channel flows round Fold C and is forced to migrate westward (Figs. 5.7, 5.8). In this area, lateral channel migration dominates in the lower part as the channel moves away from the tip of Folds B, C and J. However, the channel then become entrenched and developed dominantly by vertical aggradation. The consequence of this channel

process is that both the container width and depth increased with time. Moreover, the preserved container fill thickness is high because of lower overall channel incision relative to aggradation. However, the high channel incision relative to aggradation on the flanks of Fold C has resulted in lower container width and preserved fill between 20 km and 35 km down-system (Fig. 5.12d). In essence, these observations have shown that the cut-and-fill sequences within a channel container, and their stacking pattern is a product of both channel processes and tectonic perturbations, which in turn, determines the container width and the thickness of the preserved, time-integrated container fill. In contrast, if we assume tectonic forcing is not involved, the stacking patterns would be governed purely by channel processes, and frequently leads to what is known as compensational stacking – a tendency for sediment transport systems to preferentially fill a topographic low and then migrate laterally to fill the next available low (Straub et al., 2009). In this case, the channel system is likely to be largely unconfined because channel-levee development will dominate over channel incision and erosion, and hence an unconfined complex of leveed channel belts will form (Fig. 5.13b; Janocko et al., 2013). In essence, the combination of channel incisional and aggradational processes appears to be coupled to time-integrated tectonic perturbations produced by growing structures in the study area. These processes affect the general distribution of preserved, time-integrated channel container fill, especially in the fold crest areas where the time-integrated fold uplift is significant.

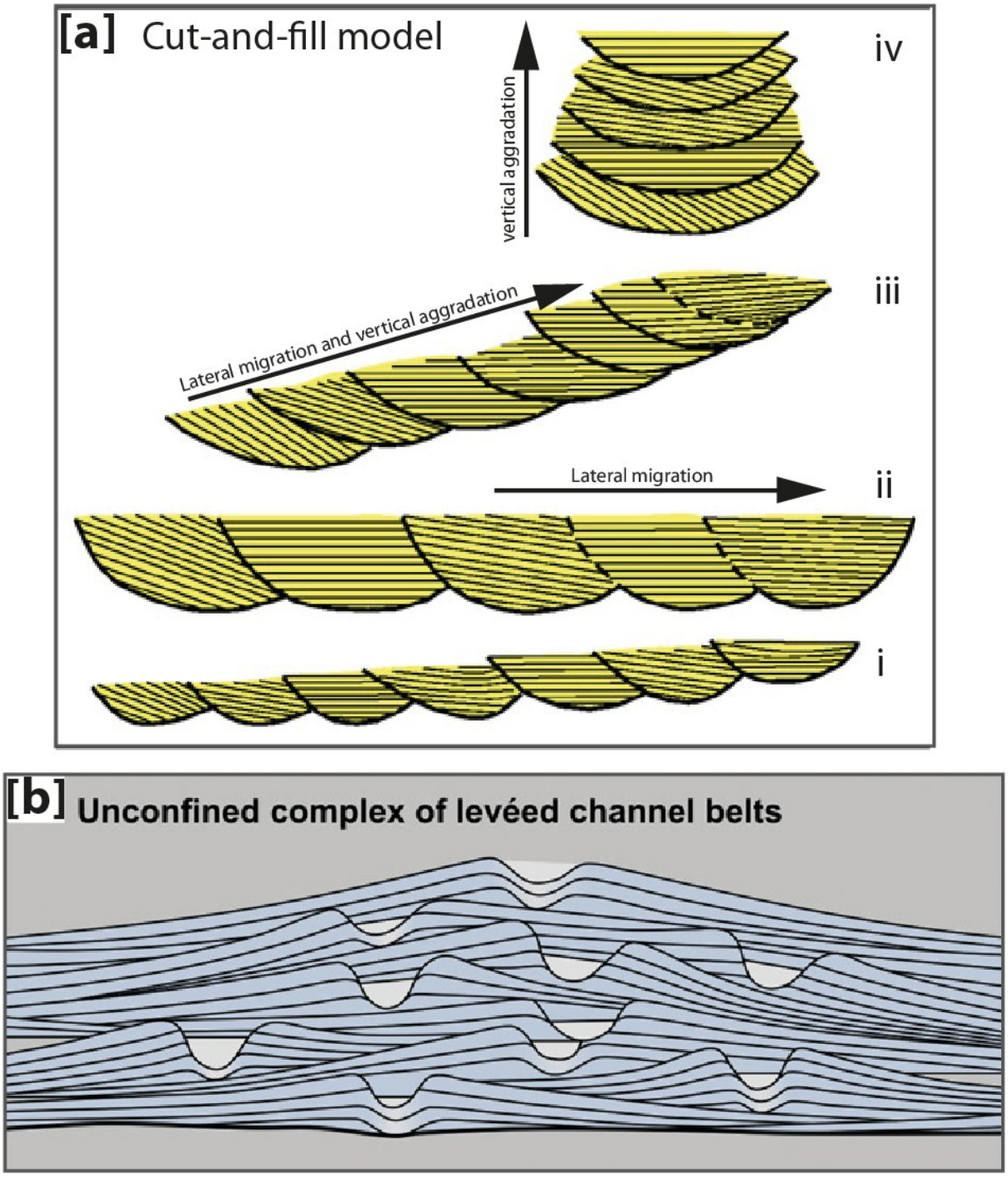


Figure 5.13: (a) Schematic diagram of stacking patterns of cut-and-fill channels within a channel complex showing lateral migration and aggradation (Modified from Kolla et al. 2007). (b) Schematic diagram of a channel-levee complex that developed purely by compensational stacking through time (from Janocko et al., 2013).

5.4.2 Fold uplift and the evolution of container fill over fold crest

Over longer periods of time (> 1 million years), the combination of active deformation and channel incisional response over the fold crest to on-going structural growth is manifested in lower, preserved time-integrated container fill thickness over the growing fold. However, modern channels associated with these containers (chapter 4 and this study) continue to incise and erode over these structures as they flow across them, and clearly cut deep into the preserved, time-integrated container fill as the folds grow. These two observations may initially seem inconsistent, but can actually be reconciled using a simple thought experiment: Let us consider an instantaneous or repeated tectonic perturbation produced by a growing fold along the channel pathway, which will deform the channel, creating a knickpoint or knickzone in the channel profile at the location of structural growth (e.g., Fig. 5.14a). At this point where uplift is occurring, elevated slopes will generate greater shear stresses and hence greater channel incison (chapter 4), creating a fill 'space' that over time would represent a time-integrate depth of incision since the channel has followed this down-system pathway (black curve, Fig. 5.14b). If this channel pathway is then temporarily abandoned, and filled with post-channel sediments as seen in many of the buried systems (e.g., Fig. 5.8), the container fill thickness over the fold crest at the time of abandonment (say 1.2 Ma) should be very high, and equivalent to the depth of 'accommodation' space created by the channel incision at that time (dash-red curve, Fig. 5.14b). We would therefore predict greater fill thicknesses on the fold crest and smaller fill thickness upstream and downstream of this. However, the results in this study obviously show the opposite trend – i.e. the preserved, time-integrated fill over the growing structure is at its lowest at the fold crest (Fig. 5.11). This is explained by the fact that over time, and assuming shortening and uplift continue (e.g., between the time of abandonment (e.g. *1.2 Ma* and today, *0 Ma*), any subsequent flows taking the same or similar channel pathway within the 'container' will erode more of the preserved fill over the fold crest, and deposit it in areas off the fold crest. The result of this is that the average container fill thickness (as opposed to the active channel incisional depth) will actually decrease through time at this structural point, while away from the fold crest (where the rate of sediment aggradation minus structural uplift is bigger) the container thickness will increase (Fig. 5.14c). Consequently, for a theoretical channel system over a period of 1.2 million years or more, the container thickness will gradually decrease near the fold crest through time. This evolution is shown schematically in Fig. 5.14c, where the present day container thickness may represent an inversion of the situation prevailing at 1.2 Ma. In summary, fold crest areas are characterized by high relative incision/erosion over aggradation, and areas off the crest of folds are characterized by high relative aggradation over incision/erosion (Fig. 5.14c). A

clear implication of this analysis (see also chapter 4) is that the depth of incision produced by the modern channel at underlying fold locations is in response to the time-integrated fold uplift and that, in principle, the magnitude of modern channel incision should approximately balance fold uplift during the current period of channel development assuming the modern channels are in a topographic steady-state (see chapter 4).

In chapter 4, analysis of absolute fold uplift on the 1.7 Ma horizon used for the shortening calculations, and the excess incision by modern channels (i.e., the increase in incision above the mean channel incision), gave values that approximately matched the fold uplift. The 1.7 Ma seismic horizon was chosen because it occurs closest to the channels incisional bases and hence assumed to broadly represent a stratigraphic horizon whose deposition, and growth can be coupled to channels developing coevally with structural deformation (see chapter 4 for details). However, since channel development began at approximately 1.2 ±1 Ma; the approximate match in excess incision produced by the modern channels to fold uplift over 1.7 Ma, shows that these channels are more than capable of keeping pace with fold uplift. Based on these findings, a conclusion was drawn that the modern channels are in a bathymetric steady-state with respect to fold uplift in the study area (*cf.* Figure 4.10 in chapter 4). With the further analyses conducted in this chapter, this conclusion can be further tested using data both from the modern channels and their associated containers. Assuming the container profiles were deformed by time-integrated uplift as demonstrated in this chapter, whilst the active channel profiles represent a topographic steady-state, a distribution of relative structural uplift down-system for the active containers can be derived. This uplift distribution can then be compared to the measured modern channel incision along each system. To do this, I assume that the (quasi-linear) bathymetric profile of the modern channel was similar to the thalweg long-profile of the container at the time of its formation, so as to derive the relative deformation of the container since ~1.2 Ma by differencing the two. Because very small differences in assumed channel pathway and gradient (as little as 0.1 degrees) can lead to significant bathymetric differences of > 70 m when considered over down-system lengths of ca. 40 km, hence, this method gives a relative rather absolute estimate of the deformation of container profile.

In this analysis, the bathymetric profile of the modern channel is shifted downward using a pinning point at the bottom end of the profile of the associated container in active channel 3 and 4 systems (pin point; Fig. 5.15a, b). For consistency, the pinning point was placed at the upper end of buried container 1 whose profile was compared to that of the modern channel 1 which is related to the buried system – so that the modern channel profile is below the container profile; nevertheless, there is a slight mismatch in the first 5 km of the down-system distance between these two profiles

(Fig. 5.15c; see also Fig. 5.4b). This method has the advantage of allowing us to estimate the distribution of apparent uplift since the time of channel development. This eliminates any uncertainty in relating fold growth measured from a particular time (say from 1.7 Ma – as per in chapter 4) to the exact timing of channel development which is generally less than 1.3 Ma.

Applying this method on the relatively well-established channel 4 system, the difference between the container profile and the associated modern channel profile is shown in Figure 5.15a. In this case, the derived along-channel distribution of apparent uplift (which is represented in 'uplift units' rather than absolute units) produces a curve that mimics the shape of the modern channel incision. The distribution of container fill thickness also shows an overall reduction in areas of both high relative uplift and modern channel incision; and increases from 35 km down-system where the estimated uplift is also low (Fig. 5.15a). The general correlation between the estimated apparent uplift and modern channel incision suggests that modern channel 4 is likely to be in a bathymetric steady-state with respect to the distribution of uplift along its path probably since this channel system began developing between 1.2 to 1.3 Ma. This may explain why the profile of modern channel 4 is slightly concave while that of the associated container is convex (see Fig. 5.10b).

However, for the relatively younger channel 3 system, the difference between the container profile and the associated modern channel profile is shown in Figure 5.15b. Here, the distribution of the modern channel incision is generally constant (at approximately 50 m). However the apparent uplift varies along the channel. Indeed, the apparent deformation and uplift of the container profile is highest in the three locations which correspond to the underlying folds (upper panel, Fig. 5.15b). This constant channel incision down-system indicates that the modern channel has not been significantly perturbed by the underlying structures during much of its existence and/or that it is more than capable of incising through these growing structures. This observation, combined with the younger age of the channel 3 (<1 Myr) system explains why the profile of the modern channel and that of the associated container have similar shapes (Fig. 5.15b).

This method can also be applied to buried container 1 where the modern channel mostly follows the pathway of the buried system (*cf.* Fig. 5.4b). Because of the slight mismatch in position of the container and the modern channel pathway, the apparent uplift in the first 5 km of the along-channel distance may not represent the real uplift units (Fig. 5.15c). However, the overall shape of the relative uplift is similar to the profile defined by modern channel 1 incision (Figs. 5.11a, 5.15c).

Generally, the along-channel distribution of apparent structural uplift derived in this study, correlates well with the down-system distribution of incision by modern channels associated with each container system with the exception of younger channel 3. Therefore, we can conclude that the total incision produced by the modern channel is of the same order of magnitude to the growth rate of the structures affecting the channel during the period of channel development. Consequently, the modern channels can keep pace with fold growth, and hence are in a topographic steady-state with respect to tectonic perturbations (see also Pirmez et al., 2000). Although, these channels can incise to keep pace with growing structures, they are also aggradational in most places due to changing channel pathways. Hence, this leads to an overall equilibrium long-profile through a combination of channel incision (in certain areas) and channel aggradation in other areas (e.g., Huyghe et al., 2004; Ferry et al., 2005). Consequently, these results suggest that the linear to concave profiles of the modern channels were produced dominantly by long-term channel incision and subsequent sediment aggradation (e.g., McHargue et al., 2011), while the slightly convex to irregular profiles of the containers are unequivocally the result of time-integrated fold uplift capable of producing maximum gradient changes of up to 400 % in the container thalweg (e.g., Fig. 5.12c). This analysis therefore demonstrates that is extremely important when interpreting submarine channel long-profiles in seismic data to distinguish carefully between active or recently active channels in which the long-profiles may record the time-integrated balance of uplift and erosion during the time period of channel activity (chapter 4), compared to the whole channel cut-and-fill system (container) thalweg, which if buried, may in fact record the time-integrated history of uplift since abandonment.

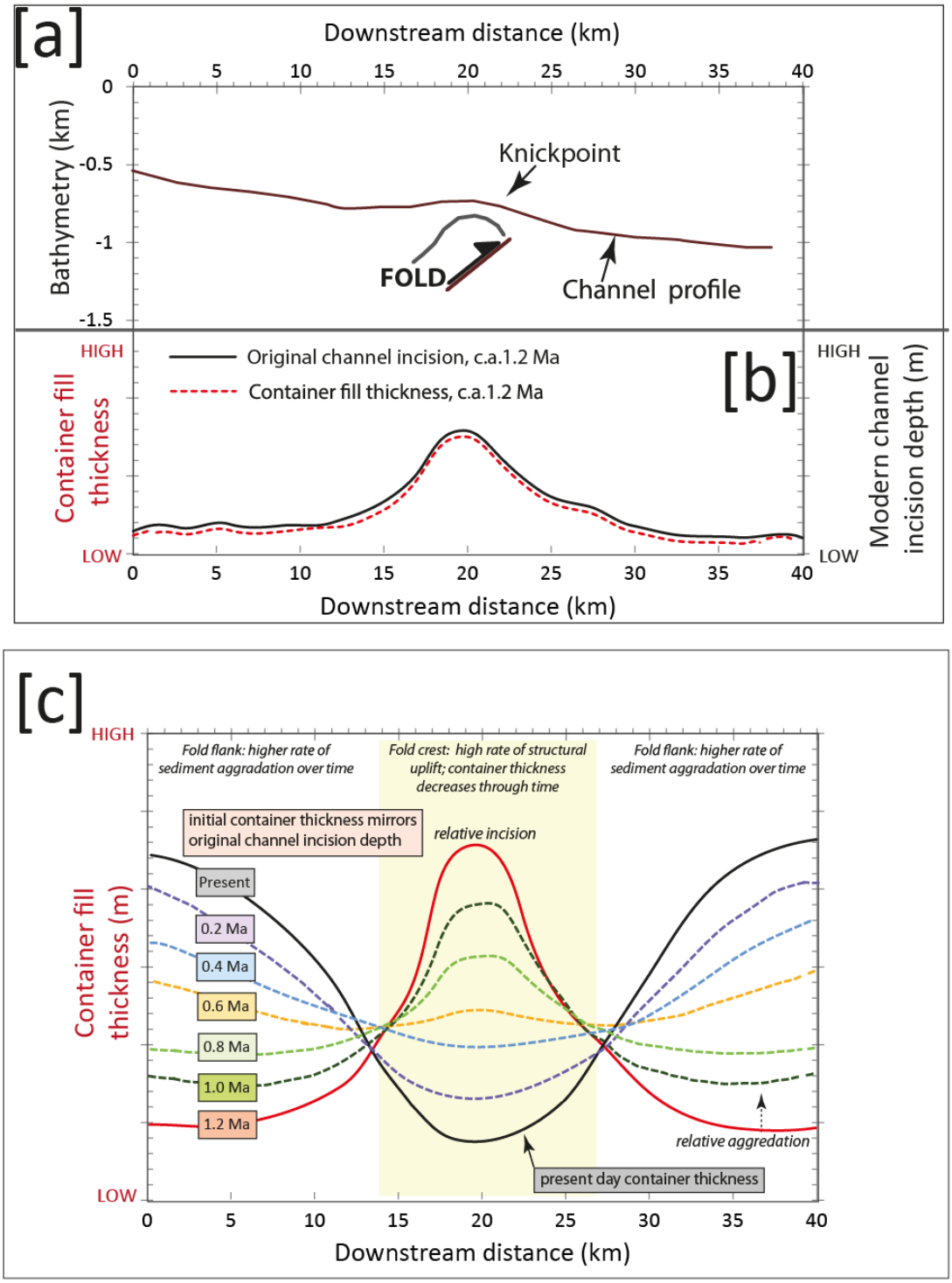


Figure 5.14: (a) Sketch of a channel profile across a growing fold, with knickpoint; (b) Black line: predicted channel incision in response to the knickpoint generated by the growing fold (in Figure 5.14a) at some time in past (e.g. 1.2 Ma); dashed red line is maximum fill of channel that could occur were channel to be abandoned; (c) Sketch illustrating the down-system variations in preserved, time-integrated container fill due to continued fold growth. Note that the bold-red line represents the modern-day channel thalweg; and significant erosion of the 1.2 Ma channel fill (dash-red line) occurred over the knickpoint area through time (from 1.2 Ma to date).

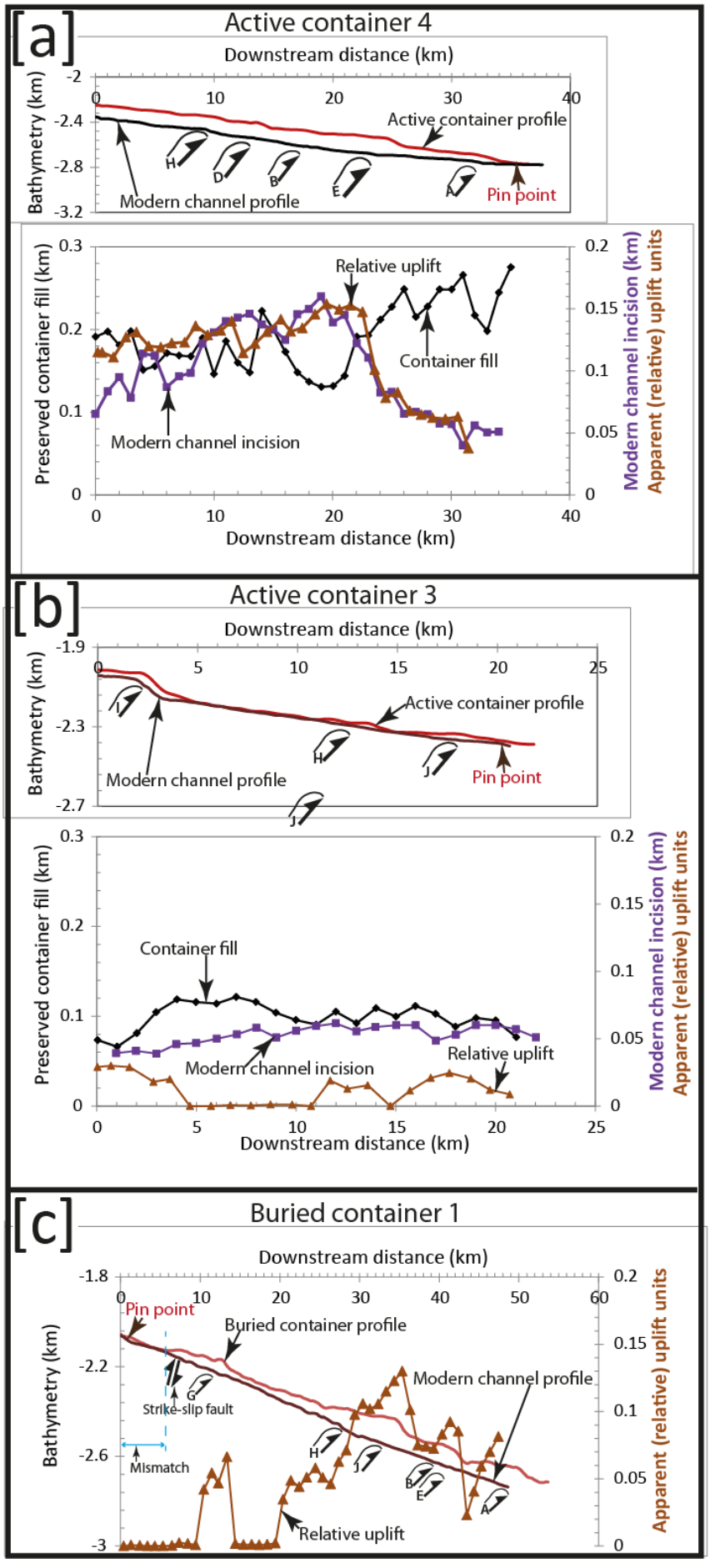


Figure 5.15: (a) and (b) Graphs of modern channel profile and container profile (upper panel); preserved thickness of the container fill, modern channel incision and the apparent distribution of uplift derived by differencing the modern profile from the container profile (lower panel) for containers 4 and 3. (c) Graph of the modern channel profile, container profile, and the apparent distribution of uplift derived by differencing the profile of modern channel 1 from the profile of buried container 1.

5.4.3 Equilibrium long-profile: modern channel versus container

Results in this study have shown that the modern channel profiles in deepwater Niger Delta are generally linear to slightly concave (see also Pirmez et al., 2000; Deptuck et al., 2007; Covault et al., 2011), while the long profiles of the containers containing active channels appear slightly convex. Those of the buried containers have a still higher convexity. Channel response to growing structures show that on-going tectonic forcing is easily recognised from the increased incision of the modern channels (chapter 4). This kind of channel process has long been reported by workers studying fluvial systems in different parts of the world (e.g., Tucker and Whipple, 2002; Whipple and Tucker, 2002, Whittaker et al., 2007a; Whittaker et al., 2008). However, unlike in fluvial settings where the equilibrium long-profile typically exhibits a concave-up geometry in which the concavity is approximately 0.5 (e.g., Hack, 1957; Howard, 1994; Whipple and Tucker, 2002; Tucker and Bras, 1998), the Niger Delta submarine channels 'equilibrium' long-profiles are generally linear to slightly concave (see also Pirmez et al., 2000; Covault et al., 2011). Assuming continuous fold uplift/growth and modern channels incision and sedimentation, then over a long period of time (>1 million years), we will expect the container profile to become slightly convex as the fold grows and the container fill gradually aggrades but thins onto the growing structure. On the other hand, we expect the modern channels to maintain relatively linear long-profiles as the channels are capable of keeping pace with fold growth. Here, an attempt is made to present a summary of this process through time (Fig. 5.16). We would expect that in a gravity system such as the Niger Delta, the onset of any structural growth prior to substantial channel development, will disrupt the seabed and create a positive relief (e.g., Fig. 5.16a), and as we have seen in this study and in chapter 4, channels will respond by increasing bed-shear stress-driven incision over the growing structure in order to restore topographic equilibrium in that location (e.g., i.e., erosive surface 1; Fig. 5.16b). If we assume the channel incision rates balance the uplift on folds and thrusts (Fig. 5.15), then by the time turbiditic flows cease along this sediment pathway, any positive relief related to fold/fault growth would have been partially or completely erased, and the channel will be temporarily abandoned and filled with abandonment channel fill and pelagic drapes (Fig. 5.16b). Therefore, the thalweg-profile of the abandoned channel will initially be roughly linear, as has been documented for the modern channel profiles in this study. McHargue et al. (2011) demonstrated that in these circumstances, channel erosion and by-pass will trigger a fall in the equilibrium profile (e.g., erosive surface 1; Fig. 5.16b); and this is followed immediately by the deposition of increasingly mud-rich sediments (e.g., channel fill; Fig. 5.16b) which causes the equilibrium profile to rise (e.g., thalweg 1; Fig. 5.16b). However, this equilibrium profile will soon be disrupted because the structures are constantly growing in a gravity-driven

system, and leading to gentle folding of the thalweg and also, of course, any erosive surface created by the previous flow events (e.g., Fig. 5.16c). The next set of turbiditic flows following the same or a similar channel pathway within the channel cut-and-fill system will work to re-establish the bathymetric steady-state between structural uplift and erosion through increased channel incision and erosion over the deformed part of the container long-profile, producing an erosive channel base within the cut-and-fill sequence (i.e., erosive surface 2; Fig. 5.16d). Depending on the erosive power of the turbiditic flows, and the duration of flows (see Pirmez and Imran, 2003; Meiburg and Kneller, 2010; Talling et al., 2012, 2013) over the growing structure, subsequent erosive surface(s) may even cut into the first erosive surface – i.e. forming a composite erosive surface (Fig. 5.16d; 5.5a; 5.6 – I; see also Mayall et al., 2006; Deptuck et al., 2007). If this process of uplift and modern channel incision/sedimentation continues, then over a million year period for example, the container fill will aggrade away from the fold crest, and will be characterized by preserved erosive surfaces that are parallel to the container profile (e.g., Fig. 5.16e, f). However, the thickness of the preserved container fill over the crest of the growing fold would be relatively low, while the container base and the modern channel thalweg will have profiles that are convex, and sub-linear respectively (Fig. 5.16f). This evolution explains both the long-profile geometries and the incision and sediment thickness distributions documented in both the containers and the active channels in this chapter. How long this equilibrium will last will depend on the frequency of flows (see Pirmez and Imran, 2003; Meiburg and Kneller, 2010; Xu, 2011) and on whether the pathway of the channel is completely abandoned as we see in buried container 2.

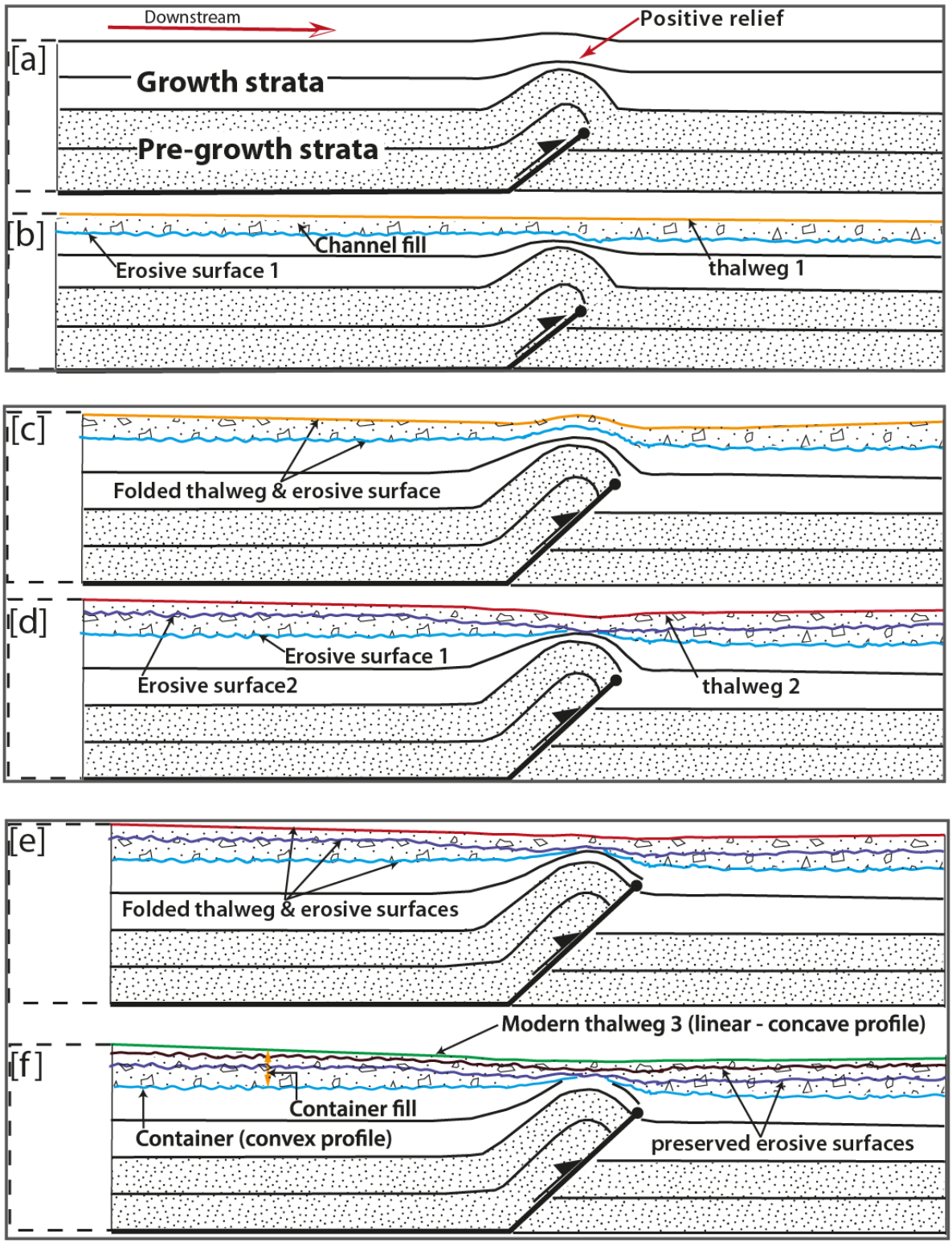


Figure 5.16: Schematic diagrams showing the processes by which submarine channel systems attain equilibrium profile: (a) structural growth and perturbation of the seabed bathymetry prior to channel development; (b) active channel erosion by turbidity currents over the knickpoint generated by structural uplift in (a). Note that after abandonment, the thalweg-profile is temporarily at equilibrium and is linear; (c) shows further structural growth and disruption of the earlier equilibrium profile; and (d) shows further erosion by a second set of turbiditic flows which restores the equilibrium; (d) and (e) show a repeat of the above processes leading to the development of a convex container profile, and a linear to concave modern channel (thalweg) profile. Note that continuous channel incision and erosion over the growing fold has resulted in the thinning of the container fill over the active structure, and preserved erosive surfaces of previous channels incision are visible as the system aggrades through time.

5.5 CONCLUSIONS

This study shows that the long profiles of the modern channels are relatively linear to slightly concave, and the profiles of the containers – the lowermost erosive surface bounding the channel complex system are generally convex. All profiles exhibit local scale steepenings (knickpoints) that are apparent near mapped structures – and implicitly therefore, represent variations in substrate uplift rate. The average gradient in all profiles is between 0.9^{o} and $1^{o.}$ However, the containers show a much higher cumulative gradient change (up to 400 %) immediately downstream of active thrusts and folds. The higher convexity of the container profiles represents cumulative structural uplift through time. Moreover, containers whose associated modern channel are still active (e.g., active container 4) are less convex compared to channel systems that have been abandoned and buried (e.g., buried container 2).

The evolution of the channel system and how it responds to tectonic perturbations determines the container width, depth and the overall stacking pattern of the cut-and-fill sequences that constitute the channel container. Lateral migration and stacking pattern dominates the lower part of the container as it moves laterally away from growing structures. When the growth of a fold no longer causes the channel to migrate laterally, the container develops dominantly by vertical aggradation.

Reaches of channels overlying regions of fold-thrust driven structural uplift exhibit a time-integrated increase in the channel system incision into the pre-channel substrate, and continuous incision by the modern channels into the preserved, time-integrated channel fill. As a consequence, the channel container shows the clear effect of time-integrated structural uplift through its overall width narrowing, deep incision and lower preserved fill over the growing structure(s). Despite the increase in channel incision over the fold crests, the systems still aggrade through time.

In essence, the overall linear to slightly concave nature of the modern seabed channel profile indicates the attempt of submarine channels to reach a topographic (bathymetric) steady state. However, this channel long-profile, if abandoned, will be disrupted because of the continual structural growth unless it is re-established by subsequent turbiditic flows. Consequently it is important to distinguish between the bases of Pleistocene cut and fill sequences, which may be abandoned but deformed by structural growth, and modern (open at the sea-bed) channels which fundamentally reflect the interaction between both tectonics and on-going erosion.

CHAPTER 6

STRUCTURAL CONTROLS ON SEISMIC FACIES DISTRIBUTION IN THE TOE-THRUST OF DEEPWATER NIGER DELTA

6.1 INTRODUCTION

Ancient and modern submarine channels, together with associated deepwater fans, have been recognised and studied for a long time (e.g., Normark, 1970, 1978; Mutti and Normark, 1987, 1991). For example, Mutti and Normark (1991) documented five basic elements of turbidite systems that are recognisable in both ancient and modern turbidite deposits to include; (1) major erosional features such as grooves from mass flows, (2) channels, (3) overbank deposits, (4) lobes, and (5) channel-lobe-transition deposits. In particular, studies on the modern Amazon deep-sea fan has greatly increased our understanding of the internal architecture and geometry of submarine channel systems (e.g., Damuth and Flood, 1985; Damuth et al., 1983, 1988; Piper and Normark, 2001 amongst many others). The increasing availability of 3D seismic data as a result of hydrocarbon exploration in passive margin settings in recent times means that both submarine channels and geological structures at, or near, the seabed are better imaged (e.g., Mayal and Stewart, 2000; Pirmez et al., 2000; Mayall et al., 2006, 2010; Deptuck et al., 2003, 2007 Clark and Cartwright, 2009, 2011). As a consequence, a number of studies have taken advantage of the development of 3D seismic imaging in deepwater settings to study the relationship between submarine channels and structures, such as growing folds and thrusts, which may affect their pathways (e.g., Pirmez et al., 2000; Fennesu, 2003; Morgan, 2004; Huyghe et al., 2004; Ferry et al., 2005; Heinio and Davies, 2007; Gee and Gawthorpe, 2006; Clark and Cartwright, 2009, 2011; Mayall et al., 2010). To a large extent, much of this work is aimed at understanding how these structures control the distribution of reservoir facies (e.g., Clark and Pickering, 1996b; Prather et al., 1998, 2000; Mayall and Stewart, 2000; Kolla et al., 2001; Fonnesu, 2003; Posamentier and Kolla, 2003; Posamentier 2003; Droz et al., 2003; Mayall et al., 2006). A key issue that has evolved from this work is that there is a need to

improve our understanding of how deepwater channel systems distribute sediments across actively growing structures in time and space. In particular, a better insight into the spatial and temporal variations of reservoir facies in deepwater settings requires detailed analyses of these interactions on a range of scales with the aid of good-quality seismic datasets.

This chapter aims to constrain the factors that control the deposition of channel-related facies (such as channel-axis sands, levees and sheet sands/splays) in the study area. Specifically, the study relates the potential distribution of sand facies to the spatial distribution of actively growing structures having seabed relief since Plio-Pleistocene times.

6.2 Previous studies on deepwater structures and seismic facies

Near-seafloor tectonic activity can create topography that determines the location and configuration of depocentres and sediment transport systems (Prather et al., 1998; Mayall et al., 2010). Consequently, the geometry and architecture of turbidite slope channels that deliver sediment to these depocentres, and how they disperse sediments is controlled by the regional slope (e.g., Goff, 2001; Gerber et al., 2009) but also the local slope topography and tectonic perturbations created by these structures (e.g., Clark et al., 1992; Clark and Pickering, 1996; Pirmez et al., 2000; Gee and Gawthorpe, 2006; chapter 4, 5). In structurally complex deepwater settings, localised structural growth can lead to channel pathway deflection and diversion, depending on the timing and rate of structural growth (e.g., Gee and Gawthorpe, 2006; Gee et al., 2007; Clark and Cartwright, 2009, 2011; Mayall et al., 2010; chapters 3, 4). However, a combination of factors, including the erosive power of the channel, and ratio of structural growth rate to sediment accumulation rate can allow the channel to incise across growing folds and thrusts on the sea bed (e.g., Morley, 2009; Mayall et al., 2010; chapter 4, 5). Consequently, the interaction between submarine channels and growing structures will automatically govern how deepwater facies (made up of a mix of both reservoir and non-reservoir sediments) are generated and distributed both spatially and through time (e.g., Clark and Pickering 1996a; Mayall and Stewart, 2000; Posamentier and Kolla, 2003; Beaubouef, 2004; Mayall et al., 2006; Heinio and Davies, 2006; Morley and Leong, 2008).

Many studies describing seismic facies distribution and stacking pattern through time have alluded to the fact that a large proportion of channel-reservoir facies are often deposited outside the channel system in the form of crevasse splays, and their deposition is often controlled by active structures at, or near the seabed (e.g., Flood et al., 1991; Pirmez and Flood, 1997; Mayall and

Stewart, 2000; Pirmez et al., 2000; Posamentier and Kolla, 2003; Mayall et al., 2010; McHargue et al., 2011). For instance, a marked reduction in gradient as channels exit a structurally-constrained area into an unconfined depocentre may lead to the deposition of laterally extensive sheet-sands of reservoir quality (e.g., Hackbarth and Shaw, 1994; Prather et al., 1998, 2000; Booth et al., 2000; Winker and Booth, 2000; Posamentier and Kolla, 2003; Gee and Gawthorpe, 2006). The deposition of these sheet-sands occur through a process known as 'flow flaring' – i.e. a process where flow vectors with increased magnitude are directed downward and outward against the channel-levee and resulting in the deposition of sheet-sands (Posamentier and Kolla, 2003). Because these sand-rich deposits are characterised by high amplitudes, they are easily imaged on seismic amplitude maps (e.g., Mayall and Stewart, 2000; Cross et al., 2009; Janocko et al., 2013). For example, Figure 6.1a shows sand-rich levees (brownish to dark-brown colours) deposited in the overbank areas of a channel system from offshore West Africa (Janocko et al., 2013). Figure 6.1b shows a lobe-shaped sand-rich deposit known as a crevasse splay because it was deposited from flows that breached through the channel levee (Janocko et al., 2013); and Figure 6.1e shows similar sand-rich splays which are deposited in front of channelized flows in the Nile Delta (referred to as frontal splays; Cross et al., 2009). A seismic section (A – A') across the channel-levee system in Figure 6.1a, shows the high amplitude reflections of the levees that dip away from the channel axis (Fig. 6.1c); and a similar section (B – B') across the channel system in Figure 6.1b is characterised by relatively lower seismic amplitude reflections because this channel is not associated with sand-rich levees in that area (Fig. 6.1d). Generally, high resolution data (Hackbarth and Shaw, 1994; Twichell et al., 1992; Posamantier and Kolla, 2003; Jones et al., 2012); and field analogues (e.g., Elliot, 2000; Janocko et al., 2013) show that some sheet-sand deposits probably consist of distributary channel-complexes. However, the resolution of most seismic datasets is not good enough to image these small-scale distributary channels. Consequently, in seismic sections, they are often amalgamated into composite channel units that are imaged as high amplitude, continuous seismic reflections (e.g., Fig. 6.1f; see also Mayall and Stewart, 2000; Cross et al., 2009).

Submarine channel systems, just like their fluvial counterparts are often sinuous and characterised with meander bends (e.g., Fig. 6.1a, b; see Kolla et al., 2007; Normark et al., 2008; Janocko et al., 2013). As a consequence, coarse-grained sands often accumulate on the outer banks of these meander bends as turbidity flows are more likely to spill over the outer banks (e.g., Hackbarth and Shaw, 1994; Normark et al., 2002; Posamentier and Kolla, 2003). Consequently, the channel-levee in such outer bank areas is usually asymmetric (e.g., Fig. 6.1c; see Posamentier and Kolla, 2003). A number of studies based on numerical modelling and physical experiments had provided a better insight into the processes operating within submarine channels meander bends (e.g., Peakall et al.,

2000, 2007; Corney et al., 2006; Straub et al., 2008, 2011 amongst many others). For example, modelling of flows within submarine channel bends shows that the direction of helical circulation is reversed when the maximum down-stream vertical velocity distribution is near the channel bed (Corney et al., 2006; Straub et al., 2008). This process results in basal flow being directed outward and towards the outer bank of a meander bend, thus leading to the deposition and accumulation of sands in the outer bends of submarine channels (see Normark et al., 2002).

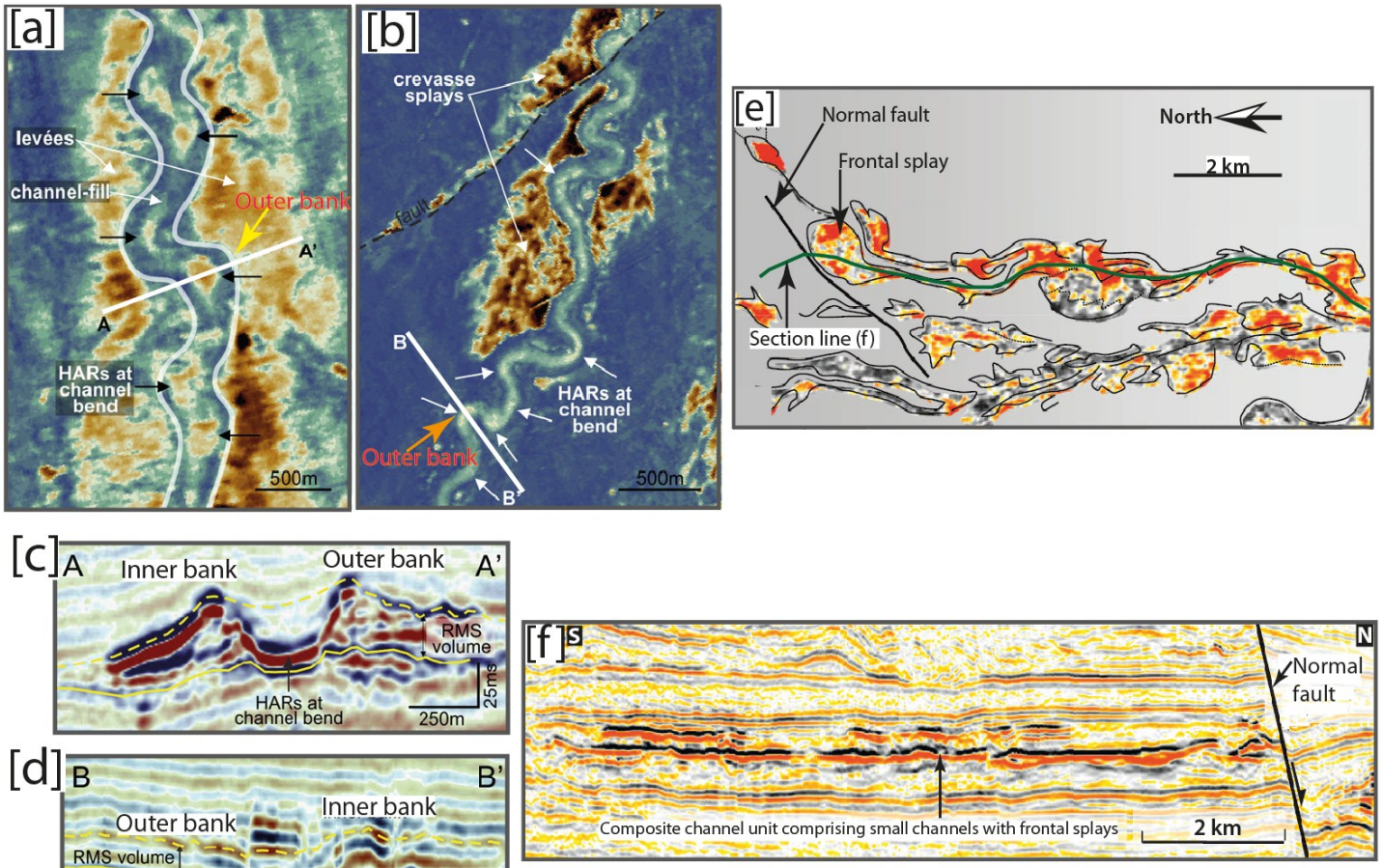


Figure 6.1: (a) and (b) show amplitude maps of submarine channels characterised by high-amplitude levees and high-amplitude crevasse splay (from Janocko et al., 2013); (c) and (d) are seismic sections A – A' and B – B' in Figure 6.1a and 6.1b respectively; (e) is an amplitude map showing channels with associated frontal splays (from Cross et al., 2009); (f) is a section along the frontal splays shown in Figure 6.1e. These high-amplitudes indicate that the systems are rich in sands deposited either as levees or splays.

6.3 DESCRIPTIVE TERMINOLOGY USED IN THIS STUDY

In both modern and ancient deepwater systems on the submarine slope, the basic mappable, seismically recognisable components include: (a) slumps and debris flow facies; (b) channels and associated levees; (c) sheet-sands (splays)/overbank sediment waves; and (d) pelagic/hemi-pelagic drapes (Mutti and Normark, 1991; Flood et al., 1991; Pirmez and Flood, 1997; Sikkema and Wojcik, 2000; Mayall and Stewart, 2000; Posamentier and Kolla, 2003; Mayall et al., 2006, 2010). These facies are normally recognisable in seismic data because of variation in amplitudes of the seismic reflections they generate, and have served as the key for predicting reservoir quality sand distribution in complex deepwater settings (Mayall and Stewart, 2000; Posamentier and Kolla, 2003; Mayall et al., 2006; Gee et al., 2007; Cross et al., 2009; Janocko et al., 2013). However, a variety of terminologies have been used in the sedimentological literature to describe some of these seismic facies. For example, fan-shaped sand bodies that are deposited to the side of channelized flows have been referred to as crevasse splays – shown in Figure 6.1b (e.g., Flood et al., 1991; Mayall and Stewart, 2000; Posamentier and Kolla, 2003; Mayall et al., 2010; Janocko et al., 2013), or lateral splays (Cross et al., 2009), or channel overspill (Gee et al., 2007). Fan-shaped sands deposited in front of channelized flows – shown in Figure 6.1e have been referred to as frontal splays (e.g., Posamentier and Kolla, 2003; Cross et al., 2009). In this study, fan-shaped sand bodies that are deposited to the sides of a channelized flow are referred to as '*crevasse splays*'. High amplitude seismic reflections at the base of channels, which have been referred to as High Amplitude Reflection Packages (HARPs) by Flood et al. (1991) and High Amplitude Reflections (HARs) by Janocko et al. (2013 – Fig. 6.1c, d); have been interpreted as coarse-grained channel-axis sediments (Gee et al., 2007) or basal lags (Mayal and Stewart, 2000; Mayall et al., 2006). In this study, similar packages are referred to as '*channel axis sands*'. Overbank deposits bounding the channel system, and dipping away from the channel axis, are referred to as levees (Mayall and Stewart, 2000; Kolla et al., 2001; Deptuck et al., 2003, 2007; Gee et al., 2007; Janocko et al., 2013; chapter 5) and they may be characterised by high amplitude seismic reflections which indicate they are sand-rich (e.g., Fig. 6.1a, c; Janocko et al., 2013), or they may be sand-poor and characterised by low amplitude seismic reflections (e.g., Fig. 6.1b, d; Mayall and Stewart, 2000; Kolla et al., 2001; Janocko et al., 2013). In this study, large-scale 'gull-wing' shaped levees (*cf.* chapter 5) that flank the channel system complex are referred to as '*outer levees'* whereas the smaller-scale levees flanking individual channels within the channel complex are referred to as '*internal levees*' (see also Babonneau et al., 2004; Deptuck et al., 2007; Kane and Hodgson, 2011). Mass transport deposits (mass flows) are characterized by low to medium amplitude, chaotic seismic reflections (Posamentier and Kolla, 2003; Heinio and Davies,

2006). These have been described as slump/slide deposits or debris-flow deposits in the Niger Delta and similar deepwater settings (Posamentier and Kolla, 2003; Heinio and Davies, 2006; Covault, 2011). For simplicity, I have referred to these kinds of deposits by their generic term known as '*mass transport deposits (MTDs)'*. Fine-grained sediments that are rich in clays, and often deposited in quieter deepwater environments have been referred to as pelagic and hemi-pelagic drapes (Droz et al., 2003) or condensed sections (Posamentier and Kolla, 2003). These facies are characterised by low frequency, continuous, low to high amplitude seismic reflections, and are referred to in this study simply as '*pelagic drapes*'.

6.4 METHODS

6.4.1 Fold growth and submarine channels

Five major submarine channels are found in the study area (Channels 1 – 5, Fig. 6.2a). These channels interact, and incise across growing structures having seabed relief (Folds A – D, Fig. 6.2a; see chapter 3). The growth histories of these four folds have been constrained in chapter 3, and these structures were classified into two groups – fault propagation, and detachment folds. For example, the seismic sections (Fig. 6.2b and 6.2c) across Folds A and B respectively show the seismic expression and geometry of the fault-propagation folds that are characterised by seabed scarps and modern channel incision across the fold crests. The detachment fold is located in the east of the study area (Fold C, Fig. 6.2a) and is characterised by a thick shale accumulation in its core (Fig. 6.2d). A large piggyback basin is located to the north of this detachment fold where the modern channel 2 is also located (Fig. 6.2a; see chapter 3). Results based on the analyses of spatial and temporal strain variation in these structures in chapter 3, show that channels incising through actively growing structures (e.g., Channel 1 across Fold B; Figs. 6.2a, c), do so in positions of recent strain minima where two separately growing structures linked along strike. Moreover, the interval growth rates at which these channels are able to cross these folds is ≤15 m/Myr (chapter 3). However, the detachment fold is characterised as having a longer wavelength structural and topographic expression, which acts counter to the regional slope direction, but has a much lower measured strain compared to the other structures (chapter 3). Nevertheless, this has led to the diversion of channel 2 for more than 20 km (Fig. 6.2a).

In this study, the results of these structural growth analyses and their impact on modern seabed channel pathways are used as a basis for analysing the role of growing structures in governing the seismic facies distribution of Pleistocene to Recent sediments in the study area. Of particular interest is the extent to which the interaction between folds, scarps and submarine channels has controlled the distribution of deepwater facies through time.

6.4.2 Seismic facies analysis

The description of seismic facies is based on seismic reflection characteristics of the different units because of the absence of well control (e.g., Mayall and Stewart, 2000; Mayall et al., 2006; Gee et al., 2007). Any particular seismic facies can be identified from a combination of seismic reflection characteristics such as (a) amplitude variation, (b) the chaotic or coherent nature of the reflections, (c) parallelism of the reflections; (d) continuity/discontinuity of reflections and (e) the relationship of reflections to growing structures (e.g., onlap, downlap). The amplitude of the seismic reflection is determined by the acoustic impedance (the product of the difference in rock density and the velocity of the seismic P-wave) generated at the interface between two rock bodies (Hart, 1999; Kearey et al., 2002). Thus assuming a constant seismic wave-velocity, a wave travelling through a shale unit (with lower density) will generate positive acoustic impedance (high amplitude) at the interface between the shale unit and a sandstone body lying below it because of higher density in the sandstone. On the other hand, negative acoustic impedance (low amplitude) is generated at the interface between sandstone underlain by a shale unit. This process leads to variations in seismic reflection amplitudes as the seismic wave travels through different rock types. This amplitude variation together with other characteristics such as the continuity/discontinuity of reflections can be used to differentiate between different facies.

Some easily recognisable seismic facies in the study area were documented in chapter 3 and these are mainly channel-related facies that are common in deepwater settings (e.g., Mayall and Stewart, 2000; Posamentier and Kolla, 2003; Mayall et al., 2006). For example, in Figure 6.3a, recognisable seismic facies include (a) mass transport deposits which are characterized by low to medium amplitude, chaotic seismic reflections (Fig. 6.3a); (b) channel-axis sands – characterized by medium to high amplitude, discontinuous, chaotic seismic reflections and usually contained within an erosional base (channel container, Fig. 6.3a); (c) outer and inner channel-levees – these are characterised by relatively high frequency, low to high amplitude, continuous seismic reflections

(Fig. 6.3a). The outer levees are asymmetric, characterized by a gull-wing shape which wedges out laterally away from the main channel axis (see Mayall and Stewart, 2000; Kolla et al., 2001, Deptuck et al., 2007), and can be up to 4 km in lateral extent. The inner levees are housed within the channel container, which may also contain slumps and other channel fill facies (e.g., Gee et al., 2007; Janocko et al., 2013). These inner levees are of less lateral extent and often onlap onto the edge of the channel container (Fig. 6.3a); (d) Pelagic drapes are characterised by low frequency, continuous, low – high amplitude seismic reflections (Fig. 6.3b); (e) splays – these have distinct, high amplitude, continuous seismic reflections (Fig. 6.3a) and are mostly deposited by breaching through the channel levees (e.g., Mayall and Stewart, 2000; Posamentier and Kolla, 2003; Cross et al., 2009; Janocko et al., 2013).

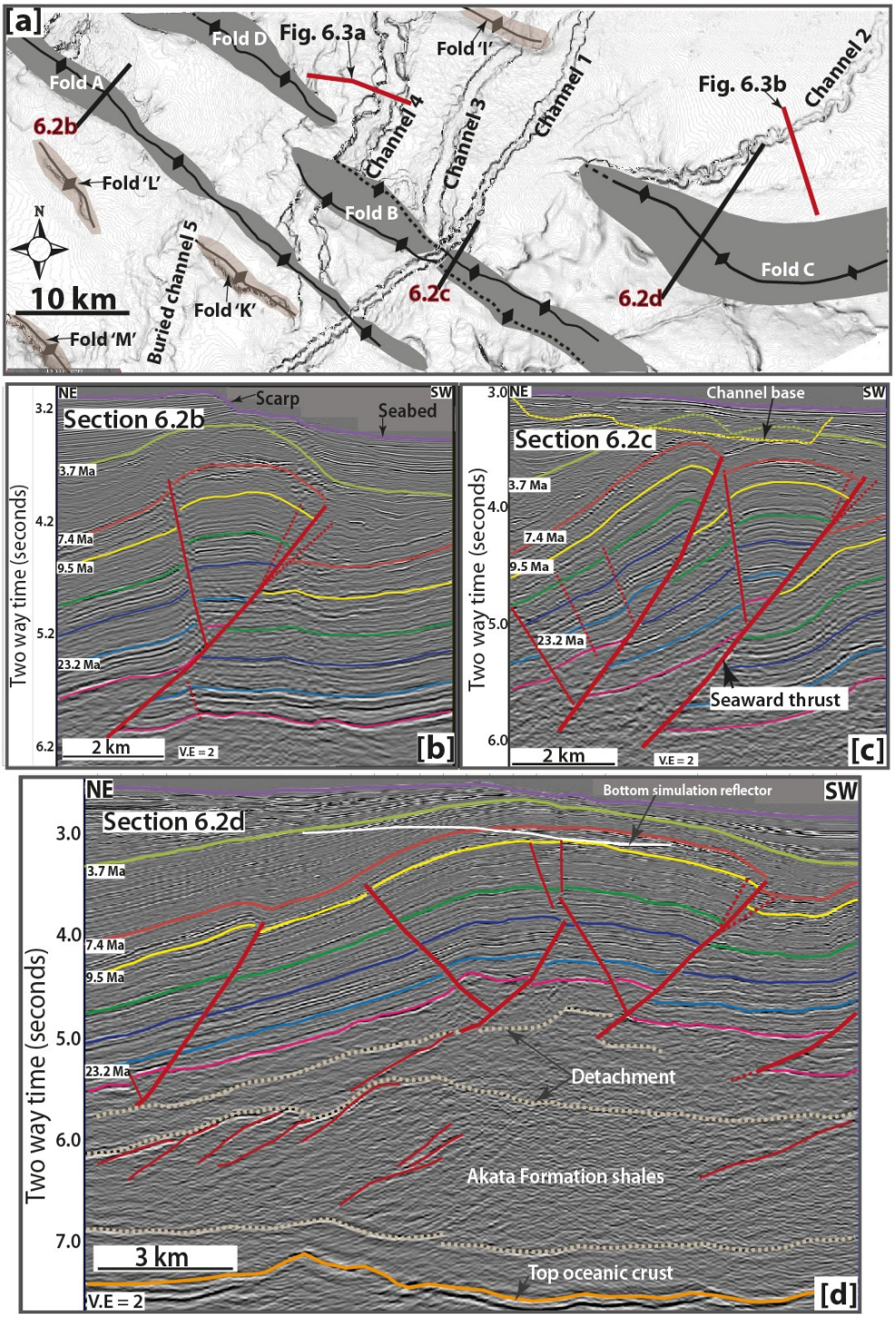


Figure 6.2: (a) Edge-attribute map of the seabed in the study area (from chapter 3) showing the outline of major folds having seabed relief (Folds A, B, C and D); and modern seabed channel systems (1, 2, 3 and 4 and a buried channel, 5) whose interaction has been documented chapter 3. Section lines 6.2b, 6.2c and 6.2d (across Folds A, B and C; are from chapter 3, and are shown in [b], [c] and [d] respectively). These sections are used to show the variation in structural style from the west (dominantly fault-propagation folds) to the east where Fold C – a detachment fold occurs (see text in methodology for description).

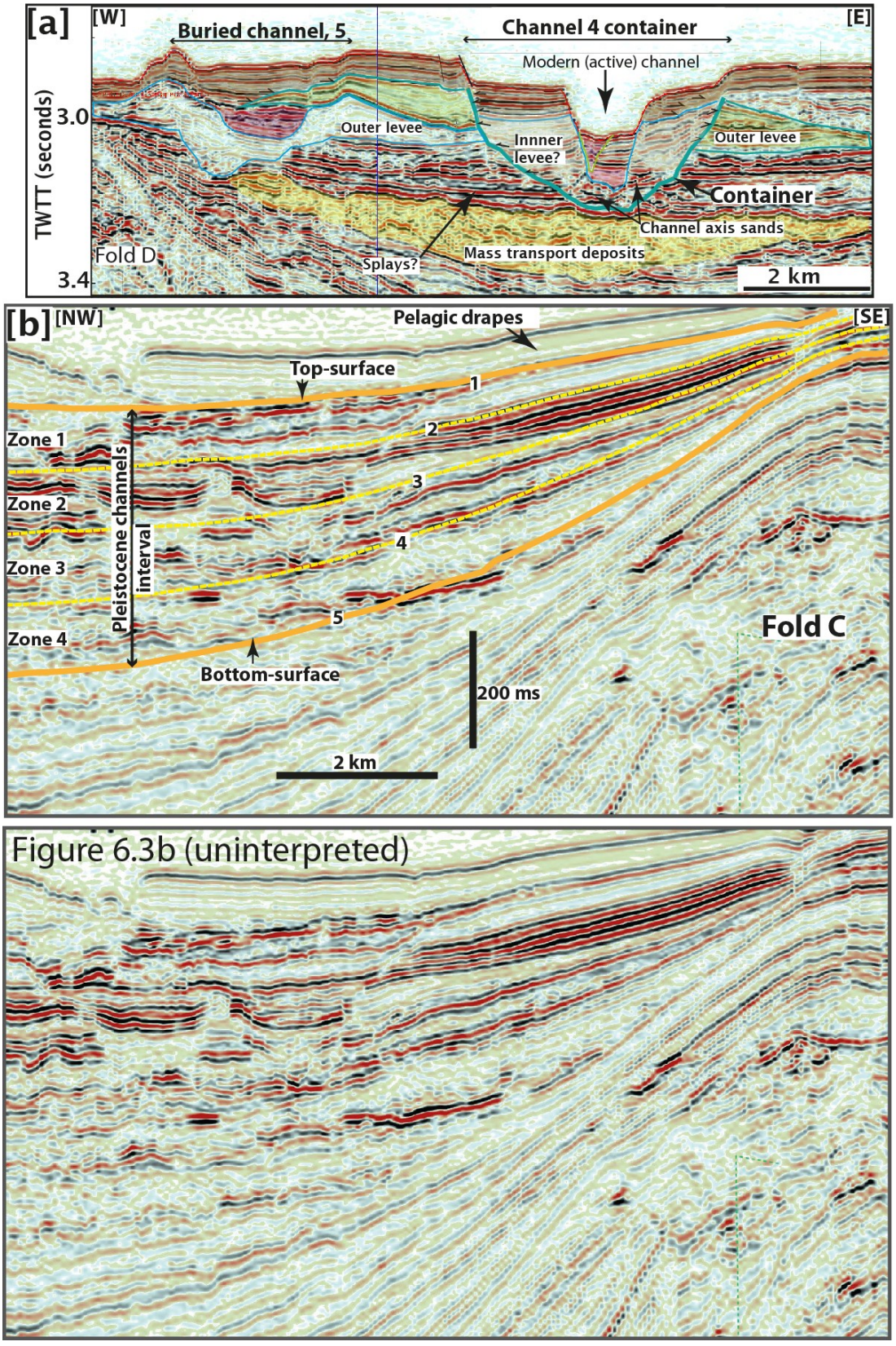


Figure 6.3: (a) Transect across the buried channel 5 and active channel 4 (taken from chapter 3; see location in Figure 6.2a) showing the different seismic facies in the study area; (b) shows the methodology for iso-proportional slicing of the Pleistocene channel interval within the piggyback basin in the east of the study area (see section location in Fig. 6.2a). The channel interval has been subdivided into four zones from which zone-specific RMS amplitudes were calculated.

6.4.3 Seismic attributes analysis

Various seismic attributes such as edge, dip-magnitude/dip-azimuth maps and Root-Mean-Square (RSM) amplitude maps were used in this study to identify and analyse seismic facies (e.g., Sheriff, 2002). The edge attribute uses a cross-correlation algorithm to compute coherence coefficients from seismic amplitudes on adjacent traces, and returns a value which represents the similarity of the waveforms. Therefore, chaotic facies albeit of low amplitudes, and discontinuities (channel edges, faults) are easily recognised. The dip-magnitude/dip-azimuth computes the variations in dip amount and dip-direction (azimuth). The RMS amplitude algorithm calculates the square root of the sum of the squared amplitudes divided by the number of samples within a specified user-defined time-window, normally associated with a mapped horizon. Both maximum positive and negative amplitudes are highlighted on resultant maps. Thus sand-rich facies (high-amplitudes) such as channel-axis fills, splays and some higher amplitude levees may be easier to identify in seismic amplitude maps. Mud-rich areas will be dominated by low amplitudes.

If the RMS amplitude windows cross-cut stratigraphy (e.g., where strata are dipping) then the results will not be valid. Therefore, where it was difficult to calculate RMS amplitudes using a 'user-defined window' from a single mapped horizon (e.g., the seabed horizon) because the chosen window would cut-through structures having seabed relief, a package of dipping stratigraphy was divided into iso-proportional layers and the surfaces used to define the RMS amplitude extraction windows (Fig 6.3b). This method was applied to the piggyback basin strata on the northern flanks of fold C. The top and the bottom horizons bounding the Pleistocene channel interval of interest were mapped and the stratigraphy was divided into four iso-proportional layers bound by surfaces that can be seen to follow the stratigraphic dip (See surfaces 2, 3, & 4 in Figure 6.3b). RMS-amplitudes extracted from these intervals make it possible to map discontinuous channels and related facies within this interval and help in systematically describing the evolution of the channel systems through time. The channel-axis sands of the cut-and-fill sequences that constitute the channel containers (*cf*. Fig. 6.3a) can be mapped by calculating RMS amplitudes within the container itself. Amplitude extraction within the containers can reveal channel systems that are generally sand-rich from those that are sand-poor (mud-filled).

6.5 RESULTS

This section presents the results of the main seismic facies and the effect of growing structures on the spatial and temporal distribution of the facies. Channel-related facies (e.g., channel-axis sands, levees and sheet-sands) and their relationship to growing fault-propagation folds in the west, and the detachment fold (Fold C) in the east of the study area are presented.

6.5.1 Channel-axis sands and levees

The RMS amplitude maps of channel containers in the study area are shown in Figure 6.4a. These channel amplitude maps are draped on the edge map of the seabed, thus showing the relationship between structures having seabed relief and the channels (Fig. 6.4a). Blue to light-blue colours represent higher amplitudes while yellow colours represent lower amplitudes. The high amplitudes occur within the channel containers and some channels are characterised by high sinuosity amplitude distributions (even though the containers are broadly linear), suggesting that some of the sands from turbidity flows within the channel were deposited in smaller sinuous channel-fills (e.g., Fig. 6.4b, c). The distribution of the high amplitudes demonstrates that all the channels have had sand deposited within them. In essence, the amplitude extractions show that most of channels contain sand-rich facies, but because amplitudes were extracted over entire fill, it is difficult to map individual smaller channels within the container. Seismic sections across the channels (e.g., Figs. 6.5 and 6.6) provide a better insight into the internal architecture of the channels and how the sand is distributed within the containers. For example, some of the high amplitudes are from chaotic packages in the lower parts of the containers (e.g., the sinuous high amplitude (brownish colour) within the active channel 1 container – Fig. 6.4b; indicated by an arrow in Fig. 6.4c). However, some occur in the middle to upper parts of the container systems (e.g., the sinuous high amplitude (blue colour) within buried channel 1 container – Fig. 6.4b; which is labelled as top-channel sands in Fig. 6.6d).

Seismic sections (sections 5a – 5f) along active channel 4 container (Fig. 6.4a) are used to describe the seismic characteristics of these channel-axis sands (Fig. 6.5). In these sections, the axis of individual cut-and-fill sequences are obvious, and are characterised by chaotic - discontinuous, high amplitude reflections (indicated by blue arrows; Fig. 6.5a – f). These occur predominantly in the lower part of the container and more rarely as isolated events higher up within the channel as the

system aggrades (e.g., Fig. 6.5e; chapter 5). These high amplitude facies are surrounded by low amplitude discontinuous fill, which could be debris flow material, slumped material from channel margins or inner levees on smaller-scale channels within the main channel complex (Fig. 6.5). The high amplitude, chaotic reflections are generated due to the high acoustic impedance produced at the interface between coarse sands and the surrounding finer-grained sands, silt or slumps. Consequently, these high amplitudes within the containers represent real sinuous smaller channels, and are interpreted as coarser-grained sands deposited along the axes of turbiditic flows that represent the several cut-and-fill sequences that form the channel system through time (see Mayall and Stewart, 2000; McHargue et al., 2011). Generally, these sections show that the active channels are characterised by erosive surfaces – cutting into the underlying stratigraphy and overall aggradation through time (see chapter 5). Moreover, the lower parts of these sections seem to be more erosional, and through time levees were developed in association with the channels (Fig. 6.5). The external levees tend to dip away from the channel systems ('gull-wing' geometry; Fig. 6.5). These levees are characterised by low – medium amplitudes seismic reflections, and also show little variation down-system due to the impact of active structures (e.g., Clark and Cartwright, 2011). Where the channel crosses growing structures, the channel cut-and-fill system shows an overall narrowing (see chapter 5), and the levees are slightly less, well-developed (e.g., Fig. 6.5f).

Seismic sections across the buried channel systems (sections 6a – c across buried channel 5; and section 6d across the buried channel 1; Figure 6.4a) are shown in Figure 6.6. Just like the active channels (e.g., Fig. 6.5), the buried systems are also characterised by 'gull-wing' levees (Fig. 6.6a – c) with the only exception being the section through the buried channel 1 shown in Figure 6.6d. The area where this section is located is very chaotic, and characterised with several small-scale buried systems and slumps/debris flows which might have eroded any preserved levees. In contrast to the active channel systems shown in Figure 6.5, bright amplitudes (indicated by blue arrows) that can be interpreted as individual channels within the channel complex, do not form a high proportion of fill. Dominant fill is low amplitude discontinuous seismic reflections which could be debris flow material, slump material from channel margins or mud-rich internal levees on smaller scale channels within the main channel complex (Fig. 6.6). For example, in Figure 6.6(b, c), the coarser material lies within the lower third of an erosional channel. However, in Figure 6.6(a, d), the systems appear to have a more mud dominated fill. The mud-dominated fill may suggest periods of channel by-pass where the sands have been transported down-dip when the channels were erosional (see Mayall and Stewart, 2000; Mitchum and Wach, 2002; McHargue et al., 2011); so that when the flows have ceased, the muds were deposited (i.e., analogous to the waxing – waning cycles described by McHargue et al., 2011), and subsequent flows then cut into the preserved mud (see chapter 5). The chaotic, high

amplitude channel axis facies in Figure 6.6c become dominantly aggradational in the centre of the mud-dominated fill – a process which has been documented in other submarine channel systems (see Mayall et al., 2006; Kolla et al., 2007).

However, at the top of these two buried channel containers (channel 1 and 5), high amplitude, seismic reflections are observed (Fig. 6.6); and have also been observed in buried channel 2 container (see Fig. 5.8a in chapter 5). These are characterised by at most, thin 2-3 parallel, high amplitude reflections with a lateral extent equivalent to the width of the container, and can be traced down-system (e.g., buried container 1; Figs. 6.4b, 6.6d). Immediately above them, continuous seismic reflections of uniform thickness that extend beyond the channel system can be observed, and are interpreted as post-channel sediments that buried the systems (Fig. 6.6a – d). This implies that the sand-rich units at the top of the buried containers were deposited in some remaining seafloor topography associated with the channels close to their point of abandonment. These may have formed from the deposition of coarse sands following sudden loss of flow power; hence, they are interpreted as top-channel sands (Fig. 6.6). This could occur, for example, when growing structures forces an active channel to abandon its path by avulsing and hence, resulting in a sudden loss of flow momentum within the original flow path (see Peakall et al., 2000). These top-channel sands were not observed in the active channel containers (e.g., Fig. 6.5); which suggests that even when these types of isolated sands are deposited within active channels, they will be eroded by subsequent flows. However, they are likely to be preserved when the channel is abandoned and buried.

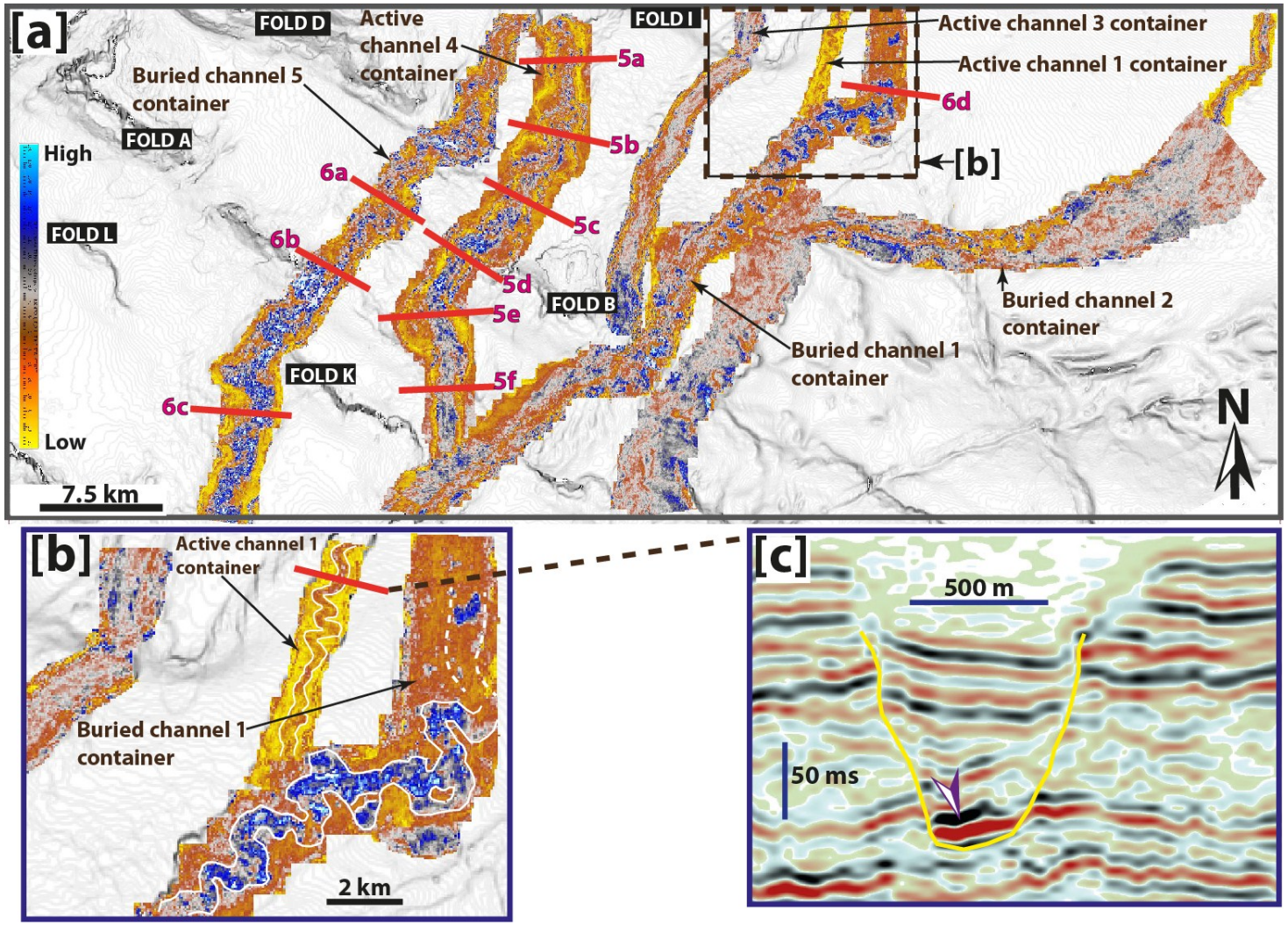


Figure 6.4: (a) Shows the RMS amplitude maps of the channel containers (extracted from both active and buried channel systems) draped on the seabed edge-map of the study area; (b) is an enlarged (zoomed) area indicated by dash-square box in Figure 6.4a; and (c) is a section across active channel 1 container (location in Fig. 6.4b) showing the sand-rich, high amplitude reflections at the base of the container (indicated by an arrow). Note that blue colours in map-view represent the high amplitudes that characterise, and define sand bodies within the containers. Section lines 5a – 5f across active channel 4 container are shown in Figure 6.5; and section lines 6a – 6d across buried channel 1 and 5 containers are shown in Figure 6.6.

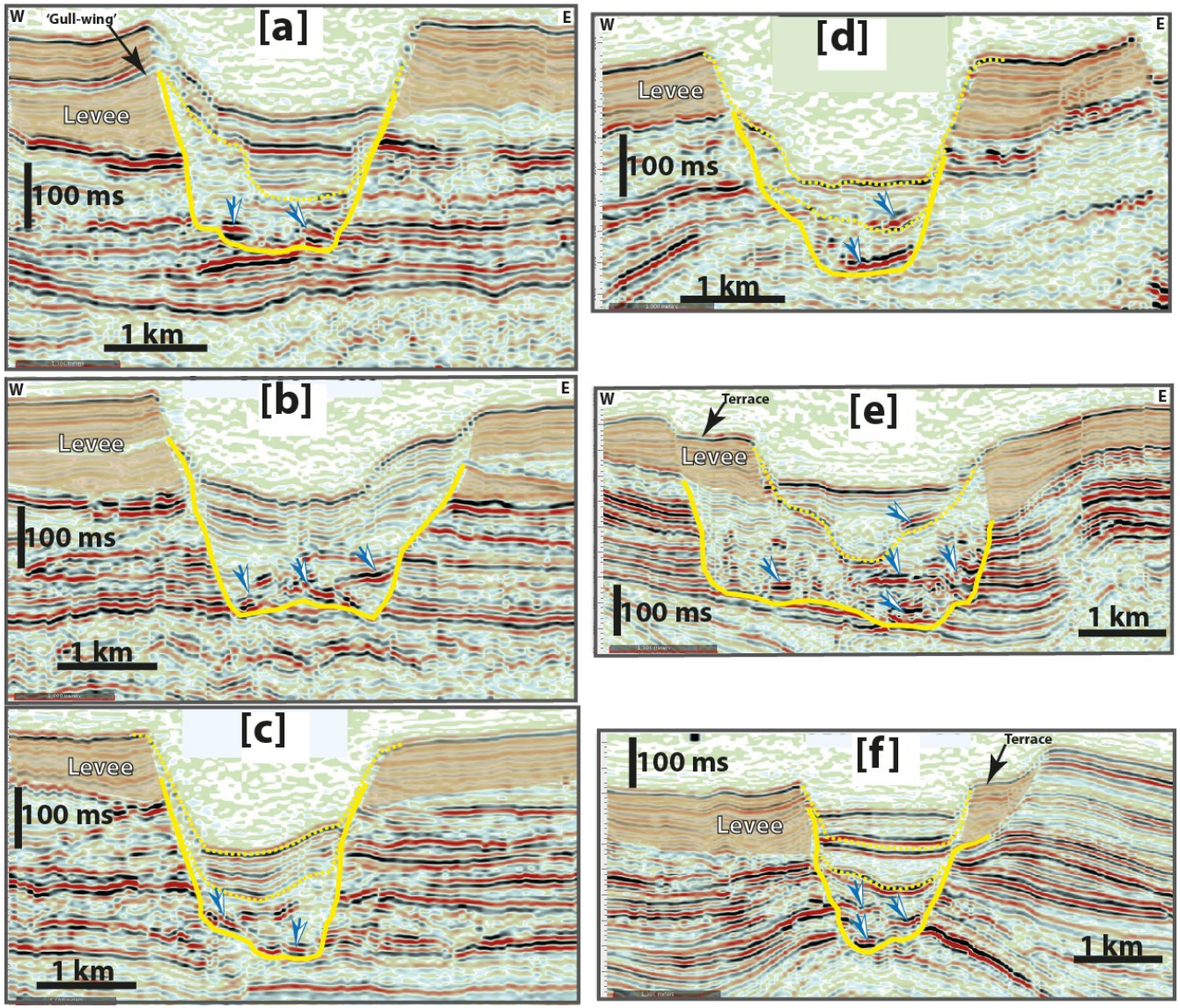


Figure 6.5: (a) Transects across active channel 4 container (see location in Fig. 6.4a) showing the seismic characteristic of active channel fill (made of high-amplitude, chaotic channel axis fills – indicated by blue arrows). Note that these systems are characterised by levees and overall system narrowing over folds (see chapter 5 for details).

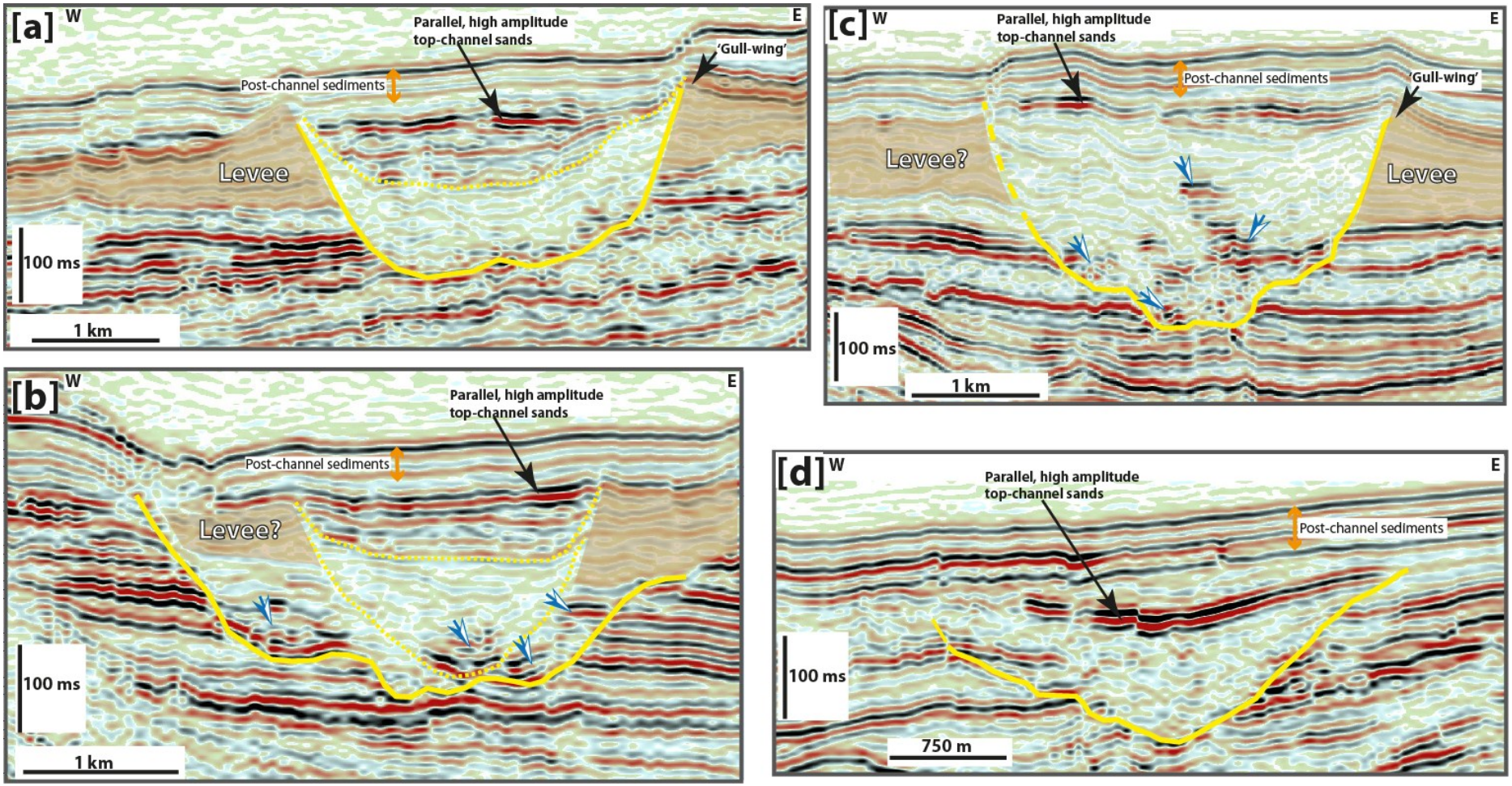


Figure 6.6: (a) to (d) Are transects across buried channel 1 and 5 containers (see location in Fig. 6.4a) showing channel axis fills in the lower part of the container; and dominantly low-amplitude fill which may represent mud, slumps or inner levees. Note that at the top of these systems, high-amplitude, parallel seismic reflection represent sand deposits at the time of channel abandonment.

6.5.2 Sheet-sands (splays) and relationship to structures in the west

In the west of the study area, a strong, high-amplitude, continuous reflection buried at about 50 ms TWTT (~40 m) beneath the seabed (labelled splay; Fig. 6.7b, c) in the strike parallel sub-basins to the west of buried channel 5 can be traced in more than one basin, between Folds D and M (Fig. 6.7a). RMS amplitude extraction in a 30 ms TWTT window (10 ms above, and 20 ms below) this high-amplitude event reveals 2 broadly lobate-shaped geometries indicated by high RMS amplitudes – blue colours (labelled Splays 1 and 2; Fig. 6.7a). These lobate-shaped features appear to have originated from two locations (location R at the tip of Fold D, and location Y which is slightly offset from the tip of Fold A) along buried channel 5 (Fig. 6.7a). Splay 1 originates from the breaching of the levee of buried channel 5 at location R which is at the tip of Fold D (Fig. 6.7a). It expands to deposit over a wide area in basin between Folds D and A, and even spills through two segments of Fold A (location X) to pond behind Fold 'L' (Fig. 6.7a). Within this splay (splay 1), channelized features can be observed (labelled (i), (ii) and (iii) – Fig. 6.7a; and seen in section as discontinuous high-amplitude zones – Fig. 6.7b). In plan-view, these channelized features seem to converge at point X which is an area with lower fold growth rate, and absence of seabed scarp (see chapter 3), before further spreading out and forming another splay lobe downslope on exiting the constriction (Fig. 6.7a). Within the sub-basin bounded by Fold A and Fold 'L', Splay 1 developed into two main branches as it avoided the structural and topographic expression associated with the growth of a seabed scarp along Fold 'L' (Fig. 6.7a). This kind of topographic expression acts counter to the regional slope direction, and is a common feature associated with folds having seabed relief in the study area (see chapter 3 for details).

Splay 2 originates from the breaching of the levee of buried channel 5 at location Y which is slightly off the tip of Fold A (Fig. 6.7a). This splay is fed by a channel that extends for approximately 10 km before spreading out into a fan-shaped deposit in the basin bounded by Folds L and M (Fig. 6.7a). In seismic section, Splay 2 form a continuous, high-amplitude reflection and the feeder channel can be observed (Fig. 6.7c). Moreover, this splay can be identified inter-bedded with mass transport deposits (MTDs) and pelagic drapes that are relatively thicker than the isolated splay horizon (e.g., Fig. 6.7c). Generally, the splays identified in the west of the study area are broadly lobate, or fan-shaped in extent, and can be up to 10 km long (parallel to slope) and more than 15 km wide (perpendicular to structures). These splays are inter-bedded with both MTDs that are characterised by chaotic seismic reflections, and pelagic drapes that are made of low frequency, parallel, continuous, low amplitude seismic reflections (e.g., Fig. 6.7c).

The most likely interpretation of these broadly lobate-shaped features is that they are sheet-sands that originated from the overspill and/or breaching of buried channel 5 levee at location R (producing Splay 1; Fig. 6.7a) and at location Y (producing Splay 2 which has a feeder-channel; Fig. 6.7a). At location R where Splay 1 originated, the present-day change in seabed gradient is approximately 4^{o} (from the downslope average of 1.2^{o}). Although this absolute gradient value at the present-day seabed may be different from the absolute value at the time of the splay development, it shows that there has been some positive topography associated with the growth of Fold D in that area (possibly since the start of fold growth between 12.8 and 9.5 Ma; see chapter 3). Moreover, the approximately 50 ms TWTT (40 m) depth from the seabed to the top of these splays could suggest the splays were deposited not long ago (~0.1 – 0.3 Ma assuming a uniform sediment accumulation), and definitely younger than when structural growth began. Hence, the presence of this kind of topographic relief, coupled with channel deflection at the tip of growing folds is likely to cause flows to breach the channel bank at the sharp bends (e.g., location R; Fig. 6.7a) and overflow to deposit coarser-grained sands adjacent to the buried channel 5 (e.g., Splay 1). Such features can be interpreted as a crevasse splay (Mayall and Stewart, 2000; Posamentier and Kolla, 2003; Cross et al., 2009; Mayall et al., 2010).

However, where the change in topography is not significant (such as the gradient change at location Y which is $<0.5^{o}$) levee breaching (avulsion) may not result in flow spreading immediately adjacent to the main channel, but could result in a channelized flow (Fig. 6.7a). However, this channelized flow also expands at point *Z* where the flow crosses Fold 'L' and formed Splay 2 (Fig. 6.7a). At point *Z*, the change in present-day topographic relief is significant – approximately 1^{o}. Therefore, Splay 2 appears to be more like a frontal splay that develops in front of a channelized flow on reaching an unconfined basin or sub-basin with a lower gradient (e.g., Posamentier and Kolla, 2003; Cross et al., 2009). The discontinuous high-amplitude zones that characterised Splay 1 (labelled (i), (ii) and (iii); Fig. 6.7a, b) represent small-scale channels that are mostly below the resolution of the seismic data. These bright amplitude zones most likely form by the amalgamation of sandy units that cannot be resolved (i.e., 'seismic tuning effect' see Brown, 1999; Kearey et al., 2002). Consequently, where these small-scale sheet-sands are widely and uniformly distributed (e.g., Splay 2), their amalgamation will form a composite body that is characterised with very high amplitude, continuous seismic reflection (Fig. 6.7c; see Cross et al., 2009).

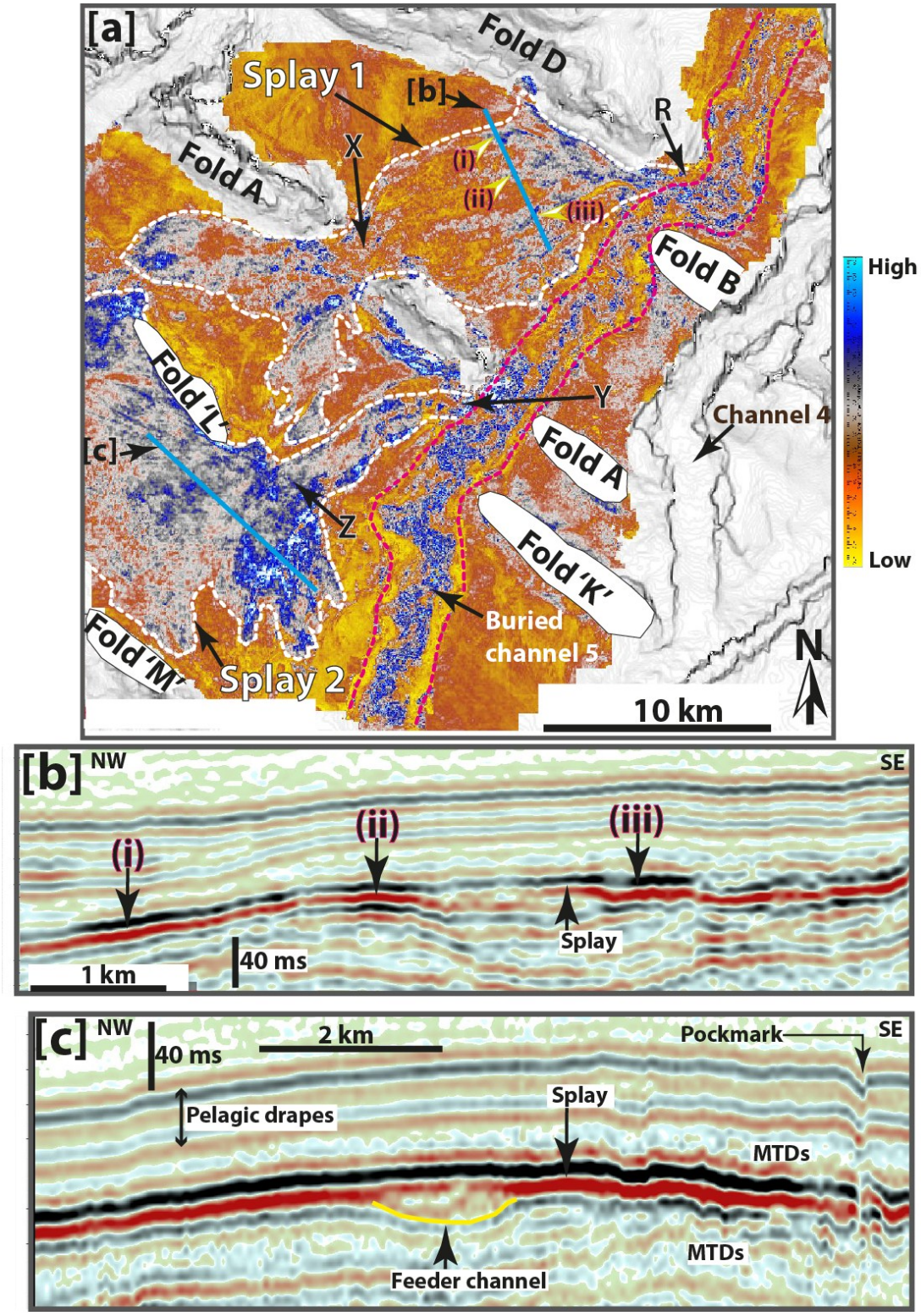


Figure 6.7: (a) Shows RMS amplitude map (blue colours are high amplitudes and yellow colours are low amplitudes) calculated using a time window of 10 ms and 20 ms above and below the high amplitude splay horizon) shown in Figures 6.7b and 6.7c. The map shows lobate-shaped splays deposited in sub-basins developed between growing folds. Note that the splays originate from breaching of levees in buried channel 5 at locations R and Y; (b) and (c) show seismic sections across splays 1 and 2 (see location in Fig. 6.7a). Note the characteristic high amplitude reflection of the splay relative to slumps and pelagic drapes.

6.5.3 Syn-kinematic sedimentation *in the east, north of Fold C*

In the east of the study area, the evolution of seismic facies within the piggyback basin that developed north of Fold C (Fig. 6.8a) is different from that observed in the west of the study area. In particular, the mechanism of channel – structure interaction and channel/sheet-sand deposition is different because of active diversion of Pleistocene channels in response to the time-integrated growth of Fold C (*cf*. chapter 3). Figure 6.8a shows the thickness distribution of the interval dominated by the Plio-Pleistocene channels. The maximum thickness of this interval in the centre of the basin is ~900 ms TWTT (or approximately 1 km assuming average seismic velocity of 2300 m/s), although only the top 400 ms TWTT were examined in detail for this chapter (i.e., zones 1 to 4; Fig. 6.3b). This thickness reduces to approximately 20 ms TWTT over the broad crest of Fold C (red – yellow colours, Fig. 6.8a). The seismic section through the top 400 ms TWTT across the piggyback basin from NW (basin centre) to the SE (top of Fold C) reveals the impact of Fold C on incoming channels and its associated effect on facies deposition through time (Fig. 6.8b).

The seismic section (Fig. 6.8b/c) is representative of what can be seen in piggyback basin in 3D (see section 6.5.4). The main seismic facies that can be seen include: (1) channel-levee systems (labelled [a] – [g]); (2) chaotic, low-amplitude reflections that represent mass transport deposits (MTDs); (3) parallel, layered, high-amplitude reflections which could be sheet-sands; and (4) parallel, layered, low-amplitude, uniform thickness pelagic drapes (Fig. 6.8b/c). In the lower part of the section, just below MTD 1, channel [a] is represented by high amplitude dipping reflections that cut into the low amplitude pre-channel substrate which appear truncated (Fig. 6.8b, c). These high amplitude in-channel reflections have been tilted on the flanks of Fold C, and can be traced from the channel towards the crest of the growing structure. MTD 1 with an incisional base overlies channel [a] (Fig. 6.8b, c). The next youngest channel at [b] developed slightly upslope on the flanks of Fold C; however, this channel appears to have migrated laterally away from Fold C to position [c] and subsequently to position [d], where it appears to have developed into a more established system with low-amplitude levees (Fig. 6.8c). The low-amplitude levee that occurs on the southeast side of channel [d] is up to 6 km in lateral extent, and has been tilted on the flanks of Fold C (Fig. 6.8c). Subsequently this channel shifted to position [e]. The channel labelled [f] appears to incise into channel [d]/[e] and is associated with the deposition of more parallel, layered sheet-sands (labelled Sands 'X') that can also be traced toward the crest of Fold C (Fig. 6.8b, c). This period of sheet-sand development is followed by a period of abandonment (or channel avulsion) indicated by the pelagic drapes, one of which can also be traced towards the crest of the structure (Pelagic drapes 1 - Fig.

6.8b, c). Pelagic drapes 1 is partly eroded by the deposition of MTD 2 which is smaller in volume compared to the MTD 1. The youngest channel system [g] is also mud-filled, but characterised by a high-amplitude gull-wing levee (Fig. 6.8b, c). The high amplitude nature of the levee associated with channel [g] suggests it is richer in coarse-grained sands – labelled Sands 'Y', while the dominantly low-amplitude reflections in channel [d]/[e] and the associated levee suggests a mud-rich channel fill (Fig. 6.8b, c). The gull-wing levee associated with the channel [g] system appears to down-lap onto a surface defined by the top of MTD 2 (Fig. 6.8b, c). On the eastern side of the channel, the levee is characterised by high amplitude seismic reflections. However, to the west, the amplitudes of the levee deposits are lower. The eastern levee has an off-lapping geometry on the flanks of Fold C relative to the underlying sheet-sands 'X' associated with the channel at position [f]. Above the channel [g] system, pelagic drapes 2 can be observed, incised by the modern-day seabed channel system (i.e., modern channel 2; see Fig. 6.2a).

Generally, major patterns can be discerned that suggest continued growth of Fold C and concomitant channel development. These include channel lateral shift through time, and the deposition of localised sheet-sands that are punctuated by periods of relative quiescence and deposition of pelagic units. For instance, the overall geometry of the growth unit (comprising all the seismic facies described in Figure 6.8b, c) shows evidence of horizon rotation towards the base of the unit (i.e., decrease in horizon dip from the oldest at the bottom to the youngest at the top) that suggests coeval sedimentation and fold growth (e.g., Burbank and Verges, 1994; Burbank et al., 1996; Clark and Cartwright, 2011). The increasingly off-lapping architectural geometry towards the top of the system defined by Sands 'X' and the sand-rich levee of channel [g] (Sands 'Y') along with the overall lateral channel shifts away from the growing fold likely indicates fold broadening through time (*cf.* Fig. 6.2d). However, in order to verify these observations, and gain a better insight into the evolution of seismic facies in this piggyback basin, it is necessary to map key horizons through time and use them to calculate RMS amplitude maps that would allow the analysis of facies evolution in this part of the basin through time (see section 6.5.4 below). This was done by applying iso-proportional slicing techniques described in the methodology section (*cf*. Fig. 6.3b). Greater emphasis is placed here on the upper two zones, which display greater degree of sand deposition (zone 1 and 2; Fig. 6.8b).

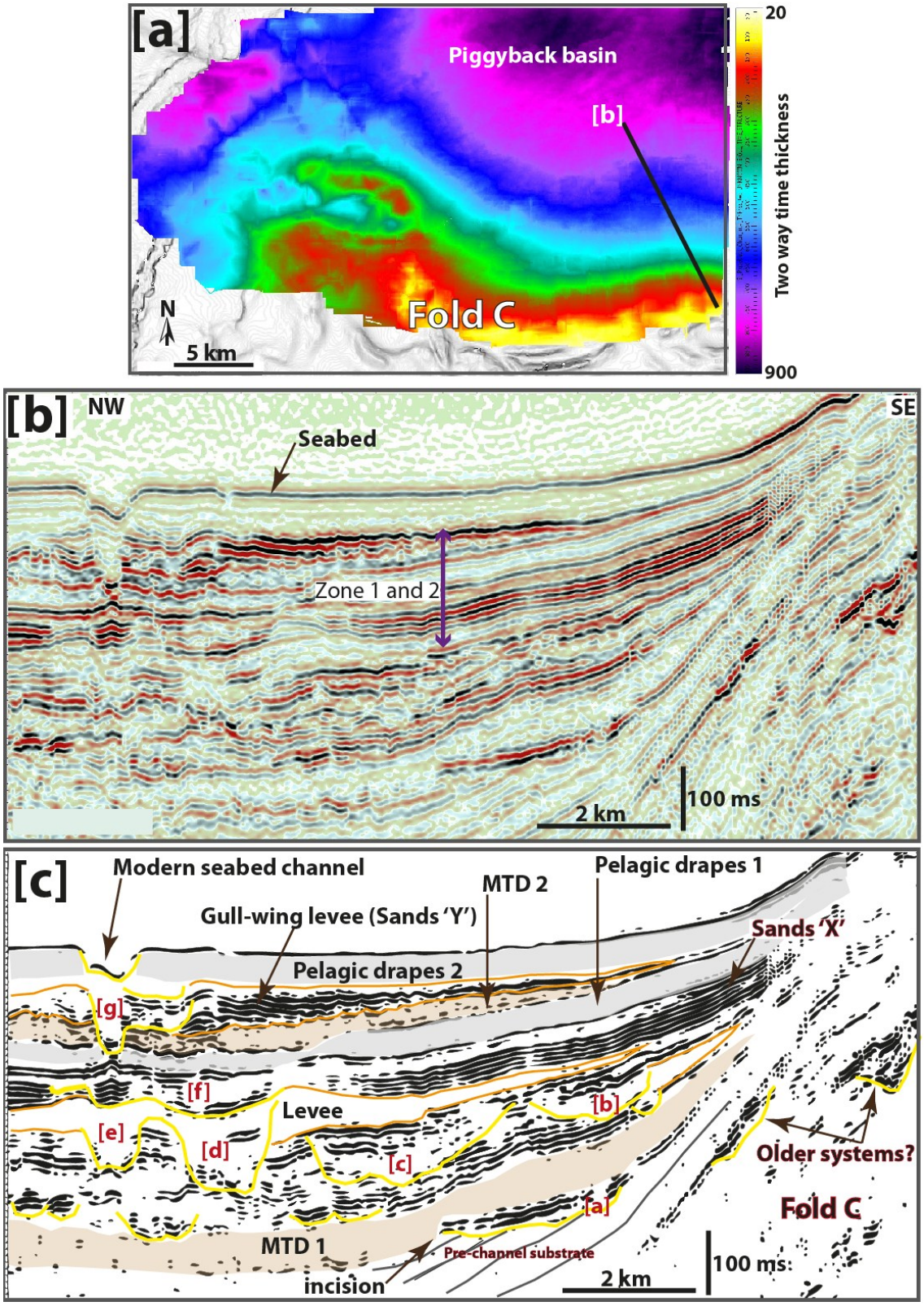


Figure 6.8: (a) Shows the two-way-time thickness map of the Plio-Pleistocene channel interval within the piggyback basin that developed north of Fold C; (b) shows a seismic section across the piggyback basin (see location in Fig. 6.8a); and (c) shows the interpreted version of the section. Note that the piggyback basin is dominated by channel/sheet-sands that show an increasing trend towards the top of the system.

6.5.4 Channel/sheet-sand evolution in the piggyback basin

Using the technique of iso-proportional slicing zone-RMS amplitudes were systematically calculated from the lower part, to the upper part of the Pleistocene channel system within the piggyback basin (zone 4 – zone 1, *cf.* Fig. 6.3b). In the lower part of the interval (zone 4/3; Fig. 6.9) a small number of channels can be observed (high-amplitudes indicated by blue colours). Channel [a] in zone 4 (see Fig. 6.8) appears to flow parallel to Fold C from east to west before deflecting at the fold tip (Fig. 6.9a, c). This channel [a] also shows evidence of gradual northward shifts within zone 4 (from position 1 to 3; Fig. 6.9c). Higher up in zone 3, channel [c] developed further north of channel [a] (Fig. 6.9b, c; see Fig. 6.8). Overall, the amplitude extraction in zones 4 and 3 revealed an increasing trend of channel development through time from zone 4 to zone 3 (Fig. 6.9). This increasing trend of channel development is also observed in the upper part of the Pleistocene channel interval (zones 2 and 1; Fig. 6.10). The upper intervals also contain high amplitude features, approximately 5 km wide and 18 km long, that trend broadly parallel to the channels. These are the sands 'X' and 'Y' identified in the seismic section in Figure 6.8c. In zone 2, Sand 'X' which is located on the limb of Fold C, is cut-through by mud-fill channel [f] that occurs above channel [d] (Fig. 6.10a, c; see Fig. 6.8c). In this same zone, a relatively lower amplitude unit, also consisting of sub-parallel higher amplitude reflectors, indicating that it is composed of sheet sand occurs further towards the basin centre, and is incised by incoming channels, X and Y (arrowed; Fig. 6.10a, b). In zone 1, Sands 'Y', located south of the mud-fill channel labelled [g] are slightly offset from Sands 'X' (Fig. 6.10b, c). These sheet-sands (X and Y) are elongated parallel to the axis of Fold C, and pinch out in the channel flow direction (Fig. 6.10a, b). Additionally, Sands 'Y' in zone 1 (Fig. 6.10b) are located off the limb of Fold C and further north of Sands 'X' in zone 2 (Fig. 6.10a, b) which suggests an element of structural control in their deposition (see Fig. 6.8b). The deposition of the sands appear to be triggered by active channel diversion in response to the growth of Fold C, as most of the sands occur on the outer bank bends of the associated channels (Fig. 6.10a, b).

Subtle wave-like perturbations are visible within the uppermost part of Sands 'X'. Edge and dip-azimuth attributes calculated from the mapped top surface of the unit reveal arcuate ridges on this surface, which are convex in the upstream direction (Fig. 6.11a, b). One possible origin of these features is sediment waves such as those described by Posamentier and Kolla (2003) on overbank deposits associated with turbidity current flow offshore Nigeria and offshore eastern Borneo. In plan-view, the waves are oblique and orthogonal to the modern-day channel flow direction (i.e., modern channel 2, Fig. 6.11b) and to buried channel systems (channel [f] and [g]) that are likely

associated with the sand deposits (Fig. 6.10). In section these features are very subtle, but there is hint that the wave shape is migrating to the east – i.e. upstream, which might indicate that these are sediment waves (Fig. 6.11b, c). However at the seismic resolution they lack the clear asymmetric geometry, and sediment accretion on the upslope limb visible on other seismically imaged sediment wave fields (Normark et al., 1980; Wynn et al., 2000a, 2000b; Normark et al., 2002; Posamentier and Kolla, 2003). Nevertheless they have wavelengths that range from 360 m to 500 m, and the wave heights range from 7 m to 8 m (Fig. 6.11c). The average slope of the limbs of these wave-like structures is approximately 2 – 3^{o}, and the trajectory defined by the crests and troughs of these waves is approximately convex-upward (white arrow) compared to that defined by the pelagic drapes 1 (black arrow) above Sand 'X' (Fig. 6.11c). Generally, their location on the outer bend of channel [f] suggests they may be associated with sand-rich levees deposited as the channel is being diverted in a similar way to Sands 'Y' (Fig. 6.10a, b); although there is no visibly preserved levee geometry. However, studies of turbidite systems in different deepwater settings by Normark et al. (2002) showed that these kinds of waves commonly develop on the outer bends of submarine channels where the overbank flow direction is parallel to the regional gradient. These authors also documented that these kinds of areas are associated with the development of thick turbidite sand beds that are often characterised by overbank sediment waves.

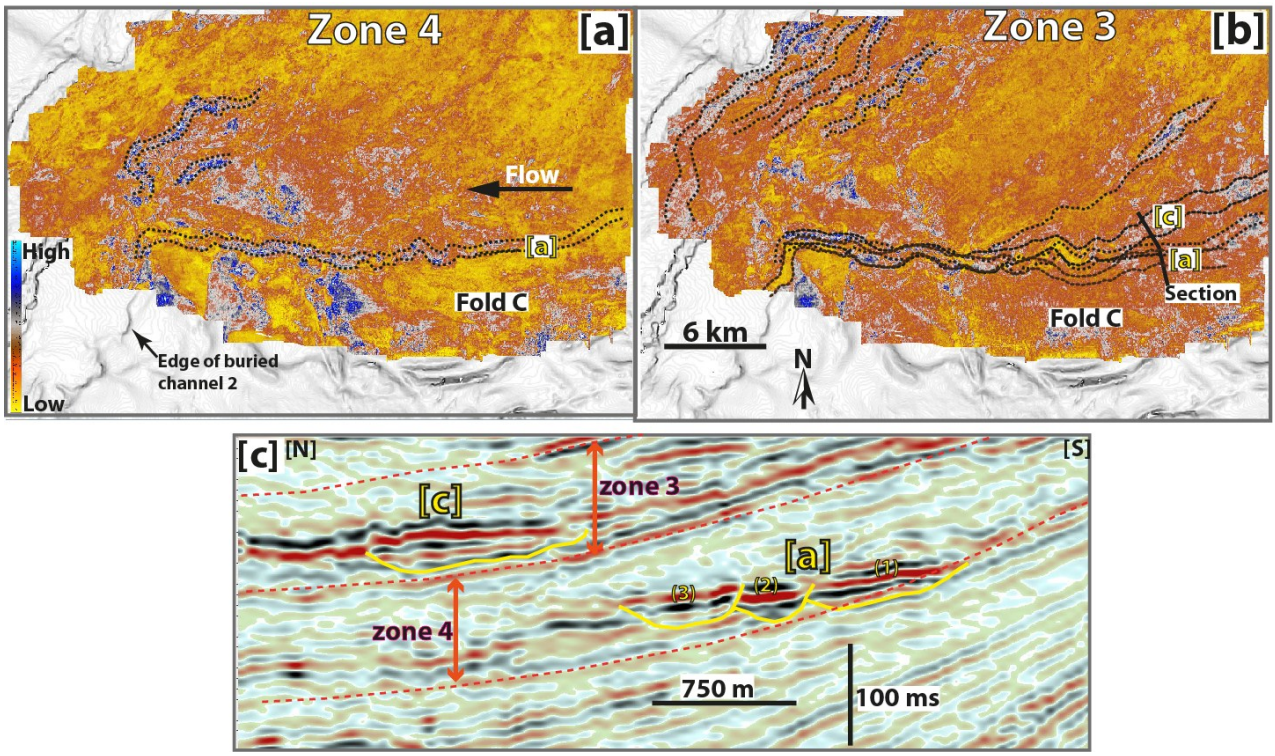


Figure 6.9: Shows zone-RMS amplitude maps of the Pleistocene channels interval within the piggyback basin: (a) zone 4 and (b) zone 3 (*cf.* Fig. 6.3b for the zones). The channels labelled *a* and *b,* flow parallel to Fold C from east to west while other systems are imaged flowing downslope. The seismic section (c), shows channel systems that are characterise by an overall northward shift from channel *a* – zone 4 to channel *b* – zone 3.

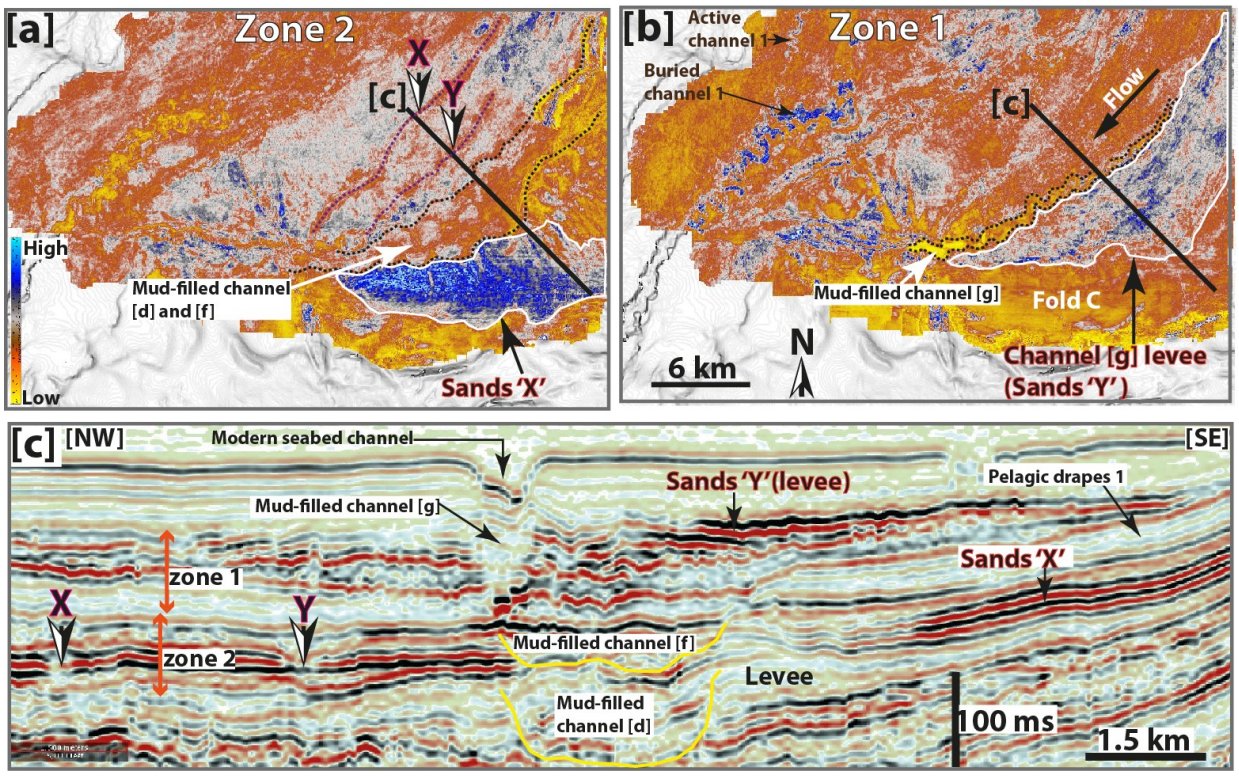


Figure 6.10: Show zone-RMS amplitude maps of the Pleistocene channels interval within the piggyback basin: (a) zone 2, (b) zone 1 (*cf.* Fig. 6.3b for the zones); and (c) seismic section showing channel/sheet-sands ('X' and 'Y') development in zones 2 and 1. These two zones at the top of the system are characterised by more sands development compared to the previous zones shown in Figure 6.9. Note that Sands 'X' in zone 2 is on the northern limb of Fold C, and Sands 'Y' in zone 1 is located further north of Fold C and Sands 'X'.

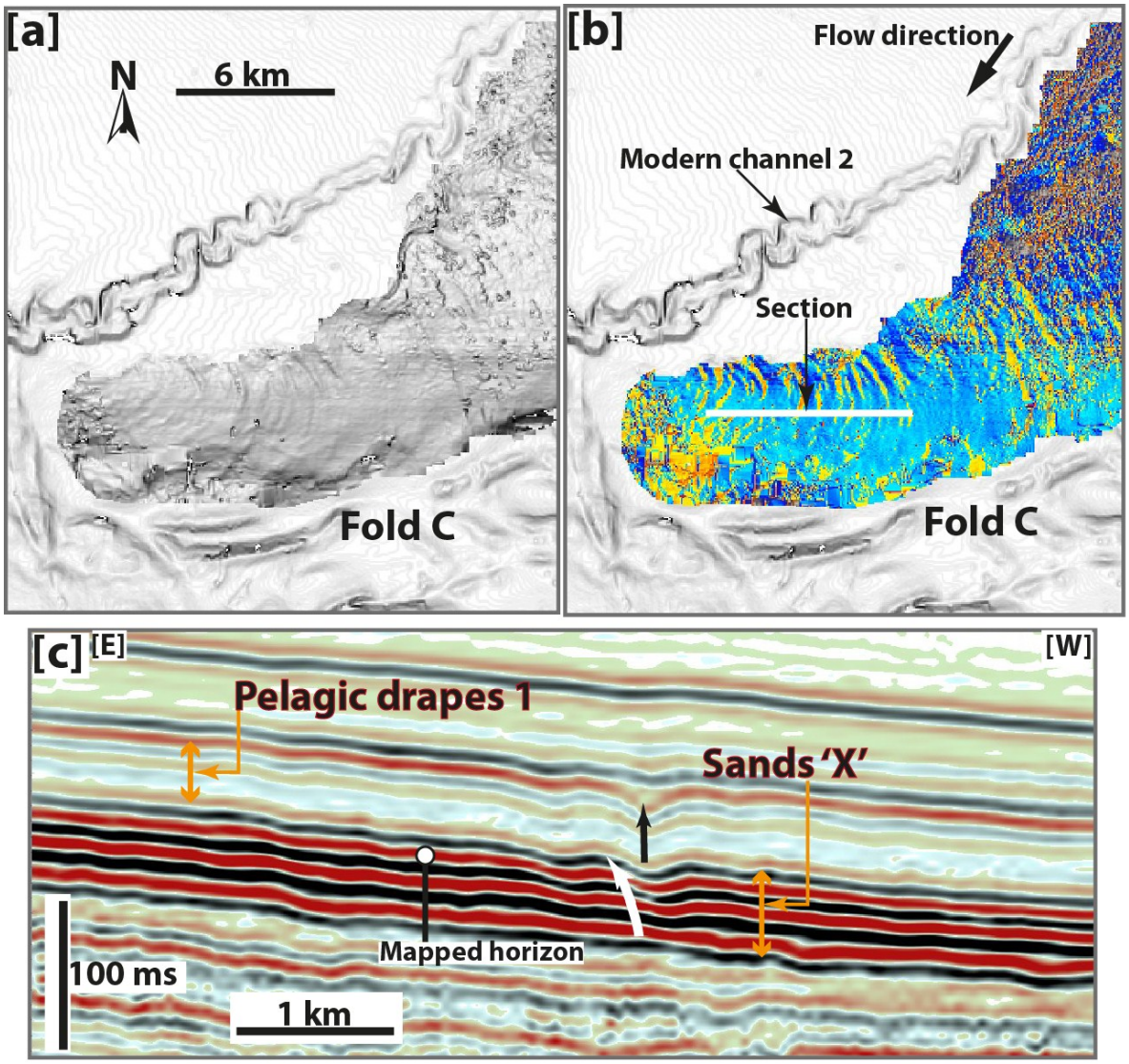


Figure 6.11: (a) shows the edge-map of the top horizon in Sands 'X' draped on seabed edge-map; (b) shows the dip-azimuth map of the same sand horizon also draped on the seabed edge-map; and (c) is an E – W seismic section showing the seismic characteristics of the sands (see location in Fig. 6.11b). These maps show the crests of sediment waves that are curvy – pointing up-stream, and oriented oblique and perpendicular to the modern seabed channel being diverted. The section shows the trajectory of the sediment waves crests and troughs which are convex-up (white arrow) and that of the low amplitude pelagic drapes 1 (black arrow).

6.6 DISCUSSION

6.6.1 Summary of the main points and interpretations

This study has found that the active channel systems (e.g., channel 4 container; Figs. 6.4 and 6.5) are characterised by greater preserved, stacked channel-axis sands compared to the buried systems which have more preserved mud (e.g., buried channels 1 and 5; Figs. 6.4 and 6.6). These buried systems are also characterised by thinly preserved, parallel high-amplitude reflections at the top of the systems, which are interpreted as top-channel sands deposited due to a sudden loss of flow power as the channel is forced to abandon its path (Fig. 6.6). The overall muddy nature of these buried systems suggests either (1) periods of channel erosion and by-pass with little or no deposition of sands, so that the systems were later filled with mud after the flows have ceased (see Mayall and Stewart, 2000; Mitchum and Wach, 2002); or (2) it may simply relate to the time-integrated flow evolution and channel erosivity. For example, the muddy parts of the buried system may represent deposition from a flow that gradually wanes through time. McHargue et al. (2011) showed that a typical turbiditic flow is associated with an increasingly mud-rich deposition through time. These authors reported that turbiditic flows are comprised of: (1) dominant erosion/sediment by-pass in the lower part, and overall amalgamation of channel elements that are rich in sands but with a low rate of aggradation; and (2) dis-organized to organized stacked channel elements that are generally mud-rich, and characterised by a high rate of aggradation in the middle to upper parts of the complex set. Consequently, the deposits from these flows are likely to be characterised by fining-upward sequences (e.g., preserved erosive surfaces that mark the bases of similar sequences in chapter 5; Figures 5.5, and 5.6). The implication is that subsequent flows will erode into these muddy fills (Fig. 6.6; see Clark and Pickering, 1996a; and discussion in chapter 5). However, because the buried systems shown in Figure 6.6 have been abandoned before subsequent flows could possibly incise deeply, most of these muddy fills are now preserved. The evidence for this sudden flow abandonment is the top-channel sands that have been preserved in these systems (Fig. 6.6). In contrast, channels that have been active for longer periods of time (up to 1.2 Ma; see chapter 5) probably had enough time to completely erode any preserved muddy-fill. Consequently, the active channel systems are characterised mostly by the preserved channel-axis sands that have been stacked as the systems gradually aggrade through time (Fig. 6.5; chapter 5; Deptuck et al., 2007; McHargue et al., 2011). Generally, these channel axes fills have the potential to form good reservoirs especially when they are stacked together into a high net-to-gross channel fill that is characterised by good to moderate fluid communication between the various cut-and-fill sequences (e.g., Mayall

and Stewart, 2000; Winker and Booth, 2000; Mayall et al., 2006; Cross et al., 2009). However, where they occur in isolation within a dominantly muddy fill, they may not form effective reservoir (e.g., the mud-rich buried systems; Fig. 6.6).

In the western part of the study area, an example of lobate-shaped, thin units of sheet-sands fed with flows spilling over the banks of buried channel 5, shows that they are often inter-bedded with thick units of MTDs and pelagic drapes within sub-basins bounded by growing fault-propagation folds (e.g., Fig. 6.7a, b, c). These fault-propagation folds have crestal widths that are approximately 2 km or less, and are often characterised by both buried and modern seabed scarps (e.g., Fig. 6.2a, b, c; chapter 3). Some of the MTDs may be sourced from the degradation of the forelimbs of the fault-propagation folds in the west (indicated by the presence of seabed scarps – see Fig. 6.2b and chapter 3). Detailed description of seabed scarps and their role as sources of mass flows (slumps and debris flows) in deepwater Niger Delta have been documented by Heinio and Davies (2006). The sheet-sands (splays) can be very extensive and cover a significant area, and are likely to have high porosities and permeability thereby constituting significant exploration targets especially in deepwater settings (Hackbarth and Shaw, 1994; Booth et al., 2000; Posamentier and Kolla, 2003; Cross et al., 2009).

Sheet-sands ('X' and 'Y') in the east (within the piggyback basin bounded by the broad detachment fold) are more likely to have been deposited in the form of sand-rich levees on the outer bends of the diverting channels, and these sheet-sands may be characterised by sediment waves (e.g., Fig. 6.10; Fig. 6.11; see also Normark et al., 1980, 2002; Wynn et al., 2000a, 2000b; Posamentier and Kolla, 2003). For example, channel, *g*, in Figure 6.10b is characterised by a low amplitude fill (mud), and the amplitudes within the levee deposited on the inner-bend of this channel are relatively low whereas the amplitudes on the outer bend is very high (Fig. 6.10b, c). These observations suggest that the active diversion of channels by the growing detachment fold (Fold C) causes the flows to breach their outer-bend banks and spill over with entrained sands which are blocked in the down-stream direction by Fold C. Consequently, these sheet-sands are characterised by elongate-shaped geometry that is parallel to the growing structure and appears to pinch-out in the down-stream direction (Fig. 6.10a, b).

In this piggyback basin area, channel development and sheet-sands deposition dominate over the deposition of MTDs and pelagic drapes. For instance, the thickness of Sands 'X' deposited within zone 2 is up to 45 m, and hence would make a very good reservoir with enhanced vertical fluid communication between separate splay bodies (Fig. 6.11c; see Hackbarth and Shaw, 1994; Booth et al., 2000; Normark et al., 2002; Posamentier and Kolla, 2003). The MTDs within the piggyback basin are likely to have been sourced from distance areas upslope as there are no prominent scarps associated with Fold C.

6.6.2 Controls on facies distribution and facies architecture

The evolution of structures in the study area varies slightly from the west (dominated by fault-propagation folds) to the east where a large detachment structure (Fold C) occurs (Fig. 6.2). Consequently, the evolution of these structures has influenced the spatial distribution, and the temporal organisation of both crevasse splays and sheet-sands in these parts of the study area. For example, in the west of the study area, the style and location of channel avulsion (breaching of levee by channelized flows) and the locus of the flows after avulsion, is controlled by the distribution of topographic and structural relief (including the presence of seabed scarps) of the fault-propagation folds (e.g., Fig. 6.7a; Fig. 6.12a). For instance, in Figure 6.7a, channelized flows are more likely to breach the channel levee at the fold tips locations where the channel is deflected and bends sharply. At these breach points, significant gradient changes (between 1^{o} to 4^{o}) in response to fold growth also occur. Thus in response to the change in topography (gradient change), the flows may expand immediately adjacent the channel and deposit a crevasse splay (e.g., Splay 1; Fig. 6.7a; see also Mayall and Stewart, 2000; Cross et al., 2009; Janocko et al., 2013). However, the flow may become channelized before it eventually expands laterally down-dip on encountering another change in topographic relief (e.g., at point Z – Fig. 6.7a). Individual channelized flows observed within Splay 1 – (labelled (i) – (iii) in Fig. 6.7a), appear to curve as they avoid the structural/topographic relief associated with Fold A prior to converging at point X. Moreover, on exiting the constriction at point X, and into the basin bounded by Folds A and 'L'; Splay 1 is defined by two main branches as it once again, avoids the structural/topographic relief associated with Fold 'L' (Fig. 6.7a). These areas of topographic relief along individual folds are often characterised by the presence of seaward-facing scarps (Fig. 6.2b; Fig. 6.12a; see also Heinio and Davies, 2006). In essence, crevasse splays that developed in the west of the study area are mostly very thin units (represented by 1 – 2 seismic reflections) inter-bedded with relatively thick units of slumps and pelagic drapes (e.g., Fig. 6.7b, c;

Fig. 6.12a). This suggests that sheet-sands (crevasse splays) deposition in the west of the study area is likely to be intermittent, and may coincide with periods of significant tectonic perturbations by the growing fault-propagation folds – which caused the channel to avulse.

In contrast, sheet-sands deposition in the east of the study area (i.e., within the piggyback basin), appear to be consistent over time forming relatively thick, stacked sand units (Fig. 6.8b). Here, sheet-sands are deposited mainly by channels that are being forced to divert by Fold C (Fig. 6.10a, b; Fig. 6.12b). These sheet-sands (sometimes characterised by sediment waves), are gradually incorporated into the northern limb of the growing detachment fold as it broadens through time (Fig. 6.8b; Fig. 6.12b). For example, the offlapping architectural geometry displayed by Sands 'X' and 'Y' (Fig. 6.10) suggests that these sands were initially deposited within the syncline to the north of Fold C (such as the present position of Sands 'Y' in Figure 6.10b), but as the fold broaden with time (*cf.* Fig. 6.2d), the sands are eventually incorporated into the northern limb of the structure (Fig. 6.12b). Consequently, the temporal organisation (architecture) of the channel systems, labelled 'older systems' (Fig. 6.8c) may indicate channel development and abandonment during early, slow growth phase – punctuated by periods of non-channel development/avulsion and deposition of pelagic drapes (e.g., Weimer, 1991; Piper et al., 1997; Pirmez et al., 1997; Beauboeuf and Friedmann, 2000; Winker and Booth 2000; Posamentier and Kolla, 2003; Droz et al., 2003). However, as channel development increases with time (between zone 3 and 1; Figs. 6.9, 6.10), the deposition of sheet-sands by diverting channels also increases. As a consequence, these sands appear stacked and characterised by offlapping architecture towards the top of the Pleistocene channel system as the detachment fold grows and incorporate the sands (Figs. 6.8b, 6.12b).

Generally, the analyses of facies distribution in this chapter have demonstrated the importance of being able to constrain the growth of structures and the potential effects on the depositional system of deepwater. These kinds of analyses can be used to predict the potential responses of deepwater channels to growing structures, and the resultant effect on the distribution of sand-grade sediments that form deepwater reservoirs (see Hackbarth and Shaw, 1994; Prather et al., 1998, 2000; Booth et al., 2000; Winker and Booth, 2000; Mayall and Stewart, 2000; Posamentier and Kolla, 2003; Gee and Gawthorpe, 2006; Mayall et al., 2010; Prather et al., 2012). The knowledge gained from these kinds of analyses can be used to develop models for complex deepwater reservoirs, which in-turn, can be used to predict reservoir facies distribution, temporal organization and how they are connected through time (e.g., Posamentier and Kolla, 2003; McHargue, et al., 2011; Prather et al., 2012).

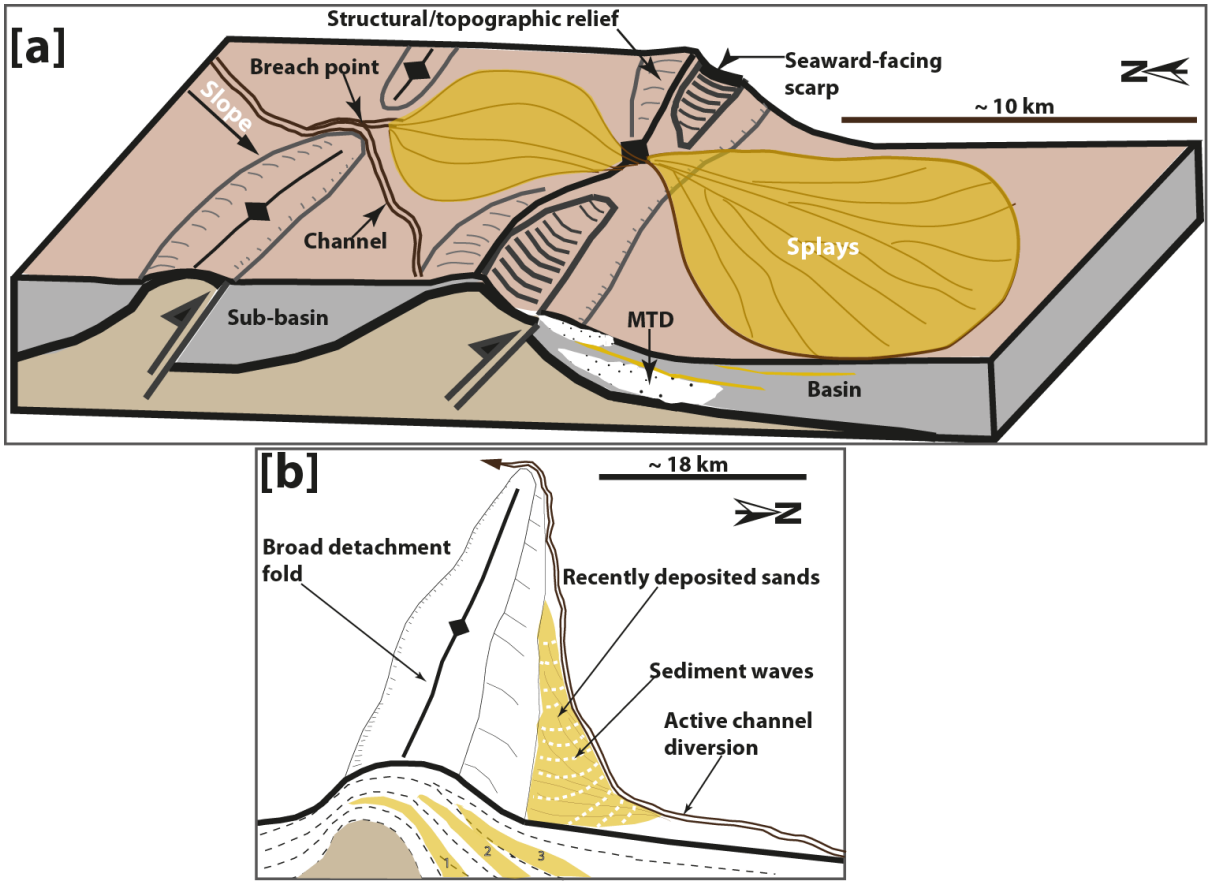


Figure 6.12: Shows cartoon description of structural controls on sheet-sands (splays) distribution in the west of the study area (a); and within the piggyback basin in the east of the study area (b). In the west, flow breaching of channel levees at fold locations results in flow spreadind and deposition of lobate-shaped crevasse splays. Note that the spatial extent of these splays is controlled by the structural and topographic relief associated with seabed scarps. In the east diverting channels are forced to deposit sheet-sands which are sometimes characterised with sediment waves. These sands are blocked by Fold C (a broad detachment structure); before being incorporated into the growing fold.

6.7 CONCLUSIONS

The channel systems in this study are characterised by preserved channel-axis sands (characterized by medium to high amplitude, discontinuous, chaotic seismic reflections which are interpreted as coarse sands/basal lags). These are concentrated in the lower part of the channel system, and are often encased within low-amplitude fill which could be debris flow material, slumped material from channel margins or internal levees on smaller scale channels within the main channel complex. Channel systems that are still active, have less preserved, low amplitude fill compared to systems that have been abandoned and buried. The buried systems are also characterised by the deposition of top-channel sands which were deposited in some remaining seafloor topography associated with the channels close to their point of abandonment.

Sheet-sands are deposited outside the channel system by turbiditic flows that are capable of breaching the channel levee either at structural locations (fold tips) or as the channel system is blocked and forced to divert. Crevasse splays deposited within sub-basins in the west of the study area are characterised by lobate-shaped geometry in plan-view (up to 10 x 15 km in area coverage); and in section, they are represented by thin units (1 – 2 seismic reflections) inter-bedded with thick units of MTDs and pelagic drapes.

The sheet-sands deposited by diverting channels in the east of the study area are elongated parallel to growing Fold C where the associated channels have had to divert. Towards the top of the system in this area, thick sand bodies form, and have been incorporated into the northern limb of Fold C.

Mass transport deposits which are characterized by low to medium amplitude, chaotic seismic reflections; and pelagic drapes which are characterised by low frequency, continuous, low – high amplitude seismic reflections are also present. These facies dominate in the west of the study area compare to the east.

Analyses of facies distribution in this study have demonstrated the importance of constraining structural growth and the resultant effect on the depositional system of deepwater in general. These kinds of analyses, and knowledge gained, can be applied to predict the responses of deepwater channels to growing structures, and the potential distribution of coarse-grained sediments that form deepwater reservoirs.

CHAPTER 7

DISCUSSION

The analyses presented in this thesis are organised into four results chapters (chapters 3 – 6), which collectively address the seismic and geomorphic expression of submarine channels in the toe-thrust region of the Niger Delta, and the interactions these channels have had with growing folds and thrusts over time. Chapter 3 addresses the growth histories of fold-thrust structures having seabed relief from the Miocene – Present; and the large-scale impact of these fold growth on the pathways of channels that developed coevally with structural deformation. Chapter 4 analyses the detailed geomorphic responses of modern channels (i.e., recently active channels) to this tectonic framework; and chapter 5 analyses the subsurface parts of these channel systems, and those recently buried, within the Pleistocene to Recent strata. In essence, these two complementary chapters (chapters 4 and 5) quantify the down-system variation in channel morphometric parameters in response to the tectonic boundary conditions governing their evolution. Consequently, these results allow us to compare the down-system trends in channel geometries and the bathymetric long profiles through time from the profiles of the lowermost erosive surfaces of the channel systems to the associated modern channel-thalweg profiles in each system. Finally, Chapter 6 analyses the overall structural controls on the distribution of seismic facies in the study area. In particular, the chapter analyses the spatial and temporal distribution of seismically recognisable facies, with particular emphasis on the distribution of sands both within the channel systems and outside the channel systems in the form of splays. The chapter also analyses the role of tectonic perturbations in determining the splay geometry and temporal architecture and how these vary from the west to the east of the study area. These four chapters present a coherent set of results that address, on both small and large scales, the evolution of sedimentation and deformation (i.e., channel – structure interactions) in the deepwater Niger Delta study area. Consequently, the results in this thesis are discussed under four themes (section 7.1 to 7.4 below) which capture and integrate the major findings in this thesis. Finally, this discussion addresses potential applications of this work, and considers some key research areas which now need to be developed, based on the work presented in this thesis.

7.1 GROWTH HISTORY OF FOLDS/THRUSTS AND THEIR EFFECTS ON CHANNEL PATHWAYS

The results in chapter 3 show that the growth of the thrust-related folds in the study area has taken place since 12.8 Ma and many of the thrusts are still actively growing although, the growth rate (fold shortening rate) has reduced significantly since 3.7 Ma (see Fig. 3.11). All structures in the study area exhibit similar growth patterns and those with structural/topographic relief (e.g., Folds A – D), are also associated with a counter-regional slope (of between 1.5^{o} and 2^{o}). However, both the height of this positive relief, and the length of the counter-regional slope associated with the fault-propagation folds that occurs in the west of the study area is low compared to the broad detachment fold that occurs in the east of the study area (see Fig. 3.15; Fig. 5.13). The positioning of channel pathways show that channels that develop coevally with structural growth and that cross structures (fault-propagation folds), do so in positions of recent strain minima and at interval strain rates that are generally less than -0.02 Ma^{-1} (15 m/Myr). However, the broad detachment fold has caused channel diversion at an even lower strain rate (Fig. 3.11).

Generally, these results indicate an overall decrease in fold growth from 3.7 Ma to date. However, the total shortening for the structures since growth began varies from approximately 4 km (Fold D; Fig. 3.11) to ~ 1km (Fold C; Fig. 3.11); giving a time-averaged maximum shortening rate of between 350 $\pm$50 and 90 $\pm$10 m/Myr (0.4 and 0.1 mm/Yr). In the last 3.7 Ma when fold growth has slowed down, the respective total shortening rates in Folds D and C is 50 $\pm$5 and 40 $\pm$5 m/Myr (0.05 and 0.04 mm/Yr). Wu and Bally (2000) reported that the observed total shortening across the Niger Delta fold belt is significantly higher than in the fold belts of the northern Gulf of Mexico. Rowan et al. (2004) reported a total maximum shortening of ~10 mm/Yr from a restored regional section (with approximately 17 interpreted thrust-folds) in the fold belt of Niger Delta. Assuming the shortening is equally distributed across the 17 folds, the rate for individual thrusts will be ~0.6 mm/Yr which is approximately the same magnitude with the maximum recorded shortening across Fold D since growth began at approximately 12.8 Ma (see chapter 3). In the offshore NW Borneo fold-thrust belt, Morley (2009) reported an average shortening rate of approximately 2 mm/Yr for a syn-growth horizon that is ~3 million years old. This author showed that the shortening of the syn-growth horizon represents approximately 10 % of total shortening across the fold belt. However, the author also reported that the estimated maximum shortening using a deeper pre-growth horizon is approximately 17 % (~3.5 mm/Yr). Thus, comparing this maximum shortening with the maximum of approximately 10 mm/Yr across the Niger Delta fold belt (Rowan et al., 2004), shows that Niger Delta thrust belt is shortening at a relatively faster rate.

This research has also documented how fold shortening varies spatially from structure to structure, and through time (see chapter 3), and that these variations can determine channel pathways. In another study from the Niger Delta thrust and fold belt, Higgins et al. (2009) also showed how the younger syn-growth strata of a major fault-propagation fold tend to overlap the growing structure, and there is a general absence of discrete onlap towards the fold crests. This qualitatively indicates a slowdown in growth through time. This slowdown in growth during the later stages of fold growth where most of the sediments continue to overlap the growing structures is also an indication that the active growth associated with the gravitational shortening of the delta may now be taken up by structures further basinward as the delta progrades (e.g., Morley, 2007, 2009). Seismic analyses of growth sequences over this period of reduced fold growth in the study area show a dominantly overlapping geometry relative to the fault-propagation folds traversed by Pleistocene to Recent channels. Previous workers both using theoretical models (e.g., Suppe et al., 1992; Hardy and Poblet, 1995) and field-based studies in terrestrial fold and thrust belts (e.g., Burbank and Verges, 1994, Burbank et al., 1996) have demonstrated that overlapping growth strata geometries signifies a slowdown in structural uplift relative the sediment supply.

The growth sequence geometry/architecture observed in this study suggests that the sediment accumulation rate within the synclines created by growing folds is relatively higher than the growth rate of these structures in the last 3.7 Ma. Hence, the implication is that the Pleistocene channels that developed coevally with deformation are likely to keep pace with fold growth, and flow perpendicular and across growing folds (especially the fault-propagation folds with both fold crest widths, and counter-regional slopes that are less than 2 km). Moreover, the overall aggradation of the channel system fill even over fold crests, and the dominantly overlapping geometry of the growth units over the last 3.7 Myrs (see chapters 3, 5, 6;), suggest that incoming channels may be able to keep pace with fold growth if there is a higher ratio of aggradation upstream of the fold barrier.

7.1.1 COMPARISON WITH FLUVIAL SETTINGS

Several studies of fluvial systems in foreland basins and fold and thrust belts have documented similar large-scale channel – structure interaction (e.g., Burbank and Verges, 1994; Burbank et al., 1996; Humphrey and Konrad, 2000; van der Beek et al., 2002). For example, Burbank et al. (1996) reported that overlapping growth sequence geometry tends to characterize areas where fluvial channels are more likely to flow perpendicular to structures; and onlapping growth sequence geometry is associated with structures where channels tend to flow parallel to them. These authors also demonstrate that some of the large scale controls that determine if a river is likely to traverse growing structures include; (1) low rates of fold crestal uplift , (2) the bedrock resistance to erosion, (3) rates of sediment aggradation and (4) the specific stream power (such as the bed-shear stress documented in chapter 4 of this thesis). Moreover, coupled numerical modeling has also been used to analyze how rivers respond to fold uplift (e.g., Humphrey and Konrad, 2000; van der Beek et al., 2002). For example, Humphrey and Konrad (2000) have shown that river sediment flux and the aggradation rate, determine how rivers respond to uplift along their courses. They show that where sediment aggradation in the upstream part of the barrier is able to keep pace with fold uplift, the channel can incise across, otherwise the channel will be diverted. However, van der Beek et al., (2002) demonstrate that while the relative rates of fold uplift and fluvial channel incision are important, the dip of the underlying detachment is also very important in controlling how fluvial systems respond to active folds acting as barriers along their paths. Generally, these studies have demonstrated the importance of fold growth rate and sediment accumulation rate (often determined by the growth sequence geometry) in determining fluvial channel response to deformation. The interaction between fold growth rate and sediment accumulation rate has been rarely addressed in the deepwater fold belt literature but Shaw et al. (2004) did note that during periods of rapid uplift of the fold crest that sedimentation would be restricted to the back-limb of folds, but that when growth slowed, and back-limb accommodation space was filled, channel systems could cross the crest of the fold. Likewise Morley (2009) in his study offshore Brunei demonstrates that regions where fold growth is slow relative to sediment supply can become pathways for sediment transport. In terms of the other factors that the fluvial literature identifies as being important in controlling when channels can cross growing folds, Mayall et al. (2010) considered that the erosive power of sediment gravity flows within channels must influence whether channels can continue to incise across a growing structure.

The results in this thesis (chapter 3) show that the general behavior of submarine channel systems can often be broadly similar to fluvial systems in terms of the relationship between fold growth and growth sequence geometry. Moreover, I have demonstrated in this thesis that submarine channels that are already in-place, and flowing across active structures, with short counter-regional slopes (i.e. short wavelengths), are likely to keep pace with structural growth rate of approximately 15 m/Myr or less. However, even at comparably lower growth rates, broad structures with greater than 5 km long counter-regional slope are likely to cause channel diversion (see Fig. 3.15 in chapter 3). Interestingly, Burbank et al. (1996) in their conclusions also predict that another factor that will facilitate the persistence of a river across a fold with topographic expression is small fold wavelengths, as has been observed in western part of the thesis study area. While there are similarities between submarine channel systems and their fluvial counterparts, it is important to note that there are significant variations in channel form and flow/depositional characteristics such as flow overspill/avulsion at meander bends as channels navigate round structures or are forced to divert (chapter 6; see also Clark and Pickering, 1996; Peakall et al., 2000; Normark et al., 2002; Mitchell, 2006; Kolla et al., 2007; Straub et al., 2008). Thus, comparison of submarine channel behavior to that of fluvial system should be treated with caution.

7.2 CONTROLS ON CHANNEL GEOMETRY AND LONG-PROFILES

The results in chapters 4 and 5 present detailed analyses of the variations in the channel system geometries as they respond to fold growth. These results show that modern channel systems have widths that lie between 1100 m and 2400 m; and incisional depths vary from 10 m to as high as 140 m for the active channel-thalweg of modern channels that are open at the seabed. These modern channels have bathymetric long-profiles that are relatively linear with concavity that ranges from -0.08 to -0.34, and an average gradient of c. 0.95^{o} (see Fig. 4.6). Modern channel incision across growing structures where relatively small knickzones develop along the channel pathway, is achieved through enhanced bed-shear stress driven incision (up to 200 Pa) and flow velocity (up to 5 m s^{-1}). However, in most cases, the modern channel widths remain fairly constant down-system, in contrast to fluvial systems in which channel width narrowing is commonly observed in areas of structural uplift (e.g. Whittaker et al., 2007a, 2007b). On the other hand, the lowermost erosive surfaces (channel 'containers') bounding cut-and-fill sequences forming the Pleistocene to Recent submarine channel systems, have profiles that are generally convex to irregular (see Fig. 5.9). Moreover, the channel system (container) is associated with an overall width narrowing, and a time-integrated channel incision into the pre-channel substrate, and into the preserved container fill by modern channels as the systems aggrade (Figs. 5.5, 5.6). Consequently, the preserved thickness of the channel fill over the crests of growing structures is low (see Fig. 5.11). These results show that the higher convexities of the container profiles represent the effect of time-integrated, cumulative structural uplift – evident from the folding of the preserved erosive surfaces within the container fill over fold crests (e.g., Fig. 5.5a in chapter 5).

This thesis has shown that the shapes of submarine channels largely depend on how they behave and respond to structures affecting their pathways. In particular, the results in this thesis have shown that modern channels widths appear insensitive to variations in fold uplift along their paths (see chapter 4). This is in stark contrast to the general behaviour of rivers (e.g., Amos and Burbank, 2007). For example, Amos and Burbank (2007) reported that fluvial system crossing small folds appear to respond by simply narrowing their widths without significant increase in incision; and when crossing large folds, they first narrow their widths, and then followed by significant increase in channel incision. However, the analyses of the cut-and-fill sequences (channel system containers) show an overall behaviour that is similar to fluvial systems. In this case, the channel containers show overall width narrowing and a time-integrated channel incision over active structures. Similar width narrowing has been reported for a buried submarine channel crossing a deepwater fold by Mayall et al. (2010)

Whilst in general, an ideal concave up-up equilibrium profile over 100s km from the shelf-edge to the basin floor is expected for submarine channel-levee with net erosion dominating the upper reaches of the system and deposition in the lower reaches (e.g. Pirmez et al. 2000; Kneller 2003; Ferry et al., 2005), modern channel-levee systems with linear profiles, akin to those documented in this thesis appear to be a characteristic of the parts of deepwater slopes with a deforming seabed (Pirmez et al., 2000; Covault et al., 2011). The results presented in chapter 5 indicate that the linear to concave profiles of the associated modern channels in this thesis represent a time-integrated channel incisional response to the time-integrated fold uplift over periods of up to 1.3 Ma (see Fig. 5.10 in chapter 5). Moreover, the modern channel profiles in this study are found to be in topographic steady-state with respect to the time-integrated structural uplift along their paths. These results imply that the steady-state long-profiles of submarine channels in a gravity-driven system like the Niger Delta, are more likely to be linear than concave.

Importantly, unlike river channels where the increase in drainage area provides a predictable increase in discharge that can be balanced by declining channel slope, it is difficult to predict how the flow evolution (including for example the incorporation of ambient sea water) in submarine channels varies with decreasing slope (see Gerber et al., 2009). Several studies of fluvial systems have demonstrated the existence of a clear relationship between concave-up river long profiles, and stream power driven incision, hence emphasising the importance of channel slope and discharge in achieving topographic steady state – for which a well-established power-law relationship exists (see Hack et al., 1953; Howard, 1994; Tucker and Bras, 1998; Whipple and Tucker, 2002; Tucker and Whipple, 2002; Whittaker et al., 2007a; Yanites et al., 2011; Whittaker, 2012). Many attempts have been made to analyse, and possibly formulate a 'power-law' relationship that underpins the form or time-integrated evolution of a steady-state or 'equilibrium' submarine channel profiles in an equivalent manner to fluvial systems, but these have yielded different results for different settings because submarine systems show a great diversity in form and morphology which depend on many variables (e.g., Clark and Pickering, 1996a; Prather et al., 1998; Pirmez et al., 2000; Kneller, 2003; Mitchell, 2006; Gerber et al., 2009; Covault et al., 2011; Konsoer et al., 2013).

In general, this work suggests that (i) slope and incisional depth are important in any erosional law and that a physically reasonable starting point is that channel incision is linearly proportional to bed-shear stress and hence channel slope; (ii) that channel width is not as sensitive as in fluvial channels; (iii) the existence of local knickpoints in the quasi-linear channel long-profiles near growing folds, suggests that any long-term erosional law needs to have both an 'advective' component as well as a diffusional one, as also demonstrated by Mitchell (2006). However any submarine equivalent of a

stream power erosion law needs to address the fact that the frequency and size of flows must be taken into account (see Xu et al., 2010; Xu, 2011; Talling et al., 2012, 2013). Therefore, a wider range of studies forensically examining submarine channel evolution is clearly required to broaden our overall understanding of how submarine channel systems behave and evolve through time for a range of fault and fold growth rates. It is suggested that first-order estimates of the distributions and potential magnitudes of flow velocities and the down-stream variations in bed-shear stress (chapter 4) from well-constrained channel geometry data is an effective way of analysing submarine channel evolution, and this could be applied to other seismic data sets. These parameters are often very difficult to measure directly from real flows, and only very few examples of natural flow velocities have been reported based on indirect analysis from submarine cable breaks or from direct measurement using measuring instruments – that are often destroyed by the devastating nature of turbiditic flows (e.g., Xu et al., 2004, 2010; Meiburg and Kneller, 2010; Xu, 2011; Talling et al., 2012, 2013). Moreover, there has not been an accurate, direct measurement of turbiditic flow concentration despite years of trial; these are often estimated/assumed, or obtained from modelling (see Pirmez and Imran, 2003; Xu, 2011; Talling et al., 2012); and the coefficient of bed-friction has never been measured directly – these are often estimated using values from large rivers (e.g., Konsoer et al., 2013). Despite these problems the approach in this thesis gives good insights into how turbiditic flow parameters may vary down channel systems affected by structural deformation.

7.3 CONTROLS ON CONTAINER ARCHITECTURE AND SEISMIC FACIES DISTRIBUTION

The results presented in chapter 5 show that variations in container width and container fill thickness is caused by both the time-integrated channel incision/erosion down-system, and the process of continued channel deflection/migration away from the tip of growing structures. High channel incision over the crests of growing folds causes the container to narrow its width with an overall lower deposition/preservation of container fill over time. Continued channel deflection/migration away from the tip of growing structures causes the container width to increase with an overall higher deposition/preservation of container fill (e.g., Fig. 5.8 in chapter 5). Consequently, the results documented in this thesis show that the evolution of the container system is related to both the effect of tectonic perturbation and channel incisional and depositional processes through time. These controls also vary from channel to channel, and down-system of individual channels. For example, in buried container 2, active deflection of incoming channels by Fold C has caused the container system to widen significantly upstream and downstream of Fold C (Fig. 5.7 in chapter 5). In contrast, significant container narrowing occurs in a region close to the tip of Fold C where the channels have incised, and are able to keep pace with fold growth for a very long time (up to 1.3 Myrs). This suggests that both tectonic and channel processes can govern the stacking pattern of the cut-and fill sequences observed within the container system (e.g., Fig. 5.8). This implies that stacking patterns often reported in submarine channel systems (e.g., Mayall et al., 2006; Deptuck et al., 2007; Janocko et al., 2013) as being related to channel processes especially at meander bends (e.g., Kolla et al., 2007) may only be partially true, and merit careful examination if associated with growing structures. The stacking patterns of the cut-and-fill sequences in submarine channel systems forming on an actively deforming seabed are likely to have developed through a combination of tectonic and channel processes in which the tectonic boundary conditions governed the long-term evolution of the system (see chapter 5). For example, in Figure 5.8b, we see a trend of dominantly lateral migration to the west in the lower part of buried container 2 in response to the growth of Fold C; and as the channel moves further away from the growing fold, deposition/aggradation and levee development became dominant as the tectonic influence reduces. Consequently, both the container width and depth increased with time, and the preserved container fill thickness is high because of lower overall channel incision relative to aggradation. However, the high channel incision relative to aggradation on the flanks of Fold C (where modern channels following the path of buried container 2 continue to incise across; Fig. 5.7b) has resulted in lower container width and preserved fill/depth between 20 km and 35 km down-system (see Fig. 5.12d). In essence, the combination of channel incisional and aggradational processes appears to be coupled

to time-integrated tectonic perturbations produced by growing structures in the study area. These processes have affected the general distribution of preserved, time-integrated channel container fill, especially in the fold crest areas where the time-integrated fold uplift is significant. Mayall et al. (2010) in their study of slope channel systems responding to growing folds and salt structures show a variety of similar features such as offset stacking of channels on flanks of growing structure, and they also document that coarse basal lags can become stacked and amalgamated; amongst other related things.

The growth of folds and thrusts which have influenced the general evolution of the channel container, have also influenced the spatial distribution, and the temporal organisation of sands deposited in crevasse splays and lobe-like splays in the study area. For example, in chapter 6, channels are observed to be more likely to breach through their flow paths at fold tips locations in response to tectonic perturbations created by these folds. Consequently, sands are deposited in both crevasse splays and lobe-like splays fed from a side channel within localized depocentres between the growing folds. Likewise Mayall et al. (2010) document a similar splay that developed in response to a structurally induced deflection of a channel, with overspill from the channel at the sharp bend. The implication is that continued tectonic perturbations are likely to determine both the spatial and the temporal organization of reservoir facies in deepwater environments. For example, splays may occur not only as pre-avulsion features such as those described on modern fans but may form by turbiditic flows that are capable of breaching the channel levee at fold tips locations as the channel systems negotiate sharp beds. The variation in structural styles also determines the depositional style and organization of levee sands on the flanks of fold C in the study area (chapter 6). Hence, this work has shown that channel – structure interaction also influences the distribution and location of sands that form important reservoir targets in deepwater hydrocarbon exploration.

7.4 WHAT ARE THE CIRCUMSTANCES IN WHICH CHANNELS CAN CUT ACROSS GROWING FOLDS AND THRUSTS IN DEEPWATER FOLD AND THRUST BELTS?

Studies of both channels in deepwater settings (e.g., Shaw et al., 2004; Morley, 2009; Clark and Cartwright, 2009; Mayall et al., 2010) and channels in terrestrial settings (e.g., Burbank et al., 1996; Amos and Burbank, 2007; see section 7.1.1 for details) have documented some of the controlling factors that may likely play key roles in determining whether channels are capable of flowing perpendicular to structures or not. For example, Morley (2009) in his study of fault-propagation folds in the offshore NW Borneo thrust and fold belt, showed that the transport pathways of gravity flows are influenced by anticline surface topography. He further described qualitatively, a range of factors that may facilitate channel incision across folds such as channel exploitation of relay areas between folds, exploitation of weak points on fold crest (e.g., created by mud pipes and gas chimneys) and slow growth rates relative to sediment supply. Clark and Cartwright (2009) discuss specific structural geometries expressed at seabed that will cause channels to be deflected and diverted around structures, or blocked behind them; and Mayall et al. (2010) demonstrate various responses of channel systems to growing structures and emphasize the importance of erosive power of the flows in the turbidity channels in maintaining a channels pathway across a growing structure. In chapters 3, 4, and 5 of this thesis some of the controls on how channels cross growing structures are addressed in more detail than previous work; they are summarised and discussed further here.

In Chapter 3 , the along-strike variations in strain and strain rate show that channels preferentially tend to deflect to the lateral tips of growing folds, as seen also in the examples documented by Clark and Cartwright (2009) in the Levant Basin fold belt. However, they are also capable of incising across the fault-propagation folds in low areas where two folds have linked. These areas of fold linkage are typically characterized by interval growth rates that are less than 15 m/Myr (see chapter 3). This implies that the channel systems, once in-place over the fold crest (analogous to antecedent rivers; Burbank et al., 1996), they are likely to keep pace with growth that is not more than 15 m/Myr. Analyses of the channel flow parameters (velocity, and incision power) as demonstrated in chapter 4, show that there is a marked increase in channel bed-shear stress and flow velocity over fold crests as the channel incise across. This implies that the flow power of the channels is likely to play a role in determining the overall channel response to fold uplift (see also Burbank et al., 1996). However, since the estimates of the maximum change in bed-shear stress and flow velocity are of the same order of magnitude in these systems, the incision power is not considered as a major control (e.g., Humphrey and Konrad, 2000).

This research has also provided new insights into the inherent structural control that growing folds and thrusts exert on Niger Delta channel systems. The results in chapter 3 revealed that the fault-propagation folds that occur largely in the west of the study area, and traversed by channels are characteristically very narrow, and are associated with a counter-regional dip that is less than 2 km long, and the average topographic height associated with this counter-regional dip is ~80 ±5 m (see Fig. 3.15 in chapter 3). However, the detachment fold (Fold C) that occurs in the east of the study area is very broad and is associated with a counter-regional dip that is greater than 5 km long, and the average topographic height associated with this counter-regional dip is ~140 ±10 m (see Fig. 3.15 in chapter 3). Moreover, this fold has caused complete channel diversion (see Fig. 5.7b). Consequently, a wide fold (such as Fold C in the east of the study area) characterised by a structural and topographic relief that is associated with a long (>5km) counter-regional dip is more likely to cause incoming flows to deflect or divert no matter the growth rate (Fig. 7.1a, b). The length of the counter-regional dip and the topographic height may be too large for incoming flows to overcome once they are blocked, hence, it is easier for the flow to be deflected to the lateral tip of the fold or relay areas between growing folds. This likely explains why both the buried channel 2 system and the modern channel 2 have been deflected by Fold C. In contrast, narrow structures (such as the fault-propagation folds in the west of the study area) with structural and topographic relief in which the counter-regional dip is less than 2 km, and the average topographic relief is approximately ~80 ±5 m may be more susceptible to being overcome by turbidity flows, especially if the related seabed relief is very subtle (Fig. 7.1c, d) and the rate of sediment aggradation in the upstream area of the fold is able to keep pace with uplift rate. In such a case, the crest of the fold can be eroded by the shear-stress generated by the sediments crossing it, and hence carving a path for subsequent flows. Humphrey and Konrad (2000) used theoretical modelling to demonstrate that initial fold uplift tends to reduce the dip of the slope upstream of the growing fold and that incoming rivers (flows) tend to deposit sediments within the accommodation space created following the reduction in dip, and hence it allows flows to begin to incise across if the rate of sediment aggradation can keep pace with uplift rate.

Additionally, this thesis demonstrates that the exact timing of fold growth and channel development is also very important (see chapter 3). A channel may initiate incision across a structure during a period when growth has significantly reduced; or has temporarily ceased (growth hiatus) as represented by the variations in the geometries of discrete growth packages through time (e.g., onlap, overlap in Fig. 3.15c; Shaw et al., 2004). Over this period of growth hiatus, the fold may be blanketed by post-growth sediment (Fig. 7.1e). In this case, the channel sees no positive topography and can easily carve-out a path. However, once the channel path has been established during a

hiatus or a significant slowdown in growth, active turbidite channels with widths of ~1000 – 2000 m flowing at predicted velocities of a few metres a second are clearly able to keep pace with subsequent growth rates that are not more than 15 m/Myr as demonstrated in chapter 3, by increasing channel incision and cutting deep into the pre-channel substrate (Fig. 7.1f; see also Figs. 5.5a, 5.6 – i). A limitation of this study is that the seismic resolution only allows the mapping of major growth units associated with folds from the onset of fold growth and small-scale packages that may represent periods of hiatus are not obvious at the seismic resolution; so they have not been detected. In the schematic diagram in Figures 7.1(e, f) packages that represent periods of hiatus are shown at a highly exaggerated vertical scale for descriptive purposes only.

Generally, once a channel is able to make a path across a growing fold, and become fully-contained, the ability to migrate laterally is governed by the ratio of the modern channel width to that of the associated container. The narrower the container width (e.g., where container 4 crosses Folds B and E in Figure 5.4b), the ratio will approach 1 since the width of incoming channel is equivalent to that of the container. That means incoming channels have no alternative than to keep incising across if the growth rate is not more than 15 m/Myr. However, if the ratio is low, incoming channels can easily be deflected within the container (with a concomitant increase in sinuosity; Huyghe et al., 2004; Ferry et al., 2005; Geogiopoulou and Cartwright, 2013) which can lead to gradual widening of the container (where the incoming channel is shifted to the edge of the container) and possible channel avulsion (e.g., at fold tip locations; see chapter 6).

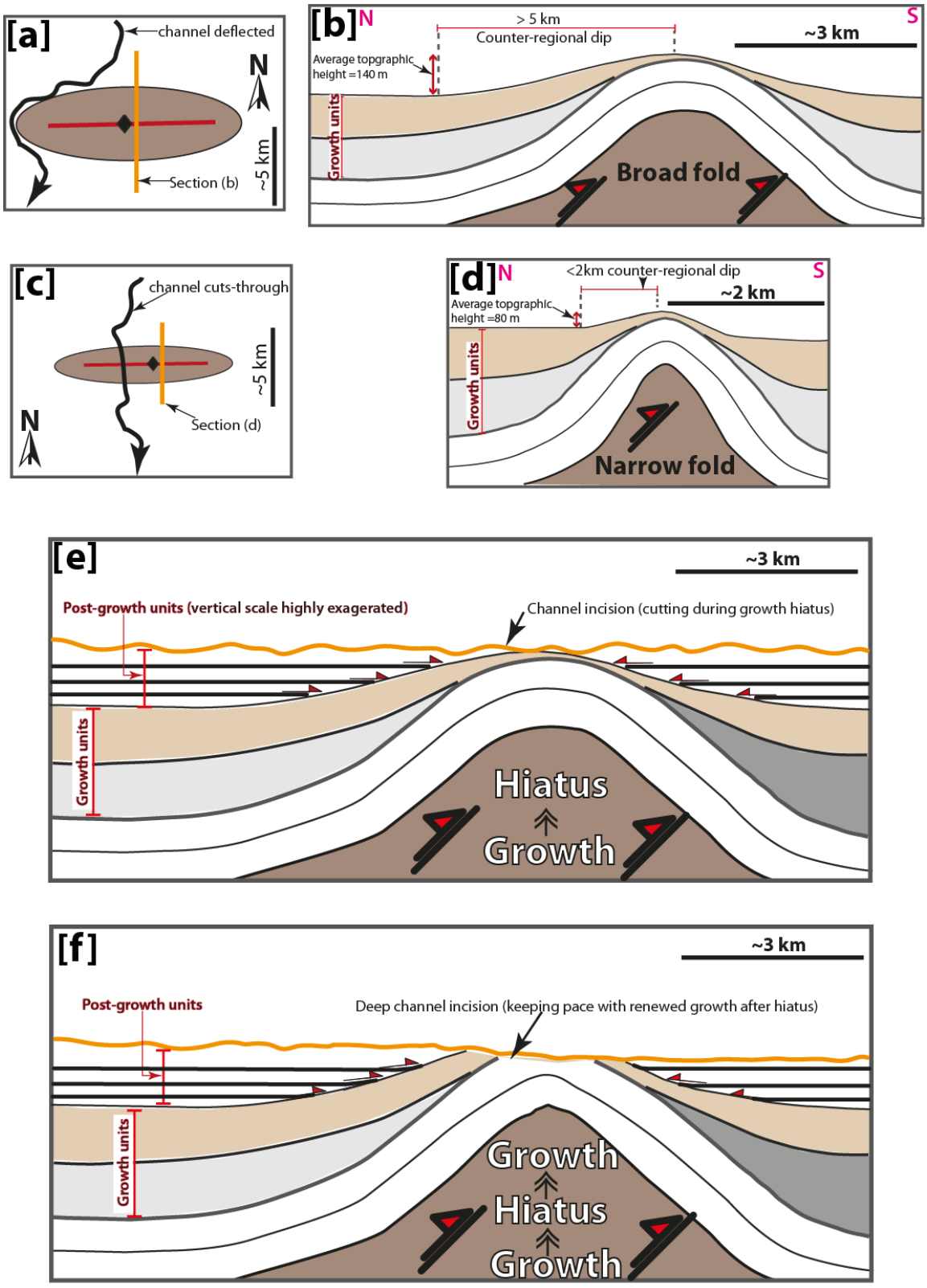


Figure 7.1: (a) and (b) respectively show a map-view and section of a broad fold that is associated with more than 5 km counter-regional dip and c.140 m topographic height thereby, causing channel deflection; (c) and (d) respectively show a map-view and section of a narrow fold that is associated with less than 2 km counter-regional dip and c.80 m topographic height that is easier for incoming channels to cut-across; (e) fold whose initial growth phase (characterized by growth units) is followed by a short period of non-growth during which the structure is blanketed by post-growth sediments. (f) Shows resumption in the growth of the same fold, and a channel keeping pace with the renewed growth by increasing incision.

7.5 GENERAL STUDY APPLICATION

The general approach in this thesis which involves the application of techniques traditionally used in terrestrial landform studies, to study channels and structures that occur at or near the seafloor, can serve as a vital tool in analyzing the temporal geomorphology of deepwater environments and how it affects channel systems, as was predicted by Posamentier et al. (2007). This method can easily be applied in any gravity-driven deepwater setting (e.g., offshore Angola, offshore Gulf of Mexico) where submarine channels interact with active structures to study their linked structural and sedimentological evolution. The ability to reconstruct the subsurface geomorphology (ancient surfaces) and map buried channels in 3D from the seismic data is an added advantage over traditional geomorphology. Hence, this allows for the application of surface geomorphic techniques to ancient environments especially where the seismic quality is very good (this is known as seismic geomorphology; Posamentier et al., 2007; Prather et al., 2012).

The displacement-distance relationship for growing structures and how it effects channel pathways (chapter 3), can be used together with the analyses of seismic facies (chapter 6) to predict deepwater channel responses to growing structures and how they distribute sediments. This can lead to a better understanding of structural controls on the depositional system of deepwater, the potential distribution of reservoir sands and how these sands become connected through time. The knowledge gained from these kinds of analyses can be used to develop models for complex deepwater reservoirs (see Prather et al., 2012). These models can then be applied to predict reservoir facies distribution in complex deepwater settings.

7.6 RESEARCH LIMITATIONS

1. The data sets used in this thesis has a resolution of approximately 10 – 13 m in the Pleistocene to Recent interval characterised by coeval channel development and deformation. While this was robust enough to conduct the analyses presented in this study, the data does not allow us to resolve small-scale variations in growth sequence geometries. Additionally the lack of well-control means that the seismic facies analysis cannot be tied specifically to cores or wireline log responses. Finally the age data used in this study was from a tie line (see Fig. 2.3 in chapter 2), and the absence of any biostratigraphic constraints in the shallower level of interest from 3.7 Ma to present limits the temporal resolution of fold growth and the accurate estimate of channel age.

2. The results of the down-system variations in flow velocities and bed-shear stress presented in chapter 4 are end-members and estimates that depend on the present-day channel geometry and typical sediment concentrations. Although, real flow parameters are expected to lie somewhere between these end-members; at the current state of knowledge, it is not possible to know the dynamics of every single flow that passed through each channel, and their overall contribution in sculpting the present-day channel geometry. Hence, the method used in this thesis (considering submarine channel incision over say a million year timescale) is very simple because we don't know (and we are unlikely to ever know; see Metivier et al., 2005) the time history of these parameters in a more detailed way.

3. The initiation of channel incision across a growing structure has yet to be fully constrained as this may be controlled by several factors some of which have been discussed in this thesis (see also Morley, 2009).

4. The analysis of the Pleistocene channel evolution in general and their potential attainment of topographic steady-state were based on the 3D seismic data only within the study area. This limits the length of the channel systems studied, and does not address the whole channel evolution from the shelf edge to the basin floor.

7.7 FURTHER WORK

1. Extending the study to seismic datasets to the north of the study area, would allow a more regional study of the channel systems that can be traced up-dip to the shelf areas where they appear to originate (Fig. 2.3a). This would extend the lengths of some of the systems already studied, and hence allow a better understanding of how these systems respond to different structures (e.g., extensional structures upslope, and contractional structures downslope; Fig. 2.2a, b) with differing growth rates.

2. Moreover, there is a need to apply the methods of constraining channel evolution documented in chapters 4 and 5 (or similar methods) to deepwater channel systems in other settings. This will allow full studies for a range of other submarine channel systems of differing sizes, crossing folds/thrusts with different rates/shapes. This will lead to a better insight about submarine channel responses to growing structures and how they relate or vary in different settings. Consequently, that may pave the way for the development of power-law relationship(s) for submarine channels in general, or for channels in different settings.

3. Numerical models and physical experiments (e.g., Middleton, 1967; Parker 1982; Corney et al., 1996; Imran et al., 1999; Peakall et al., 2000; Kneller and Buckee, 2000; Metivier et al., 2005; Straub et al., 2008), calibrated to observation data (e.g., Xu, 2011; Talling et al., 2012) and seismic data might be the way forward in understanding how submarine channels initiate incision across actively growing folds. Moreover, this kind of approach would be needed to analyse the variations in channel erosivity through time (i.e., taking into account the dynamics of turbidity currents and how they initiate, and maintain incision through time) for a better understanding of the process of sculpting the channel geometry (e.g., Parker, 1982; Imran et al. 1998, 1999; Peakall et al. 2000; Metivier et al., 2005). All of this will depend on the availability of measured, real turbidity flow parameters that are yet to be fully constrained (Talling et al., 2012, 2013), and hence the need for turbidite monitoring. Field analogue studies of turbidite systems may also provide an indirect way of estimating some flow characteristics such as the down-system variations in the coefficient of bed-friction which hitherto, has been based on estimates from rivers (e.g., Konsoer et al., 2013).

4. Finally future studies of the sort reported in this thesis where Pleistocene to Recent sedimentary processes are investigated in the context of a deforming seabed would benefit hugely from a targeted collection of well-bore or shallow core data to complement the analysis of the acoustic data. Not only would such data allow for a much improved temporal resolution to refine the rates of structural growth and estimates of channel ages, but would also allow a calibration of the sediment composition with the acoustic data to verify seismic facies analysis. Ideally such a study would be accompanied by higher frequency, and hence higher resolution, 2D or even 3D seismic imaging. A unique example of such a long term research project has been the investigation of the salt-controlled Brazos-Trinity slope mini-basin system in the Central Gulf of Mexico, where temporal resolutions of 12 kyr have been achieved in combination with vertical resolutions of 1-2 m from very high resolution seismic data (see Prather et al., 2012 and Pirmez et al., 2012 and references therein).

CHAPTER 8

CONCLUSIONS

In this thesis, channel systems that range in age from approximately 1.3 Ma to present, and interacting with structures (folds/thrusts) that have been growing since ca. 12 Ma in the toe thrust region of the deepwater Niger Delta have been identified and studied. These channels include the most recently active channels (i.e., modern channels open at the seabed) and those buried within the Pleistocene to Recent strata. The thesis combines the use of seismic data with geomorphic, structural and sedimentological techniques to analyse carefully the coupled development of the channels and the structures through time.

The main conclusions of this thesis are as follows:

1. Major structures with seabed relief are oriented perpendicular to the regional gradient and to modern seabed channels flowing down-dip. Fault-propagation folds dominate the western part of the study area, and a broad detachment fold occurs in the east of the study area. All structures started to grow between 12.8 Ma and 9.5 Ma; and the growth of these structures vary spatially along-strike and through time. The maximum interval growth rate (strain rate) occurred between 9.5 Ma and 3.7 Ma, and has reduced significantly in the last 3.7 million years during which submarine channels that range in age from ~0.6 Ma to 1.3 Ma also occurred. Total fold shortening measured in metres, varies from ~ 4km (Fold D) to ~1km (Fold (C); giving a time-averaged maximum shortening rate of between 350 $\pm$50 and 90 $\pm$10 m/Ma (0.4 and 0.1 mm/yr) and then 50 $\pm$5 and 40 $\pm$5 m/Ma (0.05 and 0.04 mm/yr) in the last 3.7 Ma.

2. Shortening – distance relationships show that the fault/thrust structures have linked laterally over time. However, while points of fold linkage (recognised from minima in shortening-strike graphs) may remain persistent in regions of low displacement during the life of fold growth (e.g., Fold B), the locations of fold strain minima observed in older horizons may not necessarily coincide with regions of strain minima in younger syn-growth horizons for some folds (e.g., Fold A). Consequently, identification of strain minima for prediction of sediment pathways can be misleading if displacement measurements are not made explicitly for strata that bracket the time interval of the channel systems.

3. Modern seabed channels pathways are affected by the growth of structures with seabed relief. These channels preferentially tend to deflect towards relay or lateral tips of folds, and the broad detachment fold (with a greater than 5 km wide crest) causes channel diversion such that the channel flows parallel to the fold axis. However, some channels continue to incise through the growing structures that occur in the central and western parts of the study area by exploiting low areas or positions of recent strain minima at interval strain rates that are generally less than -0.02 Ma^{-1} (15 m/Myr or less). The study shows that folds with similar counter-regional slopes, but which extend over a broader area (e.g., Fold C), may cause channel diversion even at very low strain rates of -0.002 Ma^{-1} (-7 x 10^{-17} s^{-1}).

4. This study shows that average widths of modern seabed channels range from as low as 1100 m to as high as 2400 m, and that typical incisional depths vary from as low as 10 m to as high as 140 m. The modern channel widths are insensitive to active folds affecting channel pathways. However, channel depths tend to show a large spread in distribution, with significantly enhanced incision in the region where channels cross seabed structures.

5. The long profiles of the modern channels are relatively linear with concavity that ranges from -0.08 to- 0.34 with an average gradient of 0.9^{o} – 1^{o}. Local scale knickpoints are apparent near mapped structures and implicitly therefore, related to variations in substrate uplift rate. Areas of significant increase in channel gradient caused by long time-integrated structural uplift are typically associated with more than 70 % increase in modern channel incision.

6. The bed-shear stress of the modern channels has been estimated to be between 50 – 200 Pa for flows with a sediment concentration of 0.6 %, and flow velocities are predicted to range from 0.8 ms^{-1} to as high as 5 ms^{-1}. These range of flow velocities are consistent with reported values of turbidite flow velocities from rare direct field observations reported by others (e.g., Meiburg and Kneller, 2010; Talling et al., 2012, 2013). A comparison of the down-system distribution of bed-shear stress with the magnitude and distribution of fold-driven uplift suggests that these channels are capable or more than capable of keeping pace with structural growth and that they can achieve topographic (bathymetric) steady-state.

7. While the profiles of the modern channels are relatively linear, they are different to those of the associated containers (the erosional surface bounding several cut-and-fill sequences) which are convex to irregular. Moreover, the container profiles show a much higher cumulative gradient change increase (up to 400 %) at the locations of active thrusts and folds compared to the modern channels whose change is less than 100 %. The analyses of these container systems show that they have responded to time-integrated increase in channel gradient by increasing incision into the pre-channel substrate; and modern channels have continued to incise into the preserved, time-integrated channel fill. As a consequence, the channel container shows the clear effect of time-integrated structural uplift through its overall width narrowing, deep incision and lower preserved fill over the growing structure(s). Despite the increase in channel incision over the fold crests, the systems are broadly aggradational through time.

8. The evolution of the channel system (container) and how it responds to tectonic perturbations determines the container width, depth and the overall stacking pattern of the cut-and-fill sequences. A laterally migrating stacking pattern dominates the lower part of the container as it moves away from growing structures. When the growth of a fold no longer causes the channel to migrate laterally, the container develops dominantly by vertical aggradation.

9. The overall linear to slightly concave nature of the modern seabed channel profile represents the geomorphic expression of time-integrated channel incision. On the other hand, the convex to irregular nature of the container profile represents the geomorphic expression of time-integrated deformation from continuous fold growth since abandonment. Consequently, future seismic studies of submarine channels need to carefully distinguish between active channel long-profiles and the long profiles of cut-and-fill sequences which may not represent a channel long profile that was active at the time.

10. Analyses of seismic facies for the Pleistocene to Recent interval reveal 4 main facies which include; (1) channel axes sands and top-channel sands (2) sheet-sands or crevasse splays (3) slump deposits and (4) pelagic drapes. The growth of structures affects the location of channel avulsion, the locus and the deposition/distribution of sheet-sands (splays). These splays are often deposited outside the channel system by turbiditic flows that are capable of breaching the channel levee either at structural locations (fold tips) or as the channel system is blocked and forced to divert. Splays deposited within sub-basins in the west of the study area are characterised by lobate-shaped geometry in plan-view. However, splays deposited by diverting channels in the east of the study area are elongated parallel to growing detachment fold causing the channels to divert. A general understanding of the temporal evolution of these splays (reservoir-quality sands) is of importance to hydrocarbon exploration in complex deepwater settings that are often considered high risk environments.

REFERENCES CITED

Allen, J.R.L., 1965. Late Quaternary Niger Delta and adjacent areas: sedimentary environments and lithofacies: AAPG Bulletin, 49, 547–600.

Allmendinger, R., 1998. Inverse and forward numerical modeling of trishear fault-propagation folds. Tectonics, 17, 640–656.

Amblas, D., Gerber, T.P., Canals, M., Pratson, L.F., Urgeles, R., Lastras, G., Calafat, A.M., 2011. Transient erosion in the Valentia Trough turbidite systems, NW Mediterranean Basin. Geomorphology, 130, 173 –184.

Amos, C.B., Burbank, D.W., 2007. Channel width response to differential uplift. Jour. of Geophysical Research, 112, F02010, doi:10.1029/2006JF000672.

Anderson, J.E., Cartwright, J., Drysdall, S.J., and Vivian, N., 2000. Controls on turbidite sand deposition during gravity-driven extension of a passive margin: examples from Miocene sediments in Block 4, Angola. Marine and Petroleum Geology, 17, 1165 –1203.

Avbovbo, A.A., 1978. Tertiary lithostratigraphy of the Niger Delta. AAPG Bulletin, 62, 295 –300.

Babonneau, N., Savoye, B., Cremer, M., and Klein, B., 2002. Morphology and architecture of the present canyon and channel system of the Zaire deep-sea fan. Marine and Petroleum Geology, 19, 445–467.

Babonneau, N., Savoye, B., Cremer, M., Bez, M., 2004. Mutliple terraces within the deep incised Zaire Valley (ZaiAngo Project): are they confined levees? In: Lomas, S.A., Joseph, P. (Eds.). Geological Society Special Publications, 222, 91–114.

Babonneau, N., Savoye, B., Cremer, M., Bez, M., 2010. Sedimentary architecture in meanders of a submarine channel: detailed study of the present day Congo turbidite channel (ZaiAngo Project). Journal of Sedimentary Research, 80, 852 – 866.

Bagnold, R.A., 1962. Auto-suspension of transported sediment: turbidity currents. Proceedings of the Royal Society A: Mathematical, Physical & *Engineering Sciences* 265, 315-319.

Beaubouef, R.T., Friedmann, S.J., 2000. High-resolution seismic/sequence stratigraphic framework for the evolution of Pleistocene intra slope basins, Western Gulf of Mexico: depositional models and reservoir analogs. In: Weimer, P., Slatt, R.M., Coleman, J., Rosen, N.C., Nelson, H., Bouma, A.H., Styzen, M.J., Lawrence, D.T. (Eds.), Deep-Water Reservoirs of the World: Gulf Coast Society of the Society of Economic Paleontologists and Mineralogists Foundation, 20th Annual Research Conference, 40–60.

Beaubouef, R.T., 2004. Deep-water leveed-channel complexes of the Cerro Torro Formation, Upper Cretaceous, southern Chile. AAPG Bulleting, 88 (11), 1471–1500.

Bergen, K.J., Shaw, J.H., 2010. Displacement profiles and displacement-length scaling relationships of thrust faults constrained by seismic reflection data. GSA Bulletin 122, 1209-1219.

Bernard, S.S., Avouac, J.-P., Dominguez, S., and Simoes, M., 2007. Kinematics of fault-related folding derived from a sandbox experiment, Journal of Geophysical Research, 112, B03S12, doi:10.1029/2005JB004149.

Bilotti, F.D., Shaw, J.H., 2005. Deepwater Niger Delta fold and thrust belt modelled as a critical-taper wedge: the influence of elevated basal fluid pressure on structural styles. AAPG Bulleting, 89, 1475-1491.

Booth, J.R., Duvernay, A.E., III, Pfeiffer, D.S., Styzen, M.J., 2000. Sequence stratigraphic framework, depositional models, and stacking patterns of ponded and slope fan systems in the Auger Basin: Central Gulf of Mexico Slope, in: Weimer, P., Slatt, R.M., Coleman, J., Rosen, N.C., Nelson, H., Bouma, A.H., Styzen, M.J., and Lawrence, D.T., (Eds.), Deep-water reservoirs of the world: Gulf Coast Society of the Society of Economic Paleontologists and Mineralogists Foundation, 20th Annual Research Conference, 82–103.

Bouma, A.H., 1985. Submarine fans and related turbidite systems. New York, NY: Springer-Verlag.

Briggs, S.E., Davies, R.J., Cartwright, J.A., Morgan, R., 2006. Multiple detachment levels and their control on fold styles in the compressional domain of the deepwater west Niger Delta. Basin Research, 18, 435–450.

Brown, A.R., 1999. Interpretation of three-dimensional seismic data. AAPG Memoir 42, fifth ed., 510p.

Burbank, D.W., Verges, N., 1994. Reconstruction of topography and related depositional systems during active thrusting. Journal of Geophysical Research, 99, 281-297.

Burbank, D.W., Meigs, A., Bronzovic, N., 1996. Interaction of growing folds and coeval depositional systems. Basin Research, 8, 199-223.

Burke, K.C.B., 1972. Longshore drift, submarine canyon, and submarine fans. AAPG Bulletin, 56, 1975-1983.

Butler, R.W.H., Grasso, M., and Lickorish, W.H., 1995. Plio-Quaternary megasequence geometry and its tectonic controls within the Maghrebian thrust belt of south-central Sicily. Terra Nova, 7, 171–178.

Cartwright, J.A., Trudgill, B.D., Mansfield, C., 1995. An explanation for the scatter in displacement and length data during fault growth by segment linkage. Journal of Structural Geology, 17, 672- 679.

Chapman, T.J., and Williams, G.D., 1984. Displacement-distance methods in the analysis of fold-thrust structures and linked-fault systems. Geological Society London, 141, 121-128.

Clark, J.D., Kenyon, N.H., Pickering, K.T., 1992. Quantitative analysis of the geometry of submarine channels: Implications for the classification of submarine fans: Geology, 20, 633-636.

Clark, J.D., Pickering, K.T., 1996a. Submarine Channels: Processes and Architecture: Vallis Press, London, 231p.

Clark, J.D., Pickering, K.T., 1996b. Architectural elements and growth patterns of submarine channels: applications to Hydrocarbon exploration. AAPG Bulletin, 80 (2), 194–221.

Clark, I.R., Cartwright, J.A., 2009. Interactions between submarine channel systems and deformation in deepwater fold belts: examples from the Levant Basin, Eastern Mediterranean sea. Marine and Petroleum Geology, 26, 1465-1482.

Clark, I.R., Cartwright, J.A., 2011. Key controls on submarine channel development in structurally active settings. Marine and Petroleum Geology, 28, 1333-1349.

Clark, I.R., Cartwright, J.A., 2012. Interactions between coeval sedimentation and deformation from the Niger Delta deepwater fold belt. SEPM Special Publication, 99, 243–267.

Cohen, H.A., McClay, K., 1996. Sedimentation and shale tectonics of the northwestern Niger Delta front. Marine and Petroleum Geology 13, 313–328.

Corredor, F., Shaw, J.H., Bilotti, F., 2005. Structural styles in the deep-water fold and thrust belts of the Niger Delta. AAPG Bulletin, 89, 753-780.

Corney, R.K.T., Peakall, J., Parsons, D.R., Elliott, L., Amos, K.J., Best, J.L., Keevil, G.M., Ingham, D.B., 2006. The orientation of helical flow in curved channels: Sedimentology 53, 249–257.

Covault, J.A., Graham, S.A., 2010. Submarine fans at all sea-level stands: tectono-morphologic and climatic controls on terrigenous sediment delivery to the deep-sea. Geological Society of America, 38, 939-942.

Covault, J.A., 2011. Submarine fans and canyon-channel systems: a review of processes, products, and models. Nature Education Knowledge 3(10):4.

Covault, J.A., Fildeni, A., Romans, B.W., McHarque, T., 2011. The natural range of submarine canyon-and-channel longitudinal profiles. Geosphere, 7, 313-332.

Cramez, C., Jackson, M.P.A., 2000. Superposed deformation straddling the continental-oceanic transition in deep-water Angola. Marine and Petroleum Geology, 17, 1095-1109.

Cross, N.E., Cunningham, A., Cook, R.J., Taha, A., Esmaie, E., El Swidan, N., 2009. Three-dimensional seismic geomorphology of a deep-water channel slope system: the Sequoia field, offshore west Nile Delta, Egypt. AAPG Bulletin, 93, 1063-1086.

Daëron, M., Avouac, J.-P., Charreau, J., 2007. Modeling the shortening history of a fault tip fold using structural and geomorphic records of deformation. Journal of Geophysical Research, 112, B03S13, doi:10.1029/2006JB004460.

Dahlstrom, C.D.A., 1969. Balanced cross sections. Canadian Journal of Earth Sciences, 6, 743–757.

Damuth, J.E., 1994. Neogene gravity tectonics and depositional processes on the deep Niger Delta continental margin. Marine and Petroleum Geology, 11, 320–346.

Damuth, J.E., Flood, R.D., 1984. Morphology, sedimentation processes and growth pattern of the Amazon deep-sea fan: Geo Marine Letters, 3, 109-117.

Damuth, J.E., Flood, R.D., 1985. Amazon Fan, Atlantic Ocean. In: Bauma, A.H., Normark, W.R., Barnes, N.E., (Eds.), Submarine fans and related turbidite systems: Springer, New York, 97–106.

Damuth, J.E., Flood, R.D., Knowsmann, R.O., Belderson, R.H., Gorini, M.A., 1988. Anatomy and growth patterns of Amazon deep-sea fan as revealed by long-range side-scan sonar (GLORIA) and high-resolution seismic studies. AAPG Bulletin, 72, 885–911.

Damuth, J.E., Kolla, V., Flood, R.D., Kowsmann, R.O., Monteiro, M.C., Gorini, M.A., Palma, J.J.C., Belderson, R.H., 1983. Distributary channel meandering and bifurcation patterns on Amazon deep-sea fan as revealed by long-range side-scan sonar (GLORIA). Geology, 11, 94–98.

Das, H.S., Imran, J., Pirmez, C., Mohrig, D., 2004. Numerical modeling of flow and bed evolution in meandering submarine channels. Journal of Geophysical Research: Oceans, 109(C10), 1978–2012.

Davies, K., Burbank, D.W., Fisher, D., Wallace, S., Nobes, D., 2005. Thrust-fault growth and segment linkage in the active Ostler fault zone, New Zealand. Journal of Structural Geology, 27, 1528–1546.

De Sitter, L.V., 1956. Structural geology. New York, McGraw-Hill, 552p.

Deptuck, M.E., Steffens, G.S., Barton, M., Pirmez, C., 2003. Architecture and evolution of upper fan channel-belts on the Niger Delta slope and in the Arabian Sea. Marine and Petroleum Geology, 20, 649-676.

Deptuck, M.E., Sylvester, Z., Pirmez, C., O'byrne, C., 2007. Migration-aggradation history and 3-D seismic geomorphology of submarine channels in the Pleistocene Benin-major Canyon, western Niger Delta slope. Marine and Petroleum Geology, 24, 406-433.

Doust, H., Omatsola, E., 1990. Niger Delta. In: Edwards, J.D. and Santogrossi, P.A. (Eds.), Divergent /passive margin basins. AAPG Memoir, 48, 201-238.

Droz, L., Marsset, T., Ondre'as, H., Lopez, M., Savoye, B., Spy-Anderson, F.-L., 2003. Architecture of an active mud-rich turbidite system: the Zaire Fan (Congo-Angola margin south Atlantic): results from Zai Ango 1 and 2 cruises. AAPG Bulletin, 87, 1145-1168.

Elliott, T., 2000. Depositional architecture of a sand-rich, channelized turbidite system: the Upper Carboniferous Ross Sandstone Formation, western Ireland. In: Weimer, P., Slatt, R.M., Coleman, J., Rosen, N.C., Nelson, H., Bouma, A.H., Styzen, M.J., Lawrence, D.T. (Eds.), Deep-water Reservoirs of the World. SEPM Gulf Coast Section 20th Bob F. Perkins Research Conference, 342 – 373.

Evamy, B.D., Haremboure, J., Kamerling, P., Knaap, W.A., Molloy, F.A., Rowlands, P.H., 1978. Hydrocarbon habitat of Tertiary Niger Delta. AAPG Bulletin, 62, 277-298.

Fairhead, J.D., Binks, R.M., 1991. Differential opening of the Central and South Atlantic oceans and the opening of the West African rift system. Tectonophysics, 187, 191–203.

Ferry, J.N., Mulder, T., Parize, O., Raillard, S., 2005. Concept of equilibrium profile in deep water turbidite systems: effects of local physiographic changes on the nature of sedimentary processes and the geometries of deposits, in: Hodgson, D.M. and Flint, S.S. (Eds.), Submarine Slope Systems: Processes and Products. Geological Society London, 244, 181-193.

Flood, R.D., Damuth, J.E., 1987. Quantitative characteristics of sinuous distributary channels on the Amazon deep sea fan: GSA Bulletin, 98, 728–738.

Fonnesu, F., 2003. 3D seismic images of a low-sinuosity slope channel and related depositional lobe – West Africa deep-offshore. Marine and Petroleum Geology, 20, 615–629.

Friedman, G.M., Sanders, J.E., Kopaska-Merkel, D.C., 1992. Principles of sedimentary deposits-stratigraphy and sedimentology. Macmillan, New York.

Gawthorpe, R.L., Leeder, M.R., 2000. Tectono-sedimentary evolution of active extensional Basins. Basin Research, 12, 195 – 218.

Gee, M.J.R., and Gawthorpe, R.L., 2006. Submarine channels controlled by salt tectonics: Examples from 3D seismic data offshore Angola. Marine and Petroleum Geology, 23, 443–458.

Gee, M.J.R., Gawthorpe, R.L., Bakke, K., and Friedmann, S.J. 2007. Seismic geomorphology and evolution of submarine channels from the Angolan continental margin. Journal of Sedimentary Research, 77, 433-446.

Georgiopoulou, A., Cartwright, J.A., 2013. A critical test of the concept of submarine equilibrium profile. Marine and Petroleum Geology, 41, 35 – 47.

Gerber, T.P., Amblas, D., Wolinsky, M.A., Pratson, L.F., and Canals, M., 2009. A model for the long-profile shape of submarine canyons. Journal of Geophysical Research, 114, F03002, doi: 10.1029/2008JF001190.

Goff, J.A., 2001. Quantitative classification of canyon systems on continental slopes and a possible relationship to slope curvature. Geophysical Research Letters, 28, 4359–4362.

Hack, J.T., 1957. Studies of longitudinal stream profiles in Virginia and Maryland. US Geol. Survey Prof. Pap. 294B.

Hackbarth, C.J., Shaw, R.D., 1994. Morphology and stratigraphy of a mid-Pleistocene turbidite leveed channel from seismic, core and log data, northeastern Gulf of Mexico, in: Weimer, P., Bouma, A.H., and Perkins, B.F., (Eds.), Submarine fans and turbidite systems: Gulf Coast Society of the Society of Economic Paleontologists and Mineralogists Foundation, 15th Annual Research Conference, 127–133.

Hadler-Jacobsen, F., Gardner, M.H. and Borer, J.M., 2007. Seismic stratigraphy and geomorphic analysis of deep-marine deposition along the West African continental margin. In: Davies, R.J., Posamentier, H.W., Wood, L.J. and Cartwright, J.A. (Eds.), Seismic geomorphology: Applications to hydrocarbon exploration and production: Geological Society, London, Special Publication, 277, 47-84.

Hampton, M., Lee, H.J., Locat, J., 1996. Submarine landslides. Rev. Geophys, 34, 33–59.

Hart, B.S., 1999. Definition of subsurface stratigraphy, structure and rock properties from 3D seismic data. Earth-Science Reviews, 47, 497 – 518.

Hardy, S., Poblet, J., 1994. Geometric and numerical model of progressive limb rotation in detachment folds. Geology, 22, 371–374.

Hardy, S., Poblet, J., 1995. The velocity description of deformation. Paper 2: sediment geometries associated with fault-bend and fault-propagation folds. Marine and Petroleum Geology, 12, 165 – 176.

Hardy, S., Poblet, J., 2005. A method for relating fault geometry, slip rate and uplift data above fault-propagation folds. Basin Research, 17, 417-424.

Heinio, P., and Davies, R.J., 2006. Degradation of compressional fold belts: Deep-water Niger Delta. AAPG Bulletin, 90, 753-770.

Heinio, P., Davies, R.J., 2007. Knickpoint migration in submarine channels in response to fold growth, western Niger Delta. Marine and Petroleum Geology, 24, 434-449.

Higgins, S., Davies, R.J., Clarke, B., 2007. Antithetic fault linkages in a deep water fold and thrust belt. Journal of Structural Geology, 29, 1900–1914.

Higgins, S., Clarke, B., Davies, R.J., Cartwright, J., 2009. Internal geometry and growth history of a thrust-related anticline in a deepwater fold belt. Journal of Structural Geology, 31, 1597–1611.

Hooper, R.J., Fitzsimmons, R.J., Neil, G., and Vendeville, B.C., 2002. The role of deformation in controlling depositional patterns in the south-central Niger Delta, West Africa. Journal of Structural Geology, 24, 847-859.

Hossack, J.R., 1979. The use of balanced cross-sections in the calculation of orogenic contraction: A review. Geological Society London, 136, 705-711.

Howard, A.D., 1994. A detchment-limited model of drainage basin evolution. Water Resources Research, 30, 2261–2285.

Humphrey, N.F., Konrad, S.K., 2000. Rivers incision or diversion in response to bedrock uplift. Geology, 28, 43 – 46.

Huyghe, P., Foata, M., Deville, E., Mascle, G., 2004. Channel profiles through the active thrust front of the southern Barbados prism. GSA Bulletin, 32, 429-432.

Imran, J., Parker, G., Katopodes, N., 1998. A numerical model of channel inception on submarine fans. Journal of Geophysical Research, 103 (C1), 1219–1238.

Imran, J., Parker, G., Pirmez, C., 1999. A nonlinear model of flow in meandering submarine and subaerial channels, J. Fluid Mech., 400, 295–331.

Janocko, M., Nemec, W., Henriksen, S., Warchol. M, 2013. The diversity of deep-water sinuous channel belts and slope valley-fill complexes. Marine and Petroleum Geology, 41, 7 – 34.

Jermannaud, P., Rouby, D., Robin, C., Nalpas, T., Guillocheau, F., Raillard, S., 2010. Plio-Pleistocene sequence stratigraphic architecture of the Eastern Niger Delta: a record of eustasy and aridification of Africa. Marine and Petroleum Geology, 27, 810–821.

Johnson, M., Stow, D.V.A., 1998. Deep-water massive sands, California: tectonic settings and sand supply controls. Geoscience, 98, *Abstract volume* , p.12.

Jones, G., Mayall, M., Lonergan, L., 2012. Contrasting depositional styles on a slope system and their control by salt tectonics: through-going channels, ponded fans, and mass transport complexes. GCSSEPM, 503 – 533.

Kane, I.A., Hodgson, D.M., 2011. Sedimentological criteria to differentiate submarine channel levee subenvironments: exhumed examples from the Rosario Fm. (Upper Cretaceous) of Baja California, Mexico, and the Fort Brown Fm. (Permian), Karoo Basin, S. Africa. Marine and Petroleum Geology, 28, 807 – 823.

Keary, P., Brooks, M., Hill, I., 2002. An introduction to geophysical exploration. Blackwell Science, 262p.

Kneller, B., Buckee, C., 2000. The structure and fluid mechanics of turbidity currents: a review of some recent studies and their geological implications. Sedimentology, 47, 62–94.

Kneller, B., 2003. The influence of flow parameters on turbidite slope channel architecture. Marine and Petroleum Geology, 20(6), 901-910.

Knox, G.J., Omatsola, E.M., 1989. Development of the Cenezoic Niger Delta in terms of the 'escalator regression' model and impact on hydrocarbon distribution, in: Van Der Linden, W.J.M., Cloetingh, S.A.P.L., Kaasscheiter, J.P.K., Van Ger Graaf, W.J.E., Vandenberglie, J., and Van Der Gun, J.A.M. (Eds.), Proceedings of the KNGMG Symposium Coastal Lowlands. Geology and Geotechnology, 181-202.

Kolla, V., Bourges, P.H., Urruty, J.-M., Safa, P., 2001. Evolution of deep-water Tertiary sinuous channels offshore Angola (West Africa) and implications for reservoir architecture: AAPG Bulletin, 85, 1373–1405.

Kolla, V., 2007. A review of sinuous channels avulsion patterns in some major deep-sea fans and factors controlling them. Marine and Petroleum Geology, 24, 450-469.

Kolla, V., Posamentier, H.W. and Wood, L.J., 2007. Deep-water and fluvial sinuous channels – Characteristics, similarities and dissimilarities, and modes of formation. Marine and Petroleum Geology, 24, 388-405.

Komar, P.D., 1977. Computer simulation of turbidity current flow and the study of deep-sea channels and fan sedimentation.The Sea, 6, edited by E.D. Goldberg, Wiley, New York, 603-621.

Konsoer, K., Zinger J., Parker G., 2013. Bankfull hydraulic geometry of submarine channels created by turbidity currents: Relations between bankfull channel characteristics and formative flow discharge. Journal of Geophysical Research, Earth Surface, 118, 216-228.

Leopold, L.B., Maddock, T., 1953. The hydraulic geometry of stream channels and some physiographic implications. United States Geological Survey Professional Paper, 252.

Li, T., Chen, J., Thompson, J.A., Burbank, D.W., and Yang, X., 2013. Quantification of three-dimensional folding using fluvial terraces: A case study from the Mushi anticline, northern margin of the Chinese Pamir. Journal of Geophysical Research, 118, 4628 – 4647.

Maloney, D., Davies, R., Imber, J., Higgins, S., King, S., 2010. New insights into deformation mechanisms in the gravitationally driven Niger Delta deep-water fold and thrust belt. AAPG Bulletin, 94, 1401-1424.

Mascle, J., Marhino, M., Wanesson, J., 1986. The structure of the Guinean continental margin: implications for the connections between the Central and South Atlantic Oceans. Geologische Rundschau, 75, 57-70.

Mayall, M., Stewart, I., 2000. The architecture of turbidite slope channels, in: Weimer, P., Slatt, R.M., Coleman, J., Rosen, N.C., Nelson, H., Bouma, A.H., Styzen, M.J., and Lawrence, D.T., (Eds.), Deep-Water Reservoirs of the World: SEPM, Gulf Coast Section, 20th Annual Research Conference, 578 586.

Mayall, M., Jones, E., Casey, M., 2006. Turbidite channel reservoirs – key elements in facies prediction and effective development: Marine and Petroleum Geology, 23, 677–690.

Mayall, M., Lonergan, L., Bowman, A., James, S., Mills, K., Primmer, T., Pope, D., Rogers, L., and Skeene, R., 2010. The response of turbidite slope channels to growth-induced seabed topography. AAPG Bulletin, 94, 1011-1030.

McHargue, T., Pyrcz, M.J., Sullivan, M.D., Clark, J.D., Fildani, A., Romans, B.W., Covault, J.A., Levy, M., 2011. Architecture of turbidite channel systems on the continental slope: patterns and predictions. Marine and Petroleum Geology, 28, 728 –743.

Meiburg, E., Kneller, B., 2010. Turbidity currents and their deposits. Annu. Rev. Fluid Mech., 42, 135-156.

Mello, U.T., Pratson, L.F., 1999. Regional slope stability and slope-failure mechanics from the two-dimensional state of stress in an infinite slope: Marine Geology, 154, 339– 356.

Middleton, G.V., 1967. Experiments on density and turbidity currents III: deposition of sediments. Canadian Journal of Earth Sciences, 4, 475–505.

Middleton, G.V., Hampton, M.A., 1973. Sediment gravity flows: mechanics of flow and deposition. In: Middleton, G.V., Bouma, A.H., (Eds.), Turbidites and Deep-water Sedimentation. Los Angeles, CA: Society of Economic Paleontologists and Mineralogists, 1-38.

Mitchell, N.C., 2006. Morphologies of knickpoints in submarine canyons. GSA Bulletin, 118, 589–605.

Mitchum, R.M., Wach, G.D., 2002. Niger Delta Pleistocene levee-channel fans: models for offshore reservoirs. 22nd Annual Gulf Coast SEPM Foundation Bob F. Perkins Research Conference, 712-726.

Metivier, F., Lajeunesse, E., Cacas, M-C., 2005. Submarine canyons in the bathtub. Journal of Sedimentary Research, 75, 6 – 11.

Morgan, R., 2004. Structural controls on the positioning of submarine channels on the lower slopes of the Niger Delta, in: Davies, R.J., Cartwright, J.A., Stewart, S.A., Lappin, M., and Underhill, J.R. (Eds.), 3D seismic technology: application to the exploration of sedimentary basins. Geological Society London Memoirs, 29, 45-51.

Morley, C.K., Guerin, G., 1996. Comparison of gravity-driven deformation styles and behaviour associated with mobile shales and salt. Tectonics, 15, 1154–1170.

Morley, C.K., 2007. Interaction between critical wedge geometry and sediment supply in a deep-water fold belt. Geology, 35, 139 – 142.

Morley, C.K., 2009. Growth of folds in a deep-water setting. Geosphere, 5, 59-89.

Morley, C.K., Leong, L.C., 2008. Evolution of deep-water syn-kinematic sedimentation in a piggy-back basin, determined from 3D seismic reflection. Geosphere, April 2009, 89 data, Geosphere, 4, 938-962.

Mulder, T., Syvitski, J.P.M., 1995. Turbidity currents generated at river mouths during exceptional discharges to the world oceans. Journal of Geology, 103, 285–299.

Mutti, E., Normark, W.R., 1991. An integrated approach to the study of turbidite systems. In: Weimer, P., and Link, M.H., (Eds.), seismic facies and sedimentary processes of modern and ancient submarine fans. New York, Springer-Verlag, 75–106.

Mutti, E., Normark, W.R., 1987. Comparing examples of modern and ancient turbidite systems: problems and concepts. In: Legged, J.K and Zuffa, G.G. (Eds.), Marine Clastic Sedimentology: Concept and case studies. Graham & Trotman, London, 1–38.

Nelson, C.H., Escutia, C., Damuth, J.E., Twichell, D.C., 2009. Interplay of mass-transport and turbidite-system deposits in different active tectonic and passive continental margin settings: external and local controlling factors. In: Shipp, R.G., Weimer, P., Posamentier, H.W., (Eds.), Mass-Transport Deposits in Deepwater Settings, SEPM, Special Publication, 96, 39–66.

Normark, W.R., 1970. Growth patterns of deep-sea fans. AAPG Bulletin, 54, 2170–2195.

Normark, W.R., 1978. Fan valleys, channels and depositional lobes on modern submarine fans—characters for recognition of sandy turbidite environments. AAPG Bulletin, 62, 912–931.

Normark, W.R., Hess, G.R., Stow, D.A.V., Bowen, A.J., 1980. Sediment waves on the Monterey Fan levee: A preliminary physical interpretation. Marine Geology, 37, 1–18.

Normark, W.R., Piper, D.J.W., Posamentier, H., Pirmez, C., Migeon, S., 2002. Variability in form and growth of sediment waves on turbidite channel levees. Marine Geology, 192, 23 –58.

Parker, G., 1982. Conditions for the ignition of catastrophically erosive turbidity currents. Marine Geology, 46, 307–327.

Peakall, J., Mccaffrey, W.D., Kneller, B.C., 2000. A process model for the evolution, morphology and architecture of meandering submarine channels. Journal of Sedimentary Research, 70, 434 – 448.

Peakall, J., Amos, K.J., Keevil, G.M., Bradbury, P.W., Gupta, S., 2007. Flow processes and sedimentation in submarine channel bends. Marine and Petroleum Geology 24, 470 – 486.

Piper, D.J.W., Pirmez, C., Manley, P.L., Long, D., Flood, R.D., Normark, W.R., Showers, W., 1997. Mass-transport deposits of the Amazon Fan, in: Flood, R.D., Piper, D.J.W., Klaus, A., and Peterson, L.C., (Eds.), Proceedings ODP, Scientific Results, 155, 109–146.

Piper, D.J.W., Farre, J.A., Shor, A., 1985. Late quaternary slumps and debris flows on the Scotian slope. GSA Bulletin, 96, 1508-1517.

Piper, D.J.W., Normark, W.R., 2001. Sandy fans—from Amazon to Hueneme and beyond: AAPG Bulletin, 85, 1407–1438.

Pirmez, C., Flood, R.D., 1997. Morphology and structure of Amazon Channel, in: Flood, R.D., Piper, D.J.W., Klaus, A., Peterson, L.C., (Eds.), Proceedings ODP, Scientific Results, 155, 23–45.

Pirmez, C., Hiscott, R.N., Kronen, J.K., 1997. Sandy turbidite successions at the base of channel-levee systems of the Amazon Fan revealed by FMS logs and cores: unraveling the facies architecture of large submarine fans, in: Flood, R.D., Piper, D.J.W., Klaus, A., and Peterson, L.C., (Eds.), Proceedings ODP, Scientific Results, 155, 7–22.

Pirmez, C., Beaubouef, R.T., Friedmann, S.J., Mohrig, D.C., 2000. Equilibrium profile and baselevel in submarine channels: examples from Late Pleistocene systems and implications for the architecture of deepwater reservoirs. GCSSEPM Foundation 20th Annual Research Conference, 782-805

Pirmez, C., Imran, J., 2003. Reconstruction of turbidity currents in Amazon Channel. Marine and Petroleum Geology, 20, 823–849.

Pirmez, C., Prather, B.E., Mallarino, G., O'Hayer, W.W., Droxler, A.W., Winker, C.D., 2012. Chronostratigraphy of the Brazos-Trinity depositional system, western Gulf of Mexico: Implications for deepwater depositional models. Application of the principles of seismic geomorphology to continental-slope and base-of-slope systems: case studies from seafloor and near-seafloor analogues. SEPM Special Publication, 99, 111-143.

Poblet, J., Hardy, S., 1995. Reverse modelling of detachment folds; application to the Pico del Aguila anticline in the South Central Pyrenees (Spain). Journal of Structural Geology, 17, 1707–1724.

Poblet, J., Bulnes, M., McClay, K., and Hardy, S., 2004. Plots of crestal structural relief and fold area versus shortening—A graphical technique to unravel the kinematics of thrust-related folds, in: McClay, K.R. (Ed.), Thrust tectonics and hydrocarbon systems. AAPG Memoir 82, 372– 399.

Posamentier, H.W., Kolla, V., 2003. Seismic geomorphology and stratigraphy of depositional elements in deep-water settings. Journal of Sedimentary Research, 73, 367–388.

Posamentier, H.W., 2003. Depositional elements associated with a basin floor channel–levee system: case study from the Gulf of Mexico. Marine and Petroleum Geology 20, 677–690.

Posamentier, H.W., Davies, R.J., Wood, L., 2007. Seismic geomorphology—an overview. In: Davies, R.J., Posamentier, H.W., Wood, L.J., Cartwright, J.A., (Eds.), Seismic geomorphology: applications to hydrocarbon exploration and production. Geological Society of London, Special Publication 277, 1–14.

Prather, B.E., Booth, J.R., Steffens, G.S. and Craig, P.A., 1998. Classification, lithologic calibration and stratigraphic succession of seismic facies of intraslope basins, deep-water Gulf of Mexico. AAPG Bulletin, 82, 701–728.

Prather, B., 2000. Calibration and visualization of depositional process models for above-grade slopes: a case study from the Gulf of Mexico. Marine and Petroleum Geology, 17, 619-638.

Prather, B.F., Keller, F.B., Chapin, M.A., 2000. Hierarchy of deep-water architectural elements with reference to seismic resolution: Implications for reservoir prediction and modeling depositional systems. In: Weimer, P., Sian, R.M., Coleman, J.L., Rosen, N., Nelson, C.H., Bouma, A.H., Styzen, M., Lawrence, D.T. (Eds.), Global Deep-Water Reservoirs. Gulf Coast Section SFPM Foundation 20th Annual Bob F Perkins Research Conference, 817–835.

Prather, B.E., Deptuck, M., Mohrig, D., Van-Horn, B., Wynn, R.B., 2012. Application of the principles of seismic geomorphology to continental-slope and base-of-slope systems: case studies from seafloor and near-seafloor analogues. SEPM Special Publication, 99, 5 – 9.

Prior, D.B., Suhayda, J.N., Lu, N.Z., Bornhold, B.D., Keller, G.H., Wiseman, W.J., Wright, L.D., Yang, Z.S., 1989. Storm wave reactivation of a submarine landslide. Nature, 341, 47– 50.

Reading, H.G., Richards, M., 1994. Turbidite system in deep-water basin margins classified by grain size and feeder system. AAPG Bulletin, 78, 792–822.

Reijers, T.J.A., Petters, S.W., Nwajide, C.S., 1997. The Niger Delta basin. in: Selley, R.C., (Ed.), African basins. Sedimentary Basins of the World, 3, 151-172.

Rowan, M.G., 1997. Three-dimensional geometry and evolution of a segmented detachment fold, Mississippi Fan fold belt, Gulf of Mexico. Journal of Structural Geology 19, 463–480.

Rowan, M.G., Peel, F.J., Vendeville, B.C., 2004. Gravity-driven fold belts on passive margins, in: McClay, K.R. (Ed.), Thrust tectonics and hydrocarbon systems. AAPG Memoir, 82, 157-182.

Rouby, D., Nalpas, T., Jermannaud, P., Robin, C., Guillocheau, F., Raillard, S., 2011. Gravity driven deformation controlled by the migration of the delta front: the Plio-Pleistocene of the Eastern Niger Delta. Tectonophysics, 513, 1–11.

Savoye, B., Babonneau, N., Dennielou, B., Bez, M., 2009. Geological overview of the Angola–Congo margin, the Congo deep-sea fan and its submarine valleys. Archimer, 56, 2169 – 2182.

Shanmugam, G., Miola, R.J., 1988. Submarine Fans: characteristics, models, classification, and reservoir potential. Earth-Science Reviews, 24, 383-428.

Shanmugam, G., 2006. Deep-Water Processes and Facies Models: Implications for Sandstone petroleum reservoirs. Amsterdam, Elsevier, 476 p.

Shaw, J.H., Novoa, E., Connors, C.D., 2004. Structural controls on growth stratigraphy in contractional fault-related folds, in: McClay, K.R. (Ed.), Thrust tectonics and hydrocarbon systems: AAPG Memoir, 82, 400 - 412.

Shepard, F.P., McLoughlin, P.A., Marshall, N.F., Sullivan, G.G., 1977. Current-meter recordings of low speed turbidity currents. Geology, 5, 297– 301.

Sheriff, R.E., 2002. Encyclopedic dictionary of applied geophysics (4rd ed.), Society of Exploration Geophysicists, ISBN 1-56080-118-2.

Short, K.C., Stauble, A.J., 1965. Outline of geology of Niger Delta. AAPG Bulletin, 51, 761-779.

Sikkima, W., Wojcik, K.M., 2000. 3D visualization of turbidite systems, Lower Congo Basin, offshore Angola, in: Weimer, P., Slatt, R.M., Coleman, J., Rosen, N.C., Nelson, H., Bouma, A.H., Styzen, M.J., and Lawrence, D.T., (Eds.), Deep-Water Reservoirs of the World. Gulf Coast Society of the Society of Economic Paleontologists and Mineralogists Foundation, 20th Annual Research Conference, 928–939.

Simoes, M., Avouac, J.P., Chen, Y.-G., Singhvi, A.K., Wang, C.-Y., Jaiswal, M., Chan, Y.-C., Bernard, S., 2007. Kinematic analysis of the Pakuashan fault tip fold, west central Taiwan: Shortening rate and age of folding inception. Journal oF Geophysical Research, 112, B03S14, doi:10.1029/2005JB004198.

Smith, R., 2004. Silled sub-basins to connected tortuous corridors; sediment distribution systems on topographically complex sub-aqueous slopes. In: Lomas, S.A., and Joseph, P., (Eds.), Confined Turbidite Systems. Geological Society London, 222, 23-43.

Straub, K.M., Mohrig, D., McElroy, B., Buttles, J., 2008. Interactions between turbidity currents and topography in aggrading sinuous submarine channels: a laboratory study. GSA Bulletin 120, 368 – 385.

Straub, K.M., Paola, C., Mohrig, D., Wolinsky, M.A., George, T., 2009. Compensational stacking of channelized sedimentary deposits. Journal of Sedimentary Research, 79, 673 – 688.

Straub, K.M., Mohrig, D., Buttles, J., McElroy, B., Pirmez, C., 2011. Quantifying the influence of channel sinuosity on the depositional mechanics of channelized turbidity currents: a laboratory study. Marine and Petroleum Geology 28, 744 – 760.

Storti, F., Poblet, J., 1997. Growth stratal architectures associated with de´collement folds and fault propagation folds. Inferences on fold kinematics. Tectonophysics, 282, 353–373.

Stow, D.A.V., Mayall, M., 2000. Deep-water sedimentary systems: new models for the 21st century. Marine and Petroleum Geology, 17, 125–135.

Suppe, J., Medwedeff, D.A., 1990. Geometry and kinematics of fault-propagation folding. Eclogae Geologicae Elvetiae, 83, 409–454.

Suppe, J., Chou, G.T., Hook, S.C., 1992. Rates of folding and faulting determined from growth strata. In: McClay, K.R. (Ed.), Thrust Tectonics. Chapman and Hall, London, 105–121p.

Talling, P.J., Masson, D.G., Sumner, E.J., Malgesini, G., 2012. Subaqueous sediment density flows: depositional processes and deposit types. Sedimentology, 59, 1937-2003.

Talling, P.J., Paull, C.K., and Piper, D.J.W., 2013. How are subaqueous sediment density flows triggered, what is their internal structure and how does it evolve? Direct observations from monitoring of active flows. Earth Science Reviews, doi: 10.1016/j.earscirev.2013.07.005.

Tucker, G.E., Bras, R.L., 1998. Hillslope processes, drainage density, and landscape morphology. Water Resources Research, 34, 2751–2764.

Tucker, G.E., Whipple, K.X., 2002. Topographic outcomes predicted by stream erosion models: sensitivity analysis and intermodel comparison. Journal of Geophysical Research, 107(B9): doi:10.1029/2001JB000162.

Twichell, D.C., Schwab, W.C., Nelson, C.H., Kenyon, N.H., Lee, H.J., 1992. Characteristics of a sandy depositional lobe on the outer Mississippi fan from SeaMARC IA sidescan sonar images. Geology, 20(8), 689-692.

Van der Beek, P., Champel, B., Mugnier, J-L., 2002. Control of detachment dip on drainage development in regions of active fault-propagation folding. Geology, 30, 471 – 474.

Vidal-Royo, O., Cardozo, N., Munoz, J.A., Hardy, S., and Maerten, L., 2012. Multiple mechanisms driving detachment folding as deduced from 3D reconstruction and geomechanical restoration: the Pico del Aguila anticline (External Sierras,Southern Pyrenees). Basin Research, 24, 295-313.

Weimer, P., 1991. Seismic facies, characteristics and variations in channel evolution, Mississippi Fan (Plio–Pleistocene), Gulf of Mexico, in: Weimer, P., and Link, M.H., (Eds.), seismic facies and sedimentary processes of submarine fans and turbidite systems: New York, Springer-Verlag, 323–347.

Whipple, K.X., Tucker, G.E., 2002. Implications of sediment-flux dependent river incision models for landscape evolution, Journal of Geophysical Research, 107(B2), doi:10.1029/2000JB000044.

Whittaker, A.C., Cowie, P.A., Atta, l.M., 2007. Bedrock channel adjustment to tectonic forcing: Implications for predicting river incision rates. Geology, 35, 103-106

Whittaker, A.C., Attal, M., Cowie, P.A., 2008. Decoding temporal and spatial patterns of fault uplift using transient river long profiles, Geomorphology, 100, 506-526.

Whittaker, A.C., 2012. How do landscapes record tectonics and climate?. Lithosphere, 4, 160-164.

Whiteman, A.J., 1982. Nigeria: its Petroleum Geology, Resources and Potential: Graham and Trotman, 1, 166p.

Winker, C.D., Booth, J.R., 2000. Sedimentary dynamics of the salt-dominated continental slope, Gulf of Mexico: integration of observations from the sea floor, near-surface and deep subsurface, in: Weimer, P., Slatt, R.M., Coleman, J., Rosen, N.C., Nelson, H., Bouma, A.H., Styzen, M.J., and Lawrence, D.T., (Eds.), Deep-Water Reservoirs of the World: Gulf Coast Society of the Society of Economic Paleontologists and Mineralogists Foundation, 20th Annual Research Conference, 1059–1086.

Wu, S., Bally, A.W., 2000. Slope tectonics-Comparisons and contrasts of structural styles of salt and shale tectonics of the northern Gulf of Mexico with shale tectonics of offshore Nigeria. In: Mohriak, W., and Talwani, M., (Eds.), Atlantic rifts and continental margins: Washington, D.C., American Geophysical Union, 151 –172.

Wynn, R.B., Masson, D.G., Stow, D.A.V., Weaver, P.P.E., 2000a. Turbidity current sediment waves on the submarine slopes of the western Canary Islands. Marine Geology, 163, 185 –198.

Wynn, R.B., Weaver, P.P.E., Ercilla, G., Stow, D.A.V., Masson, D.G., 2000b. Sedimentary processes in the Selvage sediment- wave field, NE Atlantic: new insights into the formation of sediment waves by turbidity currents. Sedimentology, 47, 1181 –1197.

Xu, J.P., Noble, M.A., Rosenfeld, L.K., 2004. In-situ measurements of velocity structure within turbidity currents, Geophys. Res. Letters, 31, Art. No. L09311.

Xu, J.P., Swarzenski, P.W., Noble, M., Li, A.C., 2010. Eventdriven sediment flux in Hueneme and Mugu submarine canyons, southern California. Mar. Geol., 269, 74–88.

Xu, J.P., 2011. Measuring currents in submarine canyons: technological and scientific progress in the past 30 years. Geosphere, 7, 868–876.

Yanite, B.J., Tucker, G.E., Hsu, H.-L., Chen, C., Chen, Y.-G., and Mueller, K.J., 2011. The influence of sediment cover variability on long-term river incision rates: An example from the Peikang River, central Taiwan. Journal of Geophysical Research, 116, F03016, doi:10.1029/2010JF001933.